Ultrafast charge transfer in WS_2/graphene heterostructures

Dissertation

zur Erlangung des Doktorgrades an der Fakultät für Mathematik, Informatik und Naturwissenschaften

Fachbereich Physik
der Universität Hamburg

Vorgelegt von
Razvan Krause

Hamburg
2021

Gutachter der Dissertation:	Prof. Dr. Isabella Gierz-Pehla
	Prof. Dr. Ludwig Mathey
Zusammensetzung der Prüfungskommission:	
	Prof. Dr. Isabella Gierz-Pehla
	Prof. Dr. Ludwig Mathey
	Prof. Dr. Arwen Pearson
	Prof. Dr. Nils Huse
	Dr. James McIver
Vorsitzender des Prüfungskommission:	Prof. Dr. Arwen Pearson
Datum der Disputation:	30.09.2021
Vorsitzender des Promotionsausschusses:	Prof. Dr. Wolfgang Hansen
Leiter des Fachbereich Physik:	Prof. Dr. Günter H. W. Sigl
Dekan der Fakultät MIN:	Prof. Dr. Heinrich Graener

Abstract

Electronic industry is still growing with incredible speed and is continously demanding for faster and more efficient devices. But the conventional silicon- and III-V-semiconductor technology seizes up by reaching its physical limits. To catch up with miniaturization, fresh ideas and new material systems are needed.

Promising candidates are ultimately thin van-der-Waals (vdW) heterostructures built from two-dimensional (2D) crystals which can be stacked in arbitrary configurations to built nanoscale devices. Of particular interest are heterostructures built of graphene with high carrier mobility and monolayers of transitions metal dichalcogenides (TMDs) featuring a direct band gap and strong absorption of visible light. TMD/graphene heterostructures were found to show an ultrafast charge transfer after optical excitation and efficient charge separation. This is interesting for the use in photodetectors or photovoltaics but also in opto-spintronics as the charge transfer might by accompanied by a spin transfer when using circularly polarized light for spin-selective optical excitation. But until now, the microscopic mechanism behind the ultrafast charge trasfer is not yet understood and controversely debated.

In this thesis the ultrafast charge transfer in epitaxial WS_2/graphene heterostructures was investigated by means of time- and angle-resolved photoemission spectroscopy (tr-ARPES) which allows a direct view on photocarrier dynamics. A visible 2 eV pump pulse excites the heterostructure resonantly to the A-excitonic transition in WS_2. And a delayed probe pulse takes snapshots of the electronic bandstructure as a function of pump-probe delay by ejecting photoelectrons from the sample to the detector where they are analyzed in their energy and momentum.

We found evidence for ultrafast charge separation in WS_2/graphene by asymmetric population dynamics, charging shifts and an increasing hole density in graphene. The hole transfer to graphene is ultrafast with less than 200 fs while the charge separation persists for 1 ps. By combining a pump fluence dependent study with many-body theory we

developed a microscopic model for the ultrafast charge transfer and identified the main charge transfer channels. The timescale for charge separation is set by direct tunneling via band intersections close to the K point and the lifetime for charge separation is set by defect-assisted tunneling via localized Sulfur vacancies. This mechanism can also explain the ultrafast charge transfer in bilayer WS_2/graphene heterostructures with an indirect WS_2 band gap. Photoexcitation at the Σ valley of the Brillouin zone in monolayer WS_2/graphene leads to intervalley scattering to the K valley within 400 fs followed by ultrafast charge transfer. At the points in the Brillouin zone where WS_2 and graphene bands intersect a hybridization allows for charge transfer between the layers as predicted by density functional theory. We further found a non-rigid valence band shift in WS_2 which can be traced back to momentum dependent bandgap renormalization with the help of many-body GW calculations.

For the different heterostructures and excitation scenarios in this thesis the developed microscopic model was shown to be robust. It thus provides important conclusions for the design of future opto-electronic and opto-spintronic devices based on TMD/graphene heterostructures.

Zusammenfassung

Die Elektronikindustrie wächst weiterhin mit rasanter Geschwindigkeit und verlangt stets nach schnelleren und effizienteren Baugruppen. Die klassische Silizium- und III-V Halbleitertechnologie gerät allerdings ins Stocken da sie ihre physikalischen Grenzen erreicht. Um die Miniaturisierung fortzusetzen werden frische Ideen und neue Materialsysteme benötigt.

Vielversprechende Kandidaten sind ultimativ dünne van-der-Waals Heterostrukturen gebaut aus zweidimensionalen (2D) Kristallen, die in beliebigen Konfigurationen gestapelt werden können um nanoskalige Geräte zu bauen. Dabei sind von besonderem Interesse Heterostrukturen aus Graphen mit hoher Ladungsträgermobilität und Monolagen von Übergangsmetalldichalogeniden (TMDs) mit einer direkten Bandlücke und außerordentlich starker Absorption von sichtbaren Licht. TMD/Graphen Heterostrukturen zeigen nach optischer Anregung einen ultraschnellen Ladungstransfer und effiziente Ladungstrennung. Das ist interessant für ihre Verwendung in der Optoelektronik und auch der Optospintronik, da der Ladungstransfer an einen Spintransfer geknüpft sein könnte wenn man mit zirkular polarisiertem Licht Spin-selektiv anregt. Aber bisher ist der mikroskopische Mechanismus hinter dem ultraschnellen Ladungstransfer noch nicht verstanden und wird kontrovers diskutiert.

In dieser Arbeit wird der ultraschnelle Ladungstransfer in eptaktischen WS_2/Graphen Heterostrukturen mittels zeit- und winkelaufgelöster Photoemissionsspektroskopie (tr-ARPES) untersucht, welche einen direkten Blick auf die Dynamik von angeregten Ladungsträgern erlaubt. Ein sichtbarer 2 eV Anregungspuls regt die Heterostruktur resonant zum A-Exziton in WS_2 an. Und ein verzögerter Abfragepuls macht Schnappschüsse der elektronischen Bandstruktur als Funktion der Verzögerung beider Laserpulse indem Photoelektronen emittiert, die einem Detektor in ihrer Energie und Impuls analysiert werden.

Wir haben asymmetrische Besetzungsdynamik, Aufladungsverschiebungen und eine er-

höhte Lochdichte in Graphen als Beweise für ultraschnelle Ladungstrennung in WS_2/Graphen gefunden. Der Lochtransfer ins Graphen ist ultraschnell mit weniger als 200 fs während die Ladungstrennung für 1 ps anhält.
Durch Kombination einer Studie der Abhängigkeit von der Photonenflussdichte und Vielteilchentheorie haben wir ein mikroskopisches Modell für den ultraschnellen Ladungstransfer entwickelt und die primären Transferkanäle identifiziert. Die Zeitskala für Ladungstrennung wird durch direktes Tunneln über Kreuzungspunkte von Bändern in der Nähe des K Punktes bestimmt und die Lebensdauer der Ladugstrennung über Fehlstellen-unterstütztes Tunneln and Schwefel-Leerstellen. Der Mechanismus kann auch den ultraschnellen Ladungstransfer in Bilagen WS_2/Graphen mit indirekter Bandlücke in WS_2 erklären. Optische Anregung nahe des Σ-Punktes in der Brillouin-Zone in Monolagen WS_2/Graphen führt zur Intervalley-Streuung zum K Punkt innerhalb von 400 fs gefolgt von ultraschnellem Ladungstransfer. An den Punkten in der Brillouin-Zone, wo sich WS_2- und Graphen-Bänder kreuzen, wird der Ladungstransfer erlaubt durch eine Hybridisierung, die von Dichtefunktionaltheorie berechnet wurde. Wir haben weiterhin eine nicht-starre Verschiebung des Valenzbands in WS_2 gefunden, die auf impulsabhängige Bandrenormalisierung mit der Hilfe von Vielteilchen-GW Berechnungen von zurückgeführt werden konnte.
Das entwickelte mikroskopische Modell in dieser Arbeit hat sich als robust erwiesen für verschiedene Heterostrukturen und Anregungsszenarien. Deshalb bietet es wichtige Schlussfolgerungen die das Design von optoelektronischen und optospintronischen Bauteilen basierend auf TMD/Graphen Heterostrukturen.

List of Publications

The results in this thesis are based on my work as doctoral student within the Otto Hahn Group for Ultrafast Electron Dynamics of Prof. Isabella Gierz-Pehla at the Max Planck Institute for the Structure and Dynamics of Matter in Hamburg and within her Group at the Institute of Experimental and Applied Physics at Universität Regensburg. I would further like to thank the *SFB 925 "Light induced dynamics and control of strongly correlated quantum systems"* and the *SFB 1277: "Emergent relativistic effects in condensed matter"* for partly funding this work.

Publications relevant for the thesis

1. S. Aeschlimann, A. Rossi, M. Chávez-Cervantes, **R. Krause**, B. Arnoldi, B. Stadtmüller, M. Aeschlimann, S. Forti, F. Fabbri, C. Coletti and I. Gierz, *Direct evidence for ultrafast charge separation in epitaxial WS_2/graphene heterostructures*, Science Advances 6, eeay0761, 2020 [1].

   I took part at the tr-ARPES experiments.

2. **R. Krause**, S. Aeschlimann, M. Chávez-Cervantes, R. Perea-Causin, S. Brem, E. Malic, S. Forti, F. Fabbri, C. Coletti and I. Gierz, *Microscopic understanding of ultrafast charge transfer in van-der-Waals heterostructures*, under consideration in Phys. Rev. Lett., arXiv:2012.09268, 2021 [2].

   I performed the tr-ARPES experiments, analyzed the experimental data and wrote the first draft of the manuscript.

3. **R. Krause**, M. Chávez-Cervantes, S. Aeschlimann, S. Forti, F. Fabbri, A. Rossi, C. Coletti, C. Cacho, Y. Zhang, P. E. Majchrzak, R. T. Chapman, E. Springate and I. Gierz, *Ultrafast charge separation in bilayer WS_2/graphene heterostructure*

revealed by time- and angle-resolved photoemission spectroscopy, Frontiers in Physics 9, 668149, 2021 [3].

I took part at the tr-ARPES experiments, analyzed the experimental data and wrote the first draft of the manuscript.

Manuscripts in preparation

4. **R. Krause**, S. Aeschlimann, M. Chávez-Cervantes, S. Forti, F. Fabbri, C. Coletti and I. Gierz, *Intervalley scattering and ultrafast charge transfer in WS_2/graphene heterostructures*, manuscript in preparation [4].

   I performed the tr-ARPES experiments, analyzed the experimental data and wrote the first draft of the manuscript.

5. **R. Krause**, A. Steinhoff, S. Aeschlimann, M. Chávez-Cervantes, T. O. Wehling, S. Refaely-Abramson, S. Forti, F. Fabbri, C. Coletti and I. Gierz, *Momentum dependence of light-induced band gap renormalization in WS_2/graphene heterostructure*, manuscript in preparation [5].

   I performed the tr-ARPES experiments, analyzed the experimental data and wrote the first draft of the manuscript.

Other publications

I took part at the tr-ARPES experiments for the following publications:

6. S. Aeschlimann, M. Chávez-Cervantes, **R. Krause**, S. Forti, F. Fabbri, K. Hanff, K. Roßnagel, C. Coletti and I. Gierz, *"On the survival of Floquet-Bloch states in the presence of scattering"*, Nano Lett. 21, 12, 5028–5035, 2021 [6].

7. M. Chávez-Cervantes, G. Topp, S. Aeschlimann, **R. Krause**, S. Sato, M. Sentef and I. Gierz, *"Charge density wave melting in one-dimensional wires with femtosecond subgap excitation*, Phys. Rev. Lett. 123, 036405, 2019 [7].

8. M. Chávez Cervantes, **R. Krause**, S. Aeschlimann and I. Gierz, *"Band structure dynamics in indium wires"*, Phys. Rev. B 97, 201401, 2018 [8].

9. S. Aeschlimann, **R. Krause**, M. Chávez-Cervantes, H. Bromberger, R. Jago, E. Malic, A. Al-Temimy, C. Coletti, A. Cavalleri and I. Gierz, *"Ultrafast momentum imaging of pseudospin-flip excitations in graphene"*, Phys. Rev. B 96, 020301, 2017 [9].

Contents

1 Motivation **1**

2 TMD/Graphene Heterostructures **5**
2.1 Graphene . . . 5
2.1.1 Structure . . . 6
2.1.2 Band Structure and Electronic Properties . . . 7
2.2 Transition Metal Dichalcogenides (TMDs) . . . 9
2.2.1 Structure . . . 9
2.2.2 Band Structure . . . 10
2.2.3 Excitonic Transitions . . . 12
2.2.4 Spin-Valley Physics . . . 14
2.3 Van-der-Waals Heterostructures . . . 15
2.3.1 Hybridization and Proximity-Induced Effects . . . 15
2.3.2 Ultrafast Charge Transfer in TMD Heterostructures . . . 17

3 Experimental Techniques **19**
3.1 Time- and Angle Resolved Photoemission Spectroscopy (tr-ARPES) . . . 20
3.1.1 Photoemission Spectroscopy . . . 20
3.1.2 Description of Photoemission . . . 20
3.1.3 Angle- Resolved Photoemission Spectroscopy . . . 25
3.1.4 Time-and Angle-Resolved Photoemission Spectroscopy . . . 28
3.1.5 Generation of Extreme Ultraviolet (XUV) Probe Beam . . . 31
3.1.6 Pump Beam Generation . . . 36
3.1.7 Photoelectron Detection . . . 37
3.1.8 Space Charge Effects . . . 38
3.2 Sample Preparation . . . 39

3.2.1 Common Van-der-Waals Heterostructure Preparation Methods . . . 39
3.2.2 Preparation of Epitaxial WS_2/Graphene Heterostructure Samples . 42
3.3 State of the Art: Direct Evidence for Efficient Ultrafast Charge Separation Revealed by Tr-ARPES . . . 47

4 Microscopic Understanding of Ultrafast Charge Transfer 51
4.1 Introduction . . . 51
4.2 Results . . . 52
4.3 Discussion . . . 55

5 Ultrafast charge separation in bilayer WS_2/graphene heterostructure 67
5.1 Introduction . . . 67
5.2 Results . . . 69
5.3 Discussion . . . 75

6 Intervalley Scattering and Ultrafast Charge Transfer 79
6.1 Introduction . . . 79
6.2 Results . . . 80
6.3 Discussion . . . 82

7 Momentum dependence of light-induced band gap renormalization 91
7.1 Introduction . . . 91
7.2 Results . . . 92
7.3 Discussion . . . 96

8 Conclusions and Outlook 99
8.1 Conclusions . . . 99
8.2 Outlook . . . 100
8.2.1 Heterostructures of Monolayer WS_2 on Thermal Decomposited Monolayer Graphene . . . 100
8.2.2 Oscillations in Tr-ARPES Data . . . 106
8.2.3 Refinement and Substantiation of the Microscopic Model . . . 110
8.2.4 Next Generation Tr-ARPES . . . 111

Appendices 113

A Tr-ARPES Data Analysis 115
A.1 Treatment of Raw Data . . . 115
A.2 k-Space Conversion and Experimental Resolution . . . 117
A.3 Pump Fluence and Excitation Density: . . . 117

A.4 Determination of Transient Band Positions . . . 121
A.5 Fit Function for Exponential Decay . . . 123
A.6 Determination of the Equilibrium Band Gap . . . 123
A.7 Fermi-Dirac fits of Electron Distribution Inside Dirac Cone . . . 124
A.8 Estimation of the Transient Electronic Temperature in WS_2 . . . 125
A.9 Temporal Matching of Assembled Datasets . . . 127
A.10 Direct Transitions to WS_2 Bands at 3.1 eV Excitation Energy . . . 129

B Additional Tr-ARPES Data **133**
B.1 Photocarrier Dynamics of Quasi Freestanding Monolayer Graphene . . . 133
B.2 Comparison of VB Shifts with Integrated Photocurrent Above the Equilibrium Position of the Valence Band . . . 133
B.3 Additional Tr-ARPES Data for Other Pump Fluences . . . 136
B.4 Evidence for In-Gap Defect States . . . 140
B.5 Momentum Dependent Valence Band Shifts . . . 140

C Many-Body Theory **143**
C.1 Microscopic Model of Charge Transfer . . . 143
C.2 Screened Exchange in TMD Monolayers . . . 146

Bibliography **149**

Acknowledgements **168**

Chapter 1

Motivation

When getting smaller one can enter interesting new worlds – like Alice could enter wonderland by a shrinking potion [10]. Similarly, when dimensionality is shrinked particles can enter a just as colorful and seemingly illogical world: the "quantum world". Propelled by the need of faster and power efficient electronics for smartphones, computers, consumer electronics and so on, the dimensions of electronic components got continously smaller (currently 5 nm [11]) and did thereby enter the quantum world. But as quantum mechanical effects emerge, components like transistors based on silicon or III-V semiconductors reach their physical limits by shorting due to tunneling or carrier trapping at defects. Further miniaturization is restricted and the famous Moore's law seems to come to an end [12].

A possible way out are two-dimensional (2D) crystals – beeing *sub*-nm due to atomar thickness – with unique electronic properties. By now a variety of 2D materials were discovered and they span the complete range with metallic, semimetallic, semiconducting or insulating behavior [13].

The recent development of growth and transfer techniques allows arbitrary stacking of several 2D crystals to ultimately thin heterostructures with device functionality. Lattice matching conditions like in conventional heterostructures are negligible due to the relatively weak van-der-Waals (vdW) forces between the layers and countless different heterostacks can be built [14, 15]. Several proof-of-principle devices based on vdW-heterostructures have been realized: For example transistors [16–18], light emitting diods [19, 20] and photodiods [21–25]. The technical progress allows to dream of flexible electronics like photovoltaic panels embedded in clothing [26, 27].

However, of particular interest are heterostructures that combine graphene with semi-

conducting transition metal dichalcogenides (TMDs). The famous semimetallic graphene shows exceptionally high carrier mobility and long spin lifetimes [28,29]. And TMD monolayers got into the scientific spotlight due to their strong optical absorption in the visible range, strong spin-orbit coupling and a direct band gap [30–33]. Interestingly, optical excitation of the TMD monolayer is followed by ultrafast charge transfer into the graphene layer [21, 34–39] and anisotropic transfer rates lead to charge separation. In addition the charge transfer might be accompanied by spin injection into graphene when using circularly polarized light [40–42]. The efficient charge separation an the interface provides enormous potential for applications in opto-electronics and opto-spintronics. But the underlying microscopic mechanism for ultrafast charge transfer in TMD/graphene heterostructures is not understood yet.

Alice did find her path through wonderland equipped with curiosity and by continously asking questions. In a similar manner, we do ask:

- If the vdW coupling between layers is believed to be weak: Why is the charge transfer ultrafast?
- Why are transfer times for photoexcited holes and electrons asymmetric?
- What are the timescales for charge recombination?
- Is intervalley scattering of carriers involved in interlayer transfer?
- Is orbital overlap needed for charge transfer?
- Is the charge transfer accompanied by a large momentum change?
- Where does the charge transfer happen within the Brillouin zone?
- Which practical requirements have to be met for ultrafast charge separation?

The main motivation of this thesis is shining some light onto the microscopic mechanism of charge transfer and the applicability onto different samples and excitation scenarios.

To date, mainly all-optical techniques were employed to investigate ultrafast charge transfer phenomena in vdW heterostructures. But they provide a rather indirect view on photocarrier populations and lack of momentum resolution. In this thesis we developed a time- and angle-resolved photoemission spectroscopy (tr-ARPES) setup which allows a direct view on photocarrier populations in energy, momentum and time. As the interface quality is crucial for the observation of ultrafast charge transfer [37] we use high-quality epitaxial WS_2/graphene heterostructures grown by chemical vapor deposition (CVD).

When photoexcited resonant to the strong A-excitonic peak in WS_2, we observe experimental evidence for ultrafast charge transfer in: asymmetric population dynamics, charging shifts and holes transferred to graphene. After excitation, holes in WS_2 are instantaneously refilled by electrons from graphene. The remaining electrons in WS_2 and holes in graphene then build a charge separated state. By using tr-ARPES and many-body theory we find the timescale for charge separation is set by direct tunneling at the band intersections of WS_2 and graphene bands close to the K-point. The timescale for electron-hole recombination, on the other hand, is set by defect-assisted tunneling via localized S vacancies.

The developed charge transfer model is further found to be applicable for photoexcitation close to the Σ point of the Brillouin zone as well as for bilayer WS_2/graphene heterostructures. The foundation of the model is strenghtend by density functional theory calculations which predict hybridization at the points in the Brillouin zone where WS_2 and graphene bands cross. We further observed a non-rigid WS_2 valence band shift following optical excitation in a WS_2/graphene heterostructure which we can trace back to momentum dependent bandgap renormalization with the help of many-body GW calculations. The developed microscopic model for charge transfer is applicable to other TMD/graphene heterostructures and provides important conclusions for the design of novel opto-electronic and opto-spintronic devices.

The thesis is structured as follows: An introduction to TMD/graphene heterostructures is given in chapter 2. The experimental tr-ARPES setup and sample preparation is explained in chapter 3. This chapter peaks into the first direct observation of ultrafast charge transfer with a state-of-the-art tr-ARPES experiment. Chapter 4 expands the analysis and derives the microscopic model for charge transfer based on pump fluence dependent experiments. Bilayer WS_2/graphene heterostructures are investigated in chapter 5. The interplay between charge transfer and intervalley scattering is investigated in chapter 6 and the momentum dependent valence band shift in chapter 7. The thesis closes with a summary of the findings and an outlook based on the experiments of the previous chapters. And with this our journey to heterostructure wonderland will come to an end.

Chapter 2

TMD/Graphene Heterostructures

The attractiveness of nanoscale physics and devices stems from the reduction of the dimensionality. New physics come into play as soon as the spatial extend of the material becomes comparable to the de Broglie wavelength. Confinement in one, two or three spatial directions results in the formation of quantum wells, quantum wires and quantum dots, respectively.
Quantum wells, produced by sequential doping of semiconductors and intensively studied in the past, are the basis for the field effect transistor electronics in our everyday life [43]. In the two-dimensional (2D) quantum well the formation of a two-dimensional electron gas (2DEG) gives rise to quantum effects not present in the bulk case, like the quantum hall effect at low temperatures and high magnetic fields [44].
The 2D materials investigated in this thesis consist of layers with a thickness of just a few atoms with a total thickness below 1 nm. As such their properties are determined by the confinement in 2D, e.g. graphene exhibits a (half integer) quantum hall effect [45]. This chapter will introduce the quasi 2D-materials graphene and monolayer transition metal dichalcogenides and finally discuss 2D-heterostructures built from them.

2.1 Graphene

Common household scotch tape can thin down bulk graphite into a one atom thick carbon layer and produce a modern nanotechnology material. Although it was long believed that such a 2D crystal would be unstable, this discovery of graphene in 2004 has led a revolution in nanoscale physics and to a variety of technical devices and applications [45–47].

2.1.1 Structure

Graphene is ordered in a hexagonal honeycomb lattice as visualized in Fig. 2.1. The carbon atoms are sp^2 hybridized and bound to each other in-plane by σ bonds. In the out-of-plane direction the p_z orbitals form π-bonds. As highlighted in Fig. 2.1b the honeycomb lattice is composed out of two triangular sublattices (pink, violet) mirror symmetric to another [48].

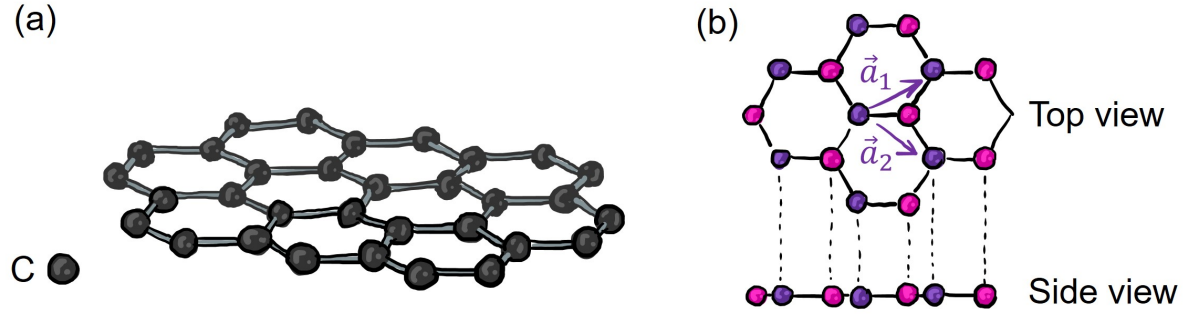

Figure 2.1: Crystal structure of graphene: (a) Lattice structure. (b) Top and side view. The unit cell is spanned by the lattice vectors $\vec{a}_1$ and $\vec{a}_2$ with length 2.46 Å [48]. Representation inspired by [49].

Graphene exhibits unique mechanical properties due to the strong σ-bonds [50]. It's Young's Modulus of 1 TPa and intrisic tensile strength of 130 GPa make it the strongest material ever measured although it is ultimately thin. Macroscopic sheets of graphene can be reversely bent and were proposed as substrate material for flexible electronics [26, 27].

2.1.2 Band Structure and Electronic Properties

Similarly, graphene's electronic properties are outstanding. The electronic and optical response is dominated by the π-bands forming two cosine-shaped bands, displayed in Fig. 2.2a [29, 51, 52]. It can be seen that the valence and conduction band touch at the K and K' points at the corners of the Brillouin zone at an energy E_D, referred to as Dirac-point. In consequence, graphene is a zero-gap semiconductor, if the chemical potential is located at E_D, and semimetallic otherwise.

A zoom-in into the band structure close to the K and K' points (see Fig. 2.2b) reveals a linear dispersion of the π-bands of $\epsilon(k) = \pm\hbar v_F|k|$, like photons [52]. v_F denotes the Fermi velocity and k the in-plane momentum. Therefore, the carriers inside graphene behave like massless Dirac fermions [47]. Due to the double-cone shape the regions around the K and K' points are called Dirac-cones (see Fig. 2.2b).

Graphene also possesses a high Fermi velocity v_F of $\sim 10^6$ m/s [52,54] which is independent of changes in chemical potential by doping or gating, thanks to the linear dispersion. But

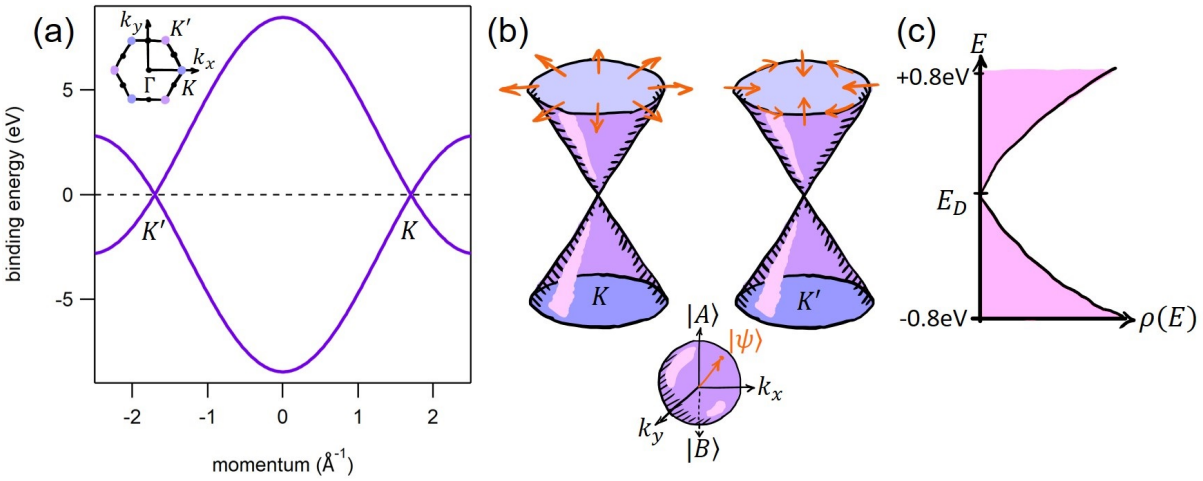

Figure 2.2: Band structure of graphene: (a) Tight binding band structure [51,52]. The inset shows the hexagonal Brillouin zone. (b) Sketch of the Dirac cones at the K and K' points with pseudospin texture indicated by the orange arrows. Adapted from [53]. The pseudospin of the wave function $|\psi\rangle$ is defined in the Bloch sphere below where $|A\rangle$ and $|B\rangle$ indicate localization on the two sublattices (cf. Fig. 2.1b). (c) Density of states $\rho(E)$ within the Dirac-cone. Adapted from [29].

the Density of states (DOS) $\rho(E)$ is strongly dependent on the position of the chemical potential and even vanishes at E_D, as can be seen in Fig. 2.2c. The linear dispersion also leads to a uniform absorbance of light in the visible range [52].

As the carbon atoms are light-weighted, the spin-orbit coupling in pristine graphene is negligible [55]. Thus, injected spin-polarized carriers show very long spin lifetimes of ns (equal to mean free paths of μm) even at room temperature [54, 56, 57]. Hence, graphene gained some interest as spin transport material in spintronics devices.

Because of the low spin-orbit coupling the Dirac-carriers are spin-degenerate. But they can be distinguished by another quantum number, the pseudospin. First of all, the pseudospin is not connected to the spin of carriers. The pseudospin results from the localization of the wave function on the sublatties $|A\rangle$ or $|B\rangle$ (indicated in Fig. 2.1b by violet and pink colors of carbon atoms). The allocation onto the sublattices gives the out-of-plane angle of pseudospin and the phase between Bloch waves gives the in-plane angle (see Bloch sphere in Fig. 2.2b). As such the pseudospin can be understood as the helicity of Dirac-carriers which is opposite at K and K' as indicated by orange arrows in Fig. 2.2b [53]. It plays a crucial role for electron-electron scattering, since pseudospin needs to be conserved and pseudospin-flip is forbidden. Hence, carrier backscattering from one side of the Dirac-cone to the other is prevented [47] and interband transitions are anisotropic [9]. The high carrier mobility in graphene at room temperature [24, 28] can then be traced back to high v_F, low defect density and pseudospin-limited backscattering.

2.2 Transition Metal Dichalcogenides (TMDs)

After the discovery of graphene, other layered van-der-Waals materials got into the scientific spotlight since they can be similarly thinned down by exfoliation [13]. Amongst them, one particularly interesting class are transition metal dichalcogenides (TMDs). They stand out by strong light-matter interaction in the visible range when thinned down to few layers. Proof-of-principle devices of TMDs in the mono and few layer form for photovoltaics and photodiodes [16, 17, 21–23, 58, 59], photocatalysis [60] or as lasing media [61–64] were shown. Further, they could be integrated into lab-on-a-chip systems making ultrathin and light-weight electronics possible [65].

2.2.1 Structure

The term Transition Metal Dichalcogenides (TMDs) simply reflects the basic formula MX_2 composed out of a transition metal atom M (Mo,W,Ti,Ta) of groups IV-VII of the periodic table and two atoms X from the chalcogen family (S, Se, Te).
Many of the TMDs grow in layered crystals. Within the quasi-two-dimensional layers, M and X atoms are bound covalently. The transition metal atom favors a trigonal-prismatic coordination leading to the hexagonal crystal structure of MX_2 shown in Fig. 2.3 for monolayer WS_2 [66].

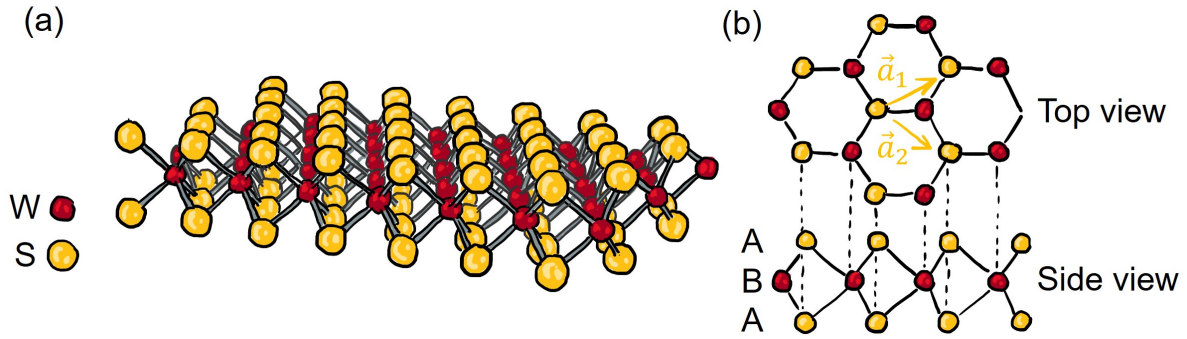

Figure 2.3: Crystal structure of monolayer WS_2: (a) 3D representation. (b) top and side view. Adapted from [49]. The in-plane lattice vectors $\vec{a}_1$ and $\vec{a}_2$ have a length of 3.15 Å [67].

TMD monolayers are represented by the crystallographic point group D_{3h} and lack inversion symmetry. This can be seen in the top view of Fig. 2.3a.
When stacked or in the bulk form, individual layers are weakly bound by van-der-Waals interaction. Such bulk stacking can exhibit several polytypes, e.g. 3R or 2H. The first corresponds to M over X and another M over X and is also called AB stacking. 2H stacking corresponds to M over X and X over M and is also called AA' stacking and it is the most

stable form for bilayer MX_2 [68]. In there, inversion symmetry is restored by a 180° in plane rotation of the second layer (A') with respect to to the first one (A) [69]. This inversion symmetry is maintained in bulk 2H-TMDs and they are described by the higher symmetric point group D_{6h} [30]. The 2H stacking yields a van-der-Waals gap between the layers of ∼3 Å [67].

The rich physics of TMDs originate to the biggest extend from anti-bonding d-orbitals of the transition metal atom M and the degree to which they are filled. When empty, the materials are semiconductors, e.g. MoS_2, $MoSe_2$, WS_2 and WSe_2. When the d-orbitals are partially filled, the materials are metals which can exhibit charge density wave, Mott insulating or superconducting ground states [67]. However, for the following discussions we will focus on the description of TMD monolayers and tungsten disulfide (WS_2) in particular.

2.2.2 Band Structure

WS_2 is a semiconducting layered TMD material. The single-particle band structure of monolayer and bilayer WS_2 is displayed in Fig. 2.4a and b, respectively. In the monolayer, the valence band maximum (VBM) and conduction band minimum (CBM) are both located at the K point forming a direct band gap. The bilayer, on the other hand, exhibits an indirect band gap with the VBM at the Γ and the CBM at the Σ valley, half way in between Γ and K. The band gap stays indirect by stacking into bulk [49, 69].

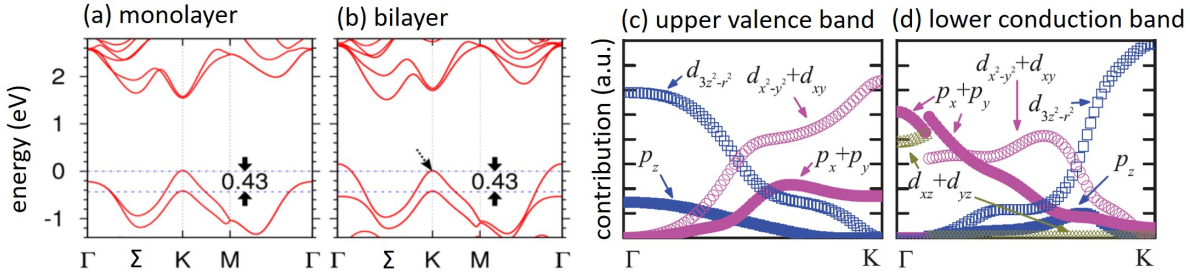

Figure 2.4: Band structure of WS_2: *Ab initio* band structure including spin orbit coupling for (a) monolayer and (b) bilayer WS_2. Adapted from [69]. (c) and (d): Orbital contributions in a monolayer WSe_2 as a function of momentum for the uppermost valence band in (c) and the lower most conduction band in (d). Calculated by first principle density functional theory. Adapted from [70].

In the monolayer, the spin degeneracy in valence and conduction band is fully lifted at the K points. This stems from broken inversion symmetry and strong spin-orbit coupling imposed by the relatively heavy M atom. A sizeable spin-orbit splitting of >0.4 eV of the valence band is found in tungsten based compounds [54]. In comparison,

conventional semiconductor quantum wells exhibit much smaller Rashba spin-splitting below 30 meV [71].

K and K' points have an opposite sign in spin-orbit-splitting in TMD monolayers due to time-reversal symmetry [69, 70]. In the conduction band the spin-orbit splitting is much smaller and opposite at K, compared to the valence band, but stronger again at the Σ valley [30]. In WS_2 bilayer, however, the restored inversion symmetry does not lift the spin-degeneracy but rather localizes the upper and lower valence band states in different layers [69].

The orbital contributions to the valence and conduction bands are displayed in Fig. 2.4c and d for the related compound WSe_2. It can be seen, that the states in the valence band at the K valley originate from in-plane orbitals ($d_{x^2-y^2} + d_{xy}$ and $p_x + p_y$) and at the Γ valley from out-of-plane orbitals ($d_{3z^2-r^2}$ and p_z). The conduction band at the K valley has out-of-plane character and is almost completely hosted by the transition metal atom ($d_{3z^2-r^2}$). Conduction band states at Γ and Σ have a mixed out-of-plane and in-plane character [30, 70]. Interlayer coupling of out-of-plane orbitals leads to a splitting of the bands at Γ when stacked into bilayer (Fig. 2.4b).

2.2.3 Excitonic Transitions

Few layer TMDs couple very efficiently to light in the visible range. Optical absorption and emission spectra are dominated by distinct peaks as it can be seen for a selection of TMD monolayers in Fig. 2.5a. Remarkably, the individual absorption spectra (grey curves) show several peaks with absorption on the order of $\sim$20 % in spite of the monolayer thickness of the crystals.

Further, the absorption peaks with the smallest energy (peak A) coincide with the peaks in photoluminescence (colored curves) [31]. These strong optical excitations are be assigned to excitonic transitions, which are energetically below the single-particle band gap of TMD monolayers. As such they determine the "optical bandgap". Excitons are bound electron-hole pairs (Fig. 2.5b). If electrons and holes that form the exciton are located at the same valley in the BZ (e.g. K-K exciton) they are called optically bright as their creation or decay is possible by a direct optical transiton. They are called optically dark, if they are located at valleys with different momentum (e.g. Σ-K exciton) or spin (e.g. $K_\uparrow$-$K_\downarrow$ exciton) [30].

The concept of excitons is well-established [73,74], but excitons in TMD monolayers gained interest due to extraordinary binding energies up to 1 eV. This is >1 order of magnitude bigger than in conventional quantum wells [75]. The large exciton binding energies in TMD monolayers are caused by the enhanced attractive Coulomb interaction between electron and hole which arises from (1) the confinement into a two-dimensional plane and

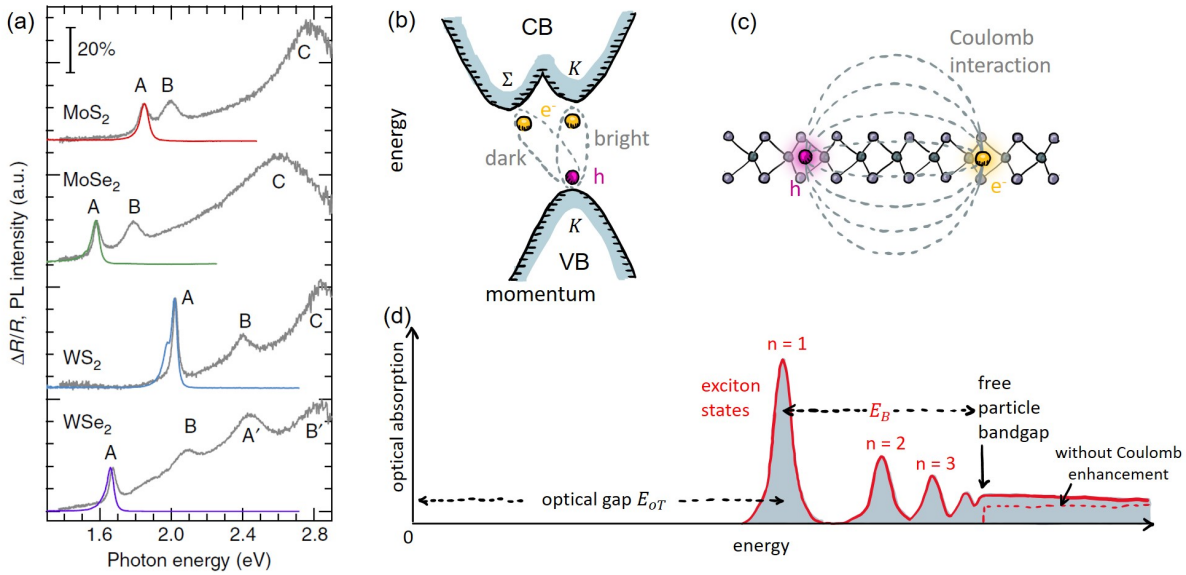

Figure 2.5: Excitons in TMDs: (a) Differential reflectance ($\Delta R/R$, grey) and photoluminescence (PL, color) spectra for several TMD monolayers. Adapted from [31]. (b) Optically bright and dark excitons in band structure picture. (c) Real space picture of the Coulomb-interaction between electron and hole. Adapted from [72]. (d) Coulomb enhancement of the optical spectrum. Adapted from [30].

(2) low dielectric screening within the TMD layer (see Fig. 2.5c). As they are strongly bound they exhibit a rather small Bohr radii of ∼1 nm [30].

By now, a variety of excitonic peaks was found and identified in optical spectra of few layer TMDs. Historically, the first peaks found were labelled A, B and C (cf. Fig. 2.5a). It turned out that the A- and B-excitonic transitions correspond to transitions from the upper (VB_A) and lower (VB_B) valence bands into the conduction band, respectively [30]. The C-peak can be either assigned to an excitonic transition [76,77] or to direct transitions at points in the Brilluin zone where conduction and valence bands are parallel [31].

Trions, charged excitons, can be obtained by photoexcitation under electrical gating as satellite peaks to the neutral exciton [78, 79]. Furthermore, the exciton itself exhibits excited states (n = 1, 2, 3, ...) called excitonic Rydberg series in analogy to the electronic states in the hydrogen atom [72]. In Fig. 2.5a the peaks A (B) correspond to n=1 and A' (B') to n=2, respectively. The exciton binding energy of the nth excited state $E_B^{(n)}$ can be calculated using $E_B^{(n)} = E_{bg} - E_{oT}^{(n)}$ with the single-particle band gap E_{bg} and the energy of the respective optical transition E_{oT}.

E_B is reduced due to enhanced screening of the Coulomb interaction between electron and hole, e.g. by placing the TMD monolayer on a substrate or by creation of photoexcited carriers. At high excitation densities E_B can approach zero and excitons dissociate into free electrons and holes. This transition is referred to as "excitonic Mott transition" in

literature and should not be confused with a metal-insulator transition [30, 80, 81].
A summary of the above can be found in a spectroscopic picture in Fig. 2.5d.
In contrast to all-optical techniques, time- and angle-resolved photoemission spectroscopy (tr-ARPES) can in principle access dark excitonic states. Signatures for excitons in tr-ARPES were predicted theoretically [80, 82, 83] and indeed observed experimentally [84–86].

2.2.4 Spin-Valley Physics

The excitonic transitions at the K and K' valleys provide optical selection rules which can be used in valleytronics, a new branch of optoelectronics [87]. The A and B excitonic transitions in monolayers are linked to the upper and lower valence bands which are spin-orbit split at the K, K' valleys by a significant amount of $\sim$0.4 eV. Consequently, they can be selectively excited by adjusting the photon energy.

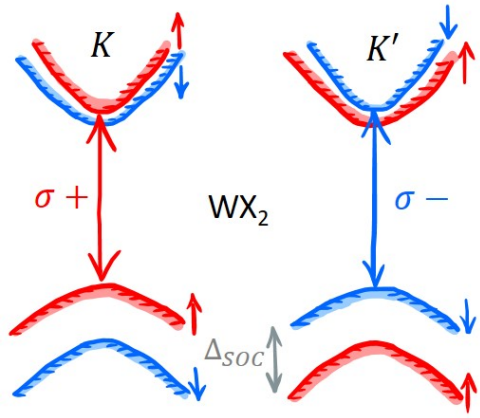

Figure 2.6: Spin- and valley-contrasting physics: Selective excitation of valleys (K, K') in TMD monolayers by circular polarized light (σ^+, σ^-). Adapted from [30].

Due to time-reversal symmetry the spin-orbit splitting is opposite at K and K'. As depicted in Fig. 2.6, circularly polarized light (σ^+, σ^-) resonant to the A-exciton selectively excites either the K or the K' valley with the corresponding spin-polarization [88]. This spin-valley locking bears great promise for opto-spintronics. When excited by circularly polarized light, the photoluminescence from excitons in monolayer TMDs is indeed found to have a high degree of circular polarization [89–93] which is further substantiated by time-resolved Kerr rotation measurements [94]. Obvioulsy, photoexcitation by linearly polarized light leads to no net spin-valley polarization [30].
In addition, the locking of the valley and spin degree of freedom gives rise to combined valley and spin Hall effect in transport [88, 95].

2.3 Van-der-Waals Heterostructures

Aside from graphite and TMDs a variety of other layered van-der-Waals materials exist and most of them can be exfoliated quite easily. Recently developed transfer techniques (see section 3.2.1) allow to stack individual 2D layers on top of each other in a LEGO-like manner to build ultimately thin heterostructures as shown in Fig. 2.7a [14]. The building bricks in this metaphor can exhibit insulating, semiconducting, superconducting, semimetallic or metallic behaviour (see overview Fig. 2.7b) opening a huge playground for the design of novel artifical materials. The weak van-der-Waals coupling between layers bypasses lattice matching conditions and enables arbitrary stacking and control of the twist angle between layers [13, 15].

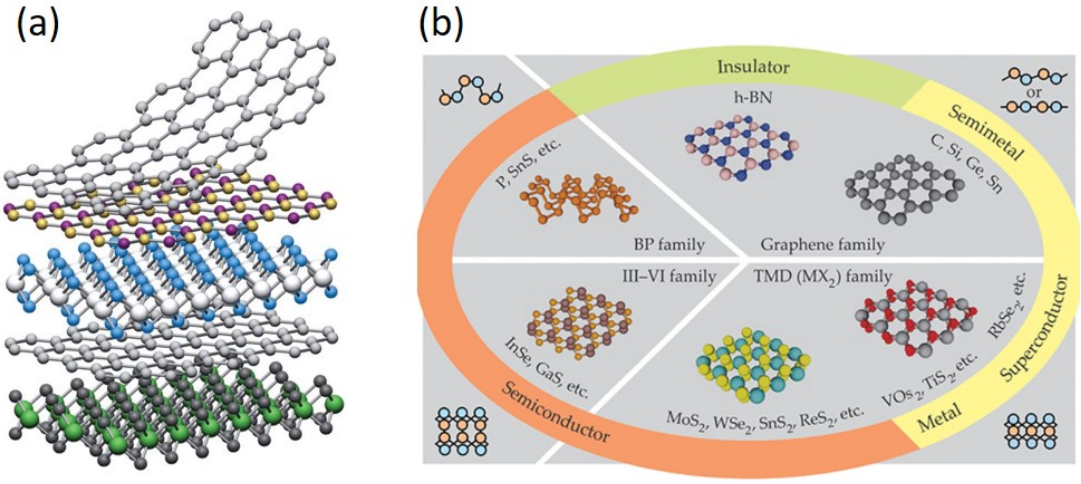

Figure 2.7: Van-der-Waals Heterostructures: (a) LEGO-like stacking of two-dimensional layers. Adapted from [14]. (b) Overview of layered van-der-Waals materials. Adapted from [13].

2.3.1 Hybridization and Proximity-Induced Effects

Although the van-der-Waals bonds are relatively weak, it was shown that hybridization between the layers occurs. This can affect the band structure significantly. Wilson et al. observed by means of μ-ARPES a splitting of valence bands at Γ in a MoS_2/WSe_2 heterostructure that is absent in the individual layers. Bands at K stayed mostly unaffected. The authors assign this fact to orbital overlap which is bigger for Γ orbitals with out-of-plane character than for K orbitals with in-plane character (cf. Fig. 2.4c). Similarly, Diaz et al. found gaps opening at band crossings in a graphene/MoS_2 heterostructure at the area in the BZ where the bands exhibit out-of-plane orbital character [96].
In addition, changing the dielectric environment of a freestanding layer by stacking it

into a heterostructure will affect it's electronic and optical properties by screening of the Coulomb-interaction (cf. Fig. 2.5c). This can renormalize the single particle band structure and affect exciton binding energies [30, 97, 98].
The van-der-Waals coupling can also lead to proximity-induced effects in neighboring layers [15]. The most prominent example is proximity-induced spin-orbit coupling in graphene [40, 99]. Such an enhanced spin-orbit coupling strength of ∼2.5 meV was indeed observed experimentally [100, 101].
All of the effects mentioned above scale with the interlayer distance. Thus, the quality of the heterostructure interface is crucial for observation of such effects [37] and should be considered when choosing a preparation method (see section 3.2.1). For the particular case of a WS_2/graphene heterostructures the interlayer distance is ∼3.45 Å.

2.3.2 Ultrafast Charge Transfer in TMD Heterostructures

Another emerging effect in some heterostructures is an ultrafast charge transfer. Photoexcited carriers can travel from one layer to the other on timescales faster than a picosecond. This seems quite surprising considering the supposedly weak van-der-Waals coupling between the layers. The use of this effect in optoelectronics and photovoltaics is obvious as photocarriers are found to be efficiently separated after the initial charge transfer.
The driving force behind the ultrafast charge transfer is simply revealed by the band alignment of both layers [66]. In van-der-Waals heterostructures of type II band alignment, made out of two semiconductors (e.g. MoS_2/WS_2), the conduction band minimum (CBM) and valence band maximum (VBM) are located in different layers (see Fig. 2.8a). Selective excitation of one layer, is then followed by charge transfer of electrons or holes into the second layer. For example consider a photoexcitation in MoS_2 in Fig. 2.8a as marked by the red arrow. Photoexcited electrons then find themselves in the global CBM, located in the MoS_2 layer, but photoexcited holes strive to relax to the global VBM, located in the WS_2 layer. As a consequence an ultrafast hole transfer is observed while electrons remain in MoS_2 [102]. The charges are then efficiently separated.
Similar ultrafast charge transfer processes were observed in several TMD heterostructures of type II band alignment [98, 103–108]. If electron or hole transfer is favored, depends on the exact alignment of the bands and, of course, the excitation itself.
The photoexcitation in TMD heterostructures of type II band alignment was often performed by resonant excitation of excitons. Although these excitons are strongly bound (see section 2.2.3) carrier tunneling between layers can lead to formation of so called interlayer exciton states which is estimated to take place within a timescale of 10 ps [109]. These states are energetically favorable due to reduced binding energy and were also observed experimentally [104, 105, 110].

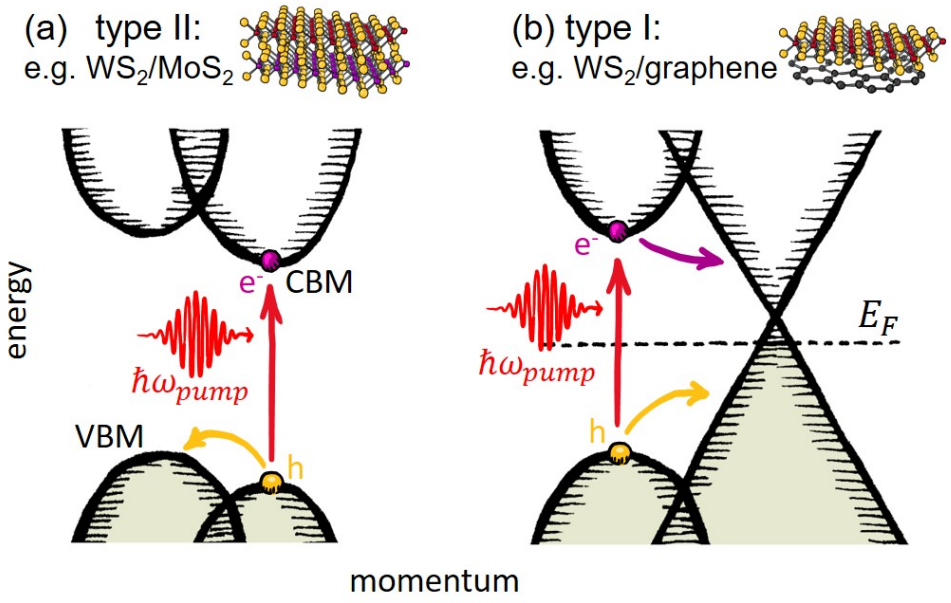

Figure 2.8: Band alignment in heterostructures: (a) Type II. (b) Type I. Red arrows indicate initial (selective) photoexcitation. Orange and violet arrows indicate subsequent charge transfer.

In heterostructures with type I band alignment the CBM and VBM are both located within the same layer as it is the case in WS_2/graphene heterostructures (see Fig. 2.8b). As a consequence photoexcited carriers in WS_2 will always strive to relax to the Fermi level (E_F) located in graphene states. The ultrafast charge transfer in this type of heterostructures is also found to happen ultrafast but — very interesting — highly asymmetric for electrons and holes. This also leads to efficient charge separation [21,34,35,37–39,111]. The ultrafast charge transfer also induces a bleaching and linewidth broadening ot the A-exciton in WS_2 when proximitized to graphene [36].

The microscopic mechanism behind the ultrafast charge transfer in TMD/graphene heterostructures is still not understood. First of all, it is unclear why the charge transfer happens on ultrafast timescales. The asymmetry of electron and hole transfer is another open question.

The ultrafast charge transfer in TMD/TMD heterostructures can be explained by intervalley scattering to regions in the Brillouin zone with significant orbital overlap between the layers at which the carriers can tunnel [112–114]. These regions are close to the Γ valley in the valence band with out-of-plane orbital character (cf. Fig. 2.4c and d). It is open if this picture holds for TMD/graphene heterostructures aswell. When resonantly excited: What is the role of excitons for interlayer transfer in TMD/graphene heterostructures?

Is charge recombination based on the same mechanism as charge separation and how long does it persist? And which practical requirements have to be met by TMD/graphene

heterostructures for ultrafast charge separation?
Thus, shining light onto the charge transfer mechanism is the major motivation for this work.

Chapter 3

Experimental Techniques

The ultrafast charge transfer in van-der-Waals heterostructures was mostly investigated by all-optical spectroscopy techniques, particularly often by transient absorption (TA) spectroscopy [34, 37–39, 98, 102, 103, 106–108, 111]. In general, TA spectroscopy probes pump-induced changes of the optical properties either at fixed wavelength or with a broadband (white light) probe. The signal is detected in both, transmission ($\frac{\Delta T}{T}$) or reflection ($\frac{\Delta R}{R}$) geometry. A transient signal is often depicted as difference from the pump-excited system to the unperturbed one [115]. To investigate the ultrafast charge transfer in TMD-heterostructures the A-exciton resonance of one layer is probed while the other layer is selectively pumped and vice versa. However, the interpretation of TA spectra and connected signal lifetimes should be done carefully as they can depend on many effects which might be linked to real carrier populations or not. Due to the lack of momentum resolution all-optical spectroscopies are blind to optically dark states (cf. Fig. 2.5b) [110].
In conclusion, all-optical techniques like TA spectroscopy provide a rather indirect picture which needs to be interpreted carefully. For a more comprehensive understanding several techniques should be complemented as it was already done by TA spectroscopy combined with time-resolved THz conductivity in [111] or time-resolved photoluminescence in [98]. We try to provide another point of view on the ultrafast charge transfer in van-der-Waals heterostructures by means of time- and angle-resolved photoemission spectroscopy (tr-ARPES), with a direct measurement of actual photocarrier populations and transient band structures. This chapter introduces the underlying principles of tr-ARPES, the experimental setup and the sample preparation. At the end we show how the technique can be used to obtain direct evidence for ultrafast charge transfer and charge separation

in vdW heterostructures.

3.1 Time- and Angle Resolved Photoemission Spectroscopy (tr-ARPES)

3.1.1 Photoemission Spectroscopy

Photoemission spectroscopy techniques are based on the photoelectric effect which was discovered by Hertz in 1887 [116]. Einstein assigned it in 1905 to the absorption of a light quantum by an electron from the sample which has then sufficient energy to escape into vacuum [117].

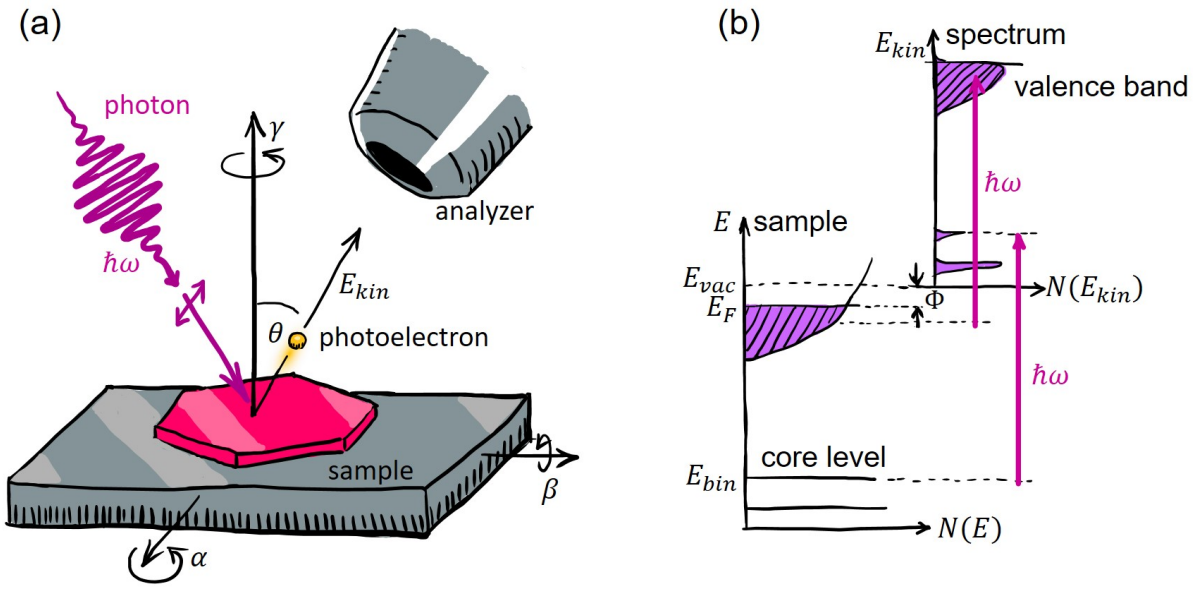

Figure 3.1: Principle of Photoemission: (a) Photoemission geometry. The emission angle is denoted as θ. The sample can be rotated around polar (α), tilt (β) or azimuthal (γ) angles. (b) Creation of photoelectron spectrum by photoemission from electronic states. Adapted from [118].

The principle is sketched in Fig. 3.1a. A photon at energy $\hbar\omega$ impinges the sample and a photoelectron is emitted into the vacuum with an kinetic energy E_{kin} at an emission angle θ. The photoelectron detector measures the photoelectron distribution $N(E_{kin}, \theta)$. E_{kin} is determined by energy conservation:

$$E_{kin} = \hbar\omega - |E_{bin}| - \Phi \tag{3.1}$$

with the binding energy of the initial state E_{bin} and the work function Φ. The latter can be thought of a potential barrier from the Fermi energy E_F to the vacuum level E_{vac}

which needs to be overcome by the electron as depicted in Fig. 3.1b [119]. It is typically in the order of 4-5 eV for most of the materials [120]. E_{bin} is calculated from the measured spectrum once E_F is known.
In the energetic picture of Fig. 3.1b, one can access lower-lying electronic levels (e.g. core levels) by higher photon energies. This is the basic principle of Photoemission Spectroscopy (PES). There is a separation into ultraviolet photoemisson spectroscopy (UPS) and X-ray photoemisson spectroscopy (XPS) focussing on valence or core level states, respectively [118].

3.1.2 Description of Photoemission

In the following, theoretical descriptions for the photoemission process will be introduced to lay the previous explanations onto a more rigid fundament. The aim is to describe spectral features measured photocurrent $N(k, \omega)$ as a function of momentum k and energy and draw important conclusions for the measurement.

Photoemission models

The simplest picture for photoemission is the three-step model. As the name suggests, the photoemission process will be separated into three indipendent steps:

- (1) Photoexcitation of an electron from a bound initial state to a free electron final state inside the solid
- (2) Transfer of the photoelectron to the surface
- (3) Transmission through the surface into vacuum

The advantage of this model is a simple factorization of the transition matrix element into the product of three parts which then can be treated separately. Step (1) includes the band structure and a dipole transition matrix element, step (2) the inelastic mean-free path of the electron and step (3) the transmission probability aswell as energy and momentum conservation [121]. Interference of the three steps is not captured and relativistic or many-body effects are neglected [122].
A more detailed picture is obtained within the one-step model. Contrary to the previous, all three processes can interfere with each other and are treated within one single coherent step. This means building a Hamiltonian into which states from the bulk, the surface and the vacuum enter and which captures the whole process from photon absorption to electron detection. This model is more sophisticated than the three-step model and rather complex and computationally intensive. [119]

Photoemission Cross Section

The following approach is loosely based on the three-step model. The photoelectron distribution N is related to the photoemission cross section by:

$$N(\vec{k}, E_{kin}) = \sum_{i,f} w_{if} \tag{3.2}$$

where i and f denote the inital and final state, respectively. The inital state before photoemission $|\Psi_i^n\rangle$ consists of an n electron bound state within the sample and the final state $|\Psi_f^n\rangle$ of one free electron in vacuum and the remaining $n-1$ electron bound state within the sample. The transition probability for photoemission w_{if} can be approximated by Fermi's Golden Rule:

$$w_{if} = \frac{2\pi}{\hbar}\left|\langle\Psi_f^n|H_{int}|\Psi_i^N\rangle\right|^2\delta(E_f^n - E_i^n - \hbar\omega) \tag{3.3}$$

with H_{int} beeing the photon interaction and E_f^n and E_i^n beeing the initial and final state energies for the n-electron system. They are related to the $n-1$ electron system by $E_i^n = E_i^{n-1} - E_{bin}^k$ and $E_f^n = E_f^{n-1} - E_{kin}$ for a photoelectron with binding energy E_{bin}^k and kinetic energy E_{kin}.

The so called sudden approximation is commonly used in photoemission description. There, the photoemission process is assumed to be abrupt such that the photoemitted electron does not interact with the remaining $n-1$ electron system. Consequently, the photoelecton wavefunction ϕ_f^k and the wave function of the remaining $n-1$ electron system Ψ_f^{n-1} are introduced. ϕ_i^k is the orbital from which the photoelectron is emitted. Using this approximation, the photoemission cross section now reads:

$$w_{if} = \frac{2\pi}{\hbar}\left|\langle\phi_f^k|H_{int}|\phi_i^k\rangle\langle\Psi_m^{n-1}|\Psi_i^{n-1}\rangle\right|^2\delta(E_f^n - E_i^n - \hbar\omega) \tag{3.4}$$

for all possible excited states m. In this expression $M_{if}^k = \langle\phi_f^k|H_{int}|\phi_i^k\rangle$ is the one-electron matrix element and $\langle\Psi_m^{n-1}|\Psi_i^{n-1}\rangle$ is the $n-1$ electron overlap integral. The photocurrent from eq. 3.2 is then proportional to:

$$N(\vec{k}, E_{kin}) \propto \sum_{i,f} M_{if}^k \sum_m \left|\langle\Psi_m^{n-1}|\Psi_i^{n-1}\rangle\right|^2\delta(E_{kin} + E_m^{n-1} - E_i^n - \hbar\omega) \tag{3.5}$$

Here, the second term is referred to as the spectral function A. The final expression for the photocurrent measured in PES is now obtained:

$$N(k, \omega) = N_0(k, \omega, A) \cdot f_{FD}(E) \cdot A(k, E) \tag{3.6}$$

with the Fermi-Dirac distribution $f_{FD}(E)$ [119]. The three terms within this expression

are discussed in the following.

Photoemission Matrix Element

$N_0(k, \omega, A)$ is proportional to the absolute square of the one-electron matrix element $|M_{if}^k|^2$ with $M_{if}^k = \langle \phi_f^k | H_{int} | \phi_i^k \rangle$. The interaction of a photon with vector potential $\vec{A}$ with an electron with charge e, mass m and momentum operator $\vec{p}$ can be treated as dipole approximation:

$$H_{int} = -\frac{e}{2mc}(\vec{A} \cdot \vec{p} + \vec{p} \cdot \vec{A}) = \frac{e}{mc}\vec{A} \cdot \vec{p} \tag{3.7}$$

with the speed of light c. Several treatments lead to this approximation. Second order terms of the vector potential A were dropped, assuming linear photon absorption, as well as terms with $\vec{\nabla}\vec{A} = 0$. Furthermore, the gauge condition $\Phi = 0$ was chosen for the scalar potential Φ and the dipole approximation applied.
Now it gets clear that the matrix element M_{if}^k is affected by dipole selection rules and the orbital symmetry [122]. Fig. 3.2 tries to visualize this statement with a sketch of the geometry of the photoemission process. The photoemission cross sections varies depending on the energy, polarization and direction (wave vector $\vec{k}$) of the incident photon with respect to the orbital to be measured. For a given photon energy $\hbar\omega$ photoemission matrix elements can strongly vary within the Brillouin zone as orbital contributions may vary (cf. Fig. 2.4c and d). This can lead to the invisibility of bands to PES. In the case of the so called dark corridor in graphene the photoemission matrix element in this region is determined by destructive interference of electrons photoemitted from the two sublattices (see section 2.1.1) [123].

Fermi-Dirac Distribution

$f_{FD}(\omega)$ is the Fermi-Dirac distribution which links the photoemission to occupied states within the sample:

$$f = \frac{1}{e^{(E-\mu)/k_B T} + 1} \tag{3.8}$$

with the chemical potential $\mu = E_F$ at 0 K. In this work, the Fermi level E_F will be defined as $E_{bin} = 0$.

The Spectral Function

The spectral function $A(E)$ describes the interaction within the remaining $n-1$ electron system and is linked to the one-electron removal Green's function. In other words, it describes the photohole created by photoemission. This gets more clear if we consider

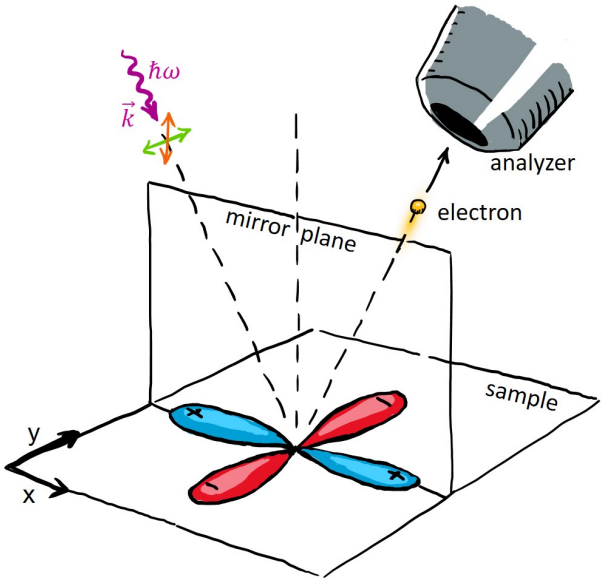

Figure 3.2: Geometry of photoemission from an atomic orbital. The one-electron matrix element in photoemission depends on energy $\hbar\omega$, polarization and direction of the photon and the symmetry of the obital under consideration. Linear light polarization in is indicated by orange and green arrows. Sketch adapted from [119].

eq. 3.5 in a noninteracting $n-1$ electron system and take $\Psi_i^{n-1} = \Psi_m^{n-1}$. In this case the second term of eq. 3.5 reduces to a δ-function. Using the Green's function formalism, the photoemission spectral function $A(E)$ is expressed in terms of the electronic self energy $\Sigma = \Sigma' + i\Sigma''$ of the photohole:

$$A(E) = -\frac{1}{\pi}\frac{|\Sigma''(E)|}{[E - \epsilon_k - \Sigma'(E)]^2 + [\Sigma''(E)]^2} \tag{3.9}$$

where the band structure enters the equation in ϵ_k.

Thus, the spectral function captures single particle and many-body effects within the self-energy picture. The real part of the self energy Σ' describes deviations from the single particle band structure ϵ_k. Such changes in dispersion follow from quasiparticle renormalizations [124]. The imaginary part of the self energy Σ'' determines the full width half maximum (FWHM) Γ of the Lorentzian shaped spectral function $A(E)$. It is linked to the finite lifetime of photohole via $\tau = \frac{\hbar}{\Gamma}$. Such spectral broadening is caused by many-body interactions like electron-electron scattering, electron-phonon-scattering or impurity-scattering [125, 126].

Electron Escape Depth

In addition to the above, the spatial depth within the sample from which spectral information can be obtained depends on the photon energy $\hbar\omega$. The mean free path λ of electrons in solids is related to the electron kinetic energy via the "universal curve" $\lambda = c_1 E_{kin}^{-2} + c_2\sqrt{E_{kin}}$, with c_1 and c_2 beeing constants (see Fig. 3.3a). It limits the depth from which photoelectrons can finally be measured (step 2 of the three-step model). In consequence, photoemission is a very surface sensitive technique. In particular, the XUV sources used in the experiments in this work had energies of 22 and 32 eV which leads to an escape depth of 4-5 Å when applying the universal curve [127, 128]. As a result, photoemission is only possible from the topmost layer within WS_2/graphene heterostructures which can be seen from a length scale comparison in Fig. 3.3b. To measure population dynamics in both layers simultaneoulsy, the WS_2 coverage must be incomplete to reach the underlying graphene. Moreover, the samples need to be prepared ultraclean as any dirt or residuals would shadow the material under investigation.

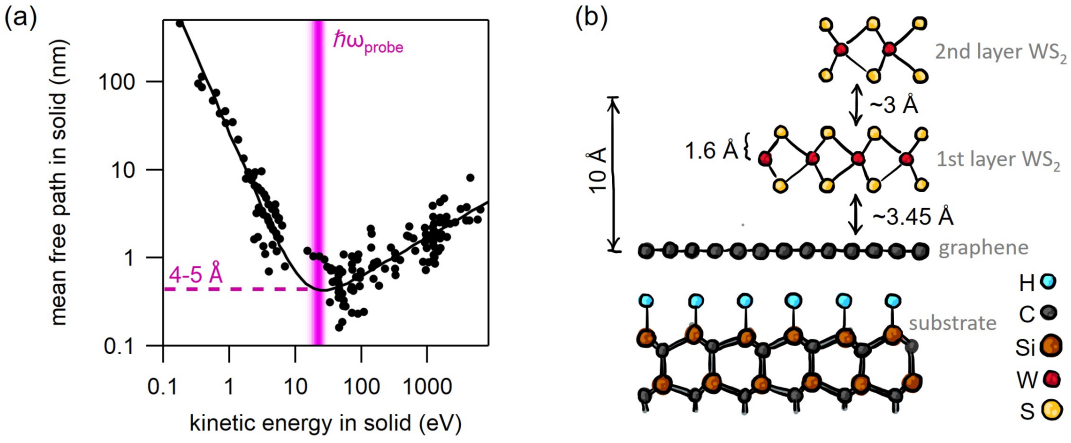

Figure 3.3: Electron escape depth. (a) Electron escape depth as a function of kinetic energy. Adapted from [127]. The pink shaded line marks the photon energies used in this thesis of 22-32 eV. (b) Length scales within the WS_2/graphene heterostructure.

3.1.3 Angle- Resolved Photoemission Spectroscopy

We can now add an extra dimension and measure the photocurrent I as a function of the emission angle θ. This technique is called Angle-Resolved Photoemission Spectroscopy (ARPES, or sometimes ARUPS), and it is perfectly suited to measure the dispersive valence bands in crystalline solids.

While the photoelectron is transmitted through the surface into vacuum (third step of the three-step model) the in-plane momentum $\hbar k_{\parallel}$ is conserved due to translation symmetry

[122]. The geometry is sketched in Fig. 3.4a. The kinematic relation of the photoelectron momentum within inside and outside the solid reads $\hbar k_{\parallel} = p_{\parallel}$. Due to energy conservation we can state:

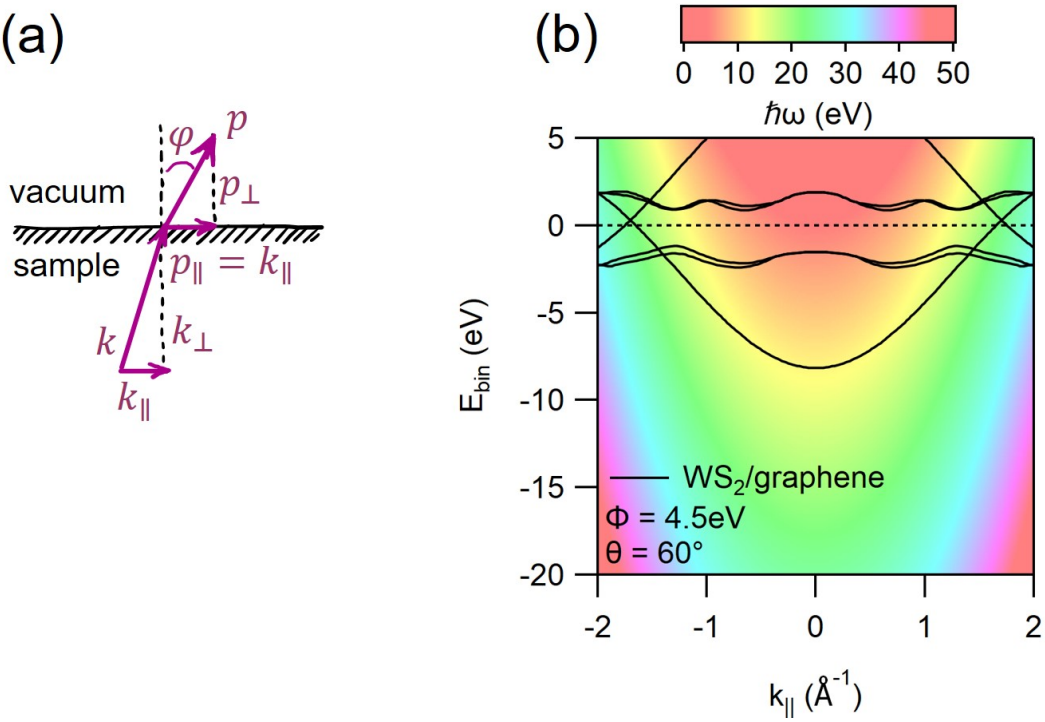

Figure 3.4: Angle- Resolved Photoemission Spectroscopy: (a) Sketch of momentum conservation. (b) Reachable binding energies and momenta for photon energies indicated by the color code. This calculation was done using eq. 3.1 and eq. 3.11 and assuming a work function $\Phi = 4.5$ eV and a (reasonable) photoemission angle $\theta = 60°$

$$\frac{\hbar^2 k^2}{2m} = \frac{p^2}{2m} + V_0 \tag{3.10}$$

with m beeing the electron mass and V_0 beeing the crystal's inner potential. In the typical ARPES geometry (see Fig. 3.1a) we then derive the following relations to the photoemission angle θ:

$$k_{\parallel} = \frac{1}{\hbar}\sqrt{2mE_{kin}} \cdot \sin\theta \tag{3.11}$$

$$k_{\perp} = \frac{1}{\hbar}\sqrt{2m(E_{kin}\cos^2\theta + V_0)} \tag{3.12}$$

which are used for transformation of the photocurrent from angle-space $I(E_{kin}, \theta)$ into momentum-space $I(E_{bin}, k_{\parallel})$. Due to the inner potential V_0, the out-of-plane momentum $k_{\perp}$ is not conserved. But it could be experimentally accessed by photon energy dependent measurements [122].

In conclusion, ARPES has access to the in-plane band structure of the sample $\epsilon(k_{\parallel})$. Thus, it is convenient to work with a two-dimensional surface Brillouin zone (BZ), which is the projection of the bulk BZ on the sample surface. In this thesis, all BZ labels refer to the surface BZ.
Furthermore, ARPES ideally requires the sample to be single crystalline over the probed spot to observe the band structure. Measuring a multi-domain crystal will show a superposition of the surface-BZs of individual domains twisted around the Γ-point. In worst case, this can completely smear out the bands in energy and momentum.
In section 3.1.1 we discussed how much photon energy $\hbar\omega$ is neccessary to reach electronic levels with higher binding energies by photoemission. From eq. 3.11 we further notice that the reachable in-plane momentum is also determined by $\hbar\omega$. Fig. 3.4c displays the theoretical band structures of WS_2 and graphene [51,69] together with a color code indicating the minimum photon energy $\hbar\omega$ which is needed to reach a certain binding energy and momentum. For example: to observe the K-point of graphene at $\sim$1.7 Å at a (reasonable) photoemission angle $\theta = 60°$ at the Fermi level E_F we need $\hbar\omega = 23\,\text{eV}$. This calculation was done using eq. 3.1 and eq. 3.11 and assuming a work function $\Phi = 4.5\,\text{eV}$.

3.1.4 Time-and Angle-Resolved Photoemission Spectroscopy

ARPES gives access to the sample's band structure in thermal equilibrium. Adding the dimension of time allows to investigate the response of the system to an (ultrashort) excitation by light, which can push the system far out of equilibrium. The excitation itself could trigger electronic transitions, couple to collective modes [129], accelerate free carriers [130] or even drive phase transitions [8]. Using tr-ARPES, it is possible to measure changes of the carrier distribution and deduce processes by which the system approaches equilibrium again. These include carrier-carrier scattering, carrier-phonon scattering which transfers energy to the lattice and many more [131].
Time- and angle resolved photoemission spectroscopy is performed within a pump-probe scheme. The pump pulse photoexcites the sample and the probe pulse monitors the spectrum via variable pump-probe delay Δt. The cross correlation between both pulses in the time domain, the instrumental response function, determines the temporal resolution of the pump-probe experiment.
For the investigation of charge transfer processes in WS_2/graphene heterostructures, the photon energy of the pump pulse is either matched to the A-excitonic transition in WS_2 at 2 eV or to above gap excitation at 3.1 eV (cf. Fig. 2.5). The probe pulse ejects photoelectrons from the sample and needs to have a sufficently high photon energy to reach the valence states of WS_2 and graphene in momentum-space (see Fig. 3.4b). As the charge transfer is supposed to happen ultrafast, the temporal widths of both pulses should obvi-

ously be minimized.

Nonlinear Optics

To generate suitable photon energies for pump and probe beam we make use of non-linear optical techniques. These are a powerful tool and the accessible spectral range reaches from XUV to THz starting from a fundamental ultrashort 790 nm pulse.
We make use of the nonlinear dependence of the polarization P on the electric field E:

$$P(E) = \varepsilon_0(\chi^{(1)}E + \chi^{(2)}E^2 + \chi^{(3)}E^3 + ...) \tag{3.13}$$

with nonlinear optical coefficients of the electric susceptibility $\chi^{(n)}$ and the vacuum permittivity ε_0.
In second order non-linear effects ($\chi^{(2)} \neq 0$) like sum frequency generation, difference frequency generation or optical parametric amplification, three photons with freqency ω_n and wave vector k_n are involved. Photon conversion has to obey energy conservation:

$$\hbar\omega_1 = \hbar\omega_2 + \hbar\omega_3 \tag{3.14}$$

and the phase matching condition:

$$\Delta k = k_1 - k_2 - k_3 \tag{3.15}$$

The conversion efficiency is maximized for a wave-vector mismatch $\Delta k = 0$ (momentum conservation). A common strategy to achieve phase matching is using media with anisotropic group velocity dispersions [132, 133]. Such media need to be non-inversion symmetric and need to possess high non-linear coefficients and a high damage threshold [132]. A widely used material for second harmonic generation and optical parametric amplification is β-barium borate (BBO), a uniaxial birefringent crystal. In there, beams disperse differently depending on their polarization referred to the optical axis. Phase matching can be optimized by adjusting the crystal angles and thickness [133].
Photon conversion by nonlinear optics builds the backbone for the experimental setup introduced in the following.

Pump-Probe Setup for Tr-ARPES

Time- and angle-resolved photoemission spectroscopy on WS_2/graphene heterostructures was performed at:

- the Hamburg setup at the Max-Planck-Institute for the Structure and Dynamics of Matter in Hamburg (chapters 4, 6 and 7)

- the Artemis setup at the Artemis user facility at the Rutherford Appleton Laboratory in Harwell, UK (chapter 5)

The two experimental setups, however, have the general setting in common and just vary in details. An general overview is provided in Fig. 3.5.

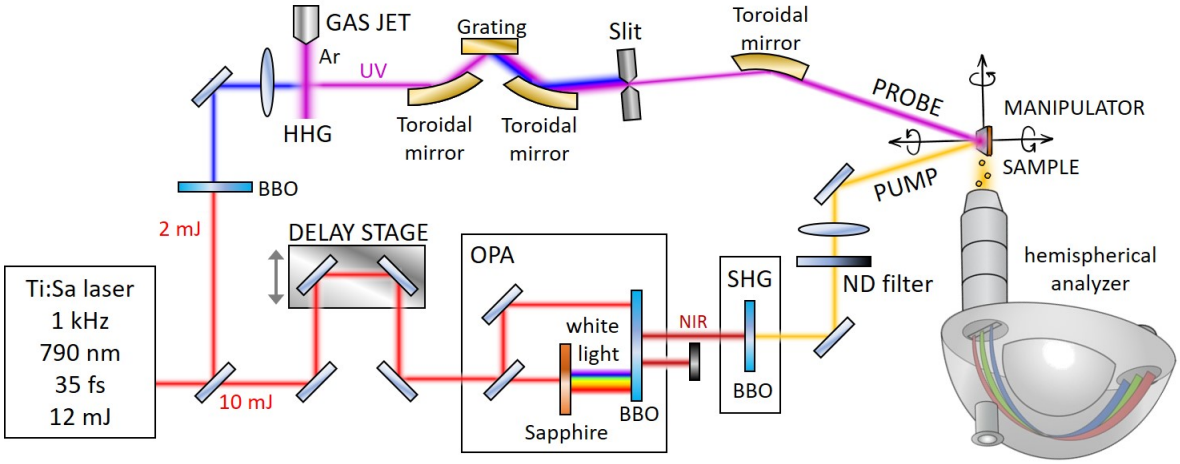

Figure 3.5: TR-ARPES Setup. The setup uses a VIS pump and a XUV probe based on a Ti:Sapphire amplifier with 1 kHz repetition rate. Details see text.

The tr-ARPES experiments were performed in an visible-pump/XUV-tr-ARPES-probe setup based on 1 kHz Titanium:Sapphire amplifiers with a central wavelength at 790 nm (1.55 eV) and 12 mJ pulse energy. The Hamburg setup used an Coherent Legend Elite Duo amplifier and the Artemis setup two KMLabs inc. USA amplifiers.
2 mJ were used for the generation of extreme ultraviolet (XUV) pulses using high harmonics generation (HHG) in an argon gas jet. Probe pulses at 21.7 eV (31.8 eV) photon energy with a nominal pulse duration of 100 fs (30 fs) were selected with a grating monochromator in the Hamburg (Artemis) setup, respectively. HHG in the Hamburg setup was driven with the second harmonic of the fundamental beam.
10 mJ of the output energy were used for the generation of visibe pump pulses. 2 eV pump pulses (chapters 4 and 5) were obtained by second harmonic generation (SHG) of the signal output of an optical parametric amplifier (HE-TOPAS from Light Conversion). 3.1 eV pump pulses (chapters 6 and 7) were generated by SHG of the fundamental laser output. A gradient neutral density filter on a rotational mount was used to vary the pump fluence by attenuating the pump power. The fluence was limited by noise on the lower side and pump-induced space charge on the upper side.
Photoemission spectra were measured with a hemispherical analyzer (SPECS Phoibos 100) in the Hamburg setup and a home-built Time-of-Flight (ToF) analyzer in the Artemis

setup. The sample rotation (see Fig. 3.1) was controlled by a manipulator. The UHV base pressure was $<2 \cdot 10^{-9}$ mbar for all measurements.
In the following, the underlying principles and technical realizations within the pump-probe setup will be described in more detail.

3.1.5 Generation of Extreme Ultraviolet (XUV) Probe Beam

High Harmonics Generation (HHG)

High Harmonics generation (HHG) is a coherent upconversion process of ultrashort laser beams focussed into noble gas jets. This technique gained attention as table-top alternative to synchrotron light source for extreme ultraviolet (XUV) light. HHG might be used in ultrafast spectroscopies like photoemission spectroscopy [134], soft-X-ray absorption spectroscopy [135] or attosecond streaking [136, 137]. In this work, we chose this technique to provide ultrashort pulses with high photon energy to enable photoemission from the edges of the Brilluoin zone.

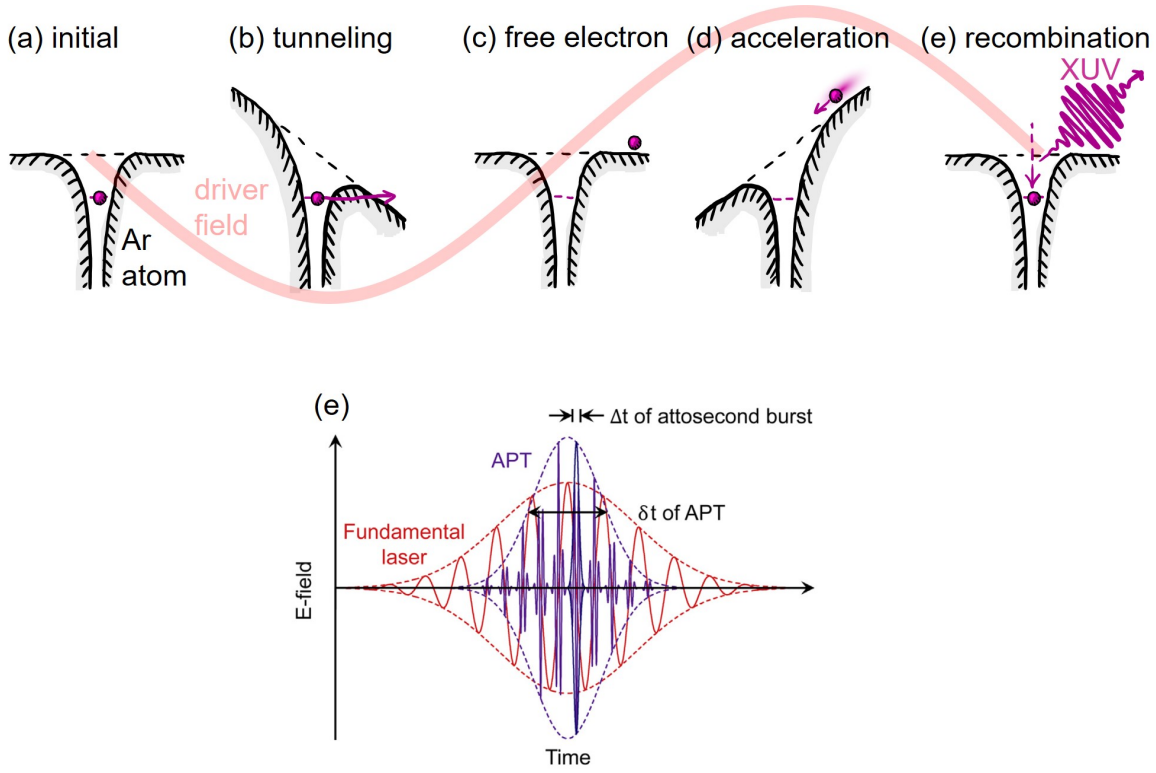

Figure 3.6: High-Order Harmonic Generation (HHG): (a)-(e) Ionization and recombination model of HHG. Adapted from [138]. (f) Temporal comparison of the fundamental laser electric field and the generated attosecond pulse train High harmonics spectrum. Adapted from [139].

The upconversion process from the driving laser pulse with frequency ω to high-order odd

harmonics with frequency $n \cdot \omega$ can be explained with an the three-step-model of HHG [140], as sketched in Fig. 3.6a-e. The Coulomb potential of noble gas atom (Fig. 3.6a) is bent under the electric field of the driving laser (red). When the bending is strong enough the wave function of an electron in the noble gas atom overlaps with the free electron state and tunneling ionization becomes possible (Fig. 3.6b). This separates electron and noble gas ion and creates a plasma (Fig. 3.6c). During the second half cycle of the driving laser the electric field changes direction and accelerates the free electron towards to parent noble gas ion (Fig. 3.6d). When it re-collides with the parent ion it's excess energy is released in form of emission of XUV radiation (Fig. 3.6e). The low probability of re-collisions limits the efficiency of the process. The re-collision is happens whenever the electric field of the driver crosses zero, creating attosecond XUV bursts [139]. The relation of the generated attosecond pulse train (APT) to the fundamental driver is shown in Fig. 3.6e. The inversion symmetry of the noble gas prohibits the creation of even order harmonics and only odd order harmonics are created [138]. In general, the many individual atomic emitters do radiate at different phases and frequencies depending on the particular trajectory and acceleration of the returning electron [136]. From this general principle we can derive important criteria for practical realization:

- The stronger the driving field, the stronger is the potential bending and the more efficient is tunneling ionization. To achieve this,the driving laser is first compressed to a narrow temporal width and second tighly focussed into the noble gas jet to achieve high electric fields.

- The broader the temporal width of the driver, the narrower is the spectral linewidth of generated harmonics. This is because the width of an individual harmonic is inverse proportional to the temporal width δt of the APT and thus to the width of the fundamental laser pulse (see Fig. 3.6d) [139].

- The better the phase matching of individual atomic emitters, the brighter are the harmonics. The phase matching condition in HHG is achieved by adjusting the dispersion n of the neutral gas ($n > 1$) and the free-electron-plasma ($n < 1$) via their densities. Thus, the noble gas is usually confined to a narrow volume within a capillary or the fundamental laser is focussed close to a gas nozzle. The gas pressure then serves as important turning knob for phase matching [139].

- The shorter the wavelength of the fundamental driver, the higher the conversion efficiency. The efficiency is proportional to λ^{-6} [141, 142]. On the other hand, the high energy cut off of the continous XUV spectrum is proportional to λ^2 [138, 143].

In this work, Argon gas in a T-shaped gas capillary (target) was used for HHG. The gas

pressure is controlled by a piezo valve. In the Artemis setup, the Argon was ionized with the fundamental laser beam and the 21st harmonic at 31.8 eV was selected.
In the Hamburg setup, the second harmonic of the fundamental laser beam, generated within a BBO crystal, is used as driver for HHG. Second harmonic generation (SHG) is a special case of sum frequency generation with $\omega_2 = \omega_3$ in eq. 3.14. Two photons of the fundamental frequency ω_2 are annihilated and a single photon with ω_1 is created with, obviously, double the frequency [132]. The 7th harmonic at 21.7 eV was used in the Hamburg setup. Typical XUV spectra obtained by HHG with the fundamental beam (red) or it's second harmonic (blue) can be seen in Fig. 3.7.

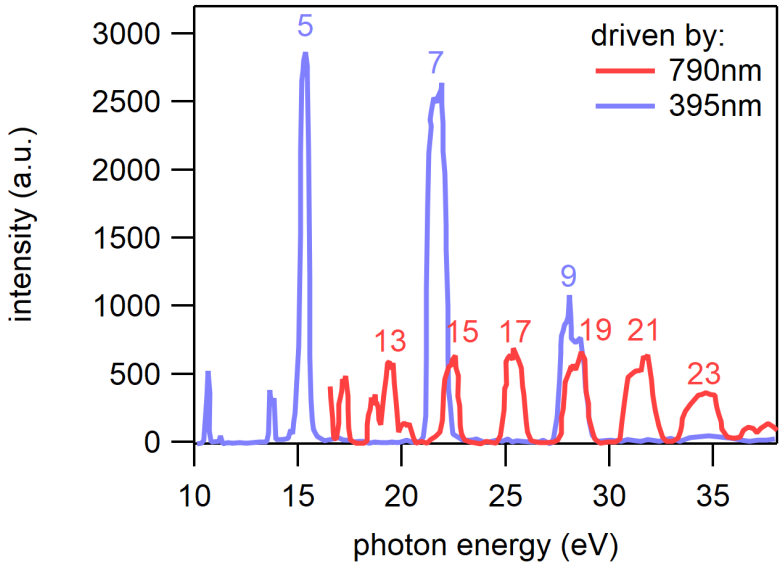

Figure 3.7: High harmonic spectrum. XUV spectra measured with a Channeltron by rotation of the monochromator's grating. The red and blue curves represent the spectra obtained by driving the HHG with the fundamental laser at 790 nm and it's second harmonic at 395 nm, respectively.

Selection of a single Harmonic

The generated XUV pulse train consists of several temporally overlapped harmonics as shown in Fig. 3.6e. Photoemission with this multi-colored XUV continuum would lead to several replica of the photoemission spectrum spaced by $2 \cdot \omega$. A grating based monochromator was used, for the isolation of single harmonics. Different gratings can be chosen to optimize temporal or energy resolution. The design is developed by F. Frassetto and L. Poletto from CNR-IFN at Padova, Italy [144, 145] and te principle is shown in Fig. 3.8a. The centerpiece of the monochromator is a gold coated grating on which individual harmonics are diffracted with slightly different angles, thus enabling their spatial separation.

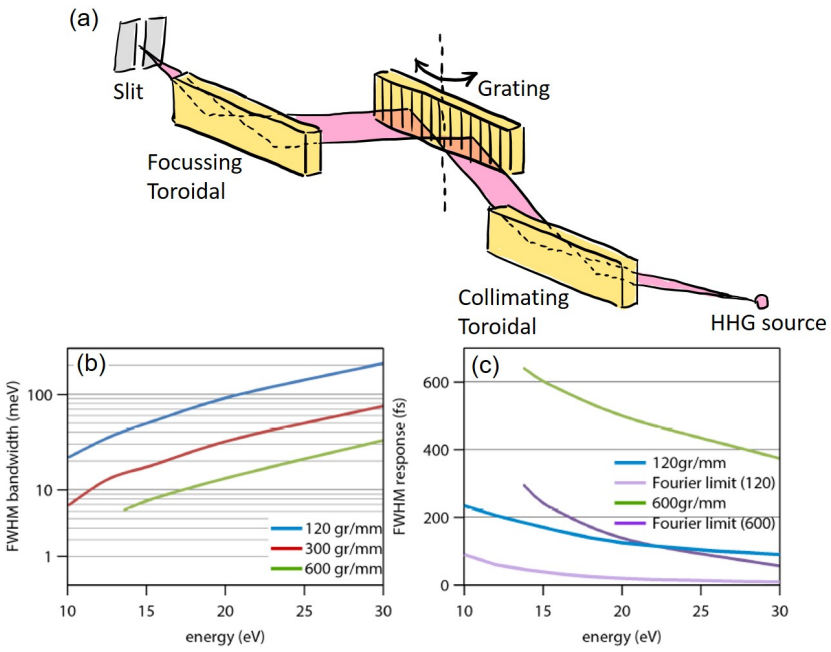

Figure 3.8: Grating based Monochromator: (a) Sketch of the monochromator. Adapted from [144]. (b) and (c) Bandwidth and temporal width characteristics of the monochromator for different gratings. The data in (b) and (c) was calculated by the designers assuming a 50 μm source and a 100 μm exit slit [144, 145].

A distant slit selects a single harmonic from the XUV spectrum. Additional focussing optics are needed for an optimal grating performance. A first gold coated toroidal mirror is used to collimate the beam before arrival at the grating. A second toroidal mirror after the grating focusses the XUV beam onto the slit position. By rotating the grating different harmonics can be sent through the slit.

The monochromator design is optimized for s polarized XUV light. To minimize abberations, the distance from both toroidal mirrors to the grating is similar. The grating is operated at classical diffraction geometry in grazing incidence. Temporal broadening originates mainly in difference in lengths of optical paths of light diffracted by different grooves of the grating. To minimize this, the grating is operated in external diffraction order, meaning the diffraction angle is bigger than the incident angle.

The monochromator design allows for a quick exchange of gratings by moving them along a linear translation stage. According to the requirements of the experiment three different gratings with 120, 300 or 600 grooves/mm could be chosen. The gratings alter the monochromator performance in the spectral bandwidth (see Fig. 3.8b) and temporal bandwidth see (Fig. 3.8c) of the XUV beam. The total transmission efficiency is expected to be 20-25 % [144, 145].

In the Hamburg setup, the experiments were performed using a grating with 120 grooves/mm

to minimize the temporal resolution. The XUV pulse duration is in the order of 100 fs for light at 21.7 eV. The focussed XUV probe spot at the sample position was measured to be $300 \times 560\,\mu m$. In the Artemis setup, we used a grating with 300 grooves/mm and yielded an XUV pulse duration of 30 fs for light at 31.8 eV.

3.1.6 Pump Beam Generation

In this work, two pump wavelengths were used to either excite the A-exciton of WS_2 resonantly (chapters 4 and 5) or above gap (chapters 6 and 7).

To match the A-exciton energy of 2 eV we used a two-step process: the first one down-converts the fundamental photon energy from 1.55 eV to 1 eV by using optical parametric amplification (OPA) and the second one upconverts it to 2 eV with second harmonic generation (SHG).

Using OPA we specify equation 3.14 into $\hbar\omega_{pump} = \hbar\omega_{signal} + \hbar\omega_{idler}$. In here, the term pump refers to the fundamental laser beam with fixed frequency. The beam to be amplified is called signal and a thrid beam, the idler, is neccesarily created due to momentum conservation (see eq. 3.15).

A commercial He-TOPAS from light conversion was used in experiments fed with 10mJ of the Ti:Sapphire laser output. Inside, the incident beam is split into four parts. As a first step, the weakest part with 1 - 3 μJ is focussed into a sapphire crystal leading to an immense spectral broadening to a white light continuum. White light generation is based on third order non-linear effects ($\chi^{(3)}$) self-focussing (Kerr lensing) and self-phase modulation at high peak electric fields. These effects can occur in all materials, sapphire is chosen in particular due to its transparency and high damage threshold [132, 146].

In a first amplification stage, the white light is focussed into a BBO crystal together with another part of the fundamental beam. The latter acts as pump, a provider of power for OPA in the BBO. Since the phase matching angle for OPA is wavelength dependent, the phase matching condition is only fulfilled for a small part of the broad white light continuum for a given angle. So the wavelength of the amplified signal can be selected from the white light continuum by rotation of the BBO crystal. Temporal overlap is controlled with a variable delay stage [132].

This concept makes OPA very versatile in creating ultrashort pulses adjustable in wavelength over a broad range, determined by the spectrum of the white light. In the high energy design of the TOPAS two following OPA-stages further amplify the signal beam. The output energy is $\sim$0.4mJ. The output beam consists of signal at 1240 nm and the idler at 2170 nm, which are perpendicular polarized to each other. Thus a polarization beam splitter can separate both beams and the idler is blocked. Subsequently, the signal was frequency doubled by a BBO creating the pump beam at 620 nm.

For above gap exciation, the fundamental beam at 1.55 eV was directly sent into SHG to create the pump beam at 3.1 eV. A Spiricon camera was used to measure the pump spot size of 0.5 ×0.5 mm and 1.2 ×1.2 mm for 2 eV and 3.1 eV, respectively. The pump fluence was then calculated from the measured pump power outside the UHV chamber as described in detail in Appendix A.3.

3.1.7 Photoelectron Detection

Photoemission spectra $I(E_{kin}, \theta)$ are obtained by filtering the emitted photoelectrons with photoelectron spectrometers before they reach the detector. The most common analyzer designs are hemispherical analyzers and Time-of-Flight analyzers which are displayed in Fig. 3.9. Raw tr-ARPES data was normalized and transformed into momentum-space after aquisition as described in detail in Appendix A.1 and A.2.

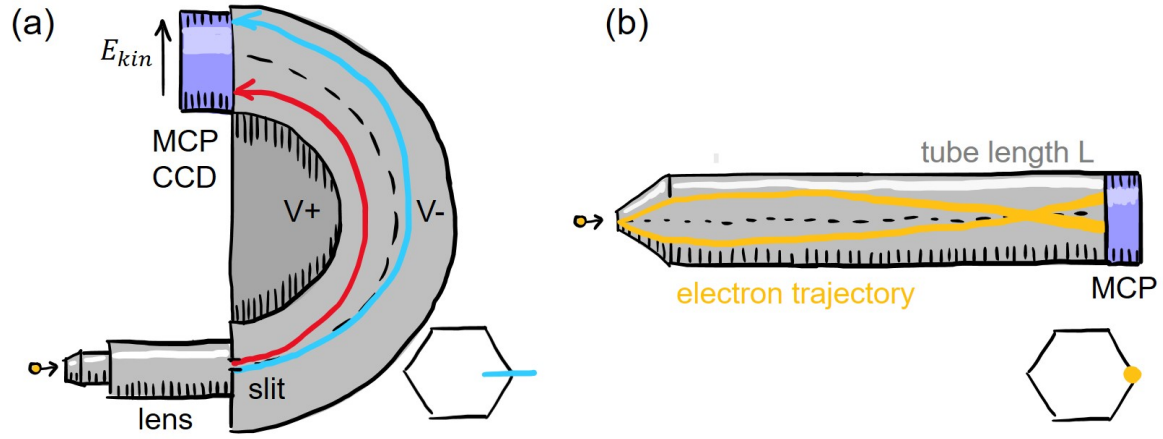

Figure 3.9: Photoelectron Analyzers: (a) Working principle of an hemispherical analyzer. $V+$ and $V-$ denote applied voltages for a static electric field. Photoelectron trajectories with low (high) kinetic energy of photoelectrons are shown in red (blue), respectively. (b) Working principle of a Time-of-Flight (ToF) Analyzer adapted from [147]. Electron trajectories are indicated in yellow. The measured region in the Brillouin zone is sketched n the bottom right, respectively

Hemispherical analyzers

Using hemisperical analyzers, the photoelectrons are filtered in their kinetic energy E_{kin} by their trajectory in a static electric field. The field is applied in between two concentric hemispheres as shown in Fig. 3.9a. Electrons with higher kinetic energy fly along a longer tajectory leading to a spatial distribution on the detector. By varying the applied voltages on the hemisphere one sets the so called pass energy, which determines the measured

kinetic energy range. Electron optics are used to attract and focus the photoelectron before it enters the hemispherical spectrometer. A slit aperture in the radial direction sets the energy resolution. Electrons in the azimuthal direction can pass within a certain range, enabling measurement of the photoemission angle θ related to momentum in one dimension (see Brillouin zone sketch in Fig. 3.9a). Finally, the detector is a micro channel plate (MCP), which converts impinging electrons into visible light which is captured by a CCD-camera.
The spectra in chapter 4, 6 and 7 were obtained using a HSA PHOIBOS 100 hemispherical analyzer from Specs with a mean radius of 100 mm operated in wide angle mode with 30° angular acceptance.

Time-of-Flight (ToF) analyzers

As the name suggests, the E_{kin} is determined by the time, in which the electrons fly from the analyzer entrance to the detector (see Fig. 3.9b). In a first approximation, this time T is linked to the electron's kinetic energy E_{kin} by: $T = \frac{L}{\sqrt{2/m \cdot E_{kin}}}$ with the electron mass m and the path length L. Obviously, higher energy electrons reach the detector faster. Photoelectrons are detected by channel electron multipliers (Channeltrons) or micro channel plates (MCPs) with a Lock-in-Amplifier [148]. The advantage of ToF-filtering is the almost vanishing electronic background. As a disadvantage, the sample needs to be rotated to measure momentum dependent spectra by using conventional ToF detectors. Next generation ToF detectors can access the k_x and k_y momentum information by advanced electron lens imaging, enabling momentum microscopy [149].
The spectra in chapter 5 were measured using a home-built Time-of-Flight analyzer with an angular acceptance of 2° [150].

3.1.8 Space Charge Effects

Photoelectron spectroscopies suffer from so called space charge effects which can reduce the energy and momentum resolution. They are caused by repulsive Coulomb-interaction between photoemitted electrons in the vacuum on their way to the analyzer.

Probe induced Space Charge

If the pump pulse photoemitts more than one photoelectron, the Coulomb-interaction amongst them can lead to repulsion. This is sketched for a cloud of photoelectrons in Fig. 3.10a. As a consequence the electron's kinetic energy and momentum are altered which typically smears out photomission spectra [151]. Within this work, probe induced space charge was reduced by closing the slit of the XUV monochromator (see Fig. 3.8).

This reduces the number of XUV photons impinging the sample and consequently the number of photoemitted electrons per pulse. Probe induced space charge vanishes in the limit of one photoelectron per pulse.

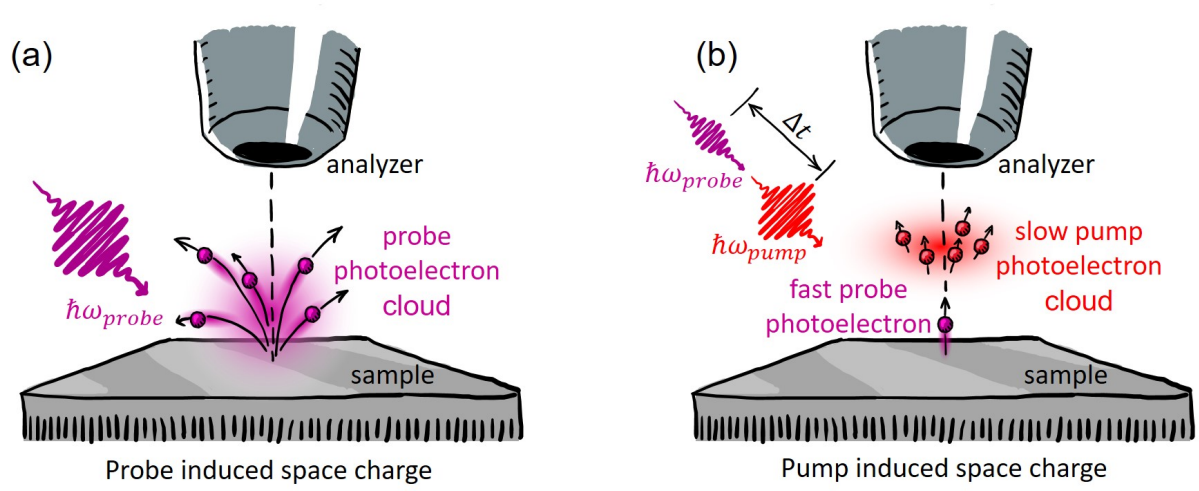

Figure 3.10: Space charge in tr-ARPES: (a) Sketch of pump induced space charge. (b) Sketch of pump-induced space charge which varies as a function of pump-probe delay Δt. Adapted from [152].

Pump induced Space Charge

On the first view, the pump photon energies used in this work (2–3.1 eV) cannot lead to photoemission as they are lower then the work function of 4-5 eV (see eq. 3.1). However, high pump fluences are often applied in tr-ARPES experiments. In this regime multi-photon absorption can overcome the work function barrier. The pump pulse then creates another electron cloud with slow, low energy electrons. Spectral broadening and spectral shifts are induced when pump- and probe-electron clouds interact with each other. As both electron clouds move towards the detector with different speeds the interaction strength strongly depends on the pump-probe delay Δt (see Fig. 3.10b). As a function of delay, probe photoelectrons are first accelerated then decellerated again leading to a transient spectral upshift peaking at time zero.
Such shifts reduce the measured binding energy of bands at all delays, which makes them distinguishable from other transient shifts. Additionally, the time scale of spectral shifts caused by pump-induced space charge is in the order of ps before and after time zero [152]. Pump-induced space charge cannot be ruled out completely in tr-ARPES experiments using moderate pump fluences. For the experiments in this thesis, a workaround to reduce spectral broadening and avoid spectral shifts was applied as described in Appendix A.1.

3.2 Sample Preparation

3.2.1 Common Van-der-Waals Heterostructure Preparation Methods

By now, several techniques were developed to produce monolayers of layered van-der-Waals materials and stack them into heterostructures afterwards. In here, just a short overview of possibilities is provided. The aim is to allow an evaluation of preparation methods and their influence on electronic and optical properties. As depicted in Fig. 3.11 we can seperate the preparation methods vagely into two groups: (1) mechanical exfoliation and stacking and (2) physical (van-der-Waals) epitaxy or chemical vapor deposition (CVD) [15].

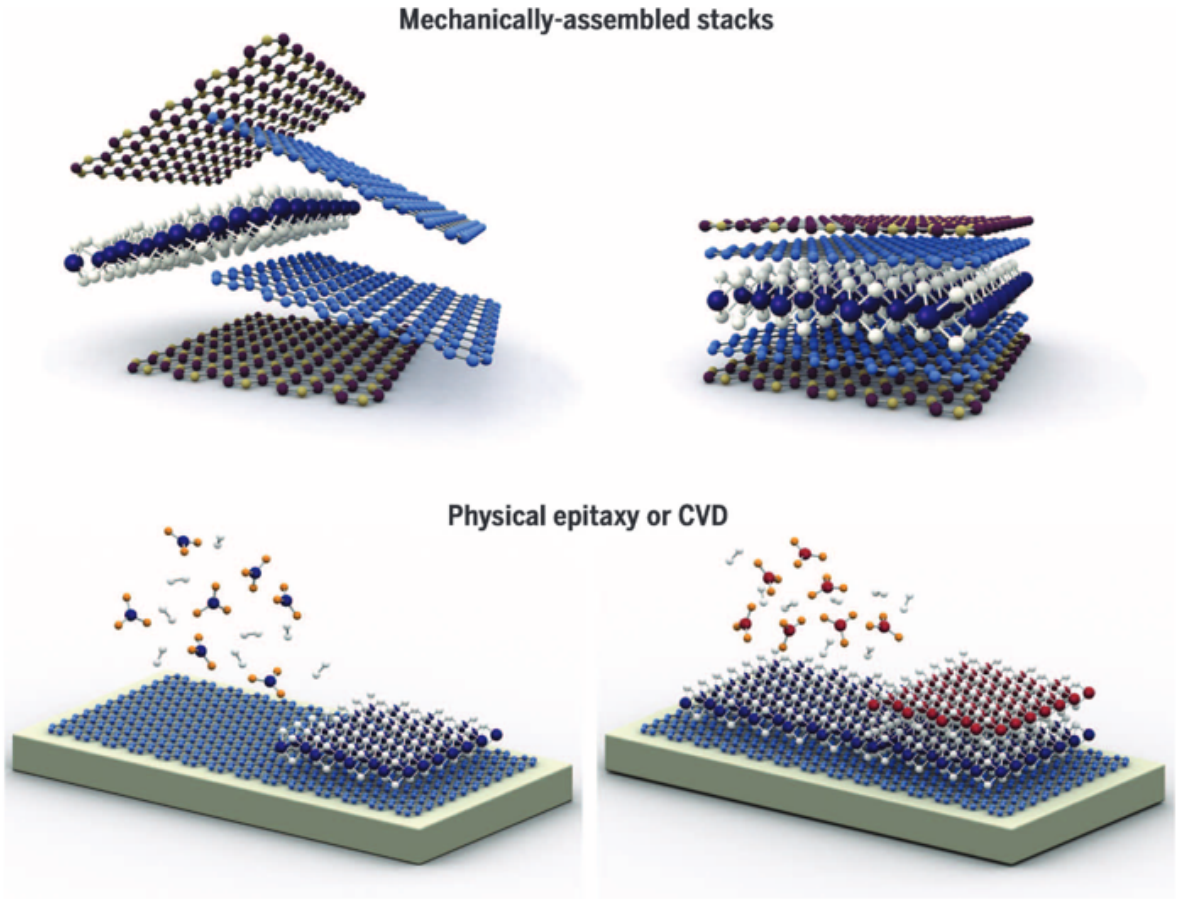

Figure 3.11: Common 2D-heterostructure preparation methods.
Adapted from [15].

Mechanical Exfoliation and Assembly

This very common method for preparation of proof-of-principle devices consists of three steps: exfoliation, searching for an appropriate flake and finally stacking [153].
First demonstrated for exfoliation of graphene from graphite, the scotch-tape method (see section 2.1) was quicky applied to other layered bulk crystals too [154]. They can be easily cleaved into few-layer and monolayer crystals, with a typical lateral size in the order of tens of μm [30].
One approach to subsequently stack the layers on top of each other is the so called wet transfer. The first layer is deposited on a sacrificial polymer membrane. Then the membrane is aligned on top of the second layer and finally the membrane is dissolved [15]. Several modifications of this technique were developed, e.g. the dry polymer based trasfer [153].
Another approach are pick-and-lift (or tear-and-stack) techniques. An adhesive polymer stamp collects one of the flakes by lifting it off the substrate. Then the stamp collects the next flake and so on. Since the polymer stamp lifts the flakes just by van-der-Waals forces this methods are also called van-der-Waals self assembly [15].
The advantage of these mechanical exfoliation and assembly methods is the direct control of the stacking order and controlled engineering of the twist angle between layers. It is further relatively easy, cheap and applicable to all sorts of 2D crystals [153]. On the other hand, residual glues and polymers can remain on top and in between the flakes. This leads often to imperfect interfaces. Although some automatized robotic fabrication attempts were made [153], this technique is hardly scalable to large areas [155].

Van-der-Waals Epitaxy

A completely different procedure for building van-der-Waals heterostructures is based on direct growth by chemical vapor epitaxy (CVD). The process is exemplarily sketched for the growth of WS_2 on a graphene/SiC substrate in Fig. 3.12. Substrate and precursors (e.g. WO_3 and S powders) are placed within a reactor, often a quartz tube. The precursors are selectively heated, sublimed and transported by a carrier gas (e.g. Ar) to the substrate surface where they react with each other and deposit the crystal [156]. Crystals grow along preferred orientations determined by the van-der-Waals interactions with the substrate. This leads to the alternative name for this technique: Van-der-Waals Epitaxy [155]. Lateral sizes of monolayer single crystals $>500\,\mu$m were reported and a variety of substrates can be used. For the growth of heterostructures one can built reactors in a row [156].
The interface of epitaxially grown heterostructures is close to perfection and nearly strain free. The process is in principle scalable for industial application [158], although some

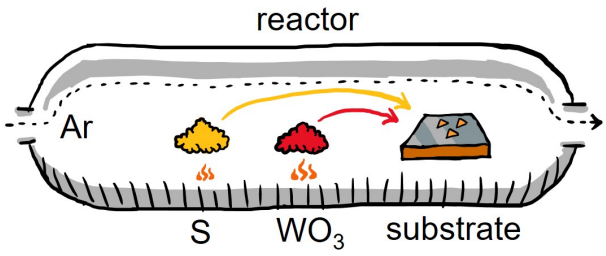

Figure 3.12: Chemical vapor deposition of WS_2 on a graphene/SiC substrate. Colored arrows indicate the mass flow of precursors. Selective heating of precursors is depicted by flame symbols. Adapted from [157].

process engineering is needed for compound growth parameters. A disadvantage is the inability of changing the twist angle between layers. It is worth noticing that CVD-grown monolayers or heterostructures can still be picked up and transferred to another substrate afterwards [156].

3.2.2 Preparation of Epitaxial WS_2/Graphene Heterostructure Samples

Epitaxial Growth of Graphene

Graphene samples were grown in UHV by thermal graphitization of silicon carbide (SiC). N-doped 6H-SiC(0001) wafers with a miscut below 0.5° bought from SiCrystal GmbH were first cleaned and smoothed via etching in hydrogen atmosphere (see Fig. 3.13a). In a second step they were graphitized by annealing in argon atmosphere until a carbon buffer layer with a $(6\sqrt{3}\times6\sqrt{3})$R30° surface reconstruction was formed (see Fig. 3.13b) [159,160]. This layer is called zero-layer (ZL) and it is still bond to Si-atoms in the layer below. In consequence it doesn't form π-bands but two non-dispersive bands at -0.5 eV and -1.3 eV binding energy instead [161].
The carbon buffer layer was then decoupled from the substrate via hydrogen intercalation at 800°C in order to obtain a quasi-free-standing graphene monolayer as skteched in Fig. 3.13c [163]. The whole process was carried out in a commercial Black Magic™ reactor from Aixtron.

Epitaxial Growth of WS_2

The WS_2 growth was carried out in a standard hot-wall reactor by CVD as already introduced in Fig. 3.12 [164, 165]. WO_3 and S powders with a weight ratio of 1:50 were used as precursors. The WO_3 and S powders were kept at 900°C and 120°C, respectively.

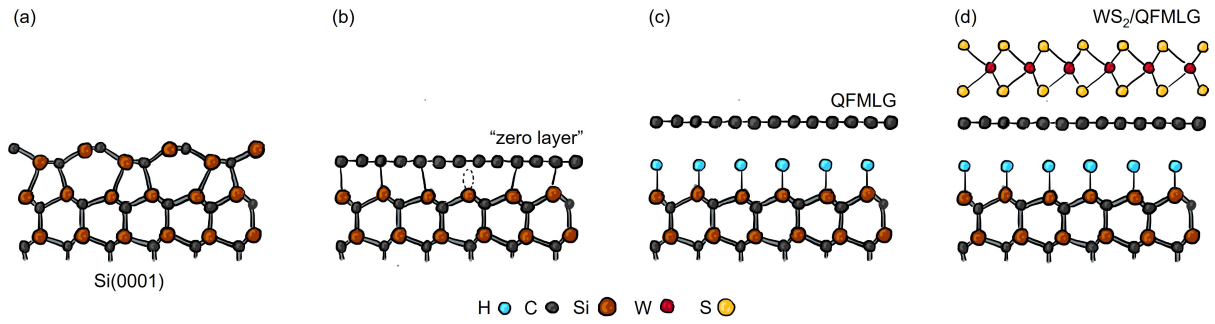

Figure 3.13: Preparation of epitaxial WS_2/graphene heterostructure samples: (a) Cleaned an hydrogen etched SiC(0001). (b) Graphitization. The dashed ellipse denote a dangling bond. (c) Quasi freestanding monolayer graphene (QFMLG) obtained by Hydrogen intercalation. (d) Deposition of WS_2 by CVD. (a)-(c) Adapted from [162].

The WO_3 powder was placed close to the substrate. Argon was used as carrier gas with a flow of 80 sccm. The pressure in the reactor was kept at 1 mbar. The synthesis process took 30 min. Fig. 3.13d depicts the finally obtained WS_2/graphene heterostructure on the SiC substrate.

Sample Characterization

Several methods were used to characterize the heterostructure samples after preparation. An exemplary micrograph obtained by secondary electron microscopy (SEM) is shown in Fig. 3.14a. The epitaxial grown WS_2 (dark grey) forms triangular islands on the graphene substrate (light grey). The coverage is estimated to be $\sim$40 %. By this incomplete coverage, the samples are suitable for measuring ARPES from WS_2 and graphene layers simultaneously, as explained in section 3.1.1 and Fig. 3.3. Two different domains of WS_2 triangles can be seen with an angle of 60° between them. Some islands are found to merge and overlap. The island side length is in the range or 300-700 nm. For the sample investigated in chapter 5 an estimation of the bilayer WS_2 content was done by SEM topographical contrast maps.

The findings from SEM analysis were confirmed by atomic force microscopy (AFM) in Fig. 3.14b. In here a content of bilayer WS_2 of $\sim$10 % can be determined. The graphene/SiC substrate below the WS_2 islands shows the typical terrace structure [166].

The sample crystal structure was investigated by low energy electon diffraction (LEED). Fig. 3.14c shows diffraction pattern obtained with an electron energy of 78 eV. A perfect azimuthal alignment between graphene and WS_2 was achieved as the relative angle in between diffraction peaks vanishes. As the SEM and AFM analysis obtained two domains of WS_2 islands we conclude that they are either aligned with their ΓK- or the $\Gamma K'$ direction

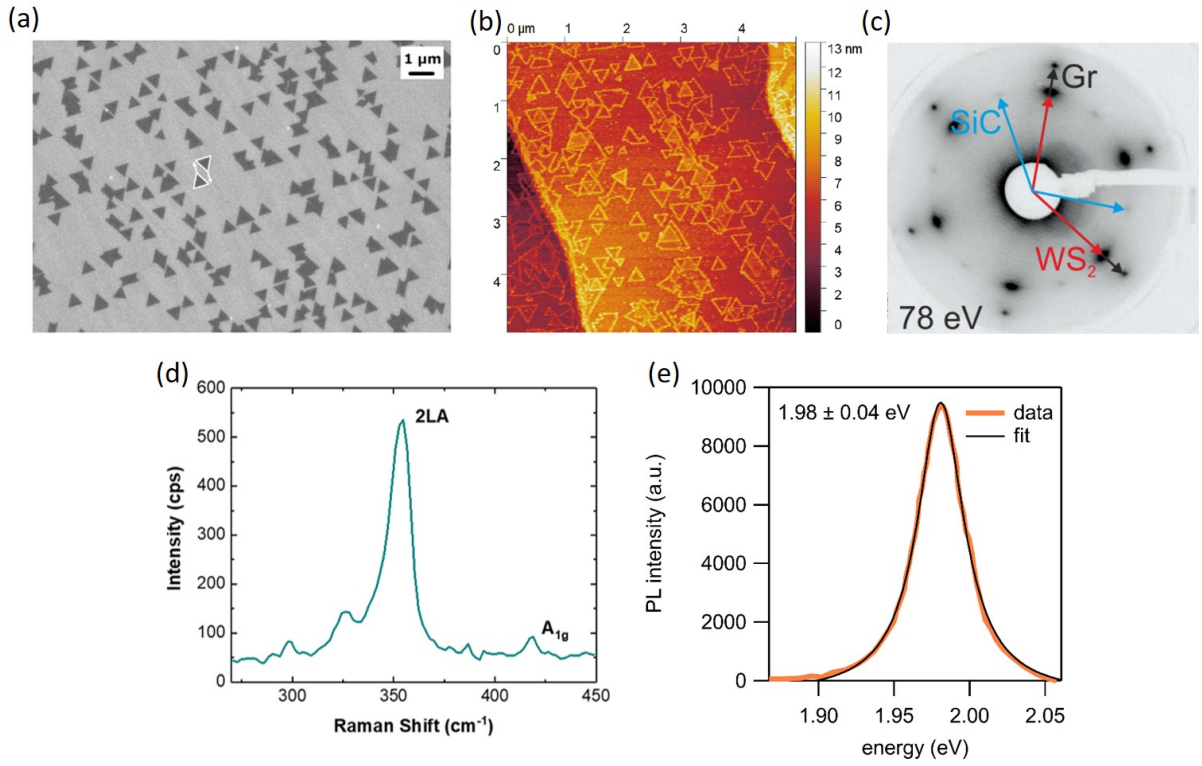

Figure 3.14: Characterization of the epitaxial WS_2/graphene heterostructure sample: (a) Secondary electron microscopy (SEM, ZEISS Merlin) picture. (b) Atomic force micrograph (Anasys AFM). (c) Low energy electron diffraction (LEED) pattern at electron energy of 78 eV. Blue, black, and red arrows point to the diffraction spots of the SiC substrate, the graphene layer, and the WS_2 layer, respectively. (d) Raman spectrum. (e) Photoluminescence (PL) spectrum. Raman, and PL spectra were performed with 1mW 532 nm laser excitation using a 100x-N.A.0.90 objective at room temperature (Renishaw, InVia).

along the ΓK-direction of the graphene layer.

Fig. 3.14d displays the Raman spectrum of a WS_2/graphene heterostructure. A ratio of >5 between the $2LA$ and A_{1g} peak intensities and the A_{1g} peak position at 419 cm^{-1} indicate a high monolayer content [167] in agreement with the AFM results.

The photoluminescence (PL) spectrum of the heterostructure in Fig. 3.14e is sharply centered at 625 nm (1.98 eV) attributed to the WS_2 A-excitonic transiton (cf. section 2.2.3).

Finally, a precise determination of the band structure of the WS_2/graphene heterostructure was possible by equilibrium high-resolution ARPES. Fig. 3.15 displays the spectrum measured in collaboration with the group of Martin Aeschlimann at the Technische Universität Kaiserslautern, Germany. The Dirac point E_D is located 300 meV above the Fermi level. The upper WS_2 valence band at K at -1.2 eV and the spin splitting of the WS_2 valence bands at K is $\sim$430 meV. By comparison with theoretical band structures of the individual layers (white dashed lines) [51, 69] no obvious hybridization can be seen (cf.

section 2.3).

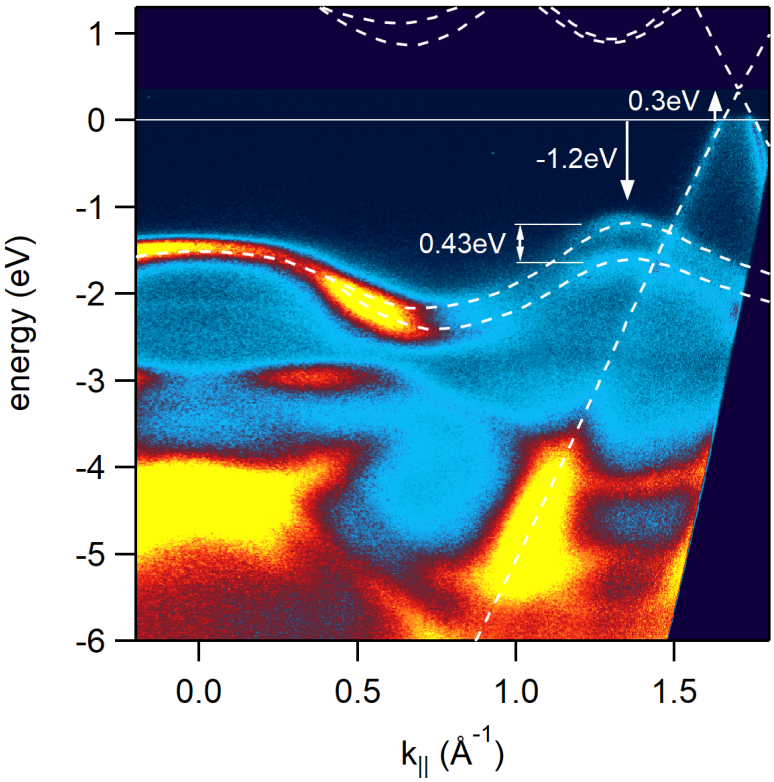

Figure 3.15: Equilibrium high-resolution ARPES spectrum of the WS_2/graphene heterostructure measured along the ΓK-direction with an unpolarized helium lamp. Measured in collaboration with the group of Martin Aeschlimann at the Technische Universität Kaiserslautern, Germany. White dashed lines denote the theoretical band structure [69] for WS_2 and graphene [51].

3.3 State of the Art: Direct Evidence for Efficient Ultrafast Charge Separation Revealed by Tr-ARPES

This section summarizes the published results from:
S. Aeschlimann, M. Chavez-Cervantes, **R. Krause**, A. Rossi, S. Forti, F. Fabbri, C. Coletti, and I. Gierz, *Direct evidence for ultrafast charge separation in epitaxial WS_2/graphene heterostructures*, Science Advances 6, 2020, eeay0761 [1].

As stated at the beginning of this chapter, the investigation of ultrafast charge transfer phenomena was only performed by all-optical techniques so far. To provide a direct picture of photocarrier populations we performed a tr-ARPES experiment in an epitaxial WS_2/graphene heterostructure.
The sample was grown as described in section 3.2.2. A pump with photon energy of 2 eV, resonant to the A-exciton transition in WS_2, excited the sample and a delayed 26 eV XUV-probe pulse was used for photoemission. TR-ARPES snapshots at the K-points of WS_2 and graphene were taken at multiple pump-probe delays.
After photoexcitation, we found that the WS_2 valence band shifts up by 90 meV and the graphene π-band shifts down by 50 meV. The exponential lifetime of these shifts is found to be 1.2 ps for the valence band of WS_2 and 1.7 ps for the graphene π-band. These peak shifts provide first evidence of a transient charging of the two layers, where additional positive (negative) charge increases (decreases) the binding energy of the electronic states. The conduction band of the WS_2 layer is found to be populated by the probe pulse with a lifetime of 1.1 ps. Within the experimental energy and time resolution no holes in the valence band of WS_2 could be found. Interestingly, we find that the gain of electrons above the equilibrium chemical potential in graphene has a much shorter lifetime (180 fs) compared to the loss of electrons below the equilibrium chemical potential (1.8 ps). The asymmetry between gain and loss is found to be absent in the pump-probe signal of uncovered monolayer graphene (cf. Fig. B.1 in Appendix), indicating that the asymmetry is a consequence of interlayer coupling in the WS_2/graphene heterostructure. The observation of a short-lived gain and long-lived loss above and below the equilibrium chemical potential, respectively, indicates that electrons are efficiently removed from the graphene layer upon photo-excitation of the heterostructure. As a result the graphene layer becomes positively charged which is consistent with the increase in binding energy of the π-band. This picture is completed with a calculation of transferred holes to graphene. We find that a total number of $\sim 5 \times 10^{12}/\mathrm{cm}^2$ are transferred from WS_2 to graphene with an exponential lifetime of 1.5 ps. The lifetime of the charge-separated transient state was found to be ~ 1 ps.
From these findings the following microscopic picture for the ultrafast charge transfer in

the WS_2/graphene heterostructure emerges (see sketches in Fig. 3.16a and b). Photo-excitation of the WS_2/graphene heterostructure at 2 eV dominantly populates the A-exciton in WS_2 (Fig. 3.16a). Additional electronic excitations across the Dirac point in graphene as well as between WS_2 and graphene bands are energetically possible but considerably less efficient. The photo-excited holes in the valence band of WS_2 are refilled by electrons originating from the graphene π-band on a timescale short compared to our temporal resolution (Fig. 3.16a). The photo-excited electrons in the conduction band of WS_2 have a lifetime of $\sim$1 ps (Fig. 3.16b). However, it takes $\sim$2 ps to refill the holes in the graphene π-band (Fig. 3.16b). This indicates that, aside from direct electron transfer between the WS_2 conduction band and the graphene π-band, additional relaxation pathways — possibly via defect states [168] — need to be considered to understand the full dynamics. The asymmetry of electron and hole transfer times was attributed to the fact that the number of available final states for hole transfer is bigger than for electron transfer.

In the transient state after photo-excitation the photo-excited electrons reside in the conduction band of WS_2 while the photo-excited holes are located in the π-band of graphene (see sketch in Fig. 3.16c). As a result the layers are oppositely charged. This accounts for the observed transient peak shifts, the asymmetry of the graphene pump-probe signal, the absence of holes in the valence band of WS_2, as well as the additional holes in the π-band of the graphene π-band. The lifetime of this charge-separated state is $\sim$1 ps. In combination with spin-selective optical excitation using circularly polarized light [88,91,93] the observed ultrafast charge transfer might be accompanied by spin transfer. In this case, the investigated WS_2/graphene heterostructure might be used for efficient optical spin injection into graphene resulting in novel optospintronic devices.

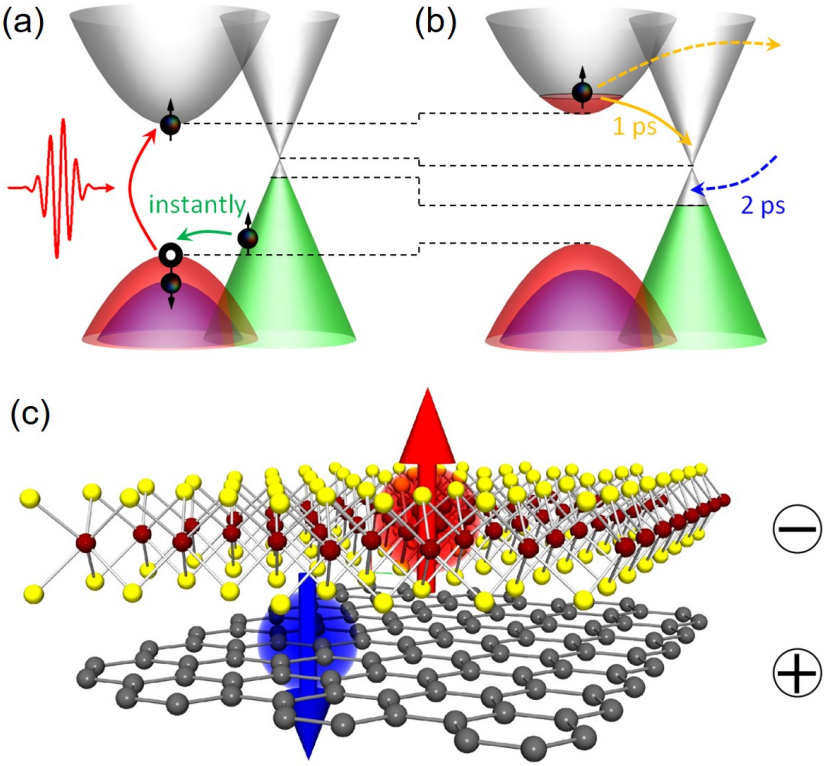

Figure 3.16: Sketch of ultrafast charge transfer deduced from tr-ARPES data. (a) Photo-excitation at resonance to the WS_2 A-exciton at 2 eV injects electrons into the conduction band of WS_2. The corresponding holes in the valence band of WS_2 are instantly refilled by electrons from the graphene π-band. (b) The photo-excited carriers in the conduction band of WS_2 have a lifetime of $\sim$1 ps. The holes in the graphene π-band live for $\sim$2 ps, indicating the importance of additional scattering channels indicated by dashed arrows. Black dashed lines in (a) and (b) indicate band shifts and changes in chemical potential. (c) In the transient state the WS_2 layer is negatively charged while the graphene layer is positively charged. For spin-selective excitation with circularly polarized light the photo-excited electrons in WS_2 and the corresponding holes in graphene are expected to show opposite spin polarization.

Chapter 4

Microscopic Understanding of Ultrafast Charge Transfer

Tthe following chapter is based on the manuscript:
R. Krause, S. Aeschlimann, M. Chavez-Cervantes, R. Perea-Causin, S. Brem, E. Malic, S. Forti, F. Fabbri, C. Coletti and I. Gierz, *Microscopic understanding of ultrafast charge transfer in van-der-Waals heterostructures*, under consideration in Phys. Rev. Lett., arXiv:2012.09268, 2021. [2].

4.1 Introduction

Despite the enormous potential for future applications in the field of optoelectronics and optospintronics, the microscopic mechanism underlying the ultrafast charge transfer processes in TMD/graphene and similar heterostructures remains poorly understood.
In this work we tackle this problem with a combination of time- and angle-resolved photoemission spectroscopy (tr-ARPES) and microscopic many-particle theory [169–171] where the measured asymmetry of the population dynamics above and below the Fermi level as well as transient band shifts serve as smoking gun evidence for ultrafast charge separation. We find that both electron and hole transfer become faster with increasing pump fluence for resonant excitation of the A-exciton in WS_2 of our epitaxial WS_2/graphene hetrostructures [164, 165]. We explain this with the help of a tunneling model where hot carriers transfer from WS_2 to graphene at those points in momentum space where the respective bands cross and where charge transfer becomes possible without energy or momentum transfer. These crossing points are separated from the VBM and CBM of WS_2 by an energy barrier. The higher the non-equilibrium carrier temperature, the easier it becomes for the carriers to overcome these barriers and to tunnel into the graphene layer.

Surprisingly, we also find that the lifetime of the charge separated state increases with increasing fluence. This trend is not captured by our microscopic simulation indicating the importance of defects. We propose that in-gap states related to S vacancies [168, 172, 173] efficiently trap photoexcited electrons in the WS_2 layer [111] and thereby set the lifetime for the charge separated state. The microscopic insights gained in the present study will guide the design of future optoelectronic and optospintronic devices where defects and band alignment will serve as important control parameters.

4.2 Results

Tr-ARPES experiments were carried out at the Hamburg setup (see section 3.1.4) using XUV probe pulses at $\hbar\omega_{probe}$=21.7 eV and visible pump pulses at $\hbar\omega_{pump}$=2 eV. The photocurrent was measured with a hemispherical analyzer (see section 3.1.7). The energy and temporal resolution were 120-170 meV and 200 fs, respectively. After normalization of raw data and detector background subtraction the spectra were transformed into k-space. Further details can be found in the Appendix A.1 and A.2.

In Fig. 4.1 we show tr-ARPES snapshots measured along the ΓK-direction of the hexagonal Brillouin zone close to the graphene and WS_2 K-points for different pump-probe delays after photoexcitation at $\hbar\omega_{\mathrm{pump}} = 2\,\mathrm{eV}$ with a pump fluence of $2.85\,\mathrm{mJ/cm^2}$ (Fig. 4.1a-d) together with the pump-induced changes of the photocurrent (Fig. 4.1e-h). Within our experimental resolution (170 meV in this particular data set) the unperturbed band structure measured at negative pump-probe delay (Fig. 4.1a) is well described by the sum of the calculated band structures of the individual layers [51, 69] (thin white dashed lines in Fig. 4.1a) after applying rigid band shifts to account for doping and to reproduce the experimentally observed WS_2 band gap. At the peak of the pump-probe signal ($t = 0.2\,\mathrm{ps}$ in Fig. 4.1b and f) we observe a gain of photoelectrons at the bottom of the WS_2 conduction band (CB), a strong gain-and-loss signal for the WS_2 valence band (VB), and a strong gain-and-loss signal for the graphene Dirac cone. We interpret these features in terms of electron-hole pair generation followed by ultrafast charge separation (see section 3.3) as discussed in detail below.

For further analysis we present momentum-resolved population dynamics (Fig. 4.2) as well as transient peak positions of the individual electronic bands (Fig. 4.3) that serve as smoking gun evidence for ultrafast charge separation in the system. The data points in Fig. 4.2a and b were obtained by integrating the photocurrent over the areas indicated by the colored boxes in Fig. 4.1f. They show the population dynamics of the WS_2 valence and conduction band (Fig. 4.2a) and the population dynamics of the graphene Dirac cone (Fig. 4.2b) as a function of pump-probe delay. Thin black lines are single exponential fits to the data (see Appendix A.5). We find that gain and loss traces for

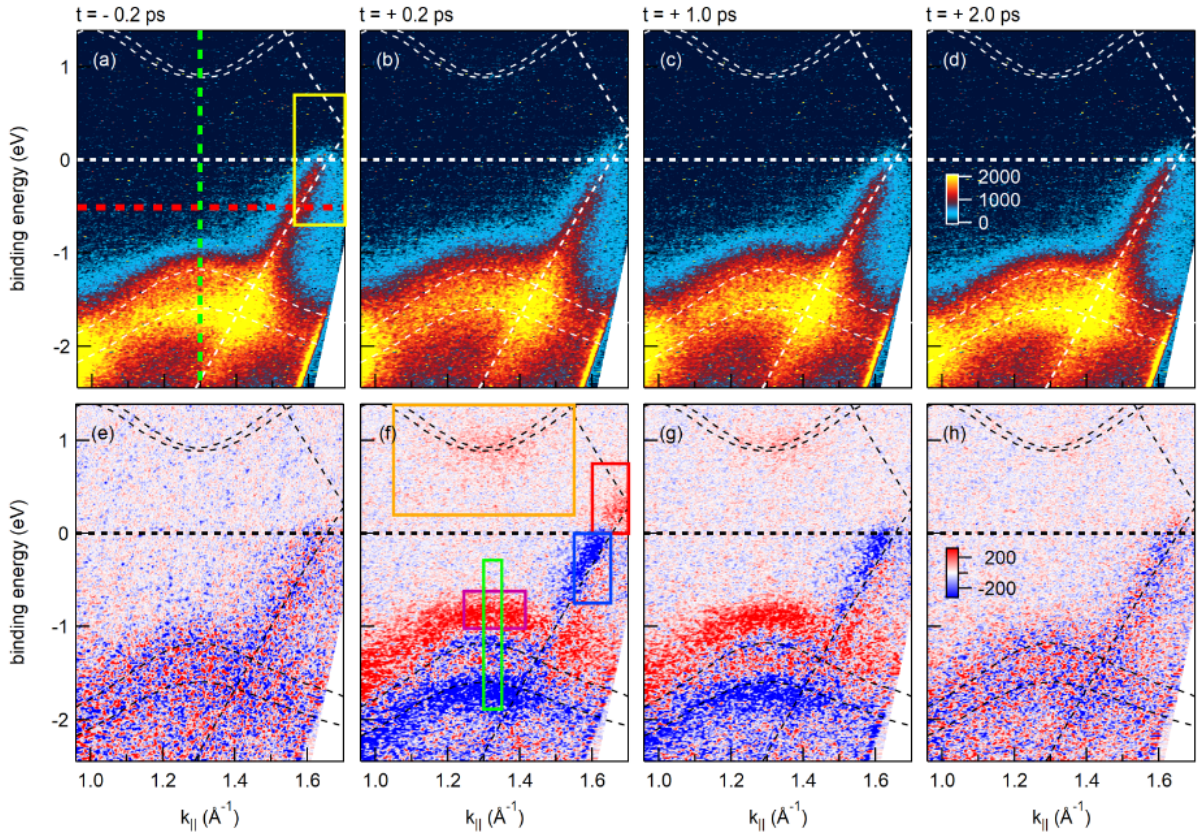

Figure 4.1: tr-ARPES snapshots of WS_2/graphene heterostructure before and after optical excitation: (a) Photocurrent measured along the ΓK-direction at negative pump-probe delay. Colored dashed lines indicate the position of the line profiles used to determine the transient band positions in Fig. 4.3c and e. The yellow box indicates the region where the Fermi-Dirac fits for Fig. 4.7c were performed. (b)-(d) Photocurrent for different pump-probe time delays after photoexcitation at $\hbar\omega_{pump}$= 2 eV with a pump fluence of 2.85 mJ/cm^2. (e)-(h) Pump-induced changes of the photocurrent for different pump-probe delays. Red and blue indicate gain and loss of photoelectrons, respectively, with respect to the photocurrent measured at negative pump-probe delay. The colored boxes in (f) indicate the area of integration for the pump-probe traces shown in Fig. 4.2a and b. Thin white (a-d) and black (e-h) dashed lines represent the calculated band structures of graphene [51] and WS_2 [69]. A rigid band shift of -0.81 eV and -1.19 eV was applied to the WS_2 CB and VB, respectively. The graphene Dirac cone was shifted by +0.3 eV to account for the observed hole doping [163]. Thick white (a-d) and black (e-h) dashed lines mark the position of the Fermi level.

both WS_2 and graphene are asymmetric. The WS_2 valence and conduction band show a short-lived loss ($\tau = 100 \pm 40$ fs) and long-lived gain ($\tau = 1.3 \pm 0.1$ ps), respectively. The situation is reversed in the graphene layer where the gain above the Fermi level is found to be short-lived ($\tau = 210 \pm 20$ fs) and the loss below the Fermi level is found to

be long-lived ($\tau = 1.50 \pm 0.06\,\mathrm{ps}$). This behavior is not observed in individual graphene and WS_2 layers (see Appendix B.1) and indicates ultrafast charge separation. In detail, the short lifetime of the loss in the WS_2 VB and the gain above the Fermi level in the graphene Dirac cone indicate that the photoexcited holes in the WS_2 layer are rapidly (on a timescale comparable to the temporal resolution of 200 fs) refilled by electrons from graphene. The photoexcited electrons, on the other hand, are found to remain in the WS_2 CB for $\tau = 1.3 \pm 0.1\,\mathrm{ps}$.

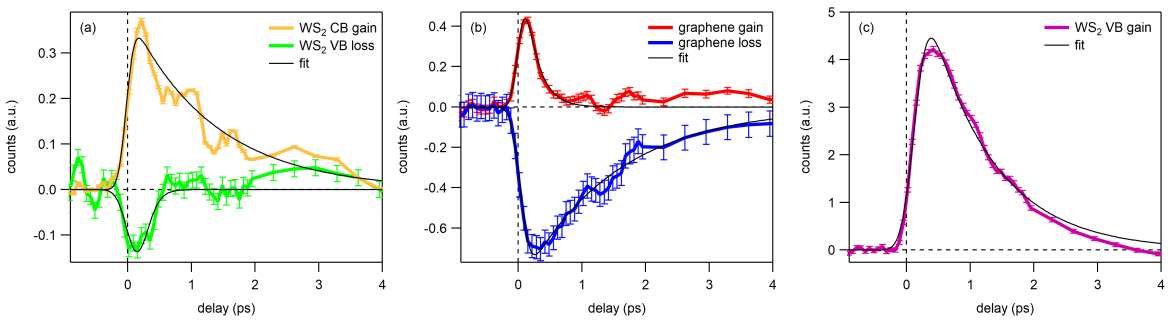

Figure 4.2: Momentum resolved population dynamics in WS_2/graphene heterostructure: (a) Gain in the WS_2 CB (orange) and loss in the WS_2 VB (green) obtained by integrating the counts over the areas indicated by the orange and green boxes in Fig. 4.1f, respectively. (b) Graphene dynamics: Gain above the Fermi level (red) and loss below the Fermi level (blue) obtained by integrating the counts over the areas indicated by the red and blue boxes in Fig. 4.1f, respectively. (c) Gain above the equilibrium position of the upper WS_2 VB obtained by integrating the counts over the area indicated by the purple box in Fig. 4.1f. Thin black lines are single exponential fits to the data (see Appendix A.5). All data was obtained with a pump fluence of $2.85\,\mathrm{mJ/cm^2}$.

The resulting charge separated transient state leaves the WS_2 layer negatively charged and the graphene layer positively charged. This is expected to decrease the binding energy of the WS_2 states and increase the binding energy of the graphene states (see section 3.3). In Fig. 4.3a we plot the transient peak positions of the upper WS_2 VB and the WS_2 CB that were obtained by fitting energy distribution curves (EDCs) through the K-point of WS_2 (dashed green line in Fig. 4.1a) with a Gaussian (see Appendix A.4). The energy difference between the WS_2 CB and VB directly yields the transient band gap E_{gap} shown in the lower part of Fig. 4.3a. From an exponential fit to the data (see Appendix A.5 and A.6) we deduce an equilibrium gap size of 2.08 eV and a lifetime of $\tau = 0.8 \pm 0.4\,\mathrm{ps}$ for the transient band gap renormalization ΔE_{gap}. The renormalization is a consequence of increased screening in the presence of photoexcited carriers and is commonly observed in photodoped TMD monolayers [81, 97, 174–176]. The effects of renormalization and charging onto WS_2 CB and VB is sketched in Fig. 4.3b.

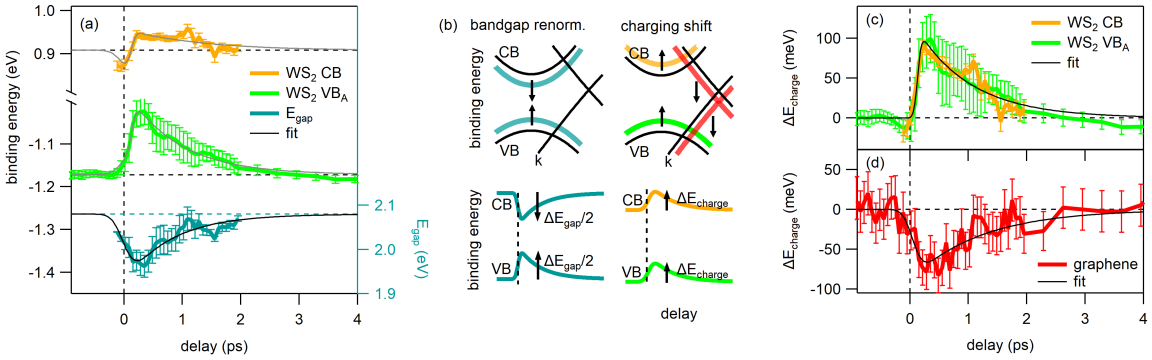

Figure 4.3: Transient band positions: (a) Position of the WS_2 CB (orange) obtained from Gaussian fits of line profiles obtained by integrating the photocurrent over the momentum range indicated by the orange box Fig. 4.1f and position of upper VB of WS_2 (green) obtained from Gaussian fits of line profiles extracted along the dashed green line in Fig. 4.1a as a function of pump-probe time delay. The transient band gap of WS_2 (turquois) was obtained by subtracting the transient position of the VB from the transient position of the CB. (b) Sketch of the effect of bandgap renormalization and charging shift onto CB and VB. (c) Charging-induced shift of WS_2 VB and CB obtained by adding (subtracting) $|\Delta E_{gap}|/2$ to (from) the VB (CB) position in panel a. (d) Transient shift of the graphene Dirac cone obtained from Lorentzian fits of the line profile extracted along the red dashed line in Fig. 4.1a. The resulting momentum shift was converted into an energy shift by multiplying with the slope of the band. Black lines are single exponential fits to the data. Gray lines in panel a were calculated from the exponential fitst for E_{gap} in panel a and the exponential fits in panel c. All data was obtained with a pump fluence of $2.85\,\mathrm{mJ/cm^2}$.

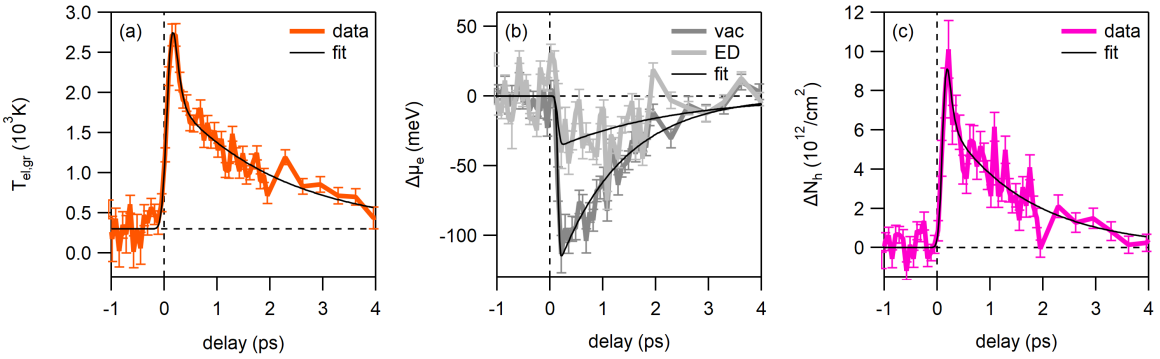

Figure 4.4: Hot carrier dynamics in graphene: This data was obtained from Fermi-Dirac fits to the carrier distribution inside the yellow box in Fig. 4.1a. Electronic temperature together with double-exponential fits (a), chemical potential together with single-exponential fit (b), and number of holes transferred into the graphene layer together with single-exponential fit (c) as a function of pump-probe delay.

Assuming that band gap renormalization shifts the WS_2 VB up and the WS_2 CB down by the same amount $|\Delta E_{\text{gap}}|/2$ we can subtract its contribution from the transient peak positions in Fig. 4.3a yielding the data in Fig. 4.3c where both the WS_2 valence and conduction band are found to shift up by $\sim$100 meV with a lifetime of $\tau = 1.03 \pm 0.07$ ps. This shift is attributed to the transient negative charging of the WS_2 layer. The transient position of graphene's Dirac cone in Fig. 4.3d was extracted from Lorentzian fits of momentum distribution curves (MDCs) at $E = -0.5$ eV extracted along the dashed red line in Fig. 4.1a. The resulting momentum shift was converted into an energy shift by multiplying with the slope of the band $\nu_F = 7$ eVÅ [29]. The observed increase in binding energy with an exponential lifetime of 1.08 ± 0.06 ps is a direct consequence of the additional positive charge on the graphene layer due to ultrafast hole transfer.

In order to experimentally determine the number of holes that are transferred from WS_2 to graphene we fit the carrier distribution inside the Dirac cone obtained by integrating the tr-ARPES data over the momentum region indicated by the yellow box in Fig. 4.1a with a Fermi-Dirac distribution (see Appendix A.7). The resulting electronic temperature T_{el} and chemical potential μ_{vac} are shown in Fig. 4.4a and b, respectively. The number of holes transferred into the graphene layer shown in Fig. 4.4c is then obtained from T_{el} and μ_{ED} as described in Appendix A.7. The expontial lifetime of the holes inside the Dirac cone is found to be $\tau = 1.3 \pm 0.1$ ps.

In order to gain access to the microscopic mechanism underlying the observed ultrafast charge transfer phenomena we now investigate the pump fluence dependence of the data presented in Figs. 4.2-4.4. In Fig. 5 we show the fluence dependence of different quantities at t = 200 fs where the pump-probe signal reaches its maximum (for detailed data on other fluences see Appendix B.3). While the counts in the different boxes from Fig. 4.1e

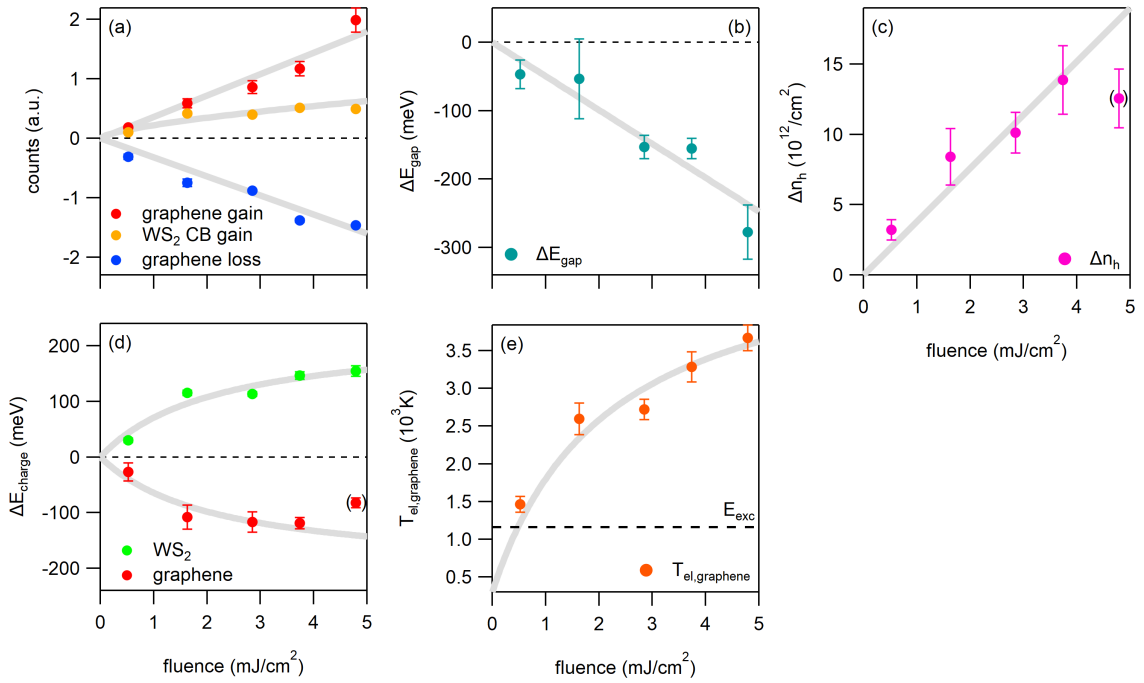

Figure 4.5: Fluence dependence of different parameters at the peak of the pump-probe signal (t=0.2 ps): (a) Pump-induced change of photocurrent inside colored boxes from Fig. 4.1f. (b) Change of the WS_2 band gap from Fig. 4.3c. (c) Number of holes transferred into the graphene layer from Fig. 4.4c. (d) Charging-induced WS_2 and graphene band shifts from Fig. 4.3c and d. (e) Peak electronic temperature of Dirac carriers from Fig. 4.4a. E_{exc} marks the exciton binding energy. Light gray lines are guides to the eye. The datapoints in brackets were obtained on areas of the sample with lower WS_2 coverage (see Appendix A.1).

(Fig. 4.5a), the change of the WS_2 band gap (Fig. 4.5b), and the number of holes transferred into the graphene layer (Fig. 4.5c) show a linear fluence dependence, the charging-induced band shifts (Fig. 4.5d) as well as the peak electronic temperature of the carriers inside the Dirac cone (Fig. 4.5e) show a sublinear dependence on the fluence F. These curves could be fitted using a saturation fit model $f(F) = a \cdot \frac{F}{1+F/F_S}$ [177] with scaling factor a yielding a saturation fluence F_S of $2\pm1\,\mathrm{mJ/cm^2}$ (see grey guides to the eye).
Note that the peak electronic temperature in Fig. 4.5e of more than 1400 K is bigger than the exciton binding energy E_{exc} of ∼100 meV (1160 K). The latter was obtained by subtracting the A-exciton peak energy of 1.98 eV (cf. Fig. 3.14e) from the equilibrium band gap in WS_2 of 2.08 eV (cf. Fig. 4.3a) [30]. An estimation of the electronic temperature in WS_2 can be found in Appendix A.8. Assuming that the carrier temperatures in graphene and WS_2 are similar, we conclude that the photoexcited excitons rapidly decay into free electron-hole pairs.
The pump fluence dependence of the electron and hole transfer rates as well as the lifetime of the charge separated state were determined as follows. As discussed above, the short-

lived loss in the WS_2 VB (Fig. 4.2a) is directly linked to the short-lived gain above the Fermi level in the Dirac cone of graphene (Fig. 4.2b). The signal-to-noise ratio, however, is much better in the latter case, which is why we focus on the graphene gain rather than the WS_2 VB loss to analyze the pump fluence dependence of the ultrafast hole transfer. The result is shown in Fig. 4.6a. We find that the hole transfer time of ~ 1 ps observed at the lowest pump fluence rapidly drops to a value short compared to our temporal resolution of 200 fs with increasing fluence. Figure 4.6b shows the pump fluence dependence of the lifetime of the photoexcited electrons in the conduction band of WS_2 from Fig. 4.2a. This value is found to decrease linearly from $\sim$ 2 ps at the lowest fluence to below 1 ps at the highest fluence. In Fig. 4.6c we plot the pump fluence dependence of the gain above the equilibrium position of the upper WS_2 VB (Fig. 4.2c) obtained by integrating the photocurrent over the area indicated by the pink box in Fig. 4.1f. We confirmed that this quantity shows the same fluence dependence as the charging-induced band shifts in Fig. 4.3c (see Appendix B.2) that are directly linked to the charge separated state albeit with an improved signal-to-noise ratio. From Fig. 4.6c we find that the lifetime of the charge separated state linearly increases with increasing fluence from $\sim$ 0.8 ps at the lowest fluence to $\sim$ 1.4 ps at the highest fluence.

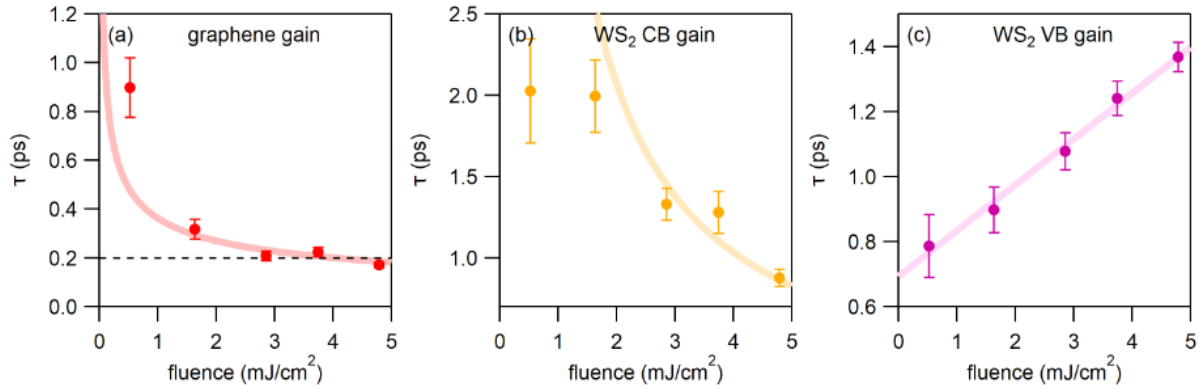

Figure 4.6: fluence dependence of ultrafast charge separation and recombination: (a) Lifetime of graphene gain from Fig. 4.2b as a function of fluence. The black dashed line represents our temporal resolution of 200 fs. (b) Lifetime of photoexcited electrons in the WS_2 CB from Fig. 4.2a as a function of fluence. (c) Lifetime of gain above the equilibrium position of the upper WS_2 VB obtained by integrating the photocurrent over the area marked by the pink box in Fig. 4.1f and by fitting the resulting population dynamics with a single exponential decay. Thick lines in a and b were obtained by inverting and rescaling the guides to the eye from Fig. 4.7e to match the data points. The thick line in c is a guide to the eye.

In summary, Fig. 4.6 shows that the transfer rate of the holes increases with increasing fluence, the lifetime of the photoexcited electrons in the CB of WS_2 decreases with in-

creasing fluence, and the lifetime of the charge separated state increases with increasing fluence.

4.3 Discussion

Before deriving a microscopic description for the observed ultrafast charge separation in the investigated WS_2/graphene heterostructure, we compare our data to other pump fluence-dependent experimental studies on similar van-der-Waals heterostructures [39,174] and discuss whether the models proposed in literature [112, 178, 179] might also apply in our case.

Reference [174] investigated an epitaxial MoS_2/graphene heterostructure on SiC(0001) with tr-ARPES. They observed a considerable band gap renormalization that increased with increasing hole density with a maximum value of $-450\,\mathrm{meV}$ at $n_h = 1.5 \times 10^{-12}\,\mathrm{cm}^{-1}$ with pump fluences in the $\mathrm{mJ/cm^2}$ regime. These values are of the same order of magnitude as our data presented in Fig. 4.5b. Unlike the present study, Ref. [174] did not observe any indication for charge separation. We speculate that this might be related to the azimuthal alignment between the TMD and the graphene lattice which was 30° in [174] and which is 0° or 60° in the present study.

Reference [39] performed transient absorption measurements on CVD-grown WS_2/graphene heterostructures on SiO_2 but observed no systematic pump fluence dependence of the relaxation times with pump fluences in the $\mu\mathrm{J/cm^2}$ regime. The authors proposed a model where the electric field across the interface that builds up due to charge separation caused by ultrafast hole transfer from WS_2 to graphene increases the transfer rate for the electrons which can be reconciled with our observation in Fig. 3b. However, this model cannot explain our observation that the hole transfer rate also increases with increasing fluence (see Fig. 4.6).

References [112, 178, 179] proposed a coherent phonon-driven charge transfer mechanism for ultrafast charge separation in vdW heterostructures with type II band alignment. The frequency of the associated coherent oscillations, however, is too high to be resolved given the limited temporal resolution of 200 fs in the present study.

Therefore, we evoke a new scenario where carriers can tunnel from one layer to the other at the points in momentum space where the bands of the individual layers cross and where charge transfer can occur without energy or momentum transfer. In this scenario the transfer rate is proportional to $e^{-\Delta E/k_B T}$, where the energy barrier ΔE is given by the distance between the WS_2 VBM or CBM and the closest crossing point (see Fig. 4.7a) and where $k_B T$ is the thermal energy of the carriers. The temporal evolution of the energy barriers for electron and hole transfer was deduced from the transient band shifts

in Fig. 4.3 and is shown in Fig. 4.7b. The temperature of the electron-hole pairs in WS_2 is difficult to determine experimentally due to the short lifetime of the holes and the limited signal-to-noise ratio. The electronic temperature of the Dirac carriers inside the graphene layer (see Fig. 4.7c) on the other hand can be easily extracted from Fermi-Dirac fits of the transient carrier distribution inside the Dirac cone as described in the Appendix A.7. Assuming that the electronic temperature for the carriers inside the Dirac cone is similar to the one of the carriers in the WS_2 layer, we can determine the temporal evolution of the transfer rates shown in Fig. 4.7d. The peak rate is found to be faster for holes than for electrons and to increase with increasing fluence for both electrons and holes (see Fig. 4.7e) in good qualitative agreement with the data in Fig. 4.6.

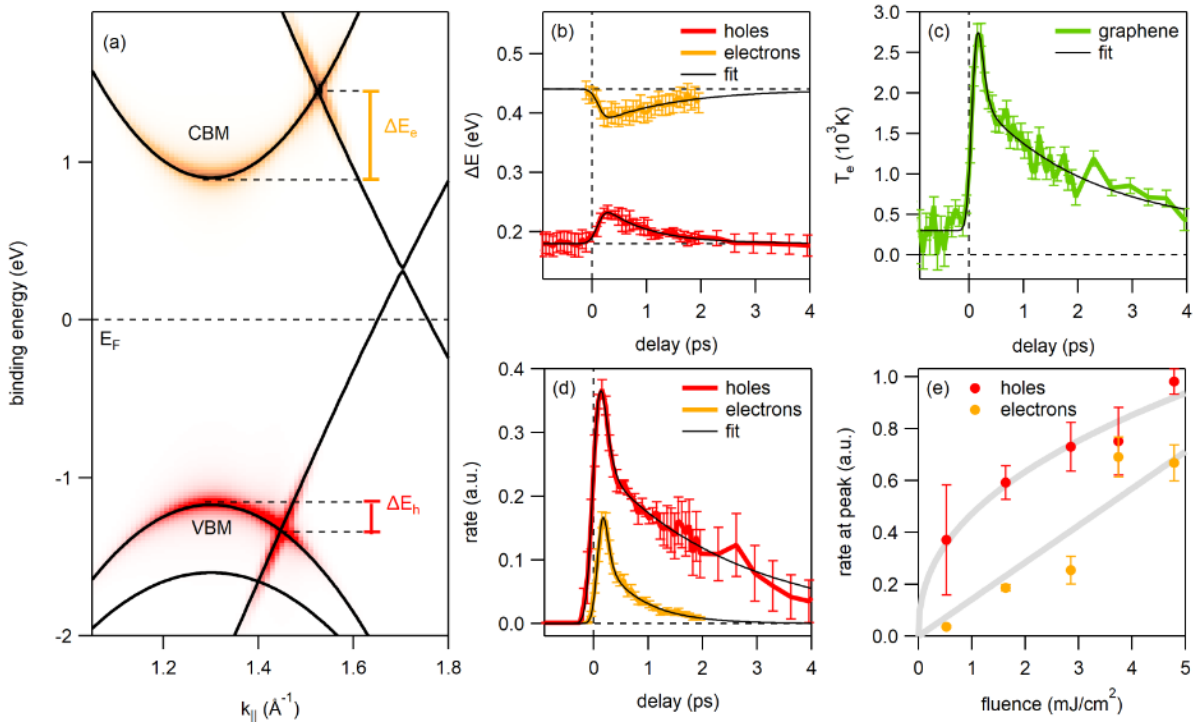

Figure 4.7: direct tunneling model: (a) Sketch of the band structure with tunneling barrier for holes (ΔE_h, red) and electrons (ΔE_e, orange) (b) Temporal evolution of the two barrier heights deduced from Fig. 4.3 together with single-exponential fit. (c) Temporal evolution of the electronic temperature inside the Dirac cone together with double-exponential fit. (d) Temporal evolution of the electron and hole transfer rates deduced from panels b and c together with double-exponential fit. (e) Pump fluence dependence of the peak transferrates for electrons and holes. Thick gray lines are guides to the eye.

To confirm the above interpretation, we calculated the transfer times for electrons and holes using a microscopic model based on the density matrix formalism [109, 169–171]. For details see Appendix C.1. The momentum dependence of the tunneling matrix element

evaluated on a tight-binding level for CB and VB is shown in Fig. 4.8a and b, respectively, together with black lines that indicate the position in momentum space where the crossing between WS_2 CB and VB, respectively, and the Dirac cone occurs. The tunneling matrix elements exhibit a strong momentum dependence that can be traced back to the pseudospin of the Dirac carriers in the graphene layer. More importantly, the tunneling matrix element in the region of interest is found to be much bigger for the VB than for the CB. In addition to the different energy barriers found in Fig. 4.6b this accounts for the experimentally observed asymmetry between electron and hole transfer. We also calculated the transfer times for holes and electrons as a function of the height of the respective energy barrier and the carrier temperature in Fig. 4.8c and d. In good qualitative agreement with our experiment, the calculated lifetimes are found to decrease with increasing carrier temperature (i. e. with increasing pump fluence), while the change in barrier height (< 100 meV in the experiment) is found to have a minor influence on the fluence dependence of the lifetimes.

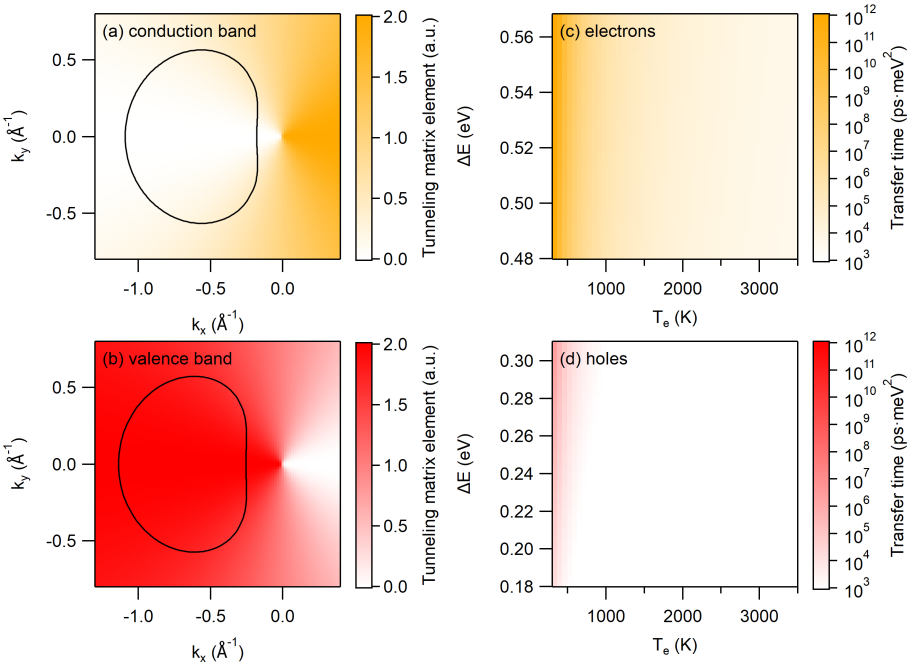

Figure 4.8: Theory: Momentum dependence of the tunneling matrix element calculated from tight-binding for CB (a) and VB (b). $k_x = k_y = 0$ corresponds to the K-point of graphene. Calculated transfer time for electrons (c) and holes (d).

While this model nicely explains the observed fluence dependence of the carrier lifetimes in Fig. 4.6a and b, it fails to reproduce the fact that the lifetime of the charge separated transient state is found to increase with increasing fluence (Fig. 4.6c). This indicates that, in addition to the direct tunneling scenario proposed above, there are additional charge

transfer channels that need to be considered for a full microscopic understanding of the ultrafast charge transfer processes in our WS_2/graphene heterostructure. A likely candidate are defect-related charge transfer channels involving S vacancies [168, 173]. It has been shown using scanning tunneling spectroscopy combined with GW calculations [173] that S vacancies give rise to two spin-orbit split states inside the band gap of WS_2. These states were proposed to efficiently trap photoexcited electrons inside the WS_2 layer and thereby enhance the lifetime of the charge separated state in commercial WS_2/ graphene heterostructures [111]. Hints for such defect states in our tr-ARPES data are shown in Appendix B.4.

In Fig. 4.9 we summarize our understanding of the relevant microscopic scattering channels that mediate the ultrafast charge transfer in our WS_2/graphene heterostructure. Direct tunneling (yellow and red arrows) sets the timescale for charge separation, while defect-assisted tunneling (blue arrows) sets the timescale for charge recombination. This model resolves two important controversies in literature. First, it remains unresolved whether charge transfer occurs at K where the orbital overlap is relatively weak or at other valleys (Γ and Σ) where orbital overlap is stronger (cf. section 2.2.2) [112, 114, 178–181]. Our findings suggest that ultrafast charge transfer in the investigated epitaxial WS_2/graphene heterostructure occurs at the band intersections close to the K-point. The second unresolved issue is related to momentum conservation during charge transfer [180, 182]. We propose that ultrafast charge separation occurs via direct tunneling with zero momentum transfer. Charge carrier recombination is dominated by defect-assisted tunneling where the strong localization of the defect states in real space leads to a delocalization over a big part of the Brillouin zone which again enables tunneling at zero momentum transfer.

In summary we combined tr-ARPES with microscopic many-particle theory to unravel the microscopic mechanism of ultrafast charge separation and recombination in epitaxial WS_2/graphene heterostructures. We find a subtle interplay between direct tunneling at the band intersections close to the K-point that sets the timescale for charge separation and defect-assisted tunneling via localized S vacancies that sets the timescale for electron-hole recombination. Our findings will guide the development of improved optoelectronic devices where defect and band structure engineering will serve as important control parameters.

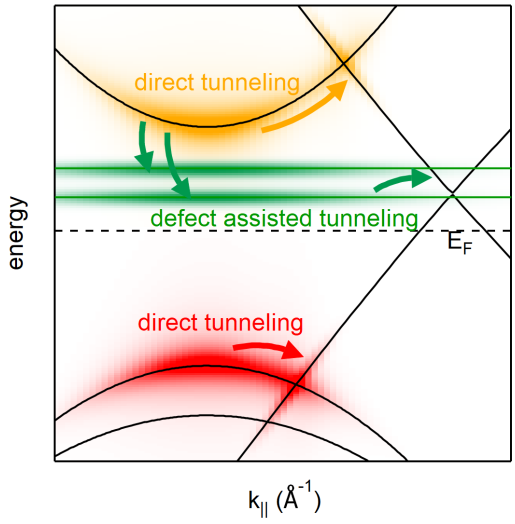

Figure 4.9: Final microscopic model including direct (yellow and red arrows) as well as defect-assisted tunneling (green arrows).

Chapter 5

Ultrafast charge separation in bilayer WS_2/graphene heterostructure

This section is based on the publication:
R. Krause, M. Chávez-Cervantes, S. Aeschlimann, S. Forti, F. Fabbri, A. Rossi, C. Coletti, C. Cacho, Y. Zhang, P. E. Majchrzak, R. T. Chapman, E. Springate and Isabella Gierz, *Ultrafast charge separation in bilayer WS_2/graphene heterostructure revealed by time- and angle-resolved photoemission spectroscopy*, Frontiers in Physics 9, 2021, 668149. [3].

5.1 Introduction

Solar energy conversion plays an important role in satisfying mankind's ever-increasing energy usage in an environmentally friendly way. Despite several decades of optimization Silicon solar cells still lack efficiency. On the other hand, highly efficient III-V multijunction solar cells are expensive and not sustainable [183,184]. Recently, van der Waals (vdW) heterostructures made of different monolayer (ML) transition metal dichalcogenides (TMDs) have emerged as a promising new solar cell platform due to their strong excitonic absorption in the visible spectral range [23,30] followed by efficient ultrafast charge separation due to type II band alignment [102–105, 110, 182] (see Fig. 5.1a). Interestingly, ultrafast charge separation was also found to occur in ML WS_2/graphene heterostructures despite the type I band alignment (see Fig. 5.1b). These heterostructures combine the benefits of a direct gap semiconductor with strong spin-orbit coupling [69, 70] and a semimetal with high-mobility carriers and long spin lifetimes [45] with great potential for novel optoelectronic and optospintronic applications [185].

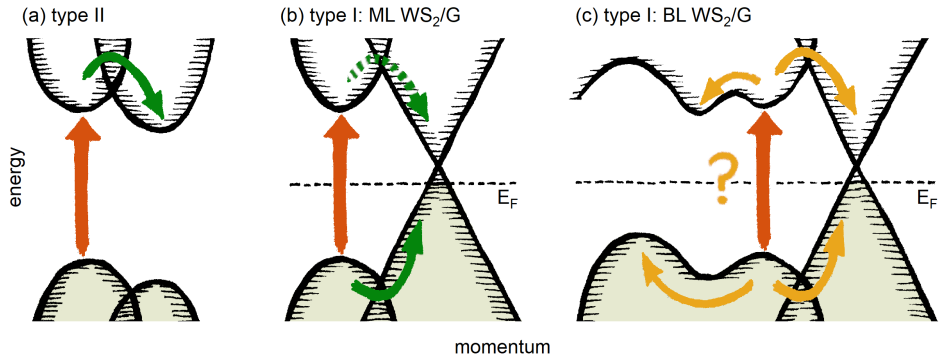

Figure 5.1: Influence of band alignment on ultrafast charge transfer in different van der Waals heterostructures: (a) Example of a heterostructure with type II band alignment favoring electron transfer. (b) Type I band alignment of a heterostructure made of monolayer WS_2 and monolayer graphene. Both electrons and holes are found to transfer to the graphene layer albeit at different rates resulting in ultrafast charge separation. (c) Band alignment of a heterostructure made of bilayer WS_2 and monolayer graphene. The influence of the indirect band gap on the microscopic scattering channels mediating ultrafast charge transfer remains unexplored.

One simple way to improve the efficiency of WS_2/graphene-based light harvesting devices might be to enhance the thickness and therefore the absorption of the WS_2 layer [32, 33, 186]. It is not *a priori* clear, however, if ultrafast charge separation survives when direct-gap monolayer WS_2 is replaced by thicker WS_2 layers with an indirect band gap (Fig. 5.1c). In this work we address this issue by exciting carriers across the direct gap at the K-point of BL WS_2 in an epitaxial BL WS_2/graphene heterostructure on SiC(0001) and tracing the relaxation of the photogenerated electron-hole pairs as a function of time, energy, and momentum using time- and angle-resolved photoemission spectroscopy (tr-ARPES). We find that photoexcited holes in BL WS_2 are transferred to the graphene layer within 100 fs. The photoexcited electrons are found to remain in the conduction band of BL WS_2 for 420 fs resulting in the formation of a charge separated transient state with a lifetime of 770 fs. These timescales are consistent with the microscopic charge transfer model proposed in chapter 4 for ML WS_2/graphene heterostructures indicating that also in the case of BL WS_2 on graphene the timescale for charge separation is determined by direct tunneling at the points in the Brillouin zone where WS_2 and graphene bands intersect.

5.2 Results

Tr-ARPES experiments were carried out at the Artemis setup (see section 3.1.4) using XUV probe pulses at $\hbar\omega_{probe}$=31.8 eV and visible pump pulses at $\hbar\omega_{pump}$=2 eV. The photocurrent was measured with a Time-of-Flight analyzer (see section 3.1.7). The energy and temporal resolution were 450 meV and 66 fs, respectively.

WS_2/graphene samples were grown similarly as described in section 3.2.2. After growth, the sample was characterized with secondary electron microscopy (SEM), Raman and photoluminescence (PL) spectroscopy, as well angle-resolved photoemission spectroscopy (ARPES).

The SEM picture in Fig. 5.2a shows dark triangular WS_2 islands that cover $\sim$ 80% of the graphene layer. The orientation of the triangles reveals the presence of two rotational domains with an angle of 60° between them. From previous low energy electron diffraction measurements on similar samples (see Fig. 3.14) we deduce that either the ΓK- or the $\Gamma K'$-direction of the WS_2 islands are aligned with the ΓK-direction of graphene. Further, the topological contrast reveals that $\sim$ 90% of the islands consist of bilayer WS_2. This is consistent with the Raman spectrum shown in Fig. 5.2b where the energy of the A_{1g} peak at 417 cm^{-1} and the intensity ratio between the central peak at 351 cm^{-1} ($2LA+E_{2g}$) and the A_{1g} peak of $\sim$ 6 are indicative of bilayer WS_2 [167]. From the PL spectrum in Fig. 5.2c we find a quenched A-exciton resonance at 635 nm (1.95 eV) which confirms the presence of bilayer WS_2 [187]. The ARPES spectrum in Fig. 5.2d was taken along the along the ΓK-direction. We find that the band structure of the heterostructure is a superposition of the band structures of the constituting materials that are indicated by the white dashed lines [51, 69]. The Dirac cone of graphene is found to be hole-doped with the Dirac-point 300 meV above the Fermi level, E_F. As expected for bilayer WS_2 [69] the maximum of the WS_2 valence band is found to be located at the Γ-point.

To investigate ultrafast charge transfer in our BL WS_2/graphene heterostructure we excited carriers across the direct band gap at the K-point of BL WS_2 using 2 eV pump pulses and probed the response of the heterostructure using tr-ARPES. In detail, we investigated the time dependence of two representative energy distributions curves (EDC 1 and EDC 2 in Fig. 5.2d) to obtain the population and band structure dynamics of the WS_2 conduction and valence band (CB and VB) and the graphene Dirac cone, respectively. The pump fluence was 6.6 mJ/cm^2 for EDC 1 (WS_2) and 9.1 mJ/cm^2 for EDC 2 (graphene).

Figures 5.3a and b show EDC 1 and EDC 2, respectively, as a function of pump-probe delay. The corresponding pump-induced changes obtained by subtracting the respective EDC at negative pump-probe delay from the transient EDCs are shown in Figs. 5.3c and d. Upon arrival of the pump pulse the WS_2 VB is found to shift towards the Fermi level in Fig. 5.3a. This up-shift is responsible for the strong gain (red) and loss (blue) signal

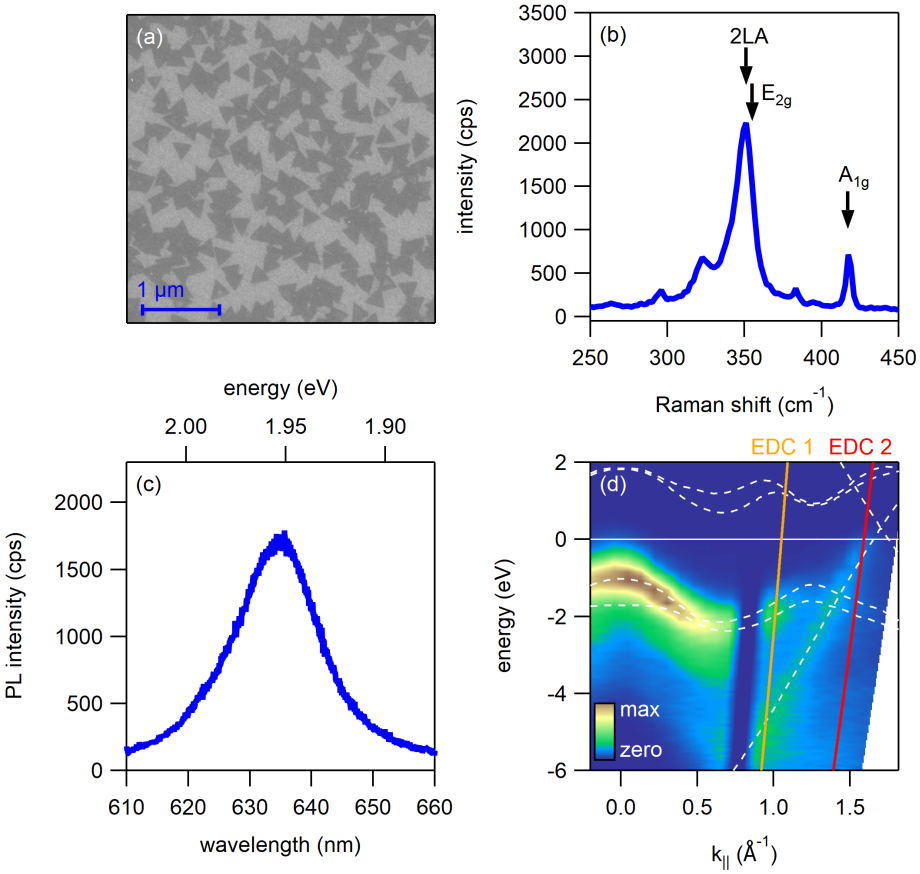

Figure 5.2: Sample characterization: (a) Secondary electron micrograph revealing triangular WS_2 islands with two different rotational domains. The picture was obtained with *in lens* mode with an accelerating voltage of 5 keV and a beam current of 96 pA. (b) Raman spectrum. Arrows indicate the phonon modes that were used to determine the layer thickness. (c) Photoluminescence (PL) spectrum. Raman and PL measurements were carried out with 1 mW laser excitation at $\lambda = 532$ nm at room temperature. (d) ARPES spectrum revealing the occupied part of the band structure of the heterostructure. Orange and red lines indicate the two energy distribution curves (EDCs) that were chosen for the time-resolved measurements in Fig. 5.3. White dashed lines denote theoretical band positions of graphene [51] and bilayer WS_2 [69]. A rigid band shift of +0.3 eV was applied to graphene bands to account for the observed p-doping. WS_2 CB and VB were rigidly shifted by -0.81 eV and -1.19 eV, respectively, to match the experimental dispersion. The thin white line marks the position of the Fermi level, E_F. At an emission angle of $\sim 23°$ the laser beam was directly reflected into the Time-of-Flight analyzer dazzling the detector and leading to a dark corridor at $\sim 0.8\,Å^{-1}$.

around −2 eV in Fig. 5.3c. Fig. 5.3c also reveals a transient gain of photoelectrons in the CB of WS_2 around +1 eV following photoexcitation. The graphene π-band in Fig. 5.3b is found to broaden and to shift down which — together with the up-shift of the WS_2 VB

at lower energy — produces the gain-loss-gain signal in the energy range between +1 and −2 eV in Fig. 5.3d.

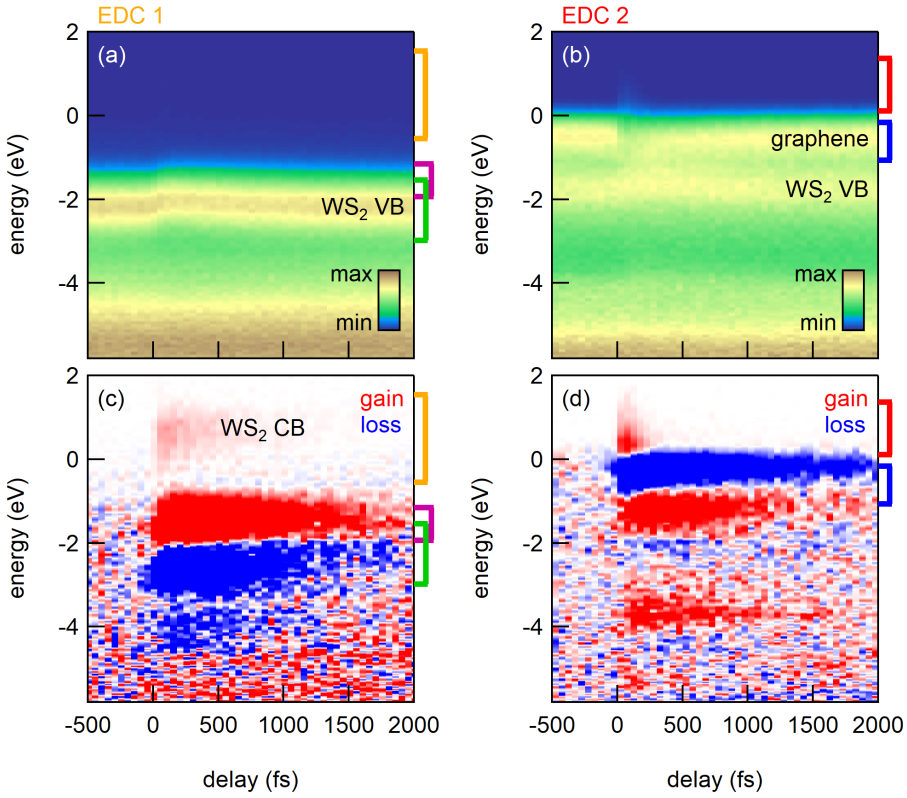

Figure 5.3: Time- and angle-resolved photoemission spectroscopy: (a) and (b): time-resolved EDCs measured along the orange (EDC 1) and red lines (EDC 2), respectively, in Fig. 5.2d as a function of pump-probe delay after photoexcitation at $\hbar\omega_{\mathrm{pump}} = 2\,\mathrm{eV}$. (c) and (d): pump-induced changes of EDC 1 and EDC 2, respectively, obtained by subtracting the equilibrium EDC taken at negative pump-probe delay from all transient EDCs. Red and blue correspond to gain and loss of photoelectrons with respect to negative pump-probe delay, respectively. Colored brackets indicate the integration ranges for the data presented in Fig. 5.4.

To analyze the transient population dynamics of the individual bands we integrated the EDCs in Fig. 5.3 over the energy range indicated by the colored brackets yielding the pump-probe traces in Fig. 5.4. Panel a shows the transient population of the WS_2 VB and CB in green and orange, respectively. The population of the WS_2 VB is found to be unaffected by the photoexcitation within the experimental signal-to-noise ratio. The WS_2 CB on the other hand exhibits a clear gain of electrons. An exponential fit to the data yields a lifetime of the electrons in the WS_2 CB of $\tau = 420 \pm 20\,\mathrm{fs}$. Fig. 5.4b shows the gain above and the loss below the Fermi level in graphene. We find a short-lived gain ($\tau = 97 \pm 3\,\mathrm{fs}$) and a long-lived loss ($\tau = 840 \pm 30\,\mathrm{fs}$). The transient up-shift of the WS_2

VB gives rise to a gain of photoelectrons above its equlibrium position that is plotted as a function of pump-probe delay in Fig. 5.4c. An exponential fit to the data yields a lifetime of $\tau = 770 \pm 30$ fs.

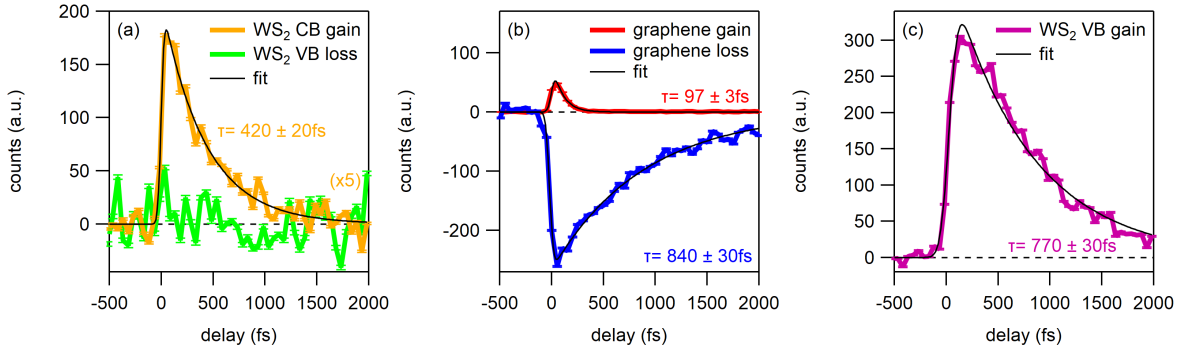

Figure 5.4: Population dynamics of WS_2 and graphene states: (a) Transient occupation of WS_2 conduction band (CB, orange) and valence band (VB, green). The curves were obtained by integrating the photocurrent over the energy range marked by the orange and green brackets in Fig. 5.3a for CB and VB, respectively. (b) Transient photocarrier dynamics of graphene. The curves were obtained by integrating the photocurrent over the energy range marked by the red and blue brackets in Fig. 5.3b corresponding to the gain above E_F and the loss below E_F, respectively. (c) Photocurrent integrated over the energy range marked by the purple bracket in Fig. 5.3c as a function of pump-probe delay. Black lines are exponential fits to data.

In agreement with the previous chapters we interpret these timescales as follows: The absence of holes in the WS_2 VB together with the short-lived gain in graphene indicates that the photogenerated holes in the WS_2 VB are rapidly (whithin $\sim$ 100 fs) refilled by electrons from the Dirac cone. The photoexcited electrons are found to remain in the WS_2 CB for $\sim$ 400 fs, indicating the formation of a charge-separated transient state where the holes reside in the graphene layer and the electrons reside in the WS_2 layer. This charge-separated state is expected to decrease the binding energy of the WS_2 states and to increase the binding energy of the graphene states.

Figures 5.5a and b illustrate the fitting procedure used to determine the transient peak positions of the WS_2 VB and CB and the graphene Dirac cone, respectively. Details are provided in the figure caption. The transient positions of the WS_2 CB and VB are shown in Figs. 5.5c and d, respectively. We find that the WS_2 VB shifts up by $\sim$ 110 meV with a lifetime of $\tau = 600 \pm 20$ fs (Fig. 5.5d). The transient WS_2 band gap at $k \approx 1.1$ Å^{-1} obtained by subtracting the transient position of the VB from the transient position of the CB is displayed in Fig. 5.5e. An exponential fit yields a transient band gap reduction of $\sim$230 meV with a lifetime of $\tau = 140 \pm 40$ fs. Note that the equilibrium gap size of

2.7 eV at $k \approx 1.1\,\text{Å}^{-1}$ is bigger than the direct band gap at the K-point (see Fig. 4.3). In good agreement with [81, 174, 175, 188] we attribute this band gap renormalization to the presence of photoexcited carriers that screen the Coulomb interaction.

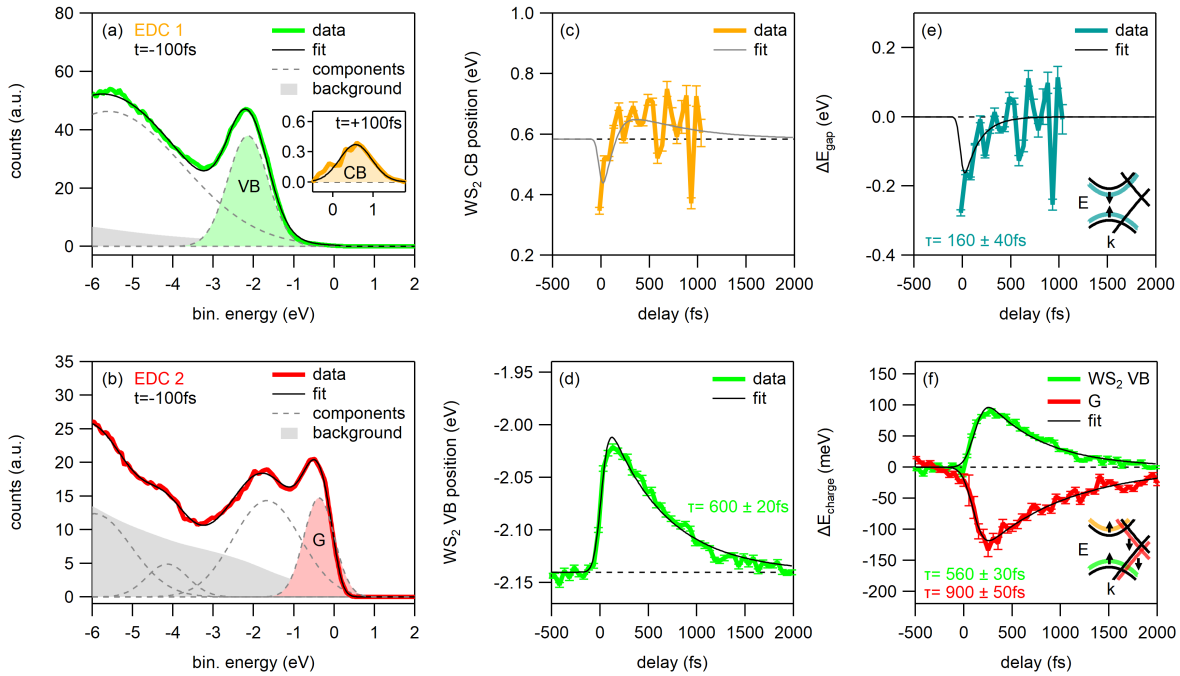

Figure 5.5: Transient band shifts: (a) EDC 1 at negative pump-probe delay together with Gaussian fit. The inset shows the difference EDC 1 at the peak of the pump-probe signal used to fit the binding energy of the WS_2 CB with a single Gaussian. (b) EDC 2 at negative pump-probe delay together with Gaussian fit. Fit components and Shirley background are displayed as dashed gray lines and gray-shaded areas, respectively, in (a) and (b). The peaks that were used to determine the transients peak positions in (c), (d) and (f) are shaded in the respective colors in (a) and (b). (c) Transient position of WS_2 CB. (d) Transient position of WS_2 VB. (e) Transient changes of WS_2 band gap calculated by subtracting (d) from (c). (f) Charging shifts of WS_2 VB and graphene Dirac cone as a function of pump-probe delay. Black lines are exponential fits to the data.

The transient band gap renormalization results in shifts of the WS_2 VB and CB that are symmetric with respect to the center of the WS_2 band gap (see inset of Fig. 5.5e). By subtracting $|\Delta E_{gap}|/2$ from the transient position of the WS_2 VB we obtain the transient VB shift shown in green in Fig. 5.5f that shows a remaining up-shift of $\sim 90\,\text{meV}$ with a lifetime of $\tau = 560 \pm 30\,\text{fs}$. At the same time the π-bands of graphene shown in red in Fig. 5.5f shift down by $\sim 110\,\text{meV}$ with a lifetime of $\tau = 900 \pm 50\,\text{fs}$. As discussed previously, these shifts are a direct consequence of the transient charge-separated state where excess negative charge on the WS_2 layer decreases the binding energy of the WS_2 states and the corresponding excess positive charge on the graphene layer increases the

binding energy of the graphene states. These charging shifts are sketched in the inset of Fig. 5.5f. At this point we are able to attribute the pump-probe signal in Fig. 5.4c to the transient up-shift of the WS_2 layer the lifetime of which is linked to the lifetime of the charge-separated states. Also, the dynamics of the WS_2 CB shown in Fig. 5.5c can now be explained by the combined effect of band gap renormalization that increases the binding energy of the WS_2 CB on the timescale of the photoexcitation and charging that decreases the binding energy of the WS_2 CB on the timescale of the hole transfer.
All things considered, our data reveals a detailed picture of the ultrafast charge separation following photoexcitation of the WS_2/graphene heterostructure. We find that (1) hole transfer from WS_2 to graphene occurs within ~ 100 fs, (2) photoexcited electrons remain inside the WS_2 CB for ~ 400 fs, and (3) the charge-separated state decays within ~ 800 fs (This number corresponds to the average of the lifetimes of the graphene loss in Fig. 5.4b, the WS_2 VB gain in Fig. 5.4c and the charging shifts in Fig. 5.5f).

5.3 Discussion

The observed lifetimes for electron and hole transfer are in good agreement with our previous tr-ARPES experiments (see section 3.3 and 4.2) and time-resolved optical techniques [111] on similar WS_2/graphene heterostructures. Next we will discuss if the microscopic model for ultrafast charge separation across the interface between monolayer WS_2 and monolayer graphene from the previous chapter also applies to heterostructures made of bilayer WS_2 and monolayer graphene.
It is not *a priori* clear whether this model also applies to heterostructures made of bilayer WS_2 and monolayer graphene because, in this case, the maximum of the WS_2 VB and the minimum of the WS_2 CB are located at Γ and Σ (in between Γ and K), respectively. As emphasized in Fig. 5.7 the observed timescales for hole transfer from WS_2 to graphene within ~ 100 fs and a lifetime of the electrons inside the WS_2 CB at K of ~ 400 fs are perfectly consistent with direct tunneling via band intersections close to the K-point. The lifetime of the charge-separated transient state of ~ 800 fs observed in the present heterostructure is consistent with defect-assisted tunneling via S vacancies in similar high-quality epitaxial samples (see section 4.3). Therefore, we conclude that, despite the band structure differences, the microscopic model for ultrafast charge transfer developed for the interface between monolayer WS_2 and monolayer graphene also applies for heterostructures made of bilayer WS_2 and monolayer graphene (see sketch in Fig. 5.7).
In summary, we have shown that ultrafast charge separation also occurs at the interface between bilayer WS_2 and monolayer graphene. Together with the enhanced absorption in the visible spectral range compared to monolayer WS_2 our findings provide important insights that will guide the design of novel optoelectronic applications.

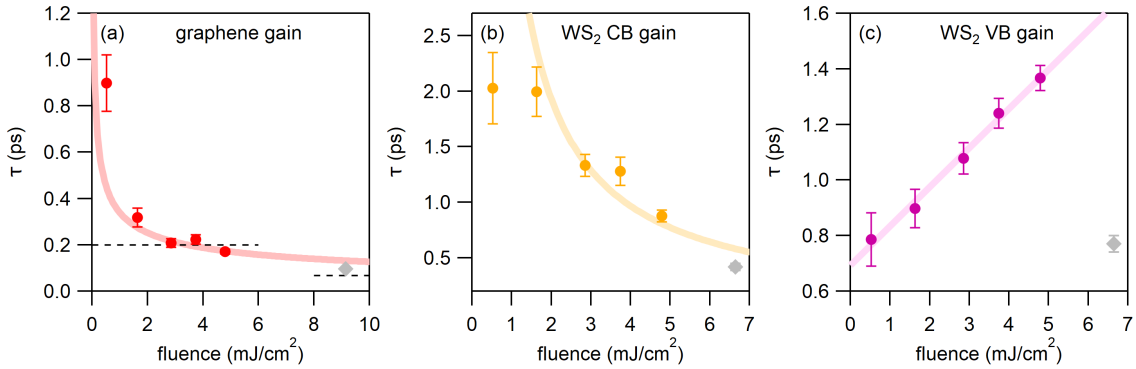

Figure 5.6: Comparison to monolayer WS_2 on graphene: Fluence dependent lifetimes from Fig. 4.6 redrawn with additional datapoints (grey) from the current experiment on bilayer WS_2 on graphene. (a) Lifetime of graphene gain.Black dashed lines denote the temporal resolution of experiments of 200 fs and 66 fs for monolayer and bilayer WS_2/graphene, respectively. (b) Lifetime of photoexcited electrons in the WS_2 CB. (c) Lifetime of gain above the equilibrium position of the upper WS_2 VB. Thick lines in a and b were obtained by inverting and rescaling the guides to the eye from Fig. 4.7e to match the data points. The thick line in c is a guide to the eye.

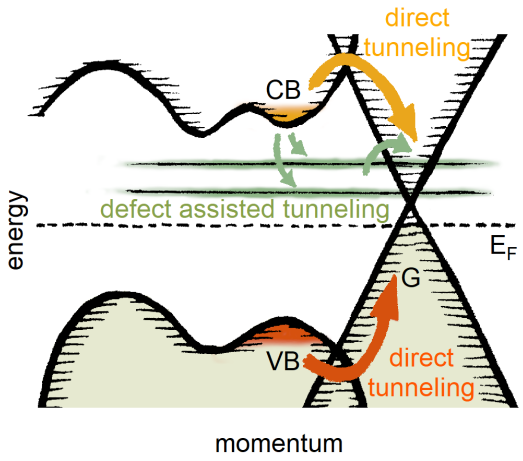

Figure 5.7: Sketch of microscopic charge transfer model. Thick yellow and red arrows indicate direct tunneling of electrons and holes, respectively, through the crossing points of the respective bands. Green arrows indicate defect-assisted tunneling of electrons via S vacancies inside the WS_2 layer.

Chapter 6

Intervalley Scattering and Ultrafast Charge Transfer

This section is based on the unpublished manuscript:
R. Krause, S. Aeschlimann, M. Chávez-Cervantes, S. Forti, F. Fabbri, C. Coletti and I. Gierz, *Intervalley scattering and ultrafast charge transfer in WS_2/graphene heterostructures*, manuscript in preparation [4].

6.1 Introduction

Different microscopic scenarios for ultrafast charge transfer in different vdW heterostructures have been proposed. In particular, it remains controversial whether ultrafast charge transfer occurs a Γ or at K and if intervalley scattering is involved. Time-resolved optical experiments cannot resolve this issue because they lack momentum resolution. Many theoretical works expect the charge transfer to occur at Γ because significant orbital overlap promises large interlayer coupling [112–114, 189]. This scenario necessarily includes intervalley scattering because carriers need to scatter from K where they are generated to Γ where they transfer to the second layer. In contrast, we proposed the scenario described in chapter 4 where charge transfer occurs at band intersections close to K. In this case intervalley scattering is not involved.
In this work we address the interplay of intervalley scattering and ultrafast charge transfer by comparing the carrier dynamics of epitaxial WS_2/graphene heterostructures following photoabsorption of 2 eV and 3.1 eV pump pulses in the WS_2 layer at the K-point and close to the Σ valley, respectively, as depicted in Fig. 6.1a. For this purpose our technique of choice is time- and angle-resolved photoemission spectroscopy (tr-ARPES) due to combined energy, momentum, and temporal resolution. Upon photoexcitation across

the direct band gap at K ($\hbar\omega_{pump}$=2 eV) we found the ultrafast charge transfer to happen at those points in BZ where WS_2 and graphene bands intersect. When photoexcited close to the Σ valley ($\hbar\omega_{pump}$=3.1 eV) we observe first an intervalley scattering of photoexcited carriers from Σ to K within 400 fs, then then charge transfer takes place similarly to the excitation at K via band intersections of WS_2 and graphene bands. We further support the charge transfer model by density functional theory calculations which predict hybridizations at the intersection points and the opening of avoided crossings.

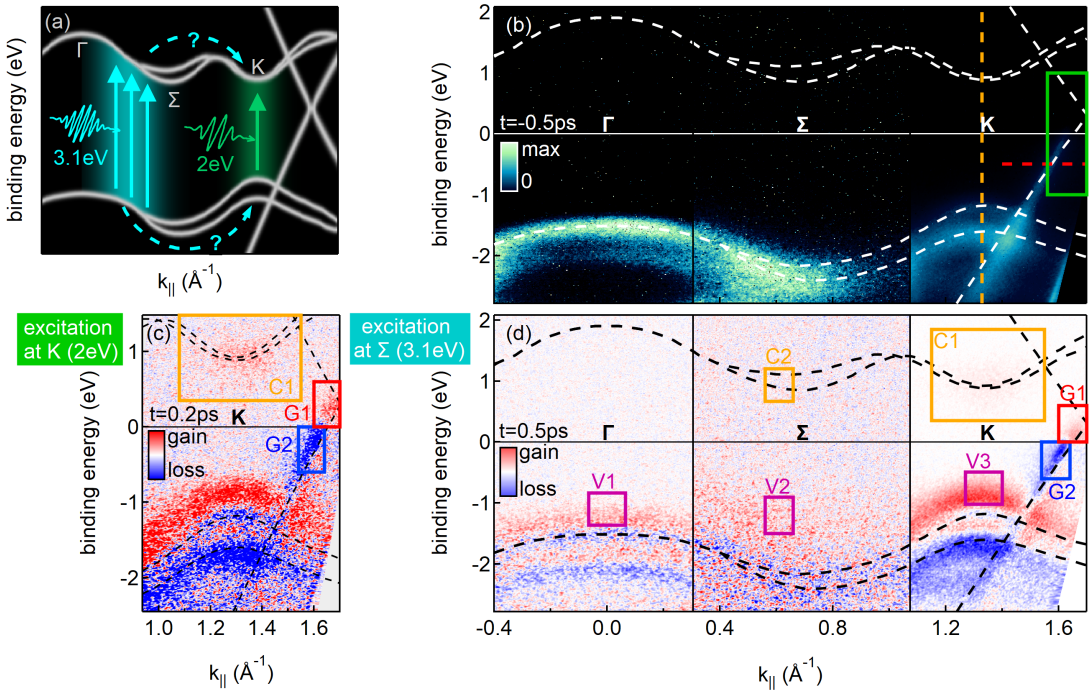

Figure 6.1: time- and angle resolved photoemission spectroscopy (tr-ARPES): (a) Pump-probe schematic employing visible pump for excitation and XUV-probe for photoemission. The energy and emission angle of photoelectons are measured. The measurement direction within the BZ is depicted on the right. (b) BZ sketch with excitation regions for 3.1 eV and 2 eV excitation and possible scattering pathways. (c) Photocurrent at negative pump-probe delay measured along the ΓΣK direction. The momentum dependent spectrum is composed out of three datasets with different signal-to-noise ratios. Colored dashed lines denote the lines for fits of transient band positions in Fig. 6.3. (d) Pump-induced changes of the photocurrent at $t = 0.5\,ps$ after excitation at 3.1 eV pump energy. Colored boxes mark the area of integration for the population dynamics in Fig. 6.2. White (c) and black (d) dashed lines denote the theoretical band structure of WS_2 [69] and graphene [51]. A rigid band shift of −0.81 eV and −1.19 eV was applied to the WS_2 conduction and valence band, respectively. The graphene Dirac cone was shifted by +0.3 eV to account for the observed hole doping. The Fermi level is indicated by continous lines at zero energy.

6.2 Results

Tr-ARPES experiments were carried out at the Hamburg setup (see section 3.1.4) using XUV probe pulses at $\hbar\omega_{probe}$=21.7 eV and visible pump pulses at $\hbar\omega_{pump}$=2 eV and $\hbar\omega_{pump}$=3.1 eV. The photocurrent was measured with a hemispherical analyzer (see section 3.1.7). The energy resolution was 170 meV (200 meV) and the temporal resolution 200 fs (300 fs) for 2 eV (3.1 eV), respectively.

The unperturbed band structure at negative pump-probe delay is presented in Fig. 6.1b as an assembly of three datasets taken along the $\Gamma\Sigma K$ direction (see Appendix B.2 for matching of datasets). No deviations from monolayer WS_2 and graphene band structures are found [51, 69], thus no obvious hybridizations, in agreement the HR-ARPES measurements in Fig. 3.15. Further, the spin-orbit split valence band of WS_2 at K is nicely resolved and the graphene layer is hole doped by $\sim$300 meV.

Fig. 6.1c displays the changes in photocurrent upon excitation at K ($\hbar\omega_{pump} = 2$ eV), obtained by subtracting the equilibrium ARPES spectrum from the spectrum at peak of the pump signal (+0.2 ps). Gain and loss in photocurrent signal stems from population dynamics and band shift due to bandgap renormalization and charge separation. The π-bands of graphene show strong gain (loss) above (below) the Fermi level, respectively. The conduction band (CB) of WS_2 shows a gain of photoelectrons at K. In the valence band (VB) of WS_2, on the other hand, a strong gain above and loss below the equilibrium band position can be seen which suggests an upshift of the VB.

The changes in photocurrent at peak of the pump-probe signal (+0.5 ps) after excitation at Σ ($\hbar\omega_{pump} = 3.1$ eV) are shown in Fig. 6.1d. At the right edge, the π-bands of graphene show a similar gain-and-loss signal. Also a population of the WS_2CB at K is visible. Further, a weak population signal can be found close to Σ (within box C1). The gain-and-loss signal above and below the equilibrium band position of WS_2 VB is extended over the whole momentum range.

Next, we investigate population dynamics in the heterostructure. The integrated photocurrent within the colored boxes of Fig. 6.1c and d is displayed as a function of pump-probe delay in the upper (lower) panel of Fig. 6.2 for excitation at K (Σ), respectively. When photoexcited at K the CB at this valley (box C2) is populated directly by the laser pulse and decays within 1.3 ± 0.1 ps (Fig. 6.2a) as determined by an exponential fit (Appendix A.5). Photoexcited holes in the WS_2 VB can be determined by Gaussian fits of energy distribution curves along the orange dashed line in Fig. 6.1b by a reduction of peak area after excitation (details see Appendix A.4). Holes in the VB live for 100$\pm$40 fs which is faster than the temporal resolution of 200 fs. Fig. 6.2b show the gain (loss) above (below) the Fermi level in graphene which exhibits a lifetime of 210$\pm$20 fs (1.50 ± 0.06 ps), respectively. This asymmetry in photocarrier lifetimes is a signature of ultrafast charge

transfer (cf. chapter 4) and not observed in single layer graphene/SiC(0001) (cf. Appendix B.1).

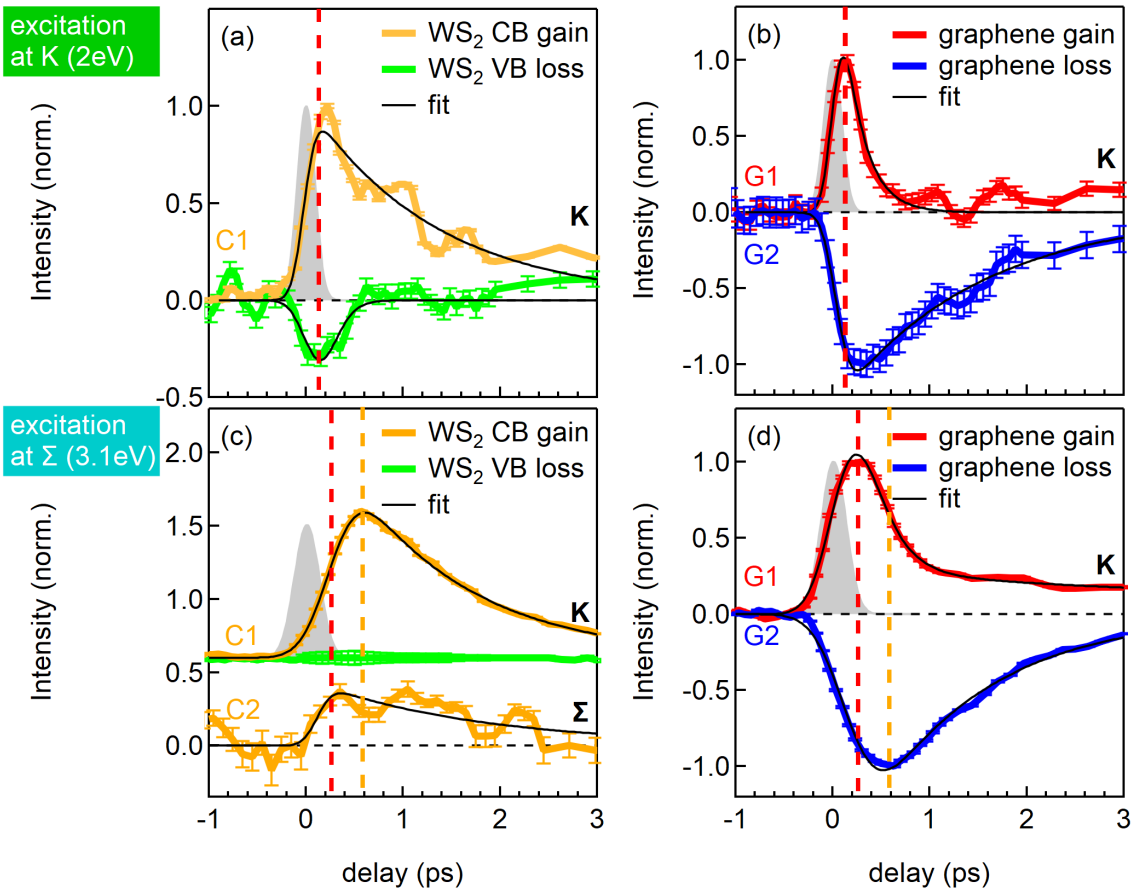

Figure 6.2: Momentum dependent population dynamics: Comparison of excitation at K and Σ in the upper and lower row, respectively. (a) and (c) Gain in WS_2 conduction band (orange) and loss in WS_2 valence band (green). CB curves were obtained by integrating the photocurrent within the orange boxes (C1, C2) in Fig. 6.1c and d. The VB curve was determined through Gaussian fits of transient energy distribution curves along the orange line in Fig. 6.1c. (b) and (d) Gain (red) and loss (blue) within the π-band of graphene obtained by integration of the photocurrent within the red (G1) and blue boxes (G2) in Fig. 6.1c and d. Black curves are fits to data. The grey shaded area is the pump pulse. Vertical dashed lines visualize the delay of signals peaking: graphene gain (b, G1) in red and WS_2 conduction band gain at K (a, C2) in orange.

The population dynamics upon photoexcitation at Σ are shown in the lower panel of Fig. 6.2. The CB at Σ (box C1) is populated initially with the pump pulse and stays for 1.8 ± 0.5 ps while the CB at K (box C2) is populated ~ 400 fs afterwards and lives for 1.24 ± 0.02 ps (Fig. 6.2c). The signal-to-noise ratio does not allow to resolve holes in

the VB. The graphene dynamics (Fig. 6.2d) are also asymmetric. The gain above the Fermi level (box G1) can be fitted with a double exponential decay with $\tau_1 = 250 \pm 40$ fs and $\tau_2 = 6 \pm 2$ ps while the loss below the Fermi level (box G2) decays single exponentially within 1.2 ± 0.03 ps.

We performed transient fits of energy distribution curves extracted along the orange dashed line in Fig. 6.1b to investigate transient changes in band positions. A Gaussian fit model including Shirley background was applied (see Appendix A.4). Resulting transient band shifts of conduction and valence bands are presented in Fig. 6.3a. The CB shows an oscillating band position while the VB shifts upwards. By substracting the two curves in Fig. 6.3a the transient quasiparticle band gap is determined (Fig. 6.3b). It is renormalized transiently by ~ 150 meV for 0.8 ± 0.4 ps which is often observed in monolayer TMDs due to enhanced screening after photoexitation [81, 174, 175, 188].

However, to uncover an band shifts due to charging we can remove the contribution of bandgap renormalization from transient band positions. This is achieved by adding (subtracting) $|\Delta E_{gap}|/2$ to (from) transient conduction (valence) band shifts and shown in Fig. 6.3b. Both, conduction and valence bands, shift simultanoulsy upwards by ~ 100 meV for 1.03 ± 0.07 ps. The reduction of binding energy indicates a negative charging of the WS_2 layer. Hence, the oscillatory behaviour of the transient CB position is a superposition of renormalization and charging shifts with different timing. The charging shift of graphene bands was obtained by Lorentzian fits of momentum distribution curves along the red dashed line in Fig. 6.1b and converted into an energy shift by multiplication with the slope of the π-bands of $\sim$7 eVÅ. They shift down by ~ 70 meV for 1.08 ± 0.06 ps (Fig. 6.3c) which indicates a positive charging. The opposite shifts of the bands of both layers serve as evidence for charge separation at the interface of the heterostructure.

For photoexcitation at Σ (lower panel in Fig. 6.3) the picture looks similar. A bandgap renormalization of 150 meV for 2.3 ± 0.5 ps is measured. The charging shift of WS_2 (graphene) is ~ 80 meV (~ 70 meV) for 400 ± 100 fs (600 ± 130 fs), respectively. Remarkably, the charging shift peaks $\sim$400 fs later than upon excitation at K.

To measure transient changes to the carrier density in graphene we performed Fermi-Dirac fits (Fig. 6.4a) of the photoelectron distribution within the Dirac-cone in the green box in Fig. 6.1b. The transient shift of chemical potential $\Delta\mu_{vac}$ was referenced to the Dirac-point ($\Delta\mu_{ED}$) by subtracting the charging shift of graphene in Fig. 6.4b. From $\Delta\mu_{ED}$ and the transient electronic temperature in graphene T_{el} (Fig. 6.4c) we calculated transient changes to the electron density in graphene ΔN_e (see Appendix A.7). The density of transferred holes to graphene is then obtained by $\Delta N_h = -\Delta N_e$ and shown in Fig. 6.4c for excitation at K. The hole density increases immediately after photoexcitation – thereby confirming the charge transfer WS_2 to graphene – and decays within 1.3 ± 0.1 ps. On the other hand, the transferred holes peak $\sim$400 fs after photoexcitation at Σ and decay

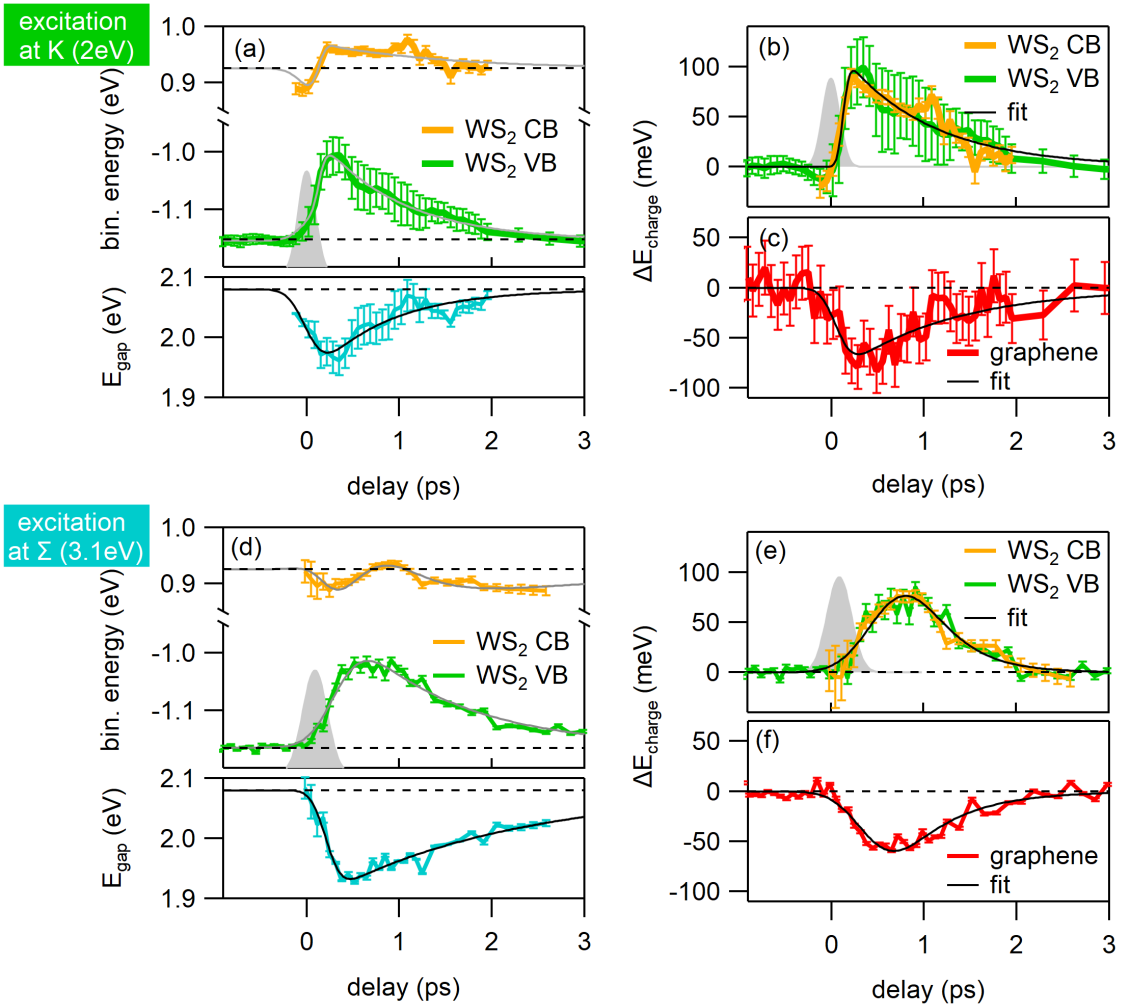

Figure 6.3: Transient changes in band positions: Comparison of excitation at K and Σ in the upper and lower row, respectively. (a) and (d) Transient position of the WS_2 conduction and valence band and transient band gap at K_{WS_2}. (b) and (e) Charging shifts of WS_2 conduction and valence bands at K_{WS_2}. (c) and (f) Charging shift of graphene. Thin black lines are fits to the data, whereas the thin grey lines in (a) are composed out of fits from transient band gap and charging shifts. The grey shaded area is the pump pulse.

within 1.9 ± 0.2 ps.

To sum up, asymmetric population dynamics, charging shifts and holes injected into graphene layer provide evidence for ultrafast charge separation upon photoexcitation at K ($\hbar\omega_{pump}$=2 eV) in the WS_2/graphene heterostructure. The hole transfer takes place within 250 fs, the electron transfer within 1.3 ps and the lifetime of holes in graphene is 1.3 ps. We found the hole transfer to be instantaneous within the experimental resolution as the WS_2 conduction band population and hole concentration inside the Dirac cone reach peak at same time. When we excite at Σ ($\hbar\omega_{pump}$=3.1 eV) we observe similar

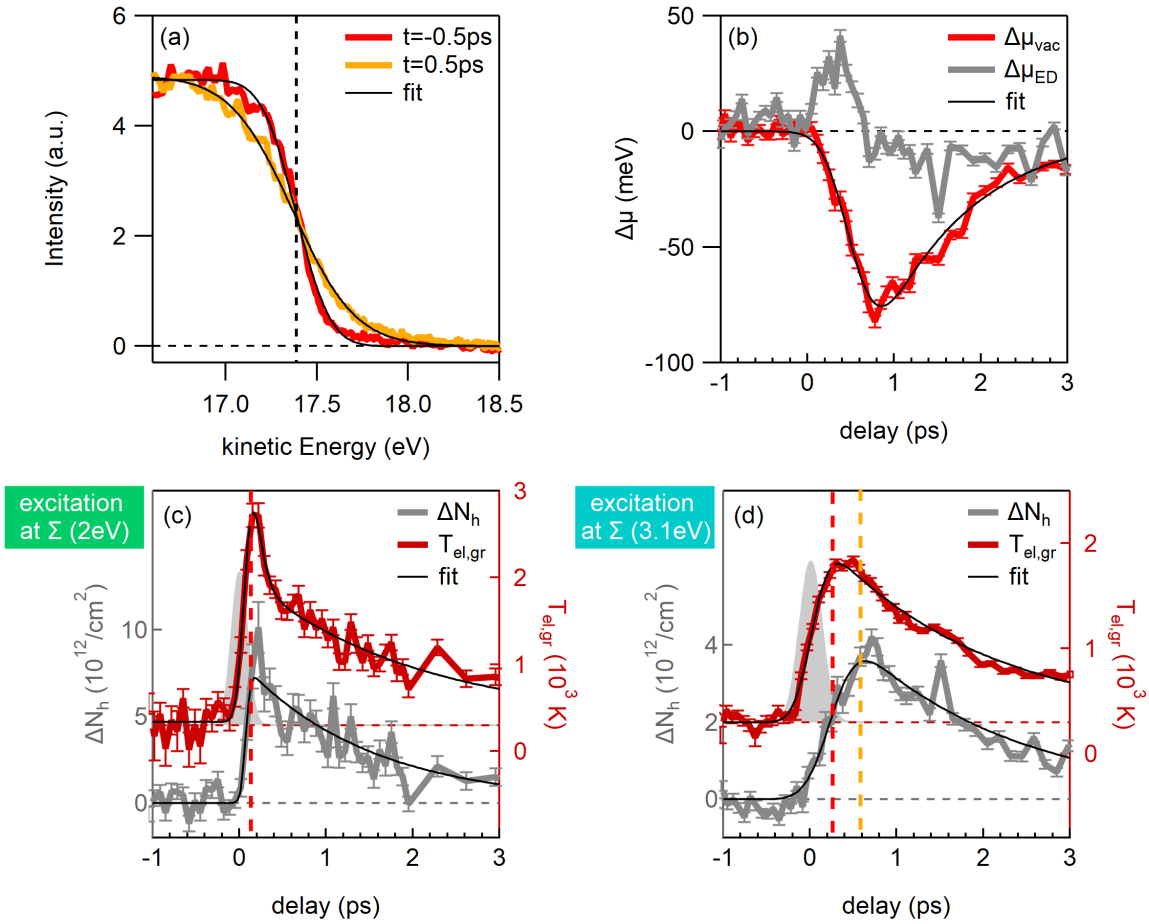

Figure 6.4: Fermi-Dirac fits of the carrier distribution in graphene: (a) Energy distribution curves at negative pump-probe delay (-0.5 ps, red) and peak of the pump-probe signal (+0.5 ps, orange) together with Fermi-Dirac-fits. The dashed vertical line denotes the equilibrium chemical potential. (b) Transient shift of the chemical potential in graphene referenced to vacuum level $\Delta\mu_{vac}$ and to Dirac-point $\Delta\mu_{ED}$. (c) and (d) transient hole density ΔN_h and electronic temperature T_{el} within the Dirac-cone for excitation at K and Σ, respectively. The grey shaded area is the pump pulse. Vertical dashed lines compare to peak of graphene gain (red, G1) and WS_2 CB gain signals at K (orange, C2) from Fig. 6.2b and a.

asymmetric population dynamics, charging shifts and hole injection into graphene. But contrary to the above a time delay of 400 fs is observed between photoexcitation (peak of graphene gain, peak of orange box at Σ) and peak of WS_2 conduction band population at K, charging shifts and the hole concentration inside Dirac cone.

6.3 Discussion

By pumping resonant to the A-exciton ($\hbar\omega_{pump}$=2 eV) the photoexcitation in WS_2 takes place at the K valley and the ultrafast hole transfer close to K (see section 4.3). For above-gap excitation in WS_2 ($\hbar\omega_{pump}$=3.1 eV) we propose the following scenario based on our findings: (1) The excitation located close to the Σ valley of the BZ (see Appendix A.10) [31, 76, 77]. (2) Photoexcited carriers scatter from Σ to K within 400 fs. (3) The hole transfer to graphene then follows close to the K valley.

The observed intervalley scattering time of 400 fs is in good agreement with previous tr-ARPES experiments on TMDs [84–86]. Once arrived at the K valley, the microscopic charge transfer model from chapter 4 for 2 eV excitation applies. In this model, photoexcited carriers can tunnel directly via band intersections of WS_2 and graphene bands with no energy or momentum transfer needed. To reach these intersection points in VB (CB) photoexcited holes (electrons) have to overcome an energy barrier from the VB maximum (CB minimum) respectively. The model was successful to describe transfer rates for direct tunneling of electrons and holes to graphene. The lifetime of the charge separated state, on the other hand, is found to strongly depend on trapping of photoexcited electrons at defect states generated by S vacancies (see section 4.3).

Within the model, the intersection points of WS_2 and graphene bands were assumed to be hybridization points at which photoexcited carriers can transit from one layer to the other. We will further substantiate this idea by density functional theory (DFT) calculations. A supercell with 4×4 WS_2 and 5×5 graphene to minimize lattice mismatch was calculated (Fig. 6.5a) and its bandstructure is shown in Fig. 6.5b. Orbital projections of the wavefunction at positions (1) and (2) in the supercell BZ reveal 100 % localization at graphene and WS_2 layers and the bands can be assigned to the π-bands and WS_2 VB, respectively. At the point of the supercell BZ (3) where these bands overlap the orbital projection reveals 36 % (64 %) localization on the graphene (WS_2) layer, respectively. Wave function mixing then leads to hybridization as highlighted by white color in Fig. 6.5b. Finally, Fig. 6.5d projects the supercell BZ onto the individual layers to compare with ARPES snapshots in Fig. 6.1. The hybridization is strong enough to open an avoided crossing of ∼50 meV in the valence band in between the K points of WS_2 and graphene. The the avoided crossing is below the energy resolution of the current experiment and was not previously observed by ARPES. But hybridizations in TMD/graphene heterostructures were actually measured. Diaz et al., found avoided crossings of ∼300 meV between the *pi*-bands of graphene and lower lying bands in MoS_2 [96] but no hybridizations in the WS_2 VB at Γ. The latter is in contrast to TMD/TMD heterostructures where bands at Γ were found to hybridize [189] due to the out-of-plane character of TMD orbitals at the BZ center [112–114]. This means the charge transfer might happen close to the Γ valley

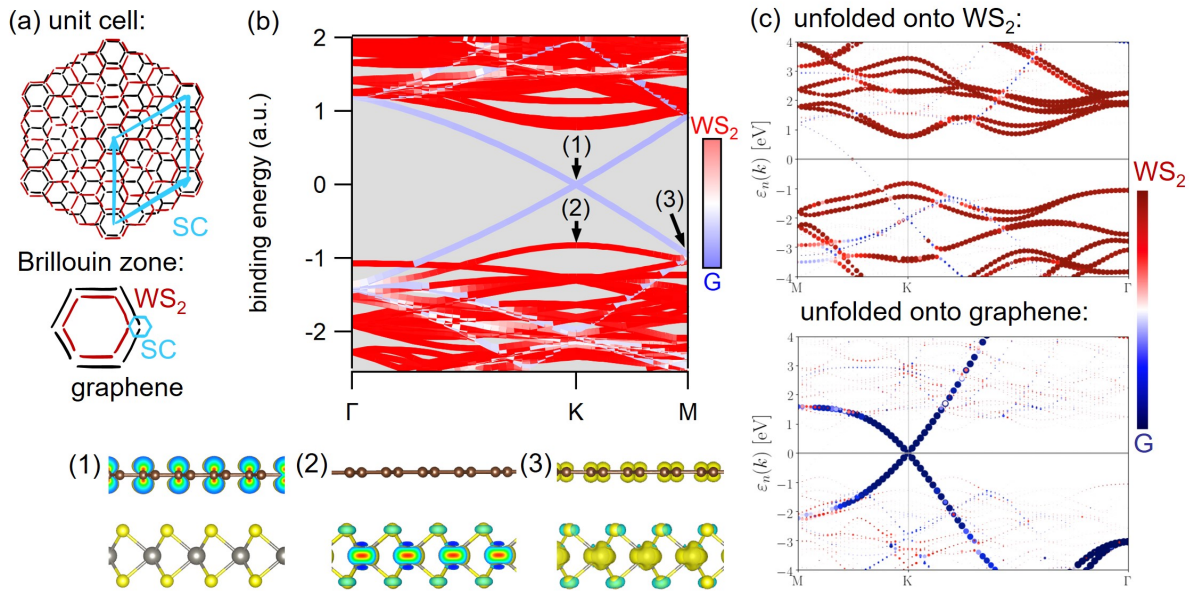

Figure 6.5: Hybridization and opening of avoided crossings: (a) Sketch of the 4×4 and 5×5 WS_2/graphene supercell in real space and k-space. (b) Supercell band structure. Arrows mark the points (1), (2) and (3) for which the orbital projection of the wavefunction is depicted below. (c) Unfolding projection of the supercell band structure onto individual WS_2 and graphene layers. The layer projection of the wavefunction is indicated by the color code and symbol size.

in TMD/TMD heterostructures, while it takes place at the K valley in TMD/graphene heterostructures.

To conclude, we investigated the interplay of intervalley scattering and ultrafast charge transfer in a WS_2/graphene heterostructure by means of tr-ARPES. When excited across the direct band gap in WS_2 at K ($\hbar\omega_{pump}$=2 eV), hot electrons and holes transfer from WS_2 to graphene close to the K valley where bands intersect. Upon photoexcitation close to the Σ valley ($\hbar\omega_{pump}$=3.1 eV) we found photoexcited carriers to scatter from Σ to K within 400 fs. Then the same scenario as above applies for the charge transfer. Density functional theory predicts hybridization at the intersection points in the order of 50 meV in the valence band which lays the foundation for direct tunneling between the layers. Our results provide important conclusions for the design of novel photodetectors and photovoltaics based on TMD/graphene heterostructures.

Chapter 7

Momentum dependence of light-induced band gap renormalization

This section is based on the manuscript:
R. Krause, A. Steinhoff, S. Aeschlimann, M. Chávez-Cervante, T. O. Wehling, S. Refaely-Abramson, S. Forti, F. Fabbri, C. Coletti and I. Gierz, *Momentum dependence of light-induced band gap renormalization in WS_2/graphene heterostructure*, manuscript in preparation [5].

7.1 Introduction

Tailoring the bandstructure of semiconductors opens up the pathway for design of novel optoelectronic applications, as tailoring GaN by doping was the breakthrough for efficient blue LEDs back then [190,191]. Nowadays, monolayers of transition metal dichalgogenides (TMDs) are in the scientific spotlight due to strong light-matter interaction in the visible range (see section 2.2.3).
The size of the quasiparticle bandgap in monolayer TMDs is strongly affected by Coulomb interaction and extremely sensitive to screening. Yet some works has been done to tailor the size of the quasiparticle bandgap in monolayer TMDs by (photo-)doping [192, 193], gating [78], stain [76] and screening in artificial van-der-Waals (vdW) heterostructures [97,194]. Light-induced band gap renormalization was predicted to be strongly momentum dependent [195], but this has never been observed experimentally.
In this chapter we present the first measurement of strongly fluence- and momentum-dependent WS_2 valence band shifts in a WS_2/graphene heterostructure observed with

time- and angle-resolved photoemission spectroscopy (tr-ARPES). The shift is found to be biggest at the K valley with 170 meV. Many-body GW calculations can trace back the VB shift to momentum dependent band gap renormalization. Tailoring band gaps, effective masses and the density of states by laser excitation is comparatively easy, reversible and opens up new approaches for optical communications.

7.2 Results

Tr-ARPES experiments were carried out at the Hamburg setup (see section 3.1.4) using XUV probe pulses at $\hbar\omega_{probe}$=21.7 eV and visible pump pulses at $\hbar\omega_{pump}$=2 eV and $\hbar\omega_{pump}$=3.1 eV. The photocurrent was measured with a hemispherical analyzer (see section 3.1.7). The energy resolution was 170 meV (200 meV) and the temporal resolution 200 fs (300 fs) for 2 eV (3.1 eV), respectively. The excitation density $n_{e/h}$ was estimated to be $\sim 3{\cdot}10^{13}\mathrm{cm}^{-2}$ ($\sim 4{\cdot}10^{12}\mathrm{cm}^{-2}$) for 2 eV (3.1 eV) excitation, respectively (details see Appendix A.3). The determination of the electronic temperature in WS_2 is very difficult as discussed in detail in Appendix A.8. A rough estimate yields 2500 K (3000 K) at peak of the pump-probe signal for 2 eV (3.1 eV) excitation, respectively.

As a starting point, we present the unperturbed band structure in Fig. 7.1a at negative pump probe delay. Like in the previous chapter it is composed out of three separate ARPES snapshots along the ΓK direction with varying signal-to-noise ratio (e.g. see dataset around Σ). However, the bandstructure of the heterostructure is nicely resolved, especially the spin splitting at the K valley. Moreover the bands are found to be just a superposition of both monolayers by comparison with overlayed theoretical bands [51,69]. We then photoexcited with $\hbar\omega$ = 3.1 eV and an excitation density of $\sim 4{\cdot}10^{12}\mathrm{cm}^{-2}$ and show pump induced changes to the spectrum in Fig. 7.1b at peak of the pump-probe signal. Changes in photocurrent were obtained by subtraction of the equilibrium ARPES spectra from the spectra at peak of pump-probe signal. Gains and losses in photocurrent can be traced back to excitation of photocarriers in WS_2 and graphene followed by an ultrafast charge transfer. A complete understanding of transient population dynamics is beyond the scope of this letter and is provided in detail in chapter 6. Herein, we focus on transient band shifts after photoexcitation. Already by eye, a strong gain-and-loss signal above and below the equilibrium position of the valence band of WS_2 can be seen in Fig. 7.1b which seems to be weaker at the Γ valley than at the K valley.
Similarly, Fig. 7.1c shows the changes in photocurrent after photoexcitation at $\hbar\omega$ = 2 eV and a density of $\sim 3{\cdot}10^{13}\mathrm{cm}^{-2}$ at peak of the pump-probe signal. The response looks quite similar to the Fig. 7.1b despite the stronger population of the WS_2 conduction band at the K valley and the stronger gain-and-loss signal at the Γ valley.

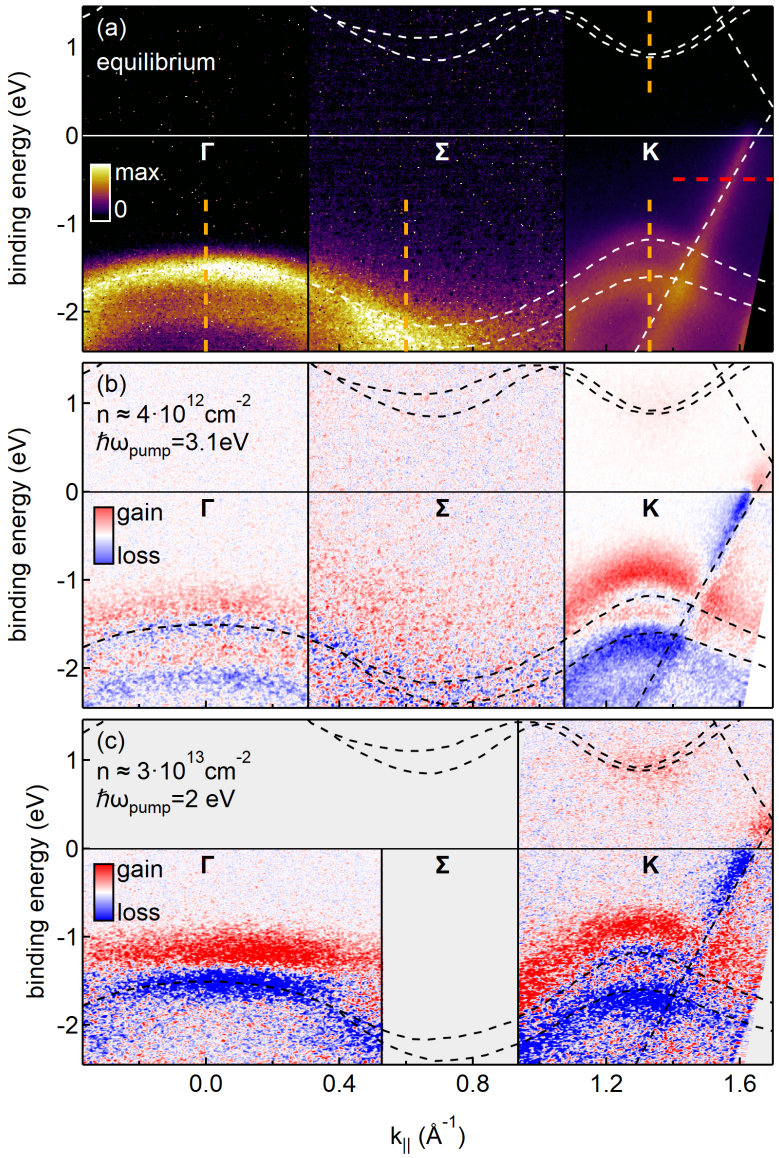

Figure 7.1: time- and angle resolved photoemission spectroscopy: (a) Photocurrent at negative pump-probe delay (-0.5 ps) measured along the ΓΣK direction. Colored dashed lines denote the momenta for fits of transient band positions in Fig. 7.2. (b) Pump-induced changes of the photocurrent at peak of the pump-probe signal (+0.5 ps) for an excitation density of $\sim 4{\cdot}10^{12}\mathrm{cm}^{-2}$ at 3.1 eV pump energy. (c) Pump-induced changes of the photocurrent at peak of the pump-probe signal (+0.2 ps) for an excitation density of $\sim 3{\cdot}10^{13}\mathrm{cm}^{-2}$ at 2 eV pump energy. White (a) and black (b and c) dashed lines denote the theoretical band structure of WS_2 [69] and graphene [51]. A rigid band shift of −0.81 eV and −1.19 eV was applied to the WS_2 conduction and valence band, respectively. The graphene Dirac cone was shifted by +0.3 eV to account for the observed hole doping.

To determine transient band positions we took linecuts along the orange dashed lines in Fig. 7.1a and fitted the energy distribution curves (EDCs) with Gaussians and Shirley-background. The fits for WS_2 valence bands along the orange linecuts at Γ, Σ and K valleys are displayed in Fig. 7.2a and for the conduction band at K in Fig. 7.2b.

Resulting shifts of the valence band at Γ, Σ and K upon 3.1 eV excitation are shown in Fig. 7.2c. The shifts point upwards and decay exponentially within 1.1 ± 0.07 ps but remarkably they vary in amplitude at different momenta. A fact on which we will focus later on. For completeness we first analyze the band shifts at the K valley in more detail. The conduction band at K shifts down, up and down again (Fig. 7.2d). This behaviour becomes clearer in the following section. From conduction and valence band shifts we can deduce the transient quasiparticle band gap at the K valley in Fig. 7.2e. First, the equilibrium gap size is 2.08 eV and the the exciton binding energy is ~100 meV by comparison with A-exciton photoluminescence of the heterostructure (see Fig. 3.14e). In comparison to WS_2 monolayers on insulating substrates [72], band gap and exciton binding energy of WS_2 are already reduced in equilibrium condition due to external screening by the graphene substrate. Second, the bandgap is further reduced after photoexcitation by ~ 150 meV for 2.3 ± 0.5 ps. This in known as dynamical bandgap renormalization and stems from enhanced screening of the Coulomb-interaction in the presence of photexcited carriers [81, 174, 175, 188].

We can deduce another contribution to the band shifts by adding (subtracting) $|\Delta E_{gap}|/2$ to (from) transient conduction (valence) band shifts, or in other words, remove the contribution of bandgap renormalization. The resulting shift is displayed in Fig. 7.2f. Here, conduction and valence bands shift upwards simultaneously by ~ 80 meV for 400 ± 100 fs. The reduction of binding energy indicates a negative charging of the WS_2 layer. We also extracted the transient shift of graphene bands (details see Appendix A.4) which shift downwards in energy (Fig. 7.2f) indicating a positive charging of the graphene layer. As proved in the previous chapters, the opposite charging induced shifts of the bands of both layers serve as evidence for ultrafast charge separation at the interface of the heterostructure. It also gets clear that the oscillatory conduction band shift in Fig. 7.2d is an overlap of bandgap renormalization and charging induced shifts with different timing. Band shifts at 2 eV excitation ($3{\cdot}10^{13}\mathrm{cm}^{-2}$) were already discussed in Fig. 4.3.

Finally, we investigate the momentum dependence of band shifts. To do so, EDCs were taken along linecuts all over the Brillouin zone of WS_2 and fitted. All fits and transient shifts can be found in the Appendix B.5. Fig. 7.3a shows the valence band shift at peak of the pump-probe signal as a function of momentum. For the excitation at 3.1 eV ($\sim 4{\cdot}10^{12}\mathrm{cm}^{-2}$) the valence band shifts almost uniquely upwards at Γ and Σ but peaks at the K valley with ~130 meV difference. This non-rigid shift previously became manifest in a stronger gain-and-loss signal at K in Fig. 7.1b. On the other hand, at 2 eV excitation

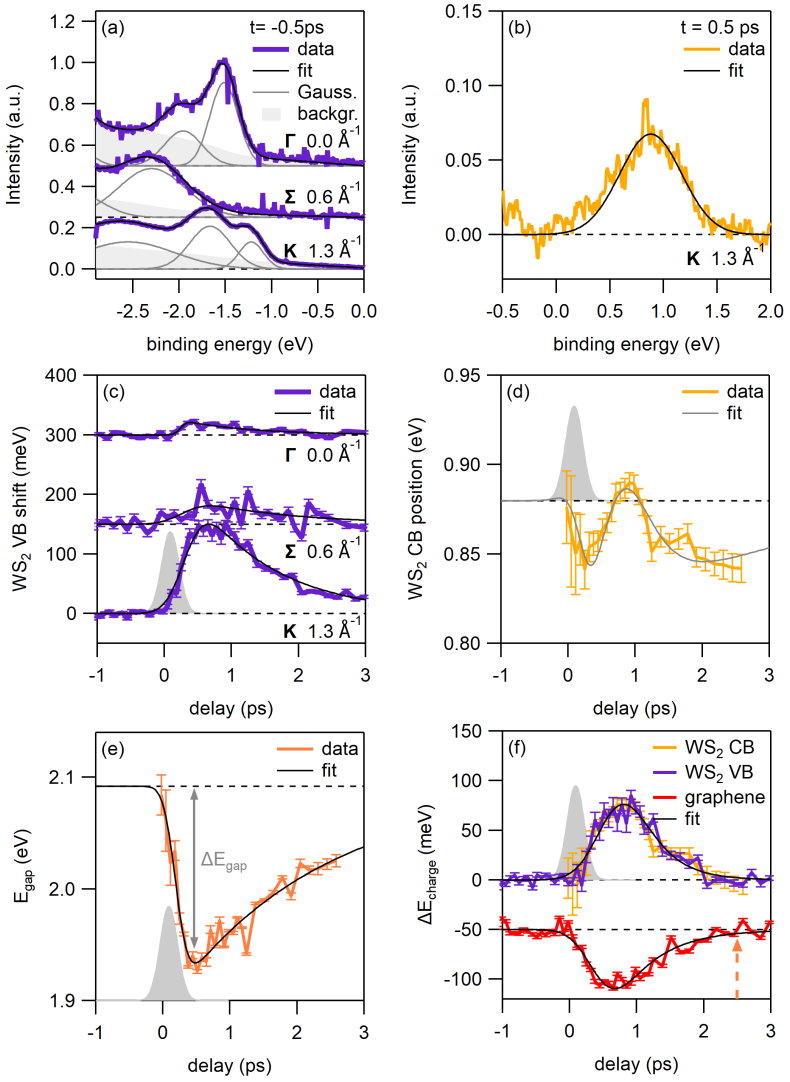

Figure 7.2: Transient shifts of WS_2 and graphene states: (a) Energy dispersive curve of WS_2 valence states at negative pump-probe delay integrated over $0.05\,^{-1}$ along the orange dashed lines in Fig. 7.1a together with fit components. (b) Difference energy dispersive curve of WS_2 conduction band at K_{WS_2} and at peak of the pump-probe signal with Gaussian fit. (c) Transient shift of the WS_2 valence band corresponding to fits in (a). (d) Position of the WS_2 conduction band at K_{WS_2} as a function of pump probe delay. (e) Transient band gap at K_{WS_2}. (f) Charging shifts of WS_2 conduction (CB) and valence bands (VB) at K_{WS_2} and graphene. Thin black lines are fits to the data, whereas the thin grey line in (e) is a composed out of fits from transient band gap (e) and charging shifts (f). The grey shaded area in (c)-(f) is the pump pulse. The orange arrow in (e) an (f) marks the delay at which the charge separated state is over. All data is presented for an excitation density of $\sim 4{\cdot}10^{12}\mathrm{cm}^{-2}$ ($\hbar\omega_{\mathrm{pump}} = 3.1\,\mathrm{eV}$).

($\sim 3{\cdot}10^{13}\mathrm{cm}^{-2}$) the valence band shift has a smaller K-Γ-difference of $\sim$40 meV and less momentum dependence (see gain-and-loss signal in Fig. 7.1c).

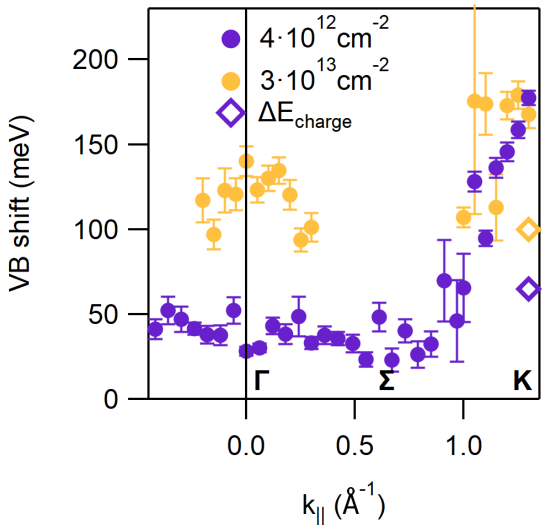

Figure 7.3: Momentum dependent valence band shift in WS_2: Shift at peak of the pump-probe signal as a function of momentum for a carrier density of $\sim 4{\cdot}10^{12}\mathrm{cm}^{-2}$ (3.1 eV) and $\sim 3{\cdot}10^{13}\mathrm{cm}^{-2}$ (2 eV). Open symbols show the amplitude of the charging shift at K at similar pump-probe-delay.

The renormalization of the WS_2 band structure due to photoexcited electrons and holes is calculated by self-consistently evaluating a GW self-energy, which is given in equations 25 and 26 from Ref. [80]. Our approach is based on band structures and Coulomb matrix elements from first principles. Environmental screening is included via the Wannier function continuum electrostatics method [196] using a macroscopic dielectric function for the given sample geometry [197]. Here, we assume that the WS_2 monolayer with a thickness of 0.6 nm rests on graphene and a SiC substrate with dielectric constants of ϵ=4 and ϵ=6.5, respectively. The renormalization was calculated for several electron densities in WS_2. In the charge separated state (cf. chapter 6) we assume all holes have already tunneled to graphene and hole density in WS_2 was set to zero.

The momentum dependent band valence band shift for different carrier densities is shown in Fig. 7.4a. The shift peaks at the K valley already at low excitation densities but the Γ valley keeps up at higher excitation densities. This result is in good qualitative agreement with the experimental observation in Fig. 7.3 and thus an excitation energy dependence can be neglected at this point. Futhermore, increasing the electronic temperature in WS_2 smears out the momentum dependence and lowers the maximal shifts (Fig. 7.4b). The conduction band shift is displayed in Fig. 7.4c. Subtraction of valence from conduction band renormalizations yields also a strongly momentum dependent band gap renormalization in Fig. 7.4d. But the calculated band gap renormalization at K is roughly half as large as the experimentally determined values (triangular symbols).

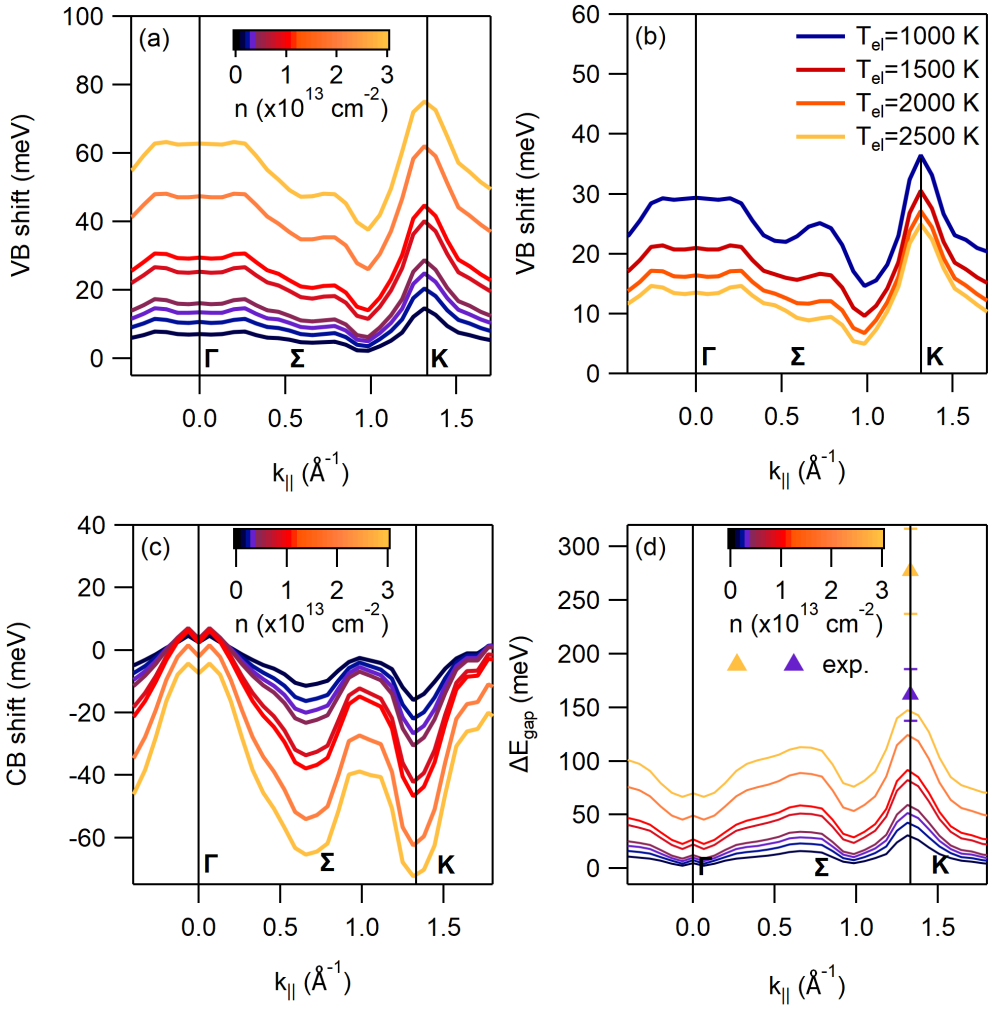

Figure 7.4: Calculated band renormalizations: (a) Valence band shift. (b) Calculated valence band shift for different electronic temperatures in WS_2 at an excitation density of $3{\cdot}10^{12}\mathrm{cm}^{-2}$. (c) Conduction band shift. (d) Band gap renormalization. Triangular symbols compare to the experimental band gap from Fig. fig:7.shifts. The electronic temperature in WS_2 was set to 2500 K for the panels a, b and c. Different excitation densities in a, b and c are indexed by a color code.

7.3 Discussion

Band gap renormalization in monolayer TMDs is a common phenomenon driven by gating [78], doping [192], substrate screening [97] or photoexcitation [81, 174, 175]. The latter was predicted to induce a momentum dependent renormalization [195] which was so far not experimentally verified.

Here, we presented the first direct observation of momentum dependent band gap renormalization by tr-ARPES combined with many-body GW calculations. We found the momentum dependence to strongly depend on the density and temperature of photoexcited

electrons in WS_2. Controlling these parameters provides an approach for fully reversible band structure engineering as discussed in more detail in Appendix C.2.
However, the calculated renormalization does agree qualitatively with the experimentally observed valence band shift but not quantitatively. A missing contribution in the calculations could be external screening from the increased hole density and electronic temperature in graphene [34].
Further, we know from the analysis at the K point in Fig. 7.2 that the valence band shift is a superposition of renormalization and charging shift. The role of the charging shift to the momentum dependent VB shift is not yet clear. It might be an initial state effect and the negative (positive) potential leads to decrease (increase) in binding energy which makes it easier (harder) for an electron to escape from the solid, respectively [118]. Or it can be the surface photovoltage (SPV) effect, a final state effect quite similar to pump-induced space charge described in section 3.1.8. Under SPV, the field of the negative (positive) charged surface accelerates (decelerates) the photoemitted electron on its way to the analyzer which increases (decreases) its kinetic energy [198, 199]. However, both scenarios can explain the direction, magnitude and time scale of the charging shift, but a momentum dependence was not reported for both of them.
To sum up, we reported the first direct observation of momentum dependent band gap renormalization after optical excitation in a WS_2/graphene heterostructure. The band shift is strongly dependent on excitation density and electronic temperature in WS_2 as determined by a combination of tr-ARPES and many-body GW calculations. Although the measured valence band shift agrees qualitatively with the calculations it cannot be described quantitatively yet. Futher contributions might be external screening by graphene and or the charging shift. These discrepancy should be subject to future experimental and theoretical investigations.

Chapter 8

Conclusions and Outlook

8.1 Conclusions

Time- and angle-resolved photoemission spectroscopy (tr-ARPES) was used in this thesis to investigate the phenomenon of ultrafast charge transfer in TMD/graphene heterostructures which has promising potential for applications in photodetectors, photovoltaics and opto-spintronics.

We built a tr-ARPES setup which enables a direct view on carrier dynamics in energy, momentum and time to investigate the ultrafast charge transfer following A-exciton resonant excitation in epitaxial WS_2/graphene heterostructures. We could determine the main signatures for ultrafast charge transfer: asymmetric population dynamics, charging shifts and an increasing hole density in graphene.

To understand the microscopic mechanism behind the ultrafast charge transfer a series of experiments followed up. We performed pump-fluence dependent measurements and excited the WS_2/graphene heterostructures with 3.1 eV light close to the Σ valley in the Brillouin zone. In addition, bilayer WS_2/graphene heterostructures were investigated. We were supported by density functional theory and microscopic many-body theory calculations in these projects.

To conclude, we find the timescale for charge separation is set by direct tunneling at points in the Brillouin zone where WS_2 and graphene bands cross. These points are close to the K point. Hybridization ensures the extension of the wave function over both layers and carriers can tunnel without energy or momentum transfer. The asymmetry in electron and hole transfer rates can be explained by the energy barrier which carriers need to overcome from conduction (valence) band minimum (maximum) to the intersection

points, respectively. The timescale for electron-hole recombination, on the other hand, is set by defect-assisted tunneling via localized S vacancies. Thus, the sample quality is an important design factor for charge separation.
We show that ultrafast charge separation at the interface between bilayer WS_2 and monolayer graphene can also explained by the same model. Upon photoexcitation close to the Σ valley we found photoexcited carriers to scatter from Σ to K within 400 fs. Then the same scenario as above applies for the charge transfer.
With full momentum view on the WS_2 valence band shift we further present a direct observation of non-rigid band shifts after optical excitation. We could show two contributions to the valence band shift which are band gap renormalization and charging shift. Many-body GW calculations of the momentum dependent band gap renormalization can reproduce the valence band shift qualitatively and reveal that it is affected by the density and temperature of photoexcited electrons in WS_2. Future investigations will show how the band gap in WS_2 is affected by external screening from the hot hole-plasma in graphene.
The experiments within this thesis have shown that the proposed microscopic model for ultrafast charge transfer is robust in different scenarios and provides an understanding for charge transfer phenomena in similar TMD/graphene heterostructures. From our results one can draw important conclusions for the design of opto-electronic devices based on van-der-Waals heterostructures.

8.2 Outlook

In the following I will present preliminary results from tr-ARPES on heterostructures of WS_2 on n-doped graphene and oscillations found in several tr-ARPES datasets. These topics provide good starting points for umpcoming research projects. Finally, I will provide approaches for refinement and substantiation of the microscopic charge transfer model and how to investigate charge transfer phenomena with next generation tr-ARPES.

8.2.1 Heterostructures of Monolayer WS_2 on Thermal Decomposited Monolayer Graphene

In this thesis, the investigated heterostructures consist of WS_2 on quasi-freestanding monolayer graphene (QFMLG), as described in section 3.2.2. We also carried out tr-ARPES measurements of heterostructures of monolayer WS_2 on thermal decomposited monolayer graphene (TDMLG) with again excitating the A-exciton in WS_2 resonantly.
TDMLG is prepared similarly to QFMLG from a SiC substrate, described in section 3.2.2. After cleaning and etching of the SiC(0001) substrate graphitization is driven further until

a monolayer of graphene forms on top of the zero layer [159]. A monolayer of WS_2 is then grown by CVD on top of the TDMLG as described in section 3.2.2. The final layer structure is sketched in Fig. 8.1a.

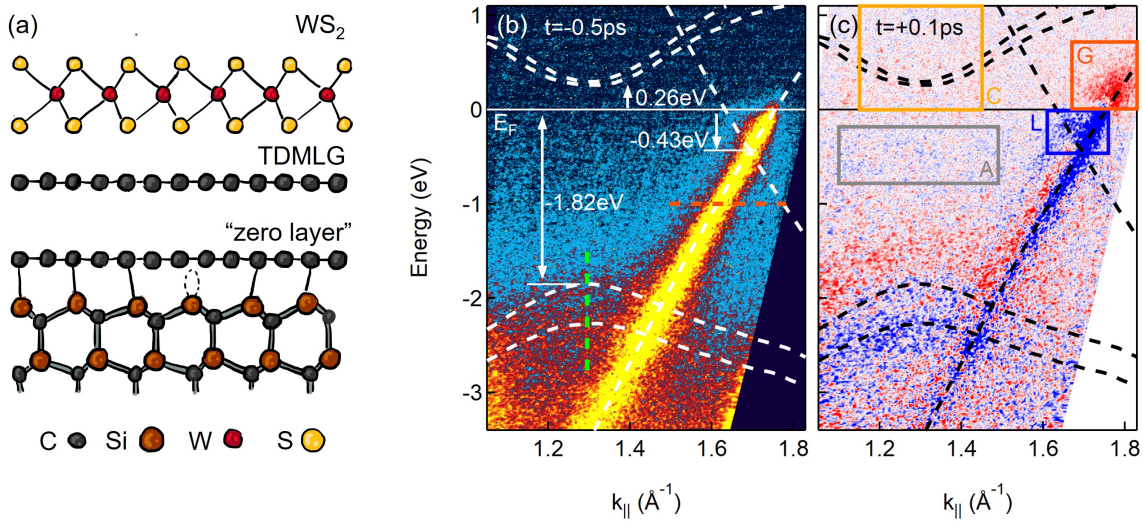

Figure 8.1: WS_2/TDMLG heterostructure: (a) Sketch of the layer structure. Adapted from [48]. (b) and (c) Tr-ARPES snapshots at negative pump-probe delay (t=-0.5 ps) and peak of the pump-probe signal (t=+0.1 ps), respectively. Dashed white and black lines denote the theoy bands of WS_2 and graphene. A rigid band shift of -1.54 eV and -1.82 eV was applied to the WS_2 CB and VB, respectively. The graphene Dirac cone was shifted by -0.43 eV to account for the observed hole doping [164]. Colored dashed lines denote the line profiles for WS_2 VB and graphene fits. Colored boxes indicate integration areas used for the dynamics in Fig. 8.2.

In contrast to the p-doped QFMLG (cf. Fig. 3.15), the TDMLG forms an n-doped layer on the SiC substrate [164]. This doping of ∼430 meV can be seen in an ARPES snapshot at negative pump-probe delay in Fig. 8.1b. The heterostructure is still of type I band alignment, although the WS_2 conduction band is just 0.26 eV above the Fermi level (E_F). Remarkably, the WS_2 bands obtain the same relative alignment to the Dirac-Point of graphene as in WS_2/QFMLG (see Fig. 3.15). Unfortunately, the WS_2 bands are measured with low signal-to-noise ratio in this datasets.

Results

The sample was excited resonant to the A-exciton at $\hbar\omega_{pump}$= 2 eV with a pump fluence of 2.5 mJ/cm^2. Fig. 8.1c shows the difference ARPES spectrum at peak to the pump-probe signal. It looks somewhat familiar to the data on WS_2/GFMLG shown in chapters 4-7. In addition, a small loss signal below E_F within the gap of WS_2 can be seen which

is marked by box A. For the investigation of photo-induced dynamics we integrated the photocurrent within the colored boxes of Fig. 8.1c and displayed them as a function of pump-probe delay in Fig. 8.2. The gain-and-loss signal in graphene is asymmetric with an exponential lifetime of $\tau = 150 \pm 40$ fs ($\tau = 750 \pm 75$ fs) for the gain (loss) above (below) E_F, respectively.

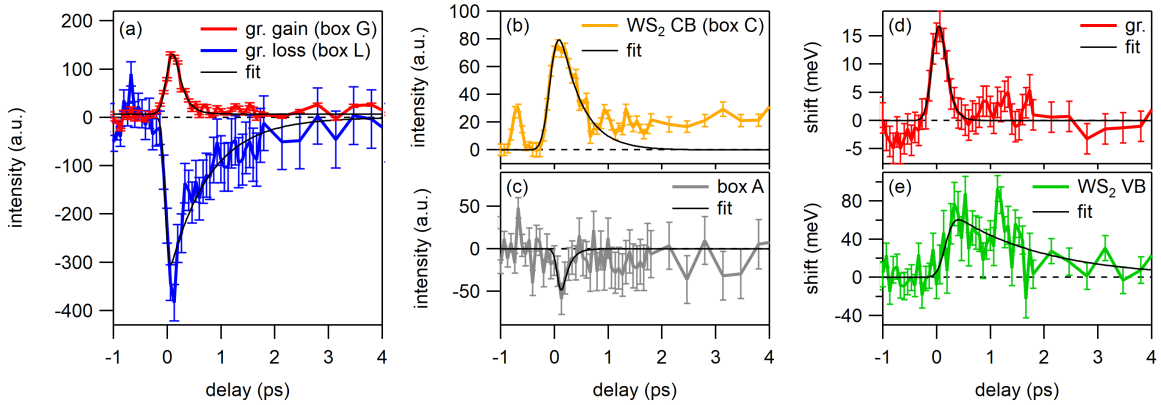

Figure 8.2: Pump-probe dynamics in WS_2/TDMLG: (a) Gain above the Fermi level (red, box G) and loss below the Fermi level (blue, box L) inside the graphene Dirac cone as a function of pump-probe delay. (b) Gain in the WS_2 CB (box C) as a function of pump-probe delay. (c) Loss within the gap of WS_2 (box A). (d) and (e) Shift of graphene and WS_2 VB respectively. Black lines are fits to data.

The low signal-to-noise ratio hindered the WS_2 CB analyis. The occupation within the orange box C was determined by integration of the photocurrent over momentum to determine EDCs. The EDCs were then fitted with a single Gaussian to obtain a transient CB population (Fig. 8.2b). The CB is populated by the laser excitation and decays within $\tau = 400 \pm 100$ fs first. At later pump-probe delays (>1 ps) the population stays constant at a finite value. Within the experimental resolution no holes in the VB of WS_2 could be found. The loss of the additional signal within box A is short lived ($\tau = 130 \pm 100$ fs, Fig. 8.2c).

The transient band position of the π-bands in Fig. 8.2d was determined by Lorentzian fits of the MDC line profiles ± 0.05 Å along the red dashed line in Fig. 8.1b. Contrary to previous experiments, the graphene bands shift upwards by ~15 meV for $\tau = 110 \pm 60$ fs. The position of the VB_A of WS_2 was determined by fits of the EDC line profiles along the green dashed line in Fig. 8.1b with a Gaussian fit model including Shirley background (cf. Appendix A.4). The transient band position is shown in Fig. 8.2e. The valence band shifts upwards by ~60 meV for $\tau = 1.7 \pm 0.8$ ps. Because ot the low signal-to-noise ratio the transient position of the CB of WS_2 could not be determined.

We performed Fermi-Dirac-fits of EDCs integrated within the range from 1.5 to 1.83 Å.

The obtained transient electronic temperature T_{el} and shift of chemical potential $\Delta\mu$ are shown in Fig. 8.3a and b. The calculated changes of the electron density in graphene is plotted in Fig. 8.3c. It reveals a short lived gain of electrons in graphene for $\tau = 140 \pm 40$ fs which is in strong contrast to the experiments on WS_2/QFMLG (cf. Fig. 4.5c).

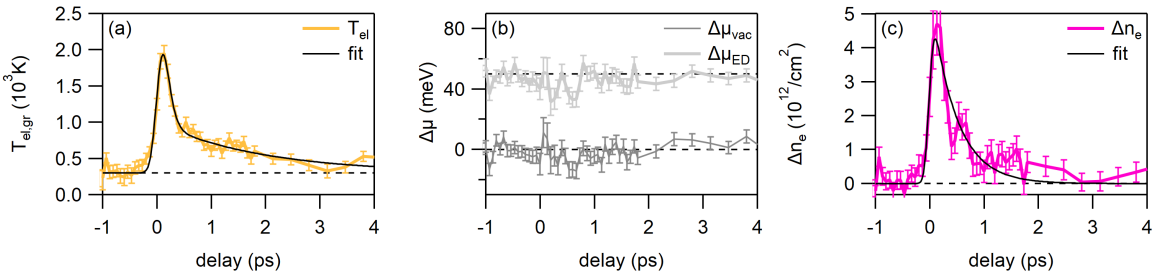

Figure 8.3: Hot carrier dynamics in TDMLG: (a) Transient electronic temperature. (b) Transient shift of chemical potential referenced to the vacuum level $\Delta\mu_{vac}$ and referenced to the Dirac-point $\Delta\mu_{ED}$. (c) Transient electron density in graphene. Black lines are fits to data.

Discussion

To sum up, we found a similar asymmetry of photoexcited carriers in graphene after photoexcitation resonant to the A-exciton in WS_2/TDMLG compared to WS_2/QFMLG. The upshift of the WS_2 VB is also comparable in magnitude (∼60 meV) and lifetime (τ =1.7 ps). But in contrast to the results from chapters 4-7, the TDMLG graphene shifts upwards (∼15 meV) after pump excitation with a lifetime of τ =140 fs and its electron density increases on a similar timescale. An additional loss signal within the gap of WS_2 is found which is also short lived (τ =130 fs). These results appear rather puzzling compared to the findings from the main text.

Some understanding of the dynamics might appear when discussing possible origins of additional states in the grey box A in Fig. 8.1c. They could be assigned either to zero layer graphene which exhibits two broad non-dispersive states at -0.3 eV and -1.2 eV (see Fig. 8.4a) [200] or defect states from S vacancies [173]. The ladder would yield two occupied defect states below E_F in WS_2 on top of TDMLG (see Fig. 8.4b) assuming a similar distance from CB minimum to the defect states on top of QFMLG.

Direct transitions by the 2 eV pump pulse from both additional states to graphene would be possible within the box A range as sketched by orange arrows in Fig. 8.4. Such transitions could explain the short lived depletion of signal within box A (Fig. 8.2c) and the short lived gain of electrons in graphene (Fig. 8.3c). Consequently, the negative charging of graphene would explain the upshift of graphene bands (Fig. 8.2d).

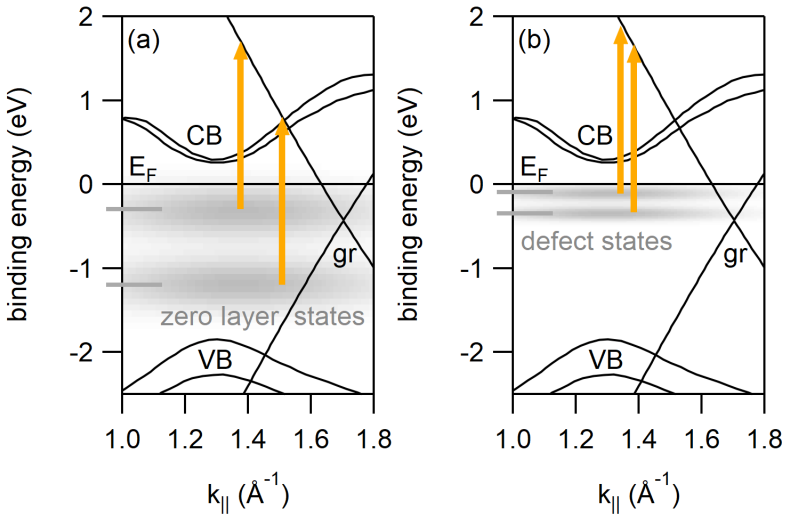

Figure 8.4: Possible origin of in-gap states: (a) In-gap states from zero layer graphene [200]. (b) In-gap defect states from S vacancies [173]. Orange arrows mark supposable transitions to graphene bands at $\hbar\omega_{pump}$ = 2 eV.

As shown in chapter 4, defect states from S vacancies can indeed be found in WS_2 monolayers (Appendix B.4) and play a major role for the dynamics. On the other hand, the zero layer is spatially closer to the monolayer graphene in TMDLG compared to the hydrogen intercalated QFMLG (cf. Fig. 8.1a and Fig. 3.13e). Thus, electronic transitions from zero layer might be possible to TDMLG but not to QFMLG. In literature tr-ARPES experiments, the data from Johannsen et al. shows a similar short-lived gain signal above the π-bands in TDMLG [201] compared to our Fig. 8.1c. This could indicate a similar upshift due to transitions from zero layer as observed in our experiment.

Besides the short-lived electron transfer to graphene, it is hard to say, if a charge separation between WS_2 and graphene takes place or not. On the one hand, the graphene gain-and-loss signal is asymmetric like in QFMLG which is a signature of ultrafast hole transfer. But on the other hand, the graphene electron density and band position do not support such a picture.

The initial hole transfer should be even faster for WS_2 on TDMLG than on QFMLG, if one compares the availability of final states for electron and hole transfer from CBM and VBM to E_F (see section 3.3). This is not found here. As the relative alignment in between WS_2 and graphene bands is unchanged, the transfer rates of carriers via the points where the bands cross should be similar. Unfortunately, the presented first results on WS_2/TDMLG could not provide answers to the charge transfer in between WS_2 and graphene. In any case, the WS_2/TDMLG experiments need to be repeated with a better experimental resolution to identify the charge transfer channels and clarify remaining

questions.

8.2.2 Oscillations in Tr-ARPES Data

We stumbled across oscillating signals in several tr-ARPES datasets within this thesis. Fig. 8.5 gives an overview of these findings which will be discussed in the following.

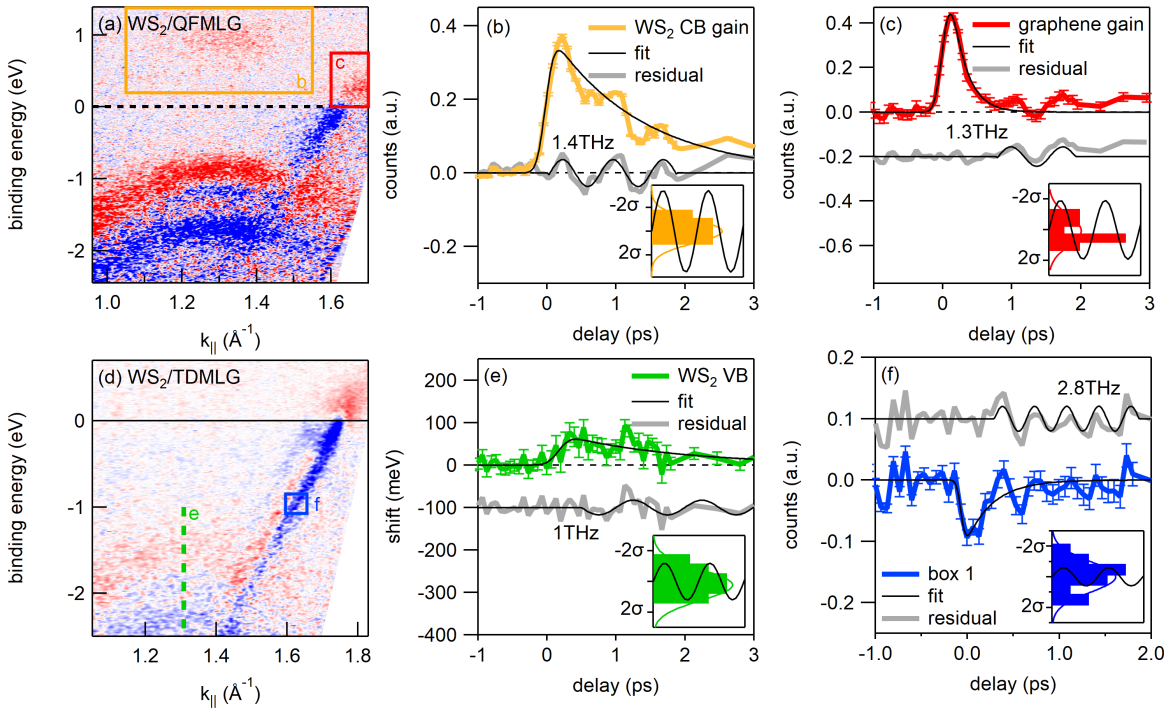

Figure 8.5: Overview of oscillations in tr-ARPES data: (a) Pump induced changes to the photocurrent in monolayer WS_2/QFMLG after excitation with $2.85\,\mathrm{mJ/cm^2}$ at $\hbar\omega = 2\,\mathrm{eV}$ at peak of the pump-probe signal ($+0.2\,\mathrm{ps}$). (b) and (c) display oscillations in WS_2 CB gain and graphene gain, resepctively. (d) Pump induced changes to the photocurrent in monolayer WS_2/TDMLG after excitation with $2.5\,\mathrm{mJ/cm^2}$ at $\hbar\omega = 2\,\mathrm{eV}$ at peak of the pump-probe signal ($+0.1\,\mathrm{ps}$). (e) and (f) display oscillations of the WS_2 VB position and wihtin the blue box in (d), respectively. Colored boxes in (a) and (d) mark the integration areas for the graphs in (b), (c) and (f). The dashed line in (d) marks the line profile for VB fits. The insets in (b), (c), (e) and (f) compare the noise at negative pump-probe delays (color) to the magnitude of oscillations (black).

Upon A-exciton resonant excitation in WS_2 on QFMLG we found oscillations in the WS_2 CB gain and graphene gain signals, as displayed within the first row of Fig. 8.5. The data was first fitted with an exponential fit function (see Appendix A.5) and the fit afterwards subtracted from data. The residual curves (grey) were fitted with a sine. To evaluate the

signal-to-noise ratio of oscillations, a histogram of the noise at negative pump-probe delay was fitted with a Gaussian distribution (with variance σ^2) and compared to the oscillation magnitude (see insets in Fig. 8.5b and c). The oscillations in WS_2 CB gain and graphene gain are at frequencies of 1.4±0.1 THz and 1.3±0.1 THz with a signal-to-noise ratio of $3.5\,\sigma$ and $1.9\,\sigma$, respectively. Moreover, these oscillations are in-phase to each other. This findings strongly suggests that WS_2 and graphene layers oscillate at a collective mode.
In WS_2 on TDMLG (second row in Fig. 8.5) a similar oscillation frequency of 1.0±0.1 THz with a signal-to-noise ratio of $1.2\,\sigma$ can be found in the transient position of WS_2 VB after similar photoexcitation.
Another oscillating signal was found within the Dirac cone in WS_2/TDMLG in a certain area marked by the blue box f in Fig. 8.5d. A sinusoidal fit revealed a frequency of 2.8±0.2 THz for oscillations of the photocurrent (see Fig. 8.5f). But the signal-to-noise ratio is with $0.67\,\sigma$ too low to prove this as a real feature. Furthermore, fits of the π-bands at corresponding energy or momentum showed no oscillations in band position or carrier population. Improved statistics or experimental resolution in future experiments is needed for this signal to become manifest.
However, the observed oscillations in the range of 1-1.5 THz were investigated in more detail. Fig. 8.6a shows the WS_2 CB as a function of pump-probe delay and momentum. It can be seen that the width of the conduction band oscillates with pump-probe delay after photoexcitation resonant to the A-exciton in WS_2. This is not observed for 3.1 eV excitation. The width of the CB was determined by a Gaussian fit and is displayed in Fig. 8.6b as a function of pump-probe delay. The oscillation frequencies for several pump fluences were in the range of 1-1.5 THz but at a pump fluence of 1.63mJ/cm^2 the CB oscillates at 2.2 THz. The central position of the CB does not shift within the error bars which indicates that the WS_2 in-plane lattice constant is not strongly deformed. A distinct dependence of oscillation frequency or amplitude on the pump fluence is not found. A possible explanation for the oscillatory broadening and shrinking of the CB is sketched in Fig. 8.6c by alternate addition and subtraction of electrons. This scheme is in accordance with the oscillating total CB population in Fig. 8.5b.
To sum up, oscillations at a frequency of 1-1.5 THz (33-50 cm$^-$1) were observed in WS_2 CB and VB and graphene, for the stacks on QFMLG and TDMLG. They just appear at A-exciton resonant excitation and do not significantly distort the lattice constants of WS_2 or graphene.
These findings are highly interesting as they can refer to collective modes of both layers, e.g. a layer breathing mode as sketched in Fig. 8.7a. The frequency range of the observed oscillations 1-1.5 THz (33-50 cm$^-$1) lies between literature data for layer breathing modes of WS_2 bulk at 0.8 THz (27.5 cm$^-$1) and graphite at 1.3 THz (43.5 cm$^-$1). Also a mixed bulk shear mode (Fig. 8.7b) may play a roles since the corresponding bulk modes are at

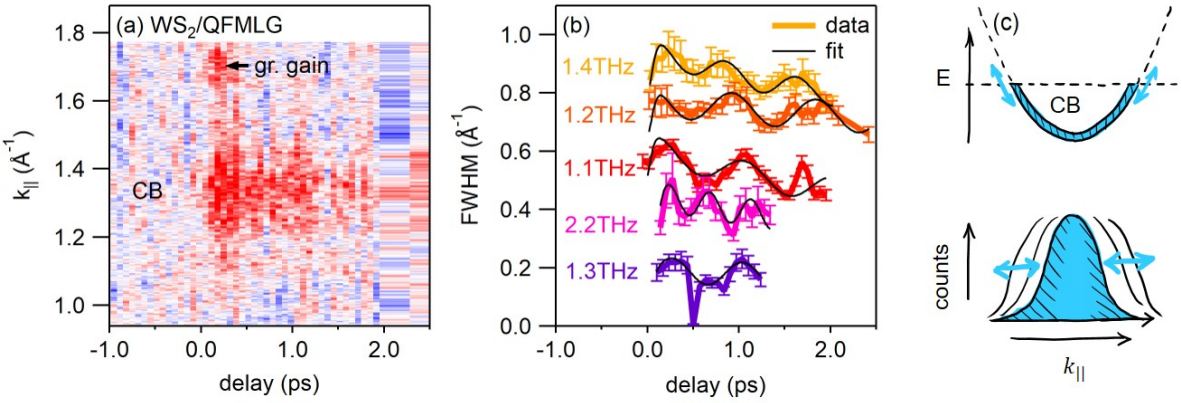

Figure 8.6: Oscillating CB width: (a) Integrated photocurrent within 0.3-1.3 eV in monolayer WS_2/QFMLG after excitation with 2.85 mJ/cm^2 at $\hbar\omega$ = 2 eV as a function of pump-probe delay and momentum. (b) Oscillation of the CB Gaussian FWHM as a function of pump-probe delay. The fluences 0.52, 1.63, 2.85, 3.74 and 4.78 mJ/cm^2 are represented by violet, pink, red, darka and light orange curves, respectively. (c) Sketch of CB population oscillations and the corresponding change of Gaussian FWHM.

1.4 THz (47.8 cm$^-$1) and 3.8 THz (128 cm$^-$1) for WS_2 and graphite, respectively [202]. In both considered modes the unit cell of individual monolayers is not distortet which is in agreement with the observations.

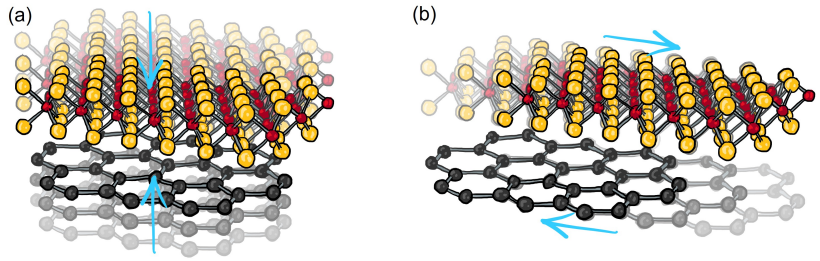

Figure 8.7: Interlayer phonon modes between WS_2 and graphene layers: (a) Layer breathing mode. (b) Layer shear mode. Not to scale. Adapted from [202].

Coherent excitation of these modes is possible by impulsive Raman scattering when the pump pulse is sufficiently shorter than a single vibrational cycle of the phonon [203]. Coupling is most efficient when the wavelength is close to a direct transition [204, 205]. This explains why the oscillations are strong at 2 eV excitation but absent at 3.1 eV excitation since the direct band gap in WS_2 is found to be 2.08 eV (see Appendic A.6).
The question rises, if charge is actually oscillating between WS_2 and graphene layers. From Fig. 8.5b and c we know that both layers gain and loose electrons coherently. Thus, the

situation is more complicated. Carrier oscillations might involve states at other regions within the Brillouin zones or even the next BZs [204]. This would lead to additional scattering channels to the ones provided in chapter 4. Wang et al. state that the out-of-plane breathing modes in a type II heterostructure affect the charge recombination time [98]. In this case a direct-to-indirect band gap transition is modulated which affects exciton decay rates. The mechanism behind the oscillations in type I heterostructures and their impact on the charge transfer, however, remains as extremely interesting question to tackle in upcoming experiments. For that purpose, temperature dependent measurements of the ultrafast charge transfer in TMD/graphene heterostructures could be carried out combined with an improved temporal resolution.

8.2.3 Refinement and Substantiation of the Microscopic Model

In chapter 4 we revealed direct tunneling and defect-assisted tunneling to be the microscopic scattering channels behind the ultrafast charge transfer. Although the model was shown to apply for bilayer WS_2/graphene (see ch. 5) and above gap excitation (see ch. 6) as well, it still can be refined and substantiated.

In our charge transfer model, direct tunneling is possible via opened anticrossings at the intersections of WS_2 and graphene bands (see Fig. 6.5). This picture is valid for epitaxial WS_2/graphene heterostructures with a twist angle of 0° or 60° between both layers such that either the ΓK or $\Gamma K'$ direction of WS_2 aligns with the ΓK direction of graphene (see section 3.2.2).

At an intermediate twist angle the band intersections will shift in energy and momentum which could alter state mixing and the opening of avoided crossings. This might impede the charge transfer between the layers in TMD/graphene heterostructures with type I band alignment. Ref. [174] did not find indications for a charge transfer at a twist angle of 30° between MoS_2 and graphene. In heterostructures of type II bad alignment on the other hand, the orbital overlap is made responsible for the charge transfer. Since the orbital overlap at Γ does not change much with layer twist the ultrafast charge transfer is found to be rather unaffected [98, 206, 207].

Lattice mismatch and twist angle lead to periodic changes of the layer stacking configuration in real space (cf. Fig. 6.5a) forming a Moiré pattern. Electronic properties like band gap or exciton binding energies can vary significantly within the discriptive Moiré supercell [170, 208–211]. The effect of a superperiodic potential of the ultrafast charge transfer in twisted WS_2/graphene heterostructures is worth to investigate in future experiments, e.g. by tr-μ-ARPES, and needs to be implemented in the microscopic model.

Defect states from S vacancies play an important role for charge separation, as shown in chapter 4. Trapping of photoexcited electrons by in-gap defect states can prolong

the lifetime of charge separation by several orders of magnitude [111]. Although hints for defect states were found (see Appendix B.4), they could be better resolved in future tr-ARPES experiments. Defect-assisted tunneling of trapped electrons and excitons to graphene states is object of current investigations by density functional theory and many-body perturbation theory. The aim is to obtain transition matrix elements which can explain the prolonged charge separation lifetimes (cf. Fig. 4.6).

8.2.4 Next Generation Tr-ARPES

As introduced in section 2.2.4 it is possible excite spin-valley selective by using circularly polarized light and create a spin-polarization [89–93]. The observed charge transfer to graphene might by accompanied by spin transfer (see Fig. 3.16c) which would inject a net spin polarization into graphene. Due to long spin-scattering lifetimes in graphene [54, 56, 57] heterostructures of WS_2/graphene are promising candidates for spintronics devices. We tried to measure the injected spin-polarization of graphene carriers with time- and spin-resolved ARPES at the Artemis setup (see section 3.1.4) in 2018. Unfortunately, the experiment failed due to technical issues with the spin-detector. A repetition of this experiment is planned at the group of Martin Aeschlimann at the Technische Universität Kaiserslautern, Germany.
However, in the present work we assign the photoexcited signal in WS_2 to free electrons and holes rather than to excitons (see section 4.2), e.g. due to elevated temperatures by using comparatively high pump fluences [81]. The lower edge of applicable pump fluence was limited by the signal-to-noise ratio for the observation of pump-induced changes. For improved statistics we usually averaged the photocurrent of an over-night-measurement in the 1 kHz laser setup (see section 3.1.4). Novel tr-ARPES setups based on high repetition rate lasers are able to obtain good statistics at a fraction of that time [212] and make it possible to apply lower pump fluences to investigate the interplay between excitons and free electron-hole pairs [80].
Lastly, with our large XUV probe spot of 300 x 560 μm we cannot distinguish between the K and K' point as our epitaxial WS_2 flakes grow in two domains rotated by 60° with a size 300-700 nm (see Fig. 3.14a). This hurdle can be tackled by using a much smaller spot size in time-resolved μ-ARPES which allows to measure excitons in single flakes of monolayer TMDs [85, 86]. An application of this technique on TMD/graphene heterostructures is highly interesting.

Appendices

Appendix A

Tr-ARPES Data Analysis

A.1 Treatment of Raw Data

The qualitiy of the tr-ARPES raw data was impaired by three main factors:

- (1) a featureless background due to dark counts on the detector as well as photoelectrons emitted from the pump rather than the probe pulse (see section 3.1.8)
- (2) fluctuating ARPES counts due to shot-to-shot intensity variations of the XUV pulses
- (3) variations of the relative intensity of WS_2 and graphene bands due to sample inhomogeneity

These problems were solved as follows:
(1) We measured the photocurrent with pump but without probe pulse and subtracted this background from the tr-ARPES snapshots.
(2) We integrated the counts over the area marked by the pink box in Fig. A.1a where the photocurrent is expected to be zero after background subtraction. This yields a photocurrent $I_{box}(t)$ that fluctuates with time t (Fig. A.1b). Next, we averaged $I_{box}(t)$ at negative delays yielding $< I_{box} >$. We then multiplied each tr-ARPES snapshot with a factor $f =< I_{box} > /I_{box}(t)$ (Fig. A.1c). The effect of this procedure on the transient photocurrent at the bottom of the conduction band obtained by integrating the tr-ARPES data over the area marked by the orange box in Fig. A.1a is illustrated in Fig. A.1d.
(3) As the WS_2 coverage in our WS_2/graphene heterostructure is not uniform, the relative intensity of the WS_2 and the graphene bands varies from spot to spot and, hence, between

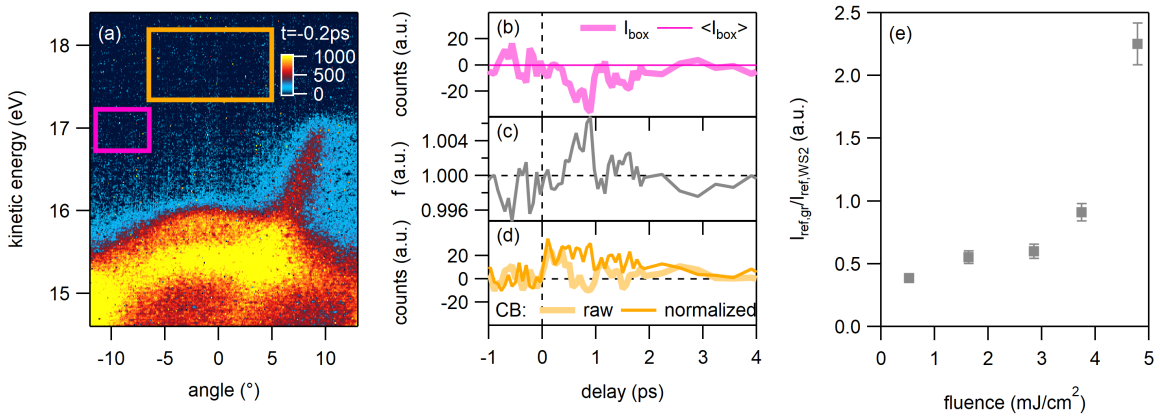

Figure A.1: Treatment of raw data: (a) Tr-ARPES snapshot at negative pump-probe delay taken with a pump fluence of 1.63 mJ/cm^2. The pink box is used to extract $I_{box}(t)$ in panel (b). The orange box captures the carriers at the bottom of the conduction band shown in panel (d). (b) Photocurrent $I_{box}(t)$ integrated over the area marked by the pink box in (a) together with its average for negative pump-probe delays $< I_{box} >$. (c) Normalization factor $f =< I_{box} > /I_{box}(t)$ as a function of pump-probe delay. (d) Effect of the raw data correction on the time dependence of the photocurrent integrated over the area marked by the orange box in panel (a). (e) Ratio of the reference intensities $I_{ref,gr}$ and $I_{ref,WS2}$ as defined in Fig. A.4c and a, respectively, for the datasets obtained with different pump fluences.

different tr-ARPES runs. In order to turn our results independent of the precise value of the WS_2 coverage we divided the pump-probe traces shown in Fig. 4.2a by the integrated intensity of the upper WS_2 valence band I_{ref,WS_2} from Fig. A.4a and the pump-probe trace shown in Fig. 4.2b by the integrated intensity of the Dirac cone $I_{ref,gr}$ from Fig. A.4c. The ratio $I_{ref,gr}/I_{ref,WS_2}$ for the different tr-ARPES runs with different pump fluences is shown in Fig. A.1c. The measurement with the highest pump fluence was done on a sample area where the WS_2 coverage was particularly low. This reduced the absolute number of photoexcited electron-hole pairs and, hence, the absolute number of holes that were transferred to the graphene layer as well as the measured shift of the Dirac cone. For this reason, the high fluence data point in Fig. 4.5c and d was set in brackets and not included for the determination of the guide to the eye.

A.2 k-Space Conversion and Experimental Resolution

As described in section 3.1.3 the photocurrent I is detected on a two-dimensional detector as a function of emission angle θ and kinetic energy E_{kin} of the photoelectrons. The conversion into $I(E_{bin}, k_{\parallel})$ is done via equations 3.11 and 3.1. ϕ is the work function of the analyzer, that – in the absence of space charge effects (see section 3.1.8) – determines

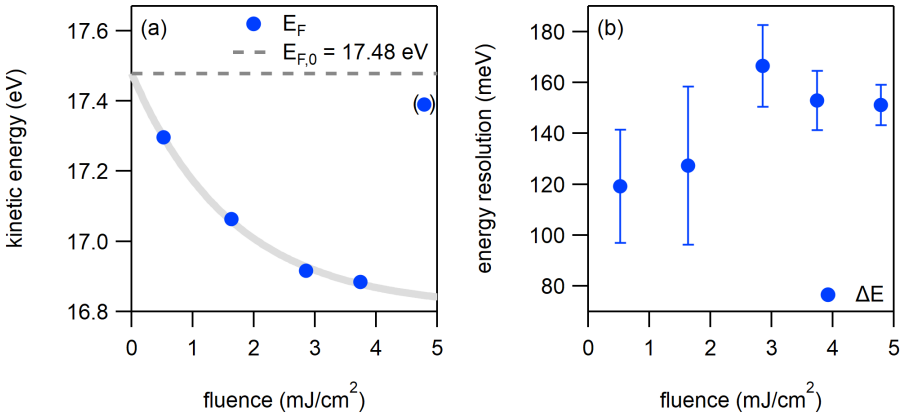

Figure A.2: Space charge effects: (a) Position of the Fermi level at negative delays as a function of pump fluence. The gray line is used to extrapolate the position of the Fermi level to zero pump fluence. The data point in brackets was obtained on an area of the sample where the WS_2 coverage was particularly low. The error bars are smaller than the symbol size. (b) Energy resolution for different pump fluences.

the kinetic energy where the Fermi level appears in the measurement.

The energy resolution of the tr-ARPES measurements was determined from Fermi-Dirac fits of the carrier distribution inside the Dirac cone at negative pump-probe delay (see Appendix A.7). These fits revealed that the kinetic energy at which the Fermi level appeared in the measurement (Fig. A.2a) as well as the energy resolution (Fig. A.2b) depend on the applied pump fluence. The temporal resolution of the tr-ARPES measurements of 200 fs was deduced from the full width at half maximum (FWHM) of the width of the derivative of the rising edge of the photocurrent integrated over the graphene gain signal marked by the red box in Fig. 4.1f. The conversion of the measured photocurrent from (E_{kin}, θ) to $(E_{bin}, k_{\parallel})$ relies on an accurate value for the kinetic energy of the Fermi level that is commonly used as energy reference in ARPES data. To solve this issue, we extrapolated the kinetic energy of the Fermi level in Fig. A.2a to zero pump fluence, yielding $E_{F,0} = 17.48\,\text{eV}$.

A.3 Pump Fluence and Excitation Density:

The pump fluence F for all datasets was calculated with:

$$F = \frac{P_{sample}}{S \cdot f_{rep}} \tag{A.1}$$

where P_{sample} is the power of the laser beam incident at the sample, S is the pump illuminated area and f_{rep} is the laser repetition rate of 1 kHz. We used a transmission

factor T to determine the power at the sample position in UHV $P_{sample} = P_{measured} \cdot T$ from the position of the power meter including reflection of the pump pulse at mirrors and transmission through windows. The pump illuminated area $S = S_{measured} \cdot 1/\cos\alpha$ takes into account the enlargement of the measured pump beam area $S_{measured}$ under tilted pump beam (Fig. A.3a). The angle α is defined here as difference between sample normal and pump beam.

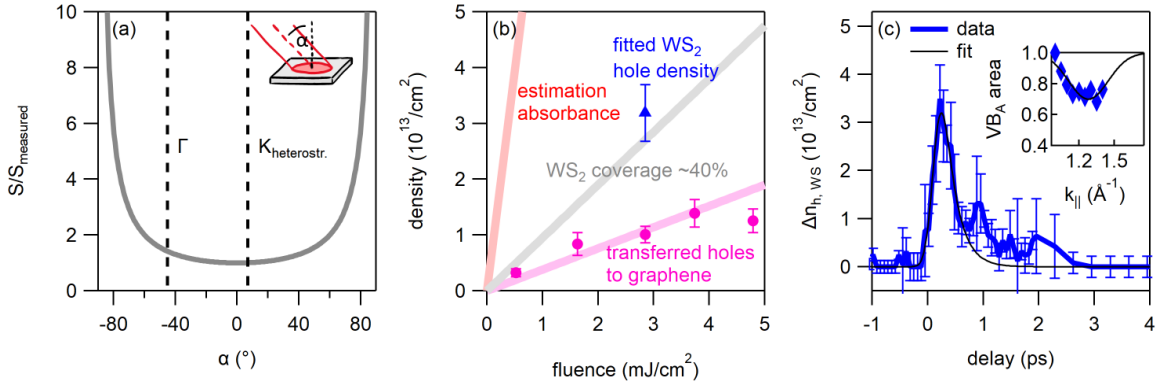

Figure A.3: Pump fluence and excitation density: (a) Dependence of the sample illuminated area on the angle α between sample normal and pump beam. Dashed lines mark typical setup configurations for measuring at Γ or K. (b) Excitation density vs. pump fluence for different estimation approaches (see text). (c) Hole density in WS_2 as function of pump-probe delay. The inset shows the WS_2 VB_A peak area depletion as a function of momentum at peak of the pump probe signal. For each EDC it was referenced to the peak area at negative pump probe delay. Black lines are fits to data.

Estimation of the Excitation Density

The estimation of meaningful excitation densities $n_{e/h}$ for the applied pump fluences turned out to be rather difficult. A first approach was done following the equation:

$$n_{e/h} = \frac{F \cdot A}{\hbar\omega} \tag{A.2}$$

with A beeing the dimensionless absorbance of the sample [175]. The excitation frequency dependent absorbance $A(\omega)$ was taken from literature for monolayer WS_2 [213] and multiplied by a factor to adapt the peak of the A-exciton to bulk WS_2 of $\sim$ 7 %. This idea is motivated by the determination of the equilibrium band gap in out sample of 2.08 eV (see Appendix A.6) which is close to bulk WS_2 of $\sim$2.1 eV [72] due to substrate screening. Fig. A.3b compares the estimation of this approach via absorbance (light red) to the measured number of holes transferred to graphene (pink). It is easily seen that this approach

overshoots the measured number of holes by orders of magnitude. This discrepancy was previously observed by Ref. [174] who calculated excitation densities in the order of 10^{14} – 10^{15}/cm^2 by this approach but just measured excitation densities of $10^{13}/cm^{-2}$.
Since we can measure the number of transferred holes to graphene with confidence (see Appendix A.7) we based a second approach for estimation of excitation density on them. We take the excitation to be equal to the number of excited holes in WS_2: $n_{e/h} = n_{h,WS_2}$ and assume all photoexcited holes to transfer to graphene. For a WS_2 coverage C the holes will then dilute in graphene after transfer due to the larger area (cf. Fig. 3.14a and b). Thus,

$$n_{e/h} = n_{h,WS_2} = 1/C \cdot n_{h,gr} \tag{A.3}$$

The resulting fluence dependent excitation density for of C=40 % is plotted in Fig. A.3b as grey curve.
This approach was further backed up by determination of excited holes in WS_2. The transient hole density in WS_2 is depicted in Fig. A.3c. First, valence band EDC fits like in Appendix A.4 were performed. The depletion of WS_2 VB_A peak area $N_h(k)$ around the K valley is shown in the inset of Fig. A.3c together with a Gaussian fit. The total number of holes per unit area is then determined by integration:

$$n_{h,WS_2} = \frac{4\pi}{S_{BZ}} \int_0^R N_h(k) k dk \tag{A.4}$$

where S_{BZ} is the area of the Brillouin zone and R is the radial extend of the Gaussian fit centered at the K valley [174]. The resulting peak hole density in WS_2 is plotted as blue data point in Fig. A.3b and matches with the previous approximation. Consequently, the excitation density was estimated using equation A.3 for the datasets.

A.4 Determination of Transient Band Positions

Transient band positions were determined either by fitting energy distribution curves (EDCs) or momentum distribution curves (MDCs) and examples are given in Fig. A.4. The EDCs in Fig. A.4a were obtained by integrating the tr-ARPES data over a momentum interval of 0.05 Å^{-1} centered at the green dashed line in Fig. 4.1a. A total of three Gaussians (one for the upper and lower WS_2 VB, respectively, and one for the background) was used to fit the spectra. While the lower and upper VB are nicely resolved at negative pump-probe delays, the broadening of the spectrum after photoexcitation makes a correct determination of the transient peak positions difficult. This difficulty could be avoided by constraining the parameters of the fit as follows:

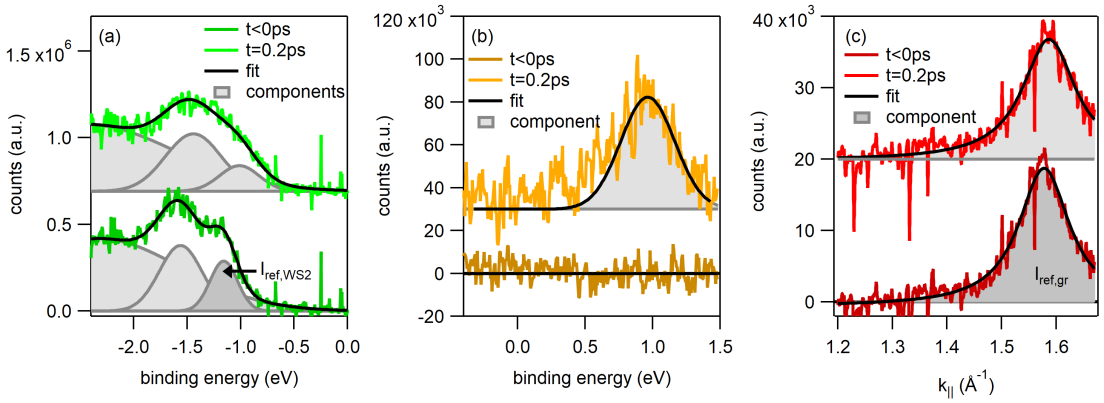

Figure A.4: Determination of transient band positions: (a) EDCs extracted along the dashed green line in Fig. 4.1a at $t < 0$ fs (light green) and at $t = 200$ fs (dark green) together with Gaussian fit (black) in the WS_2 VB region. The shaded areas indicate the three individual Gaussians used to fit the data. The area of the dark-shaded Gaussian $I_{ref,WS2}$ was used to turn the measured photocurrent independent of the WS_2 coverage. (b) EDCs extracted along the dashed green line in Fig. 4.1a from the differential tr-ARPES data shown in the lower panel of Fig. 4.1 in the WS_2 CB region for $t < 0$ fs (dark orange) and $t = 200$ fs (light orange) together with Gaussian fit (black). (c) MDCs extracted along the dashed red line in Fig. 4.1a for $t < 0$ fs (dark red) and $t = 200$ fs (light red) together with Lorentzian fit. The area of the dark-shaded Lorentzian $I_{ref,gr}$ was used to turn the measured photocurrent independent of the WS_2 coverage. The data was obtained for a pump fluence of 2.85 mJ/cm^2.

- No peak was allowed to gain spectral weight with respect to negative pump-probe delay
- Only the upper valence band (VB_A) was allowed to loose spectral weight as a result of photoexcitation
- No peak was allowed to narrow with respect to negative pump-probe delay
- The separation of the upper and lower WS_2 was fixed at 430 meV
- The position of the third Gaussian for the background was fixed at $E = -2.5$ eV.

It was also possible to determine a transient loss in peak area of the upper valence band as displayed in Fig. 4.2a). A Shirley-background was included into transient valence band fits for chapters 5–7. Previous results from chapter 4 were double checked and found to be similar to Shirley-background-including fits within the errorbars.
The EDCs in SFig. A.4b were obtained by integrating the differential tr-ARPES data in the second row of Fig. 4.1 over a momentum interval of 0.1 Å^{-1} centered at the green dashed line in Fig. 4.1a. These spectra were fitted with a single Gaussian for all pump-probe delays where the CB was found to be occupied.

The integration range for the MDCs in Fig. A.4c was ±0.06 eV around the red dashed line in Fig. 4.1a at $E = -0.5$ eV. The MDCs were fitted with a single Lorentzian peak revealing a transient shift in momentum. By multiplication with the slope of the π-bands of 7 eVÅ [51] a transient shift in binding energy of graphene bands was determined as displayed in Fig. 4.3d for example.
The dark shaded areas in Fig. A.4 $I_{ref,WS2}$ and $I_{ref,gr}$ were used as reference to turn the measured photocurrent independent of WS_2 coverage. The resulting fluence dependent excitation parameters are displayed in Fig. 4.5 in the main text.

A.5 Fit Function for Exponential Decay

The fitting function is given by

$$f(t) = \frac{a}{2}\left(1 + erf\left(\frac{(t-t_0)\tau - \sigma^2}{\sigma\,\tau}\right)\right)\exp\left(\frac{\sigma^2 - 2(t-t_0)\tau}{2\tau^2}\right) \tag{A.5}$$

where a is the amplitude of the pump-probe signal, σ is related to the full width at half maximum (FWHM) of the derivative of the rising edge via FWHM $= 2\sqrt{2\ln 2}\,\sigma$, t_0 is the middle of the rising edge, erf is the error function, and τ is the exponential lifetime. This fitting function is obtained by convolving the product of a step function and an exponential decay with a Gaussian to account for the finite rise time of the signal.

A.6 Determination of the Equilibrium Band Gap

The determination of the equlibrium quasiparticle band gap in WS_2 is hindered by the fact of the unoccupied conduction band at negative delays. To determine transient positions of CBM and VBM we performed transient fits at K ± 0.1Å^{-1} for the conduction band and ± 0.05Å^{-1} for the valence band, respectively, as described in Appendix A.4. The transient band gap is then obtained by subtraction of VBM from CBM position as shown in Fig. 4.3 in the main text. As the transient band gap subject to dynamical bandgap renormalization we had to develop a procedure for determination of the equilibrium gap size. It is based on minimization of the fit error for the transient band gaps at different pump fluences shown in Fig. A.5. The curves were fitted alltogether with an exponential decay fit function (see Appendix A.5) with the equilibrium gap size set equal for all datasets. The equilibrium gap size in the fits was then scanned from 1.9 eV to 2.5 eV. The total fit error in all datasets was found to be minimal for an equilibrium gap size of 2.08 eV.
We then get an excition binding energy of ∼100 meV by substraction of the photoluminescence peak of the WS_2/graphene heterostructure at 1.98 eV (see Fig. 3.14e) from the equilibrium quasiparticle gap size [30].

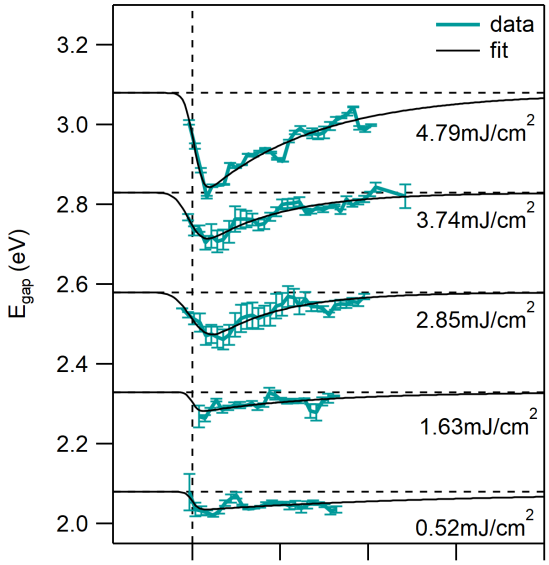

Figure A.5: Transient quasiparticle band gap for different excitation fluences at $\hbar\omega_{pump}$=2 eV. The curves were offsetted by +0.2 eV

A.7 Fermi-Dirac fits of Electron Distribution Inside Dirac Cone

In Fig. A.6 we provide an example for Fermi-Dirac fits of the transient electron distribution inside Dirac cone used to determine the electronic temperature and the chemical potential in Fig. 4.4a and b, respectively. The fitting function consisted of a Fermi-Dirac distribution (eq. 3.8) convolved with a Gaussian to account for the finite energy resolution.

From these fits the number holes transferred from the WS_2 into the graphene layer was determined as follows. The transient shift of the chemical potential referenced with respect to the graphene Dirac point $\mu_{e(ED)}$ was calculated by subtracting the graphene band shift in Fig. 4.3d from the chemical potential in Fig. B.5b that is referenced with respect to the vacuum level. From $\mu_{e(ED)}(t)$ and $T_e(t)$ (Fig. B.5a) we can then directly calculate the change of the total number of electrons in the graphene layer via

$$\Delta n_e(t) = \int_{-\infty}^{\infty} dE\, \rho(E)\, [f_{FD}(E, \mu(t), T(t)) - f_{FD}(E, \mu_0, T_0)]$$

where $\rho(E) = \frac{2A_c}{\pi} \frac{|E-ED|}{\hbar^2 v_F^2}$ is the density of states in the Dirac-cone (cf. Fig. 2.2c) with the unit cell area $A_c = \frac{3\sqrt{3}a^2}{2}$ and the lattice constant $a = 1.42\,\text{Å}$. The equilibrium chemical potential is $\mu_0 = -0.3\,\text{eV}$. The transient chemical potential is given by $\mu(t) = \mu_0 + \Delta\mu_{e(ED)}(t)$. The equilibrium temperature is $T_0 = T(t < 0\,\text{ps}) = 300\,\text{K}$. The number of transferred holes shown in Fig. 4.4c is then given by $\Delta n_h(t) = -\Delta n_e(t)$.

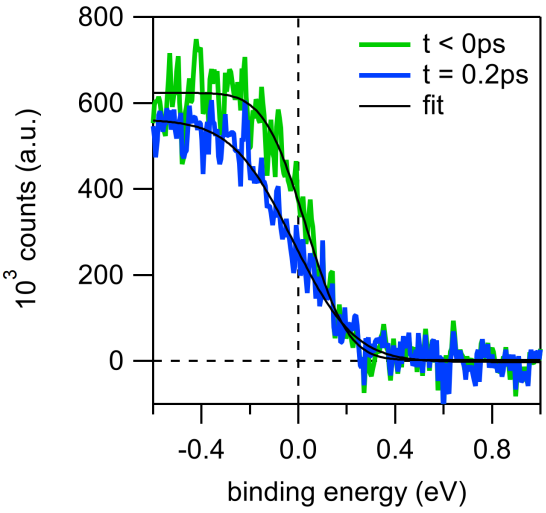

Figure A.6: Fermi-Dirac fits: EDCs obtained by integrating the counts over the momentum width of the yellow box in Fig. 4.1a at $t < 0$ fs (color) and $t = 200$ fs (color) together with Fermi-Dirac fits (black).

A.8 Estimation of the Transient Electronic Temperature in WS_2

In the semiconducting WS_2 the valence (conduction) band is completely occupied (empty) at negative pump-probe-delays, respectively. The absence of a Fermi cut-off prohibits the determination of the equilibrium electronic temperature like it was done in Appendix A.7. Transient electronic temperatures, however, could be estimated with a carefully designed fit function applied on transient hole (electron) densities in valence (conduction) band, respectively. Inspired by transient fits of the momentum-dependent distribution of holes in the valence band of MoS_2 by Ulstrup et al. [174] we developed a fit function of transient momentum-dependent distributions of electrons in the conduction band of WS_2.

Figs. A.7a-c illustrate the fit procedure. We take the band dispersion of the conduction band (Fig. A.7a) and a hot Fermi-Dirac-distribution (Fig. A.7b, cf. eq.3.8) to get a momentum-dependent distribution of electrons in the conduction band:

$$f_e(k) = \frac{1}{e^{(\epsilon(k)-\mu)/k_B T_{el}} + 1} \tag{A.6}$$

The distribution in eq. A.6 is used as fit function of momentum-dependent hot-carrier distributions. In this approach the WS_2 conduction band dispersion $\epsilon(k)$ was taken from theory data [69] and kept fixed. The quasi-chemical potential μ is kept at the conduction band minimum. This assumption will be discussed later. From Fig. A.7c it gets now clear that the transient electronic temperature T_{el,WS_2} is determined by the transient width of the momentum-dependent distribution.

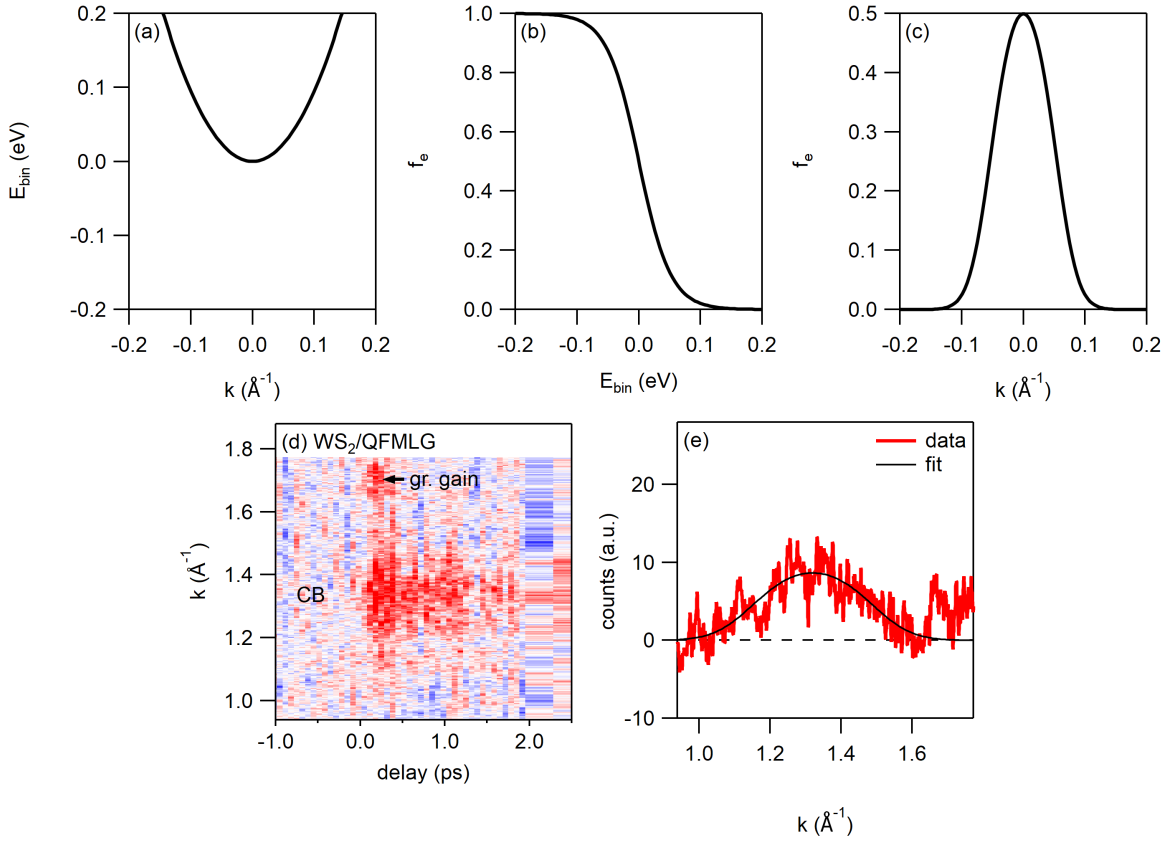

Figure A.7: Fits of the momentum distribution of electrons in CB (a) Band dispersion of CB. (b) Fermi-Dirac-distribution. (c) Momentum-dependent distribution of electrons in the conduction band according to eq. A.6. (d) Integrated photocurrent within 0.3-1.3 eV in monolayer WS_2/QFMLG after excitation with 2.85 mJ/cm^2 at $\hbar\omega = 2$ eV as a function of pump-probe delay and momentum. (e) Momentum-dependent distribution of electrons in CB at peak of the pump-probe signal together with fit.

Fig. A.7d shows tr-ARPES data of the width of the occupied conduction band after photoexcitation at $\hbar\omega = 2$ eV. The width is fitted as a function of momentum as displayed in Fig. A.7e. The results of the estimated electronic temperature in WS_2 are plotted in Fig. A.8a for the fluence dependent measurements at $\hbar\omega_{pump} = 2$ eV. For check of sanity the WS_2 temperatures are compared with the transient electronic temperature in graphene. To clarify: they don't need to be similar in both materials but values of a few thousand K are expected for our pump fluences. [214]. It can be seen that the estimated electronic temperature in WS_2 by the simple fit model matches quite well with the electronic temperature in graphene. This point is highlighted in Fig. A.8b which compares the peak electronic temperatures in graphene with the estimation in WS_2. From this, we conclude that the peak electronic temperature in WS_2 increases as a function of pump fluence sim-

ilar to the electronic temperature in graphene.

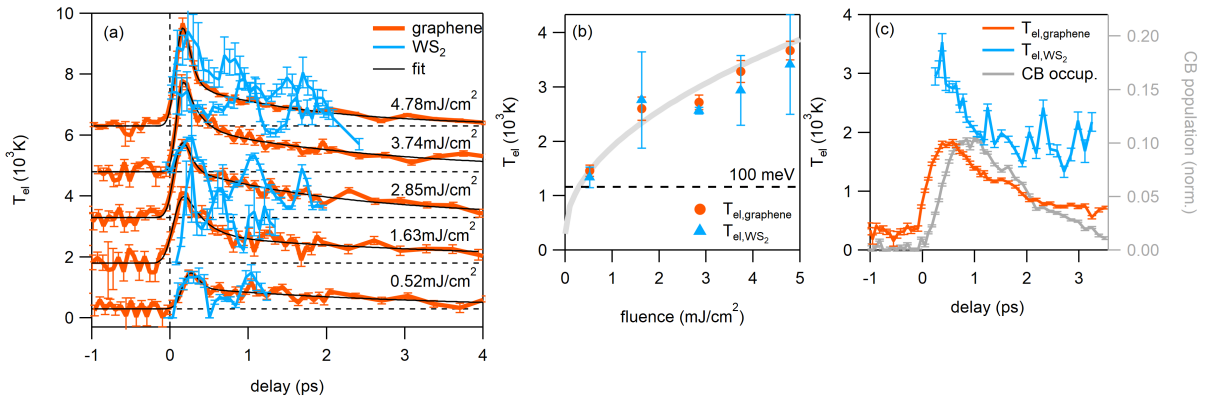

Figure A.8: Estimation of transient electronic temperature in WS_2: (a) Transient electronic temperatures in WS_2 and graphene for different pump fluences at $\hbar\omega_{pump} = 2\,\text{eV}$. (b) Peak electronic temperature as a function of pump fluence. (c) Transient electronic temperatures in WS_2 and graphene for different pump fluences at $\hbar\omega_{pump} = 3.1\,\text{eV}$. The transient population of the WS_2 CB was displayed for comparison.

Upon excitation at $\hbar\omega_{pump} = 3.1\,\text{eV}$ we estimate an electronic temperature in WS_2 which is $\sim$1000 K larger than in graphene (Fig. A.8c). By comparison to the CB population we further see that the CB is populated with hot electrons. These findings are in good agreement with the results of chapter 6. The photoexcitation in WS_2 takes place close to the Σ valley and the CB is populated by intervalley scattering within 400 fs. As the pump at 3.1 eV is resonant to the C-peak deposits excess energy into WS_2 which is higher than by A-exciton resonant pumping (2 eV).

However, oscillations of the transient electronic temperature are visible in Fig. A.8a. To our best konwledge, an oscillating electronic temperature is rather unphysical in the present case. We refer the reader to the outlook 8.2.2 in which the oscillating width of the conduction band is discussed. Here, we conclude that the oscillating electronic temperature is an artifact of oscillating carrier populations.

This is not the only weak spot of the fit model. It further neglects the width of the spectral function and the experimental resolution [215]. Further, the width of the momentum-dependent electron distribution depends not only on electronic temperature but also on the transient quasi-chemical potential as illustrated in Fig. A.9a and b. There is no reason for the quasi-chemical potential μ to be kept fixed at the conduction band minimum. Unfortunately, the fit function fails when μ is unrestrained due to the signal-to-noise ratio of the data.

Thus, the fit model should be developed for a precise determination of the electronic

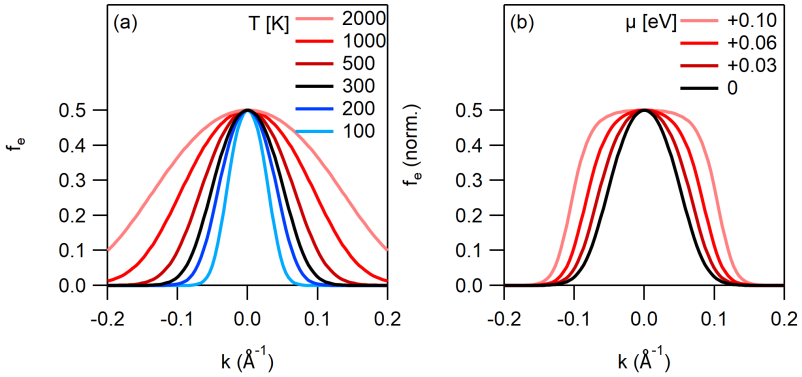

Figure A.9: Dependence of the width of the electronic distribution on electronic temperature (a) and quasi-chemical potential (b). The quasi-chemical potential is at the conduction band minimum in (a). The electronic temperature in (b) is 300 K.

temperature. A two-dimensional (2D) fit model was successfully applied in Ref. [215] for the transient dynamics in metallic TaS_2. An advanced fit model could indeed be based on 2D fits.

A.9 Temporal Matching of Assembled Datasets

When comparing pump-probe traces in between tr-ARPES datasets they need to be temporally matched as the pump-probe temporal overlap can vary in between days of data aquisition. The approach was as follows: An initial pump excitation is clearly visible the within the Dirac-cone of graphene in the K dataset (cf. Fig. 6.1b). Thus, the pump-probe delay axis of the datasets at Σ and Γ can be referenced to that.

As described in the main text of chapter 6, the identification of inital excitation signals in WS_2 at Σ or Γ was rather difficult. Thus, we based the temporal matching of the datasets on the valence band shift assuming it to take place at all momenta simultaneously.

The purple boxes in Fig. 6.1d were placed above the equilibrium position of the WS_2 VB in all three datasets. The pump-probe traces of the photocurrent integrated within the purple boxes is shown in Fig. B.2. The pump-probe delay axes of the datasets at Γ and Σ were then shifted by a to match the centers of the rising edges referenced to the dataset at K. These adjustments were below 100 fs and thus below the temporal resolution. Moreover, all three curves exhibit a similar decay time of ∼1.1 ps. This indicates a simultaneous VB upshift and legitimates the assumption for temporal matching.

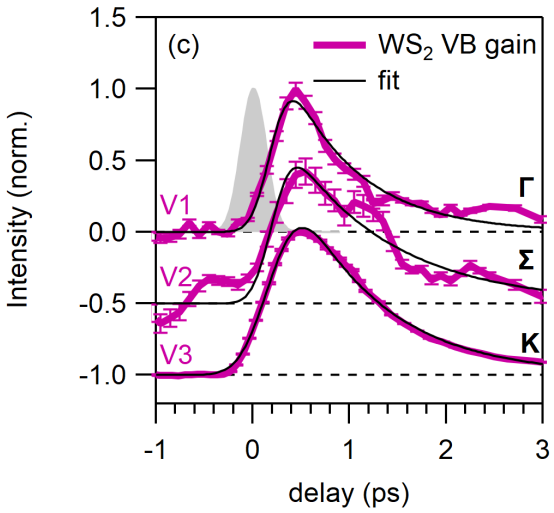

Figure A.10: Temporal matching of Γ, Σ and K datasets: Photocurrent within the purple boxes in Fig. 6.1d as a function of pump-probe delay.

A.10 Direct Transitions to WS_2 Bands at 3.1 eV Excitation Energy

The calculation of possible direct transitions into the conduction band of WS_2 is based on the theoretical band structures of WS_2 and graphene [51, 69]. The band positions were adjusted to match the experimentally determined configuration (see Fig. 3.15) and the quasiparticle bandgap was adjusted to the experimentally determined value of 2.08 eV (see Appendix. A.6).

In a next step, subtraction of valence from conduction bands yields transition energies as a function of momentum for spin-allowed transitions A-A, B-B and spin-integrated transitions from graphene to WS_2. The transition probabilities as function of momentum displayed in Fig. A.11 are then extracted for a Gaussian centered at 3.1 eV resembling our excitation pump pulse. According to Ref. [31] both transitions A-A and B-B are strong at $\sim 0.4\,\text{Å}^{-1}$. Thus, a spin-integrated direct transition close to the Σ valley seems likely. Including further limiting effects like orbital overlap (cf. section 2.2.2) and pseudospin conservation (cf. section 2.1.2) into transition probabilities was beyond the scope of this first simple estimation.

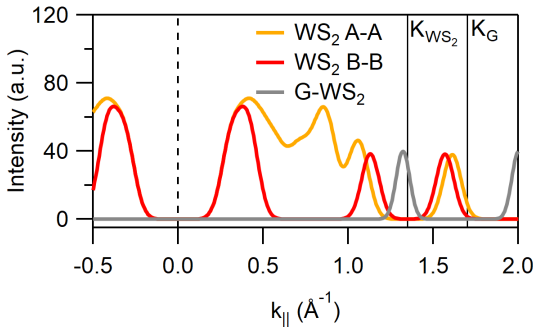

Figure A.11: Possible direct transitions into WS_2 conduction band: Transition probability as a function of momentum for spin allowed transitions (A-A and B-B) within WS_2 and direct transitions from graphene to WS_2. The probabilities are not normalized.

Appendix B

Additional Tr-ARPES Data

B.1 Photocarrier Dynamics of Quasi Freestanding Monolayer Graphene

In Fig. B.1 we present tr-ARPES results for quasi freestanding monolayer graphene (QFMLG, graphene/H-SiC(0001)) without WS_2 on top for similar pump excitation conditions as the ones for the measurements on the WS_2/graphene/H-SiC(0001) heterostructure in section 3.3 and chapter 4. Fig. B.1a and b show tr-ARPES snapshot at negative pump-probe delay and difference plot at peak of the pump-probe signal, respectively. Fig. B.1c shows extracted graphene gain and loss traces as a function of pump-probe delay.
This gain-and-loss signal has symmetric time constants in contrast to the WS_2/QFMLG heterostructure (cf. section 3.3 and chapter 4).

B.2 Comparison of VB Shifts with Integrated Photocurrent Above the Equilibrium Position of the Valence Band

In Fig B.2 we show that the gain above the equilibrium position of the upper WS_2 VB from Fig. B.3c and the WS_2 charging shift from Fig. B.4e exhibit the same fluence dependence. Hence, the lifetime of the gain above the equilibrium position of the upper WS_2 VB is a measure for the lifetime of the charge separated state.

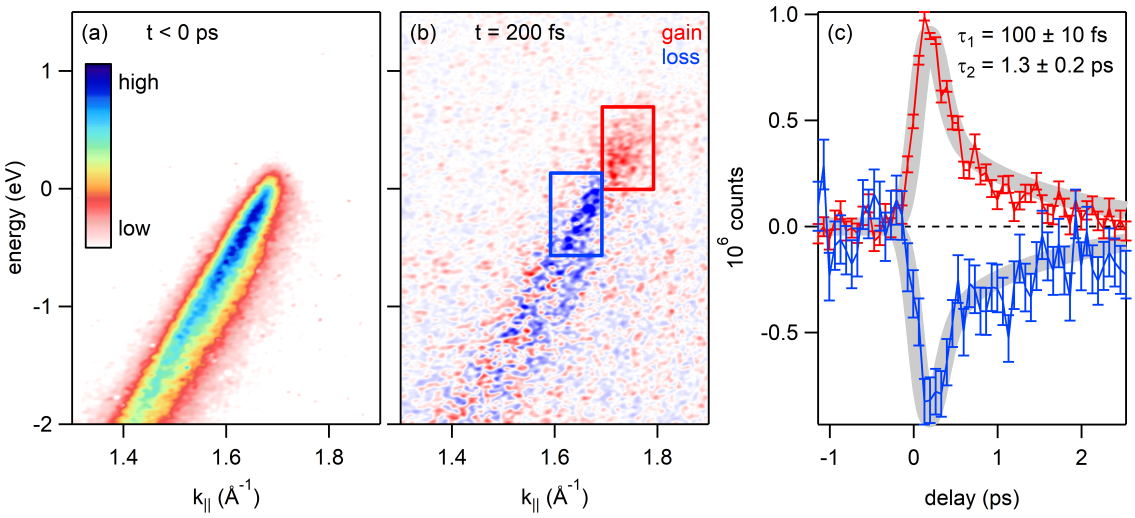

Figure B.1: Photo-carrier dynamics in graphene/H-SiC(0001). (a) Photocurrent along the ΓK-direction for negative pump-probe delay. (b) Pump-induced changes of the photocurrent 200 fs after photo-excitation at a pump photon energy of 2 eV with a pump fluence of 2 mJ/cm^2. Gain and loss of photoelectrons are shown in red and blue, respectively. (c) Pump-probe traces as a function of delay obtained by integrating the photocurrent over the area indicated by the red and blue boxes in panel (b). Thick gray lines are double-exponential fits to the data.

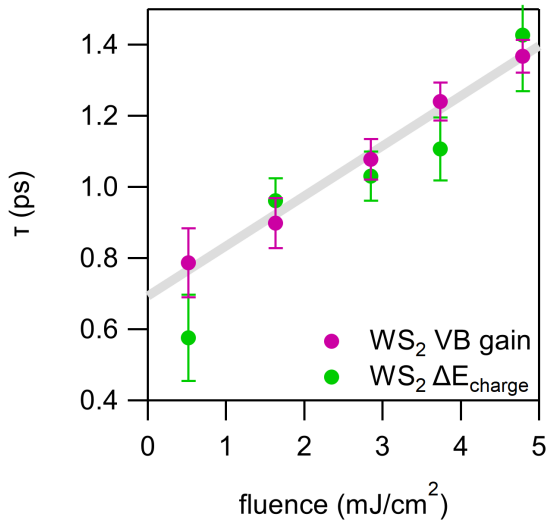

Figure B.2: Direct comparison of fluence dependence of gain above equilibrium position of upper WS_2 VB (purple) and WS_2 charging shift (green).

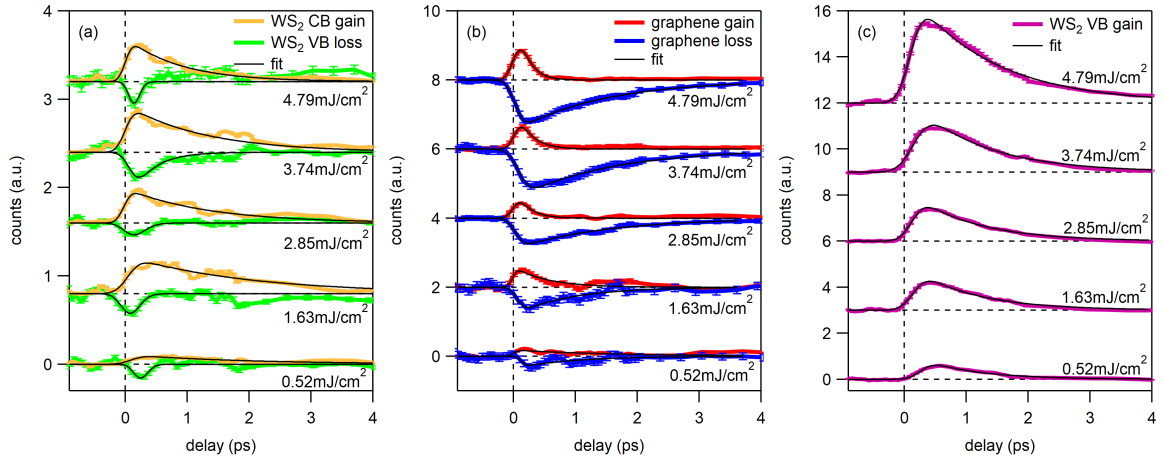

Figure B.3: Fluence dependence of the population dynamics: (a) Gain in the CB (orange) and loss in the VB (green) of WS_2. (b) Graphene dynamics: Gain above the Fermi level (red) and loss below the Fermi level (blue). (c) Gain above the equilibrium position of the upper WS_2 VB. Thin black lines are single exponential fits to the data.

B.3 Additional Tr-ARPES Data for Other Pump Fluences

The fluence dependent data corresponding to Fig. 4.2, 4.3 and 4.4 is shown in Figs. B.3, B.4 and B.5, respectively. The fluence dependence of various parameters at the peak of the pump-probe signal is summarized in the main text in Fig. 4.5.

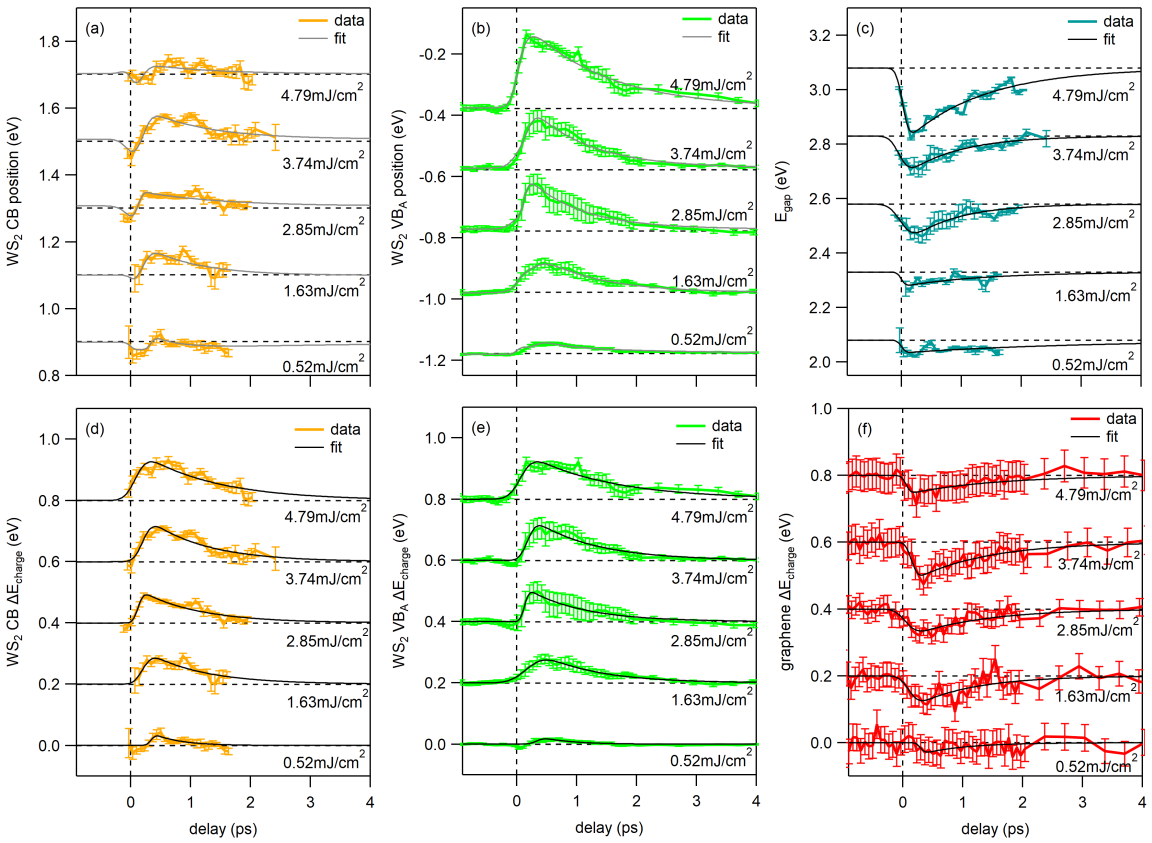

Figure B.4: Fluence dependence of the transient band positions: (a) Position of the WS_2 CB. (b) Position of the WS_2 VB. (c) Transient band gap of WS_2. (d) Shift of the WS_2 CB due to charging of the WS_2 layer. (e) Shift of the upper WS_2 VB due to charging of the WS_2 layer. (f) Shift of the Dirac cone.

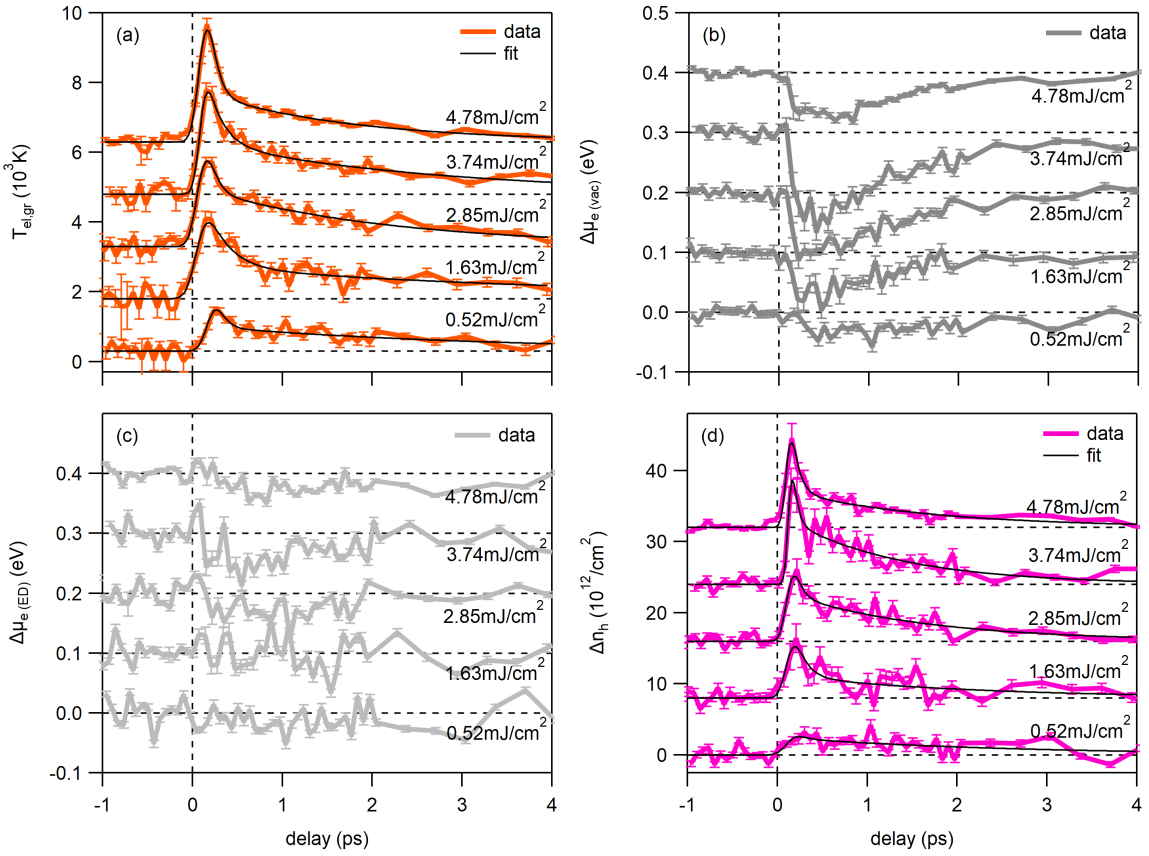

Figure B.5: Fluence dependence of hot carrier dynamics in graphene: (a) Electronic temperature, (b) chemical potential referenced with respect to the vacuum level, (c) chemical potential referenced with respect to the Dirac point, and (d) number of holes transferred from WS_2 to graphene as a function of pump-probe delay for different pump fluences.

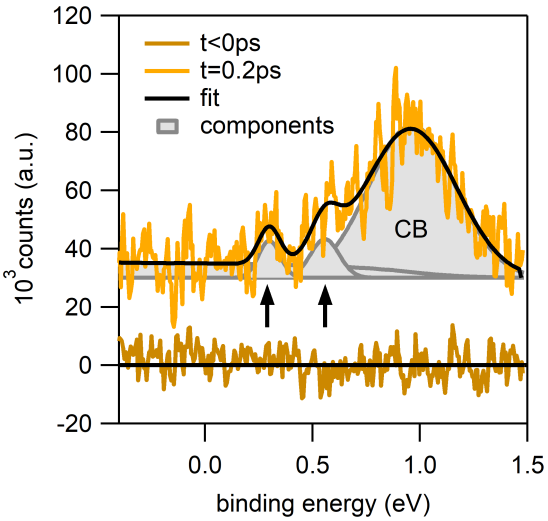

Figure B.6: Evidence for in-gap defect states. EDCs through the K-point of WS_2 in the conduction band region at negative delay and at the peak of the pump-probe signal at $t = 0.2\,\mathrm{ps}$. Gray lines indicate the Gaussian peaks used to fit the spectrum at $t = 0.2\,\mathrm{ps}$. The two Gaussians marked with black arrows are attributed to in-gap defect states due to Sulfur vacancies.

B.4 Evidence for In-Gap Defect States

In Fig. B.6 we show an energy distribution curve through the K-point of WS_2 in the energy region of the conduction band. At negative delay the WS_2 conduction band is unoccupied. At $t = 0.2\,\mathrm{ps}$ we observe a pronounced Gaussian peak at $E = 0.96\,\mathrm{eV}$ for the transiently populated WS_2 conduction band, as well as two other smaller Gaussians at $E = 0.29\,\mathrm{eV}$ and $E = 0.54\,\mathrm{eV}$ that we attribute to Sulfur vacancies in good agreement with scanning tunneling spectroscopy data in Ref. [173].

B.5 Momentum Dependent Valence Band Shifts

In Fig. 7.2 only fits of selected energy distribution curves at Γ, Σ and K were shown together with the correspnding valence band shift at that points. For the sake of completeness, we plot fits of all energy distribution curves along the Brillouin zone and the resulting shift of the valence band in Fig. B.7. This Data is shown for excitation densitites $\sim 4{\cdot}10^{12}\mathrm{cm}^{-2}$ (3.1 eV) in Panel (a) and (b) and for $\sim 3{\cdot}10^{13}\mathrm{cm}^{-2}$ (2 eV) in Panel (c) and (d). From these VB shifts the amplitude was displayed as a function of momentum in Fig. 7.3 and discussed in the main text.

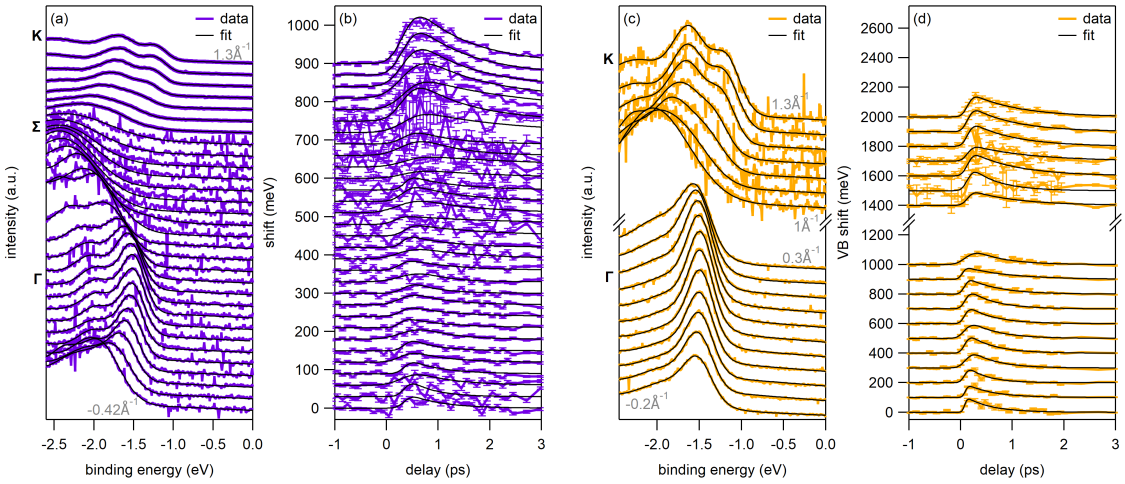

Figure B.7: Valence band fits and shifts for the whole measurement range: (a) and (b) Equilibrium energy distributon curves for datasets with an excitation density of $\sim 4{\cdot}10^{12}\mathrm{cm}^{-2}$ (3.1 eV) and corresponding transient valence band shift, respectively. (c) and (d) Equilibrium energy distributon curves for datasets with an excitation density of $\sim 3{\cdot}10^{13}\mathrm{cm}^{-2}$ (2 eV) and corresponding transient valence band shift, respectively. Black lines are fits to data. Please note the different VB shift axis scaling in (b) and (d).

Appendix C

Many-Body Theory

C.1 Microscopic Model of Charge Transfer

In the second quantization formalism, the Hamilton operator describing electron tunneling from one layer (l) to another ($\bar{l}$) is

$$H_T = \sum_{l\lambda \boldsymbol{kq}} T^{\lambda l\bar{l}}_{\boldsymbol{kq}} a^{\dagger}_{\lambda,\bar{l},\boldsymbol{k}+\boldsymbol{q}} a_{\lambda,l,\boldsymbol{k}}, \tag{C.1}$$

where $\lambda = v, c$ is the valence/conduction band, $\boldsymbol{k}$ the momentum of the initial state and $\boldsymbol{q}$ the momentum transfer of the process. The tunneling matrix element reads $T^{\lambda l\bar{l}}_{\boldsymbol{kq}} = \langle \bar{l}, \lambda, \boldsymbol{k}+\boldsymbol{q}|V_T|l, \lambda, \boldsymbol{k}\rangle$ with the tunneling potential $V_T = V_l + V_{\bar{l}}$ being the sum of the potential of each layer. In order to find an expression for $T^{\lambda,\mathrm{WS_2}\to\mathrm{g}}_{\boldsymbol{kq}}$, we use a tight-binding approach to describe the electronic wavefunctions in graphene and WS_2 [216]

$$\psi^{\mathrm{g}}_{\lambda\boldsymbol{k}}(\boldsymbol{r}) = \frac{1}{\sqrt{N_{\mathrm{g}}}} \sum_{j=A,B} c^{j}_{\lambda\boldsymbol{k}} \sum_{\boldsymbol{R}_j} \mathrm{e}^{i\boldsymbol{k}\cdot\boldsymbol{R}_j} \phi^{\mathrm{g}}_{\lambda}(\boldsymbol{r}-\boldsymbol{R}_j), \tag{C.2}$$

$$\psi^{\mathrm{WS_2}}_{\lambda\boldsymbol{k}}(\boldsymbol{r}) = \frac{1}{\sqrt{N_{\mathrm{WS_2}}}} \sum_{\boldsymbol{R}_{\mathrm{W}}} \mathrm{e}^{i\boldsymbol{k}\cdot\boldsymbol{R}_{\mathrm{W}}} \phi^{\mathrm{WS_2}}_{\lambda}(\boldsymbol{r}-\boldsymbol{R}_{\mathrm{W}}). \tag{C.3}$$

Here N_l is the number of unit cells in layer l, $c^{j}_{\lambda\boldsymbol{k}}$ are graphene's tight-binding coefficients, $\boldsymbol{R}_j$ are the atomic positions, and $\phi^{l}_{\lambda}(\boldsymbol{r})$ is the linear combination of atomic orbitals contributing to the band λ. Graphene's tight binding coefficients around the $\boldsymbol{K}$ point read $c^{A}_{\lambda\boldsymbol{k}} = \frac{1}{\sqrt{2}}$ and $c^{B}_{\lambda\boldsymbol{k}} = \frac{1}{\sqrt{2}}\sigma_{\lambda}\mathrm{e}^{i\theta_{\boldsymbol{k}-\boldsymbol{K}_{\mathrm{g}}}}$, where $\theta_{\boldsymbol{k}-\boldsymbol{K}_{\mathrm{g}}}$ is the angle of $\boldsymbol{k}$ with respect to graphene's $\boldsymbol{K}$ point. While for graphene the wavefunction has contributions from A and B lattice points, in semiconducting TMDs the main orbital contributions come from the

metal atoms [180,217]. Introducing the respective electronic wavefunctions, the tunneling matrix element reads

$$\begin{aligned} T_{\boldsymbol{kq}}^{\lambda,\mathrm{WS}_2\to\mathrm{g}} &= \int d^3\boldsymbol{r}\left[\psi_{\lambda\boldsymbol{k}+\boldsymbol{q}}^{\mathrm{g}}(\boldsymbol{r})\right]^* V_T(\boldsymbol{r})\psi_{\lambda\boldsymbol{k}}^{\mathrm{WS}_2}(\boldsymbol{r}) \\ &= \frac{1}{\sqrt{N_g N_{\mathrm{WS}_2}}}\sum_{j\boldsymbol{R}_j\boldsymbol{R}_{\mathrm{W}}}\left(c_{\lambda\boldsymbol{k}+\boldsymbol{q}}^{j}\right)^* \mathrm{e}^{-i(\boldsymbol{k}+\boldsymbol{q})\cdot\boldsymbol{R}_j}\mathrm{e}^{i\boldsymbol{k}\cdot\boldsymbol{R}_{\mathrm{W}}} \\ &\quad\times\int d^3\boldsymbol{r}\left[\phi_{\lambda}^{\mathrm{g}}(\boldsymbol{r}-\boldsymbol{R}_j)\right]^* V_T(\boldsymbol{r})\phi_{\lambda}^{\mathrm{WS}_2}(\boldsymbol{r}-\boldsymbol{R}_{\mathrm{W}}) \end{aligned} \tag{C.4}$$

Using $V_T = V_l + V_{\bar{l}}$ and the periodicity of V_l in the lattice of l and writing the orbital wave functions in terms of their in-plane Fourier transform, $\phi(\boldsymbol{r}) = \frac{1}{A}\sum_{\boldsymbol{p}}\mathrm{e}^{i\boldsymbol{p}\cdot\boldsymbol{r}_\parallel}\phi_{\boldsymbol{p}}(z)$, we can define a tunneling parameter $h_{\lambda\boldsymbol{p}}$ that contains the overlap between the orbital wave functions and the tunneling potential. The tunneling matrix element now reads

$$T_{\boldsymbol{kq}}^{\lambda,\mathrm{WS}_2\to\mathrm{g}} = \frac{1}{N_g N_{\mathrm{WS}_2}}\sum_{j\boldsymbol{R}_j\boldsymbol{R}_{\mathrm{W}}\boldsymbol{p}}\left(c_{\lambda\boldsymbol{k}+\boldsymbol{q}}^{j}\right)^* \mathrm{e}^{-i(\boldsymbol{k}+\boldsymbol{q}-\boldsymbol{p})\cdot\boldsymbol{R}_j}\mathrm{e}^{i(\boldsymbol{k}-\boldsymbol{p})\cdot\boldsymbol{R}_{\mathrm{W}}}h_{\lambda\boldsymbol{p}}, \tag{C.5}$$

with the tunneling parameter

$$h_{\lambda\boldsymbol{p}} = t_{\lambda\boldsymbol{p}}^{\mathrm{WS}_2,\mathrm{g}} + \left(t_{\lambda\boldsymbol{p}}^{\mathrm{g},\mathrm{WS}_2}\right)^*, \qquad t_{\lambda\boldsymbol{p}}^{l\bar{l}} = \frac{1}{\sqrt{N_g N_{\mathrm{WS}_2}}}\int d^3\boldsymbol{r}\mathrm{e}^{i\boldsymbol{p}\cdot\boldsymbol{r}_\parallel}\left[\phi_{\lambda\boldsymbol{p}}^{\bar{l}}(z)\right]^* V_l(\boldsymbol{r})\phi_{\lambda}^{l}(\boldsymbol{r}) \tag{C.6}$$

We perform the summation over the lattice points of each layer using $\frac{1}{N_l}\sum_{\boldsymbol{R}_{lj}}\mathrm{e}^{i\boldsymbol{k}\cdot\boldsymbol{R}_{lj}} = \sum_{G_l}\mathrm{e}^{i\boldsymbol{G}_l\cdot\boldsymbol{\delta}_{jl}}\delta_{\boldsymbol{k},\boldsymbol{G}_l}$ and determine the allowed momentum exchange $\delta_{\boldsymbol{q},\boldsymbol{G}_{\mathrm{g}}-\boldsymbol{G}_{\mathrm{WS}_2}}$, where $\boldsymbol{G}_l$ is the reciprocal lattice vector of the layer l. The lattice offsets $\boldsymbol{\delta}_{jl}$ are defined as $\boldsymbol{\delta}_A = -\boldsymbol{\delta}_{\mathrm{W}} = \frac{1}{2}\boldsymbol{R}_A^0$ and $\boldsymbol{\delta}_A = \frac{1}{2}\boldsymbol{R}_A^0 + \boldsymbol{\tau}_{AB} = \frac{1}{2}\boldsymbol{R}_B^0$, with $\boldsymbol{\tau}_{AB}$ being a vector from an A lattice point to a nearest neighbor B. This yields

$$T_{\boldsymbol{kq}}^{\lambda,\mathrm{WS}_2\to\mathrm{g}} = \sum_{j\boldsymbol{G}_{\mathrm{g}}\boldsymbol{G}_{\mathrm{WS}_2}}\left(c_{\lambda,\boldsymbol{k}+\boldsymbol{q}}^{j}\right)^* \mathrm{e}^{i\frac{1}{2}(\boldsymbol{G}_{\mathrm{g}}\cdot\boldsymbol{R}_j^0+\boldsymbol{G}_{\mathrm{WS}_2}\cdot\boldsymbol{R}_A^0)}h_{\lambda,\boldsymbol{k}+\boldsymbol{G}_{\mathrm{WS}_2}}\delta_{\boldsymbol{q},\boldsymbol{G}_{\mathrm{g}}-\boldsymbol{G}_{\mathrm{WS}_2}}. \tag{C.7}$$

In a practical scenario, the initial momentum $\boldsymbol{k}$ will lie in the vicinity of $\boldsymbol{K}_{\mathrm{WS}_2}$. Assuming that the tunneling parameter decays quickly with momentum, the significant reciprocal lattice vectors will be those connecting two K points of the Brillouin zone, i.e. $\boldsymbol{K}_l + \boldsymbol{G}_l = C_3^n\boldsymbol{K}_l$. Hence we can reduce the allowed scattering transitions to $\delta_{\boldsymbol{q},C_3^n\Delta K-\Delta K}$. Finally, the rotational symmetry of the orbitals yields $h_{\lambda,C_3^nK_{\mathrm{WS}_2}} = h_{\lambda,K_{\mathrm{WS}_2}}\mathrm{e}^{i\varphi_n}$, with $\varphi_{\lambda,n} = \frac{2\pi}{3}n(M_\lambda^{\mathrm{WS}_2} - M_\lambda^{\mathrm{g}})$, where M_λ^l is the rotational quantum number. Defining the Moiré phase $\Phi_{j,n} = \frac{1}{2}(\boldsymbol{G}_{\mathrm{g}}\cdot\boldsymbol{R}_j^0 + \boldsymbol{G}_{\mathrm{WS}_2}\cdot\boldsymbol{R}_A^0)$, the tunneling matrix element now reads

$$T_{\boldsymbol{kq}}^{\lambda,\mathrm{WS_2}\to\mathrm{g}} = \sum_{j,n=0}^{2} \left(c_{\lambda,\boldsymbol{k}+\boldsymbol{q}}^{j}\right)^{*} \mathrm{e}^{i\Phi_{j,n}} \mathrm{e}^{i\varphi_{\lambda,n}} h_{\lambda,\boldsymbol{K}_{\mathrm{WS_2}}} \delta_{\boldsymbol{q},C_3^n\Delta K-\Delta K}. \tag{C.8}$$

Now we choose the offset $\boldsymbol{R}_A^0 = 0$, resulting in $\Phi_{A,n} = 0$, $\Phi_{B,n} = -\frac{2\pi}{3}n$. Introducing graphene's tight-binding coefficients, we obtain

$$T_{\boldsymbol{kq}}^{\lambda,\mathrm{WS_2}\to\mathrm{g}} = \sum_{n=0}^{2} \left(1 + \sigma_\lambda \mathrm{e}^{i\theta_{\boldsymbol{k}+\boldsymbol{q}-\boldsymbol{K}_\mathrm{g}}} \mathrm{e}^{-i\frac{2\pi}{3}n}\right) \mathrm{e}^{i\varphi_{\lambda,n}} h_{\lambda,\boldsymbol{K}_{\mathrm{WS_2}}} \delta_{\boldsymbol{q},C_3^n\Delta K-\Delta K}. \tag{C.9}$$

Finally, we are interested in the squared absolute value of the tunneling matrix element. Note that the condition $\boldsymbol{q} = C_3^n\Delta K - \Delta K$ cannot be fulfilled by more than one n-value simultaneously. Hence the phase $\varphi_{\lambda,n}$ will in fact be a global phase which cancels out when computing the absolute value. Thus, we can write our final expression for the tunneling matrix element as

$$|T_{\boldsymbol{kq}}^{\lambda,\mathrm{WS_2}\to\mathrm{g}}|^2 = \sum_{n=0}^{2} |h_{\lambda,\boldsymbol{K}_{\mathrm{WS_2}}}|^2 \left[1 + \sigma_\lambda \cos\left(\theta_{\boldsymbol{k}-\boldsymbol{K}_\mathrm{g}+\boldsymbol{q}} - \frac{2\pi}{3}n\right)\right] \delta_{\boldsymbol{q},C_3^n\Delta K-\Delta K}. \tag{C.10}$$

Here $\sigma_\lambda = \pm 1$ for the conduction $(+)$ and the valence $(-)$ bands, $\theta_{\boldsymbol{k}-\boldsymbol{K}_\mathrm{g}+\boldsymbol{q}}$ is the angle of $\boldsymbol{k}+\boldsymbol{q}$ with respect to the closest graphene $\boldsymbol{K}_\mathrm{g}$ point, $\Delta K = K_\mathrm{g} - K_{\mathrm{WS_2}}$ is the momentum difference between graphene's and WS_2's K points, C_3^n is a $2\pi/3$ rotation operator, and h_λ contains the overlap of the wavefunctions with the tunneling potential. From this expression we obtain the behaviour shown in Fig. 5a-b, i.e. the tunneling is efficient for holes but suppressed for electrons. This effect, together with the cosine dependence, is a manifestation of graphene's pseudospin.

In order to calculate tunneling rates, we insert the tunneling Hamilton operator in the Heisenberg's equation together with the carrier occupation $\rho_{\lambda\boldsymbol{k}}^{l}$ in the density matrix formalism [52]. Within a second-order Born-Markov approximation [218], we find the following Boltzmann-like equation:

$$\dot{\rho}_{\lambda\boldsymbol{k}}^{l} = \frac{2\pi}{\hbar} \sum_{\boldsymbol{q}} |T_{\boldsymbol{kq}}^{\lambda l\bar{l}}|^2 \left[\rho_{\lambda,\boldsymbol{k}+\boldsymbol{q}}^{\bar{l}}(1-\rho_{\lambda,\boldsymbol{k}}^{l}) - \rho_{\lambda,\boldsymbol{k}}^{l}(1-\rho_{\lambda,\boldsymbol{k}+\boldsymbol{q}}^{\bar{l}})\right] \delta(\varepsilon_{\lambda,\boldsymbol{k}}^{l} - \varepsilon_{\lambda,\boldsymbol{k}+\boldsymbol{q}}^{\bar{l}}). \tag{C.11}$$

We approximate the carrier distribution in the conduction band in WS_2 with a Boltzmann distribution. Integrating over momentum leads to a rate equation for the carrier density. We thus find that the carrier density that tunnels from WS_2 to graphene follows

$$\dot{n}_\lambda^{\mathrm{WS_2}}\big|_{\mathrm{WS_2}\to\mathrm{g}} = -\tau_\lambda^{-1} n_\lambda^{\mathrm{WS_2}}, \tag{C.12}$$

where

$$\tau_\lambda^{-1} = \frac{2\pi}{\hbar A n_\lambda^{\mathrm{WS}_2}} \sum_{\boldsymbol{kq}} |T_{\boldsymbol{kq}}^{\lambda l \bar{l}}|^2 \rho_{\lambda,\boldsymbol{k}}^{\mathrm{WS}_2} (1 - \rho_{\lambda,\boldsymbol{k}+\boldsymbol{q}}^{\mathrm{g}}) \delta(\varepsilon_{\lambda,\boldsymbol{k}}^{\mathrm{WS}_2} - \varepsilon_{\lambda,\boldsymbol{k}+\boldsymbol{q}}^{\mathrm{g}}) \tag{C.13}$$

C.2 Screened Exchange in TMD Monolayers

As it might be in the interest of the reader we present here further results of the many-body GW calculations on the effect of internal dielectric screening onto WS_2 bands. The band structure at different excitation densities, displayed in Fig. C.1, can be controlled on purpose by variation of the excitation density or, in other words, the applied pump fluence. Panel (b) shows the band gap reduction at K as a function of excitation density. In Panels (c) to (f) we plot effective masses at points of interest within the Brillouin zone determined by fits of the band curvature. It can be seen that the effective masses for conduction and valence band at K decrease with excitation density, implying higher mobility in transport.

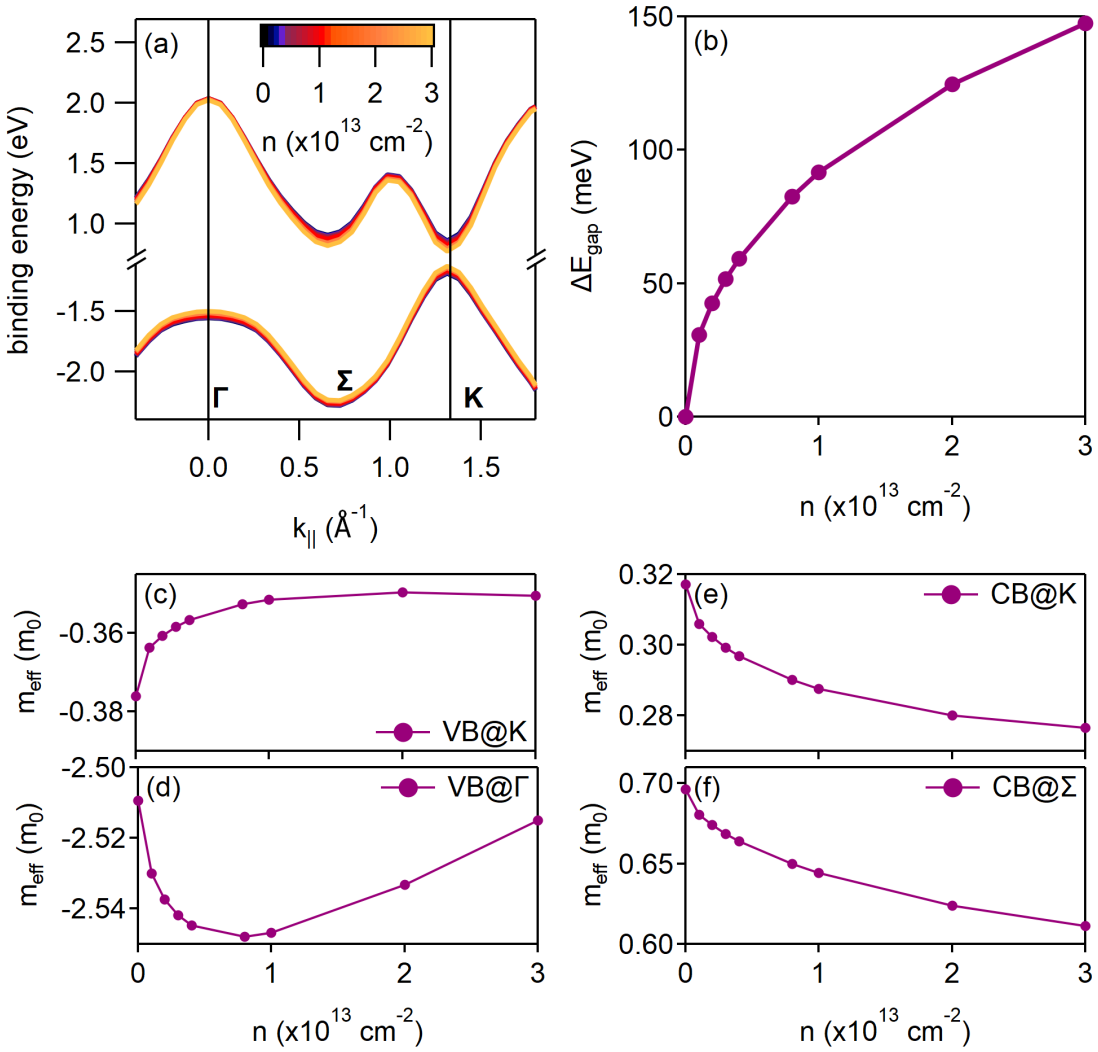

Figure C.1: Band structure engineering: (a) The non-equilibrium band structure of WS_2 displayed for different excitation densities as indexed by a color code. (b) Calculated change of the quasiparticle band gap with excitation density. (c)-(f) Change of effective masses with excitation density at certain positions in the Brillouin zone. The effective masses are displayed as multiples of the electrons rest mass m_0.

Bibliography

[1] S. Aeschlimann, A. Rossi, M. Chávez-Cervantes, R. Krause, B. Arnoldi, B. Stadtmüller, M. Aeschlimann, S. Forti, F. Fabbri, C. Coletti, and I. Gierz-Pehla, "Direct evidence for efficient ultrafast charge separation in epitaxial WS_2/graphene heterostructures," *Science Advances*, vol. 6, no. 20, p. eaay0761, 2020.

[2] R. Krause, S. Aeschlimann, M. Chavez-Cervantes, R. Perea-Causin, S. Brem, E. Malic, S. Forti, F. Fabbri, C. Coletti, and I. Gierz, "Microscopic understanding of ultrafast charge transfer in van-der-Waals heterostructures," *arXiv:2012.09268*, 2021.

[3] R. Krause, M. Chávez-Cervantes, S. Aeschlimann, S. Forti, F. Fabbri, A. Rossi, C. Coletti, C. Cacho, Y. Zhang, P. E. Majchrzak, R. T. Chapman, E. Springate, and I. Gierz, "Ultrafast charge separation in bilayer WS_2/graphene heterostructure revealed by time- and angle-resolved photoemission spectroscopy," *Frontiers in Physics*, vol. 9, apr 2021.

[4] R. Krause, S. Aeschlimann, M. Chávez-Cervantes, S. Forti, F. Fabbri, C. Coletti, and I. Gierz, "Intervalley scattering and ultrafast charge transfer in WS_2/graphene heterostructures," *manuscript in preparation*, 2021.

[5] R. Krause, A. Steinhoff, S. Aeschlimann, M. Chávez-Cervantes, T. O. Wehling, S. Refaely-Abramson, S. Forti, F. Fabbri, C. Coletti, and I. Gierz, "Momentum dependence of light-induced band gap renormalization in WS_2/graphene heterostructure," *manuscript in preparation*, 2021.

[6] S. Aeschlimann, S. A. Sato, R. Krause, M. Chávez-Cervantes, U. D. Giovannini, H. Hübener, S. Forti, C. Coletti, K. Hanff, K. Rossnagel, A. Rubio, and I. Gierz, "Survival of Floquet–Bloch states in the presence of scattering," *Nano Letters*, vol. 21, pp. 5028–5035, jun 2021.

[7] M. Chávez-Cervantes, G. Topp, S. Aeschlimann, R. Krause, S. Sato, M. Sentef, and I. Gierz, "Charge density wave melting in one-dimensional wires with femtosecond subgap excitation," *Physical Review Letters*, vol. 123, p. 036405, jul 2019.

[8] M. Chávez-Cervantes, R. Krause, S. Aeschlimann, and I. Gierz, "Band structure dynamics in indium wires," *Physical Review B*, vol. 97, p. 201401, may 2018.

[9] S. Aeschlimann, R. Krause, M. Chávez-Cervantes, H. Bromberger, R. Jago, E. Malić, A. Al-Temimy, C. Coletti, A. Cavalleri, and I. Gierz, "Ultrafast momentum imaging of pseudospin-flip excitations in graphene," *Physical Review B*, vol. 96, p. 020301, jul 2017.

[10] L. Carroll, *Alice's Adventures in Wonderland*. Macmillan & Co., 1865.

[11] S. K. Moore, "Another step toward the end of Moore's law: Samsung and TSMC move to 5-nanometer manufacturing - [news]," *IEEE Spectrum*, vol. 56, pp. 9–10, jun 2019.

[12] M.-Y. Li, S.-K. Su, H.-S. P. Wong, and L.-J. Li, "How 2D semiconductors could extend Moore's law," *Nature*, vol. 567, pp. 169–170, mar 2019.

[13] P. Ajayan, P. Kim, and K. Banerjee, "Two-dimensional van der Waals materials," *Physics Today*, vol. 69, pp. 38–44, sep 2016.

[14] A. K. Geim and I. V. Grigorieva, "Van der Waals heterostructures," *Nature*, vol. 499, no. 7459, pp. 419–425, 2013.

[15] K. S. Novoselov, A. Mishchenko, A. Carvalho, and A. H. C. Neto, "2D materials and van der Waals heterostructures," *Science*, vol. 353, p. aac9439, jul 2016.

[16] B. Radisavljevic and A. Kis, "Mobility engineering and a metal–insulator transition in monolayer MoS2," *Nature Materials*, vol. 12, pp. 815–820, jun 2013.

[17] F. Withers, O. D. Pozo-Zamudio, S. Schwarz, S. Dufferwiel, P. M. Walker, T. Godde, A. P. Rooney, A. Gholinia, C. R. Woods, P. Blake, S. J. Haigh, K. Watanabe, T. Taniguchi, I. L. Aleiner, A. K. Geim, V. I. Fal'ko, A. I. Tartakovskii, and K. S. Novoselov, "WSe_2 light-emitting tunneling transistors with enhanced brightness at room temperature," *Nano Letters*, vol. 15, pp. 8223–8228, nov 2015.

[18] B. Radisavljevic, M. B. Whitwick, and A. Kis, "Integrated circuits and logic operations based on single-layer MoS_2," *ACS Nano*, vol. 5, pp. 9934–9938, nov 2011.

[19] R. Cheng, D. Li, H. Zhou, C. Wang, A. Yin, S. Jiang, Y. Liu, Y. Chen, Y. Huang, and X. Duan, "Electroluminescence and photocurrent generation from atomically sharp WSe_2/MoS_2 heterojunction p–n diodes," *Nano Letters*, vol. 14, pp. 5590–5597, sep 2014.

[20] C.-H. Liu, G. Clark, T. Fryett, S. Wu, J. Zheng, F. Hatami, X. Xu, and A. Majumdar, "Nanocavity integrated van der Waals heterostructure light-emitting tunneling diode," *Nano Letters*, vol. 17, pp. 200–205, dec 2016.

[21] M. Massicotte, P. Schmidt, F. Vialla, K. G. Schädler, A. Reserbat-Plantey, K. Watanabe, T. Taniguchi, K. J. Tielrooij, and F. H. L. Koppens, "Picosecond photoresponse in van der Waals heterostructures," *Nature Nanotechnology*, vol. 11, pp. 42–46, oct 2015.

[22] M. Fontana, T. Deppe, A. K. Boyd, M. Rinzan, A. Y. Liu, M. Paranjape, and P. Barbara, "Electron-hole transport and photovoltaic effect in gated MoS2 schottky junctions," *Scientific Reports*, vol. 3, apr 2013.

[23] M. Bernardi, M. Palummo, and J. C. Grossman, "Extraordinary sunlight absorption and one nanometer thick photovoltaics using two-dimensional monolayer materials," *Nano Letters*, vol. 13, pp. 3664–3670, jul 2013.

[24] J. Wong, D. Jariwala, G. Tagliabue, K. Tat, A. R. Davoyan, M. C. Sherrott, and H. A. Atwater, "High photovoltaic quantum efficiency in ultrathin van der Waals heterostructures," *ACS Nano*, vol. 11, pp. 7230–7240, jun 2017.

[25] Y. Zhou, H. Tan, Y. Sheng, Y. Fan, W. Xu, and J. H. Warner, "Utilizing interlayer excitons in bilayer WS_2 for increased photovoltaic response in ultrathin graphene vertical cross-bar photodetecting tunneling transistors," *ACS Nano*, vol. 12, pp. 4669–4677, apr 2018.

[26] Y. Xu, H. Bai, G. Lu, C. Li, and G. Shi, "Flexible graphene films via the filtration of water-soluble noncovalent functionalized graphene sheets," *Journal of the American Chemical Society*, vol. 130, pp. 5856–5857, may 2008.

[27] A. C. Ferrari, F. Bonaccorso, V. Fal'ko, K. S. Novoselov, S. Roche, P. Bøggild, S. Borini, F. H. L. Koppens, V. Palermo, N. Pugno, J. A. Garrido, R. Sordan, A. Bianco, L. Ballerini, M. Prato, E. Lidorikis, J. Kivioja, C. Marinelli, T. Ryhänen, A. Morpurgo, J. N. Coleman, V. Nicolosi, L. Colombo, A. Fert, M. Garcia-Hernandez, A. Bachtold, G. F. Schneider, F. Guinea, C. Dekker, M. Barbone, Z. Sun, C. Galiotis, A. N. Grigorenko, G. Konstantatos, A. Kis, M. Katsnelson, L. Vandersypen, A. Loiseau, V. Morandi, D. Neumaier, E. Treossi, V. Pellegrini, M. Polini, A. Tredicucci, G. M. Williams, B. H. Hong, J.-H. Ahn, J. M. Kim, H. Zirath, B. J. van Wees, H. van der Zant, L. Occhipinti, A. D. Matteo, I. A. Kinloch, T. Seyller, E. Quesnel, X. Feng, K. Teo, N. Rupesinghe, P. Hakonen, S. R. T. Neil, Q. Tannock, T. Löfwander, and J. Kinaret, "Science and technology roadmap for graphene, related two-dimensional crystals, and hybrid systems," *Nanoscale*, vol. 7, no. 11, pp. 4598–4810, 2015.

[28] A. S. Mayorov, R. V. Gorbachev, S. V. Morozov, L. Britnell, R. Jalil, L. A. Ponomarenko, P. Blake, K. S. Novoselov, K. Watanabe, T. Taniguchi, and A. K. Geim, "Micrometer-scale ballistic transport in encapsulated graphene at room temperature," *Nano Letters*, vol. 11, pp. 2396–2399, jun 2011.

[29] A. H. Castro-Neto, F. Guinea, N. M. R. Peres, K. S. Novoselov, and A. K. Geim, "The electronic properties of graphene," *Reviews of Modern Physics*, vol. 81, pp. 109–162, jan 2009.

[30] G. Wang, A. Chernikov, M. M. Glazov, T. F. Heinz, X. Marie, T. Amand, and B. Urbaszek, "Colloquium: Excitons in atomically thin transition metal dichalcogenides," *Reviews of Modern Physics*, vol. 90, no. 2, p. 021001, 2018.

[31] D. Kozawa, R. Kumar, A. Carvalho, K. K. Amara, W. Zhao, S. Wang, M. Toh, R. M. Ribeiro, A. H. C. Neto, K. Matsuda, and G. Eda, "Photocarrier relaxation pathway in two-dimensional semiconducting transition metal dichalcogenides," *Nature Communications*, vol. 5, p. 4543, jul 2014.

[32] W. Zhao, Z. Ghorannevis, L. Chu, M. Toh, C. Kloc, P.-H. Tan, and G. Eda, "Evolution of electronic structure in atomically thin sheets of WS_2 and WSe_2," *ACS Nano*, vol. 7, pp. 791–797, dec 2012.

[33] B. Zhu, X. Chen, and X. Cui, "Exciton binding energy of monolayer WS_2," *Scientific Reports*, vol. 5, mar 2015.

[34] J. He, N. Kumar, M. Z. Bellus, H.-Y. Chiu, D. He, Y. Wang, and H. Zhao, "Electron transfer and coupling in graphene-tungsten disulfide van der Waals heterostructures," *Nature communications*, vol. 5, no. 1, pp. 1–5, 2014.

[35] N. Huo, Z. Wei, X. Meng, J. Kang, F. Wu, S.-S. Li, S.-H. Wei, and J. Li, "Interlayer coupling and optoelectronic properties of ultrathin two-dimensional heterostructures based on graphene, MoS_2 and WS_2," *Journal of Materials Chemistry C*, vol. 3, no. 21, pp. 5467–5473, 2015.

[36] H. M. Hill, A. F. Rigosi, A. Raja, A. Chernikov, C. Roquelet, and T. F. Heinz, "Exciton broadening in WS_2/graphene heterostructures," *Physical Review B*, vol. 96, nov 2017.

[37] L. Yuan, T.-F. Chung, A. Kuc, Y. Wan, Y. Xu, Y. P. Chen, T. Heine, and L. Huang, "Photocarrier generation from interlayer charge-transfer transitions in WS_2 -graphene heterostructures," *Science Advances*, vol. 4, p. e1700324, feb 2018.

[38] J. He, D. He, Y. Wang, and H. Zhao, "Probing effect of electric field on photocarrier transfer in graphene-WS_2 van der Waals heterostructures," *Optics express*, vol. 25, no. 3, pp. 1949–1957, 2017.

[39] Z. Song, H. Zhu, W. Shi, D. Sun, and S. Ruan, "Ultrafast charge transfer in graphene-WS_2 Van der Waals heterostructures," *Optik*, vol. 174, pp. 62–67, 2018.

[40] M. Gmitra and J. Fabian, "Graphene on transition-metal dichalcogenides: A platform for proximity spin-orbit physics and optospintronics," *Physical Review B*, vol. 92, oct 2015.

[41] Y. K. Luo, J. Xu, T. Zhu, G. Wu, E. J. McCormick, W. Zhan, M. R. Neupane, and R. K. Kawakami, "Opto-valleytronic spin injection in monolayer MoS_2/few-layer graphene hybrid spin valves," *Nano Letters*, vol. 17, pp. 3877–3883, may 2017.

[42] A. Avsar, D. Unuchek, J. Liu, O. L. Sanchez, K. Watanabe, T. Taniguchi, B. Özyilmaz, and A. Kis, "Optospintronics in graphene via proximity coupling," *ACS Nano*, vol. 11, pp. 11678–11686, nov 2017.

[43] T. Ihn, *Semiconductor Nanostructures: Quantum states and electronic transport*. Oxford university press, 2010.

[44] K. v. Klitzing, G. Dorda, and M. Pepper, "New method for high-accuracy determination of the fine-structure constant based on quantized Hall resistance," *Physical Review Letters*, vol. 45, pp. 494–497, aug 1980.

[45] K. S. Novoselov, A. K. Geim, S. V. Morozov, D. Jiang, M. I. Katsnelson, I. V. Grigorieva, S. V. Dubonos, and A. A. Firsov, "Two-dimensional gas of massless Dirac fermions in graphene," *Nature*, vol. 438, pp. 197–200, nov 2005.

[46] K. S. Novoselov, "Electric field effect in atomically thin carbon films," *Science*, vol. 306, pp. 666–669, oct 2004.

[47] A. K. Geim and K. S. Novoselov, "The rise of graphene," *Nature Materials*, vol. 6, pp. 183–191, mar 2007.

[48] G. Rius and P. Godignon, *Epitaxial Graphene on Silicon Carbide: Modeling, Characterization, and Applications*. CRC Press, 2018.

[49] A. Kuc, T. Heine, and A. Kis, "Electronic properties of transition-metal dichalcogenides," *MRS Bulletin*, vol. 40, pp. 577–584, jul 2015.

[50] C. Lee, X. Wei, J. W. Kysar, and J. Hone, "Measurement of the elastic properties and intrinsic strength of monolayer graphene," *Science*, vol. 321, pp. 385–388, jul 2008.

[51] P. R. Wallace, "The band theory of graphite," *Physical review*, vol. 71, no. 9, p. 622, 1947.

[52] E. Malic, T. Winzer, E. Bobkin, and A. Knorr, "Microscopic theory of absorption and ultrafast many-particle kinetics in graphene," *Physical Review B*, vol. 84, p. 205406, nov 2011.

[53] Y. Ren, Z. Qiao, and Q. Niu, "Topological phases in two-dimensional materials: a review," *Reports on Progress in Physics*, vol. 79, p. 066501, may 2016.

[54] W. Han, R. K. Kawakami, M. Gmitra, and J. Fabian, "Graphene spintronics," *Nature Nanotechnology*, vol. 9, pp. 794–807, oct 2014.

[55] M. Gmitra, S. Konschuh, C. Ertler, C. Ambrosch-Draxl, and J. Fabian, "Band-structure topologies of graphene: Spin-orbit coupling effects from first principles," *Physical Review B*, vol. 80, p. 235431, dec 2009.

[56] J. Ingla-Aynés, M. H. D. Guimarães, R. J. Meijerink, P. J. Zomer, and B. J. van Wees, "24-μm spin relaxation length in boron nitride encapsulated bilayer graphene," *Physical Review B*, vol. 92, p. 201410, nov 2015.

[57] M. Drögeler, C. Franzen, F. Volmer, T. Pohlmann, L. Banszerus, M. Wolter, K. Watanabe, T. Taniguchi, C. Stampfer, and B. Beschoten, "Spin lifetimes exceeding 12 ns in graphene nonlocal spin valve devices," *Nano Letters*, vol. 16, pp. 3533–3539, may 2016.

[58] N. Huo, Y. Yang, and J. Li, "Optoelectronics based on 2D TMDs and heterostructures," *Journal of Semiconductors*, vol. 38, p. 031002, mar 2017.

[59] B. W. H. Baugher, H. O. H. Churchill, Y. Yang, and P. Jarillo-Herrero, "Optoelectronic devices based on electrically tunable p–n diodes in a monolayer dichalcogenide," *Nature Nanotechnology*, vol. 9, pp. 262–267, mar 2014.

[60] W. Ho, J. C. Yu, J. Lin, J. Yu, and P. Li, "Preparation and photocatalytic behavior of MoS_2 and WS_2 nanocluster sensitized TiO_2," *Langmuir*, vol. 20, pp. 5865–5869, jun 2004.

[61] S. Wu, S. Buckley, J. R. Schaibley, L. Feng, J. Yan, D. G. Mandrus, F. Hatami, W. Yao, J. Vučković, A. Majumdar, and X. Xu, "Monolayer semiconductor nanocavity lasers with ultralow thresholds," *Nature*, vol. 520, pp. 69–72, mar 2015.

[62] Y. Ye, Z. J. Wong, X. Lu, X. Ni, H. Zhu, X. Chen, Y. Wang, and X. Zhang, "Monolayer excitonic laser," *Nature Photonics*, vol. 9, pp. 733–737, oct 2015.

[63] O. Salehzadeh, M. Djavid, N. H. Tran, I. Shih, and Z. Mi, "Optically pumped two-dimensional MoS_2 lasers operating at room-temperature," *Nano Letters*, vol. 15, pp. 5302–5306, jul 2015.

[64] Y. Li, J. Zhang, D. Huang, H. Sun, F. Fan, J. Feng, Z. Wang, and C. Z. Ning, "Room-temperature continuous-wave lasing from monolayer molybdenum ditelluride integrated with a silicon nanobeam cavity," *Nature Nanotechnology*, vol. 12, pp. 987–992, jul 2017.

[65] R. J. Toh, C. C. Mayorga-Martinez, J. Han, Z. Sofer, and M. Pumera, "Group 6 layered transition-metal dichalcogenides in Lab-on-a-Chip devices: 1T-phase WS_2 for microfluidics non-enzymatic detection of hydrogen peroxide," *Analytical Chemistry*, vol. 89, pp. 4978–4985, apr 2017.

[66] C. Gong, H. Zhang, W. Wang, L. Colombo, R. M. Wallace, and K. Cho, "Band alignment of two-dimensional transition metal dichalcogenides: Application in tunnel field effect transistors," *Applied Physics Letters*, vol. 103, p. 053513, jul 2013.

[67] J. A. Wilson and A. D. Yoffe, "The transition metal dichalcogenides discussion and interpretation of the observed optical, electrical and structural properties," *Advances in Physics*, vol. 18, pp. 193–335, may 1969.

[68] A. A. Puretzky, L. Liang, X. Li, K. Xiao, K. Wang, M. Mahjouri-Samani, L. Basile, J. C. Idrobo, B. G. Sumpter, V. Meunier, and D. B. Geohegan, "Low-frequency Raman fingerprints of two-dimensional metal dichalcogenide layer stacking configurations," *ACS Nano*, vol. 9, pp. 6333–6342, may 2015.

[69] H. Zeng, G.-B. Liu, J. Dai, Y. Yan, B. Zhu, R. He, L. Xie, S. Xu, X. Chen, W. Yao, and X. Cui, "Optical signature of symmetry variations and spin-valley coupling in atomically thin tungsten dichalcogenides," *Scientific reports*, vol. 3, p. 1608, 2013.

[70] Z. Y. Zhu, Y. C. Cheng, and U. Schwingenschlögl, "Giant spin-orbit-induced spin splitting in two-dimensional transition-metal dichalcogenide semiconductors," *Physical Review B*, vol. 84, oct 2011.

[71] Y. S. Gui, C. R. Becker, N. Dai, J. Liu, Z. J. Qiu, E. G. Novik, M. Schäfer, X. Z. Shu, J. H. Chu, H. Buhmann, and L. W. Molenkamp, "Giant spin-orbit splitting in a HgTe quantum well," *Physical Review B*, vol. 70, p. 115328, sep 2004.

[72] A. Chernikov, T. C. Berkelbach, H. M. Hill, A. Rigosi, Y. Li, O. B. Aslan, D. R. Reichman, M. S. Hybertsen, and T. F. Heinz, "Exciton binding energy and nonhydrogenic Rydberg series in monolayer WS_2," *Physical Review Letters*, vol. 113, aug 2014.

[73] J. Frenkel, "On the transformation of light into heat in solids. I," *Physical Review*, vol. 37, pp. 17–44, jan 1931.

[74] G. H. Wannier, "The structure of electronic excitation levels in insulating crystals," *Physical Review*, vol. 52, pp. 191–197, aug 1937.

[75] S. Chichibu, A. Shikanai, T. Azuhata, T. Sota, A. Kuramata, K. Horino, and S. Nakamura, "Effects of biaxial strain on exciton resonance energies of hexagonal GaN heteroepitaxial layers," *Applied Physics Letters*, vol. 68, pp. 3766–3768, jun 1996.

[76] A. Steinhoff, M. Rösner, F. Jahnke, T. O. Wehling, and C. Gies, "Influence of excited carriers on the optical and electronic properties of MoS_2," *Nano Letters*, vol. 14, pp. 3743–3748, jun 2014.

[77] D. Y. Qiu, F. H. da Jornada, and S. G. Louie, "Optical spectrum of MoS_2: Many-body effects and diversity of exciton states," *Physical Review Letters*, vol. 111, p. 216805, nov 2013.

[78] A. Chernikov, A. M. van der Zande, H. M. Hill, A. F. Rigosi, A. Velauthapillai, J. Hone, and T. F. Heinz, "Electrical tuning of exciton binding energies in monolayer WS_2," *Physical Review Letters*, vol. 115, p. 126802, sep 2015.

[79] M. He, P. Rivera, D. V. Tuan, N. P. Wilson, M. Yang, T. Taniguchi, K. Watanabe, J. Yan, D. G. Mandrus, H. Yu, H. Dery, W. Yao, and X. Xu, "Valley phonons and exciton complexes in a monolayer semiconductor," *Nature Communications*, vol. 11, jan 2020.

[80] A. Steinhoff, M. Florian, M. Rösner, G. Schönhoff, T. O. Wehling, and F. Jahnke, "Exciton fission in monolayer transition metal dichalcogenide semiconductors," *Nature communications*, vol. 8, no. 1, pp. 1–11, 2017.

[81] A. Chernikov, C. Ruppert, H. M. Hill, A. F. Rigosi, and T. F. Heinz, "Population inversion and giant bandgap renormalization in atomically thin WS_2 layers," *Nature Photonics*, vol. 9, no. 7, pp. 466–470, 2015.

[82] A. Rustagi and A. F. Kemper, "Photoemission signature of excitons," *Physical Review B*, vol. 97, no. 23, p. 235310, 2018.

[83] D. Christiansen, M. Selig, E. Malic, R. Ernstorfer, and A. Knorr, "Theory of exciton dynamics in time-resolved ARPES: Intra-and intervalley scattering in two-dimensional semiconductors," *Physical Review B*, vol. 100, no. 20, p. 205401, 2019.

[84] R. Bertoni, C. W. Nicholson, L. Waldecker, H. Hübener, C. Monney, U. D. Giovannini, M. Puppin, M. Hoesch, E. Springate, R. T. Chapman, C. Cacho, M. Wolf, A. Rubio, and R. Ernstorfer, "Generation and evolution of spin-, valley-, and layer-polarized excited carriers in inversion-symmetric WSe_2," *Physical Review Letters*, vol. 117, p. 277201, dec 2016.

[85] J. Madéo, M. K. L. Man, C. Sahoo, M. Campbell, V. Pareek, E. L. Wong, A. Al-Mahboob, N. S. Chan, A. Karmakar, B. M. K. Mariserla, X. Li, T. F. Heinz, T. Cao, and K. M. Dani, "Directly visualizing the momentum-forbidden dark excitons and their dynamics in atomically thin semiconductors," *Science*, vol. 370, pp. 1199–1204, dec 2020.

[86] R. Wallauer, R. Perea-Causin, L. Münster, S. Zajusch, S. Brem, J. Güdde, K. Tanimura, K. Lin, R. Huber, E. Malic, and U. Höfer, "Direct observation of ultrafast dark exciton formation in monolayer WS_2," 2020.

[87] W. Yao, D. Xiao, and Q. Niu, "Valley-dependent optoelectronics from inversion symmetry breaking," *Physical Review B*, vol. 77, jun 2008.

[88] D. Xiao, G.-B. Liu, W. Feng, X. Xu, and W. Yao, "Coupled spin and valley physics in monolayers of MoS_2 and other group-VI dichalcogenides," *Physical Review Letters*, vol. 108, may 2012.

[89] T. Cao, G. Wang, W. Han, H. Ye, C. Zhu, J. Shi, Q. Niu, P. Tan, E. Wang, B. Liu, and J. Feng, "Valley-selective circular dichroism of monolayer molybdenum disulphide," *Nature Communications*, vol. 3, jan 2012.

[90] I. Paradisanos, K. M. McCreary, D. Adinehloo, L. Mouchliadis, J. T. Robinson, H.-J. Chuang, A. T. Hanbicki, V. Perebeinos, B. T. Jonker, E. Stratakis, and G. Kioseoglou, "Prominent room temperature valley polarization in WS2/graphene heterostructures grown by chemical vapor deposition," *Applied Physics Letters*, vol. 116, p. 203102, may 2020.

[91] H. Zeng, J. Dai, W. Yao, D. Xiao, and X. Cui, "Valley polarization in MoS_2 monolayers by optical pumping," *Nature Nanotechnology*, vol. 7, pp. 490–493, jun 2012.

[92] K. F. Mak, K. He, J. Shan, and T. F. Heinz, "Control of valley polarization in monolayer MoS2 by optical helicity," *Nature Nanotechnology*, vol. 7, pp. 494–498, jun 2012.

[93] L. Xie and X. Cui, "Manipulating spin-polarized photocurrents in 2D transition metal dichalcogenides," *Proceedings of the National Academy of Sciences*, vol. 113, pp. 3746–3750, mar 2016.

[94] X. Song, S. Xie, K. Kang, J. Park, and V. Sih, "Long-lived hole spin/valley polarization probed by kerr rotation in monolayer WSe2," *Nano Letters*, vol. 16, pp. 5010–5014, jul 2016.

[95] K. F. Mak, K. L. McGill, J. Park, and P. L. McEuen, "The valley Hall effect in MoS_2 transistors," *Science*, vol. 344, pp. 1489–1492, jun 2014.

[96] H. C. Diaz, J. Avila, C. Chen, R. Addou, M. C. Asensio, and M. Batzill, "Direct observation of interlayer hybridization and Dirac relativistic carriers in graphene/MoS_2 van der waals heterostructures," *Nano Letters*, vol. 15, pp. 1135–1140, jan 2015.

[97] M. M. Ugeda, A. J. Bradley, S.-F. Shi, F. H. da Jornada, Y. Zhang, D. Y. Qiu, W. Ruan, S.-K. Mo, Z. Hussain, Z.-X. Shen, F. Wang, S. G. Louie, and M. F. Crommie, "Giant bandgap renormalization and excitonic effects in a monolayer transition metal dichalcogenide semiconductor," *Nature Materials*, vol. 13, pp. 1091–1095, aug 2014.

[98] Z. Wang, P. Altmann, C. Gadermaier, Y. Yang, W. Li, L. Ghirardini, C. Trovatello, M. Finazzi, L. Duò, M. Celebrano, R. Long, D. Akinwande, O. V. Prezhdo, G. Cerullo, and S. D. Conte, "Phonon-mediated interlayer charge separation and recombination in a $MoSe_2/WSe_2$ heterostructure," *Nano Letters*, vol. 21, pp. 2165–2173, feb 2021.

[99] S. Mashhadi, Y. Kim, J. Kim, D. Weber, T. Taniguchi, K. Watanabe, N. Park, B. Lotsch, J. H. Smet, M. Burghard, and K. Kern, "Spin-split band hybridization in graphene proximitized with α-RuCl3 nanosheets," *Nano Letters*, vol. 19, pp. 4659–4665, jun 2019.

[100] S. Jafarpisheh, A. W. Cummings, K. Watanabe, T. Taniguchi, B. Beschoten, and C. Stampfer, "Proximity-induced spin-orbit coupling in graphene/ $bi_{1.5}sb_{0.5}te_{1.7}se_{1.3}$ heterostructures," *Physical Review B*, vol. 98, p. 241402, dec 2018.

[101] S. Zihlmann, A. W. Cummings, J. H. Garcia, M. Kedves, K. Watanabe, T. Taniguchi, C. Schönenberger, and P. Makk, "Large spin relaxation anisotropy and valley-zeeman spin-orbit coupling in WSe2 /graphene/ h -BN heterostructures," *Physical Review B*, vol. 97, p. 075434, feb 2018.

[102] X. Hong, J. Kim, S.-F. Shi, Y. Zhang, C. Jin, Y. Sun, S. Tongay, J. Wu, Y. Zhang, and F. Wang, "Ultrafast charge transfer in atomically thin Mos_2/WS_2 heterostructures," *Nature nanotechnology*, vol. 9, no. 9, pp. 682–686, 2014.

[103] F. Ceballos, M. Z. Bellus, H.-Y. Chiu, and H. Zhao, "Ultrafast charge separation and indirect exciton formation in a MoS_2-$MoSe_2$ van der Waals heterostructure," *ACS nano*, vol. 8, no. 12, pp. 12717–12724, 2014.

[104] P. Rivera, J. R. Schaibley, A. M. Jones, J. S. Ross, S. Wu, G. Aivazian, P. Klement, K. Seyler, G. Clark, N. J. Ghimire, J. Yan, D. G. Mandrus, W. Yao, and X. Xu, "Observation of long-lived interlayer excitons in monolayer $MoSe_2$–WSe_2 heterostructures," *Nature Communications*, vol. 6, feb 2015.

[105] H. Chen, X. Wen, J. Zhang, T. Wu, Y. Gong, X. Zhang, J. Yuan, C. Yi, J. Lou, P. M. Ajayan, W. Zhuang, G. Zhang, and J. Zheng, "Ultrafast formation of interlayer hot excitons in atomically thin MoS_2/WS_2 heterostructures," *Nature Communications*, vol. 7, aug 2016.

[106] P. Zereshki, P. Yao, D. He, Y. Wang, and H. Zhao, "Interlayer charge transfer in ReS_2/WS_2 van der Waals heterostructures," *Physical Review B*, vol. 99, no. 19, p. 195438, 2019.

[107] P. Zereshki, Y. Wei, R. Long, and H. Zhao, "Layer-coupled states facilitate ultrafast charge transfer in a transition metal dichalcogenide trilayer heterostructure," *The Journal of Physical Chemistry Letters*, vol. 9, no. 20, pp. 5970–5978, 2018.

[108] Z. Nie, Y. Wang, Z. Li, Y. Sun, S. Qin, X. Liu, I. C. E. Turcu, Y. Shi, R. Zhang, Y. Ye, Y. Xu, G. Cerullo, and F. Wang, "Ultrafast free carrier dynamics in black phosphorus-molybdenum disulfide (BP/MoS_2) heterostructures," *Nanoscale Horizons*, vol. 4, no. 5, pp. 1099–1105, 2019.

[109] S. Ovesen, S. Brem, C. Linderälv, M. Kuisma, T. Korn, P. Erhart, M. Selig, and E. Malic, "Interlayer exciton dynamics in van der Waals heterostructures," *Communications Physics*, vol. 2, no. 1, pp. 1–8, 2019.

[110] P. Merkl, F. Mooshammer, P. Steinleitner, A. Girnghuber, K.-Q. Lin, P. Nagler, J. Holler, C. Schüller, J. M. Lupton, T. Korn, S. Ovesen, S. Brem, E. Malic, and R. Huber, "Ultrafast transition between exciton phases in van der Waals heterostructures," *Nature Materials*, vol. 18, pp. 691–696, apr 2019.

[111] S. Fu, I. d. Fossé, X. Jia, J. Xu, X. Yu, H. Zhang, W. Zheng, S. Krasel, Z. Chen, Z. M. Wang, K.-J. Tielrooij, M. Bonn, A. J. Houtepen, and H. I. Wang, "Long-lived charge separation following pump-energy dependent ultrafast charge transfer in graphene/WS_2 heterostructures," *arXiv preprint arXiv:2007.08932*, 2020.

[112] Q. Zheng, W. A. Saidi, Y. Xie, Z. Lan, O. V. Prezhdo, H. Petek, and J. Zhao, "Phonon-assisted ultrafast charge transfer at van der Waals heterostructure interface," *Nano letters*, vol. 17, no. 10, pp. 6435–6442, 2017.

[113] S. Latini, K. T. Winther, T. Olsen, and K. S. Thygesen, "Interlayer excitons and band alignment in MoS2/hBN/WSe_2 van der waals heterostructures," *Nano Letters*, vol. 17, pp. 938–945, jan 2017.

[114] J. Zhang, H. Hong, C. Lian, W. Ma, X. Xu, X. Zhou, H. Fu, K. Liu, and S. Meng, "Interlayer-state-coupling dependent ultrafast charge transfer in MoS_2/WS_2 bilayers," *Advanced Science*, vol. 4, p. 1700086, apr 2017.

[115] R. Berera, R. van Grondelle, and J. T. M. Kennis, "Ultrafast transient absorption spectroscopy: principles and application to photosynthetic systems," *Photosynthesis Research*, vol. 101, pp. 105–118, jul 2009.

[116] H. Hertz, "Ueber einen einfluss des ultravioletten lichtes auf die electrische entladung," *Annalen der Physik und Chemie*, vol. 267, no. 8, pp. 983–1000, 1887.

[117] A. Einstein, "Ueber einen die erzeugung und verwandlung des lichtes betreffenden heuristischen gesichtspunkt," *Annalen der Physik*, vol. 14, pp. 164–181, feb 2005.

[118] S. Hüfner, *Photoelectron spectroscopy: principles and applications*. Springer Science & Business Media, 2013.

[119] A. Damascelli, Z. Hussain, and Z.-X. Shen, "Angle-resolved photoemission studies of the cuprate superconductors," *Reviews of Modern Physics*, vol. 75, pp. 473–541, apr 2003.

[120] J. Hölzl, F. K. Schulte, and H. Wagner, *Solid surface physics*, vol. 85. Springer, 2006.

[121] C. N. Berglund and W. E. Spicer, "Photoemission studies of copper and silver: Experiment," *Physical Review*, vol. 136, pp. A1044–A1064, nov 1964.

[122] S. Moser, "An experimentalist's guide to the matrix element in angle resolved photoemission," *Journal of Electron Spectroscopy and Related Phenomena*, vol. 214, pp. 29–52, jan 2017.

[123] I. Gierz, J. Henk, H. Höchst, C. R. Ast, and K. Kern, "Illuminating the dark corridor in graphene: Polarization dependence of angle-resolved photoemission spectroscopy on graphene," *Physical Review B*, vol. 83, p. 121408, mar 2011.

[124] J. C. Johannsen, S. Ulstrup, M. Bianchi, R. Hatch, D. Guan, F. Mazzola, L. Hornekær, F. Fromm, C. Raidel, T. Seyller, and P. Hofmann, "Electron-phonon coupling in quasi-free-standing graphene," *Journal of Physics: Condensed Matter*, vol. 25, p. 094001, feb 2013.

[125] F. Reinert, "Spin orbit interaction in the photoemission spectra of noble metal surface states," *Journal of Physics: Condensed Matter*, vol. 15, pp. S693–S705, feb 2003.

[126] M. Sentef, A. F. Kemper, B. Moritz, J. K. Freericks, Z.-X. Shen, and T. P. Devereaux, "Examining electron-boson coupling using time-resolved spectroscopy," *Physical Review X*, vol. 3, p. 041033, dec 2013.

[127] M. P. Seah and W. A. Dench, "Quantitative electron spectroscopy of surfaces: A standard data base for electron inelastic mean free paths in solids," *Surface and Interface Analysis*, vol. 1, pp. 2–11, feb 1979.

[128] J. D. Koralek, J. F. Douglas, N. C. Plumb, J. D. Griffith, S. T. Cundiff, H. C. Kapteyn, M. M. Murnane, and D. S. Dessau, "Experimental setup for low-energy laser-based angle resolved photoemission spectroscopy," *Review of Scientific Instruments*, vol. 78, p. 053905, may 2007.

[129] T. F. Nova, A. Cartella, A. Cantaluppi, M. Först, D. Bossini, R. V. Mikhaylovskiy, A. V. Kimel, R. Merlin, and A. Cavalleri, "An effective magnetic field from optically driven phonons," *Nature Physics*, vol. 13, pp. 132–136, oct 2016.

[130] J. Reimann, S. Schlauderer, C. P. Schmid, F. Langer, S. Baierl, K. A. Kokh, O. E. Tereshchenko, A. Kimura, C. Lange, J. Güdde, U. Höfer, and R. Huber, "Subcycle observation of lightwave-driven Dirac currents in a topological surface band," *Nature*, vol. 562, pp. 396–400, sep 2018.

[131] S. K. Sundaram and E. Mazur, "Inducing and probing non-thermal transitions in semiconductors using femtosecond laser pulses," *Nature Materials*, vol. 1, pp. 217–224, dec 2002.

[132] G. Cerullo and S. D. Silvestri, "Ultrafast optical parametric amplifiers," *Review of Scientific Instruments*, vol. 74, pp. 1–18, jan 2003.

[133] R. L. Sutherland, D. G. McLean, and S. Kirkpatrick, *Handbook of nonlinear optics*. Marcel Dekker, New York, 2nd ed., rev. and expanded edition, 2003.

[134] I. Gierz, F. Calegari, S. Aeschlimann, M. C. Cervantes, C. Cacho, R. Chapman, E. Springate, S. Link, U. Starke, C. Ast, and A. Cavalleri, "Tracking primary thermalization events in graphene with photoemission at extreme time scales," *Physical Review Letters*, vol. 115, p. 086803, aug 2015.

[135] S. Zayko, O. Kfir, M. Heigl, M. Lohmann, M. Sivis, M. Albrecht, and C. Ropers, "Ultrafast high-harmonic nanoscopy of magnetization dynamics," 2020.

[136] F. Krausz and M. Ivanov, "Attosecond physics," *Reviews of Modern Physics*, vol. 81, pp. 163–234, feb 2009.

[137] M. Schultze, A. Wirth, I. Grguras, M. Uiberacker, T. Uphues, A. J. Verhoef, J. Gagnon, M. Hofstetter, U. Kleineberg, E. Goulielmakis, and F. Krausz, "State-of-the-art attosecond metrology," *Journal of Electron Spectroscopy and Related Phenomena*, vol. 184, pp. 68–77, apr 2011.

[138] T. Popmintchev, M.-C. Chen, P. Arpin, M. M. Murnane, and H. C. Kapteyn, "The attosecond nonlinear optics of bright coherent x-ray generation," *Nature Photonics*, vol. 4, pp. 822–832, nov 2010.

[139] S. Eich, A. Stange, A. V. Carr, J. Urbancic, T. Popmintchev, M. Wiesenmayer, K. Jansen, A. Ruffing, S. Jakobs, T. Rohwer, S. Hellmann, C. Chen, P. Matyba, L. Kipp, K. Rossnagel, M. Bauer, M. M. Murnane, H. C. Kapteyn, S. Mathias, and M. Aeschlimann, "Time- and angle-resolved photoemission spectroscopy with optimized high-harmonic pulses using frequency-doubled Ti:Sapphire lasers," *Journal of Electron Spectroscopy and Related Phenomena*, vol. 195, pp. 231–236, Aug. 2014.

[140] P. B. Corkum, "Plasma perspective on strong field multiphoton ionization," *Physical Review Letters*, vol. 71, pp. 1994–1997, sep 1993.

[141] H. Wang, Y. Xu, S. Ulonska, J. S. Robinson, P. Ranitovic, and R. A. Kaindl, "Bright high-repetition-rate source of narrowband extreme-ultraviolet harmonics beyond 22 eV," *Nature Communications*, vol. 6, p. 7459, jun 2015.

[142] A. D. Shiner, C. Trallero-Herrero, N. Kajumba, H.-C. Bandulet, D. Comtois, F. Légaré, M. Giguère, J.-C. Kieffer, P. B. Corkum, and D. M. Villeneuve, "Wavelength scaling of high harmonic generation efficiency," *Physical Review Letters*, vol. 103, p. 073902, aug 2009.

[143] J. L. Krause, K. J. Schafer, and K. C. Kulander, "High-order harmonic generation from atoms and ions in the high intensity regime," *Physical Review Letters*, vol. 68, pp. 3535–3538, jun 1992.

[144] F. Frassetto, C. Cacho, C. A. Froud, I. C. E. Turcu, P. Villoresi, W. A. Bryan, E. Springate, and L. Poletto, "Single-grating monochromator for extreme-ultraviolet ultrashort pulses," *Optics Express*, vol. 19, p. 19169, sep 2011.

[145] F. Frassetto, S. Bonora, P. Villoresi, L. Poletto, E. Springate, C. A. Froud, I. C. E. Turcu, A. J. Langley, D. S. Wolff, J. L. Collier, S. S. Dhesi, and A. Cavalleri, "Design and characterization of the XUV monochromator for ultrashort pulses at the ARTEMIS facility," in *Advances in X-Ray/EUV Optics and Components III* (S. Goto, A. M. Khounsary, and C. Morawe, eds.), SPIE, aug 2008.

[146] R. L. Fork, W. J. Tomlinson, C. V. Shank, C. Hirlimann, and R. Yen, "Femtosecond white-light continuum pulses," *Optics Letters*, vol. 8, p. 1, jan 1983.

[147] D. Kühn, F. Sorgenfrei, E. Giangrisostomi, R. Jay, A. Musazay, R. Ovsyannikov, C. Stråhlman, S. Svensson, N. Mårtensson, and A. Föhlisch, "Capabilities of angle resolved Time of Flight electron spectroscopy with the 60° wide angle acceptance lens," *Journal of Electron Spectroscopy and Related Phenomena*, vol. 224, pp. 45–50, apr 2018.

[148] E. Carpene, E. Mancini, C. Dallera, G. Ghiringhelli, C. Manzoni, G. Cerullo, and S. D. Silvestri, "A versatile apparatus for time-resolved photoemission spectroscopy via femtosecond pump-probe experiments," *Review of Scientific Instruments*, vol. 80, p. 055101, may 2009.

[149] J. Maklar, S. Dong, S. Beaulieu, T. Pincelli, M. Dendzik, Y. W. Windsor, R. P. Xian, M. Wolf, R. Ernstorfer, and L. Rettig, "A quantitative comparison of time-of-flight momentum microscopes and hemispherical analyzers for time- and angle-resolved photoemission spectroscopy experiments," *Review of Scientific Instruments*, vol. 91, p. 123112, dec 2020.

[150] C. M. Cacho, S. Vlaic, M. Malvestuto, B. Ressel, E. A. Seddon, and F. Parmigiani, "Absolute spin calibration of an electron spin polarimeter by spin-resolved photoemission from the Au(111) surface states," *Review of Scientific Instruments*, vol. 80, p. 043904, apr 2009.

[151] J. Graf, S. Hellmann, C. Jozwiak, C. L. Smallwood, Z. Hussain, R. A. Kaindl, L. Kipp, K. Rossnagel, and A. Lanzara, "Vacuum space charge effect in laser-based solid-state photoemission spectroscopy," *Journal of Applied Physics*, vol. 107, p. 014912, jan 2010.

[152] L.-P. Oloff, K. Hanff, A. Stange, G. Rohde, F. Diekmann, M. Bauer, and K. Rossnagel, "Pump laser-induced space-charge effects in HHG-driven time- and angle-resolved photoelectron spectroscopy," *Journal of Applied Physics*, vol. 119, p. 225106, jun 2016.

[153] M. Onodera, S. Masubuchi, R. Moriya, and T. Machida, "Assembly of van der Waals heterostructures: exfoliation, searching, and stacking of 2D materials," *Japanese Journal of Applied Physics*, vol. 59, p. 010101, jan 2020.

[154] K. S. Novoselov, D. Jiang, F. Schedin, T. J. Booth, V. V. Khotkevich, S. V. Morozov, and A. K. Geim, "Two-dimensional atomic crystals," *Proceedings of the National Academy of Sciences*, vol. 102, pp. 10451–10453, jul 2005.

[155] J. A. Robinson, "Growing vertical in the flatland," *ACS Nano*, vol. 10, pp. 42–45, jan 2016.

[156] Y. Zhang, Y. Yao, M. G. Sendeku, L. Yin, X. Zhan, F. Wang, Z. Wang, and J. He, "Recent progress in CVD growth of 2D transition metal dichalcogenides and related heterostructures," *Advanced Materials*, vol. 31, p. 1901694, aug 2019.

[157] C. Cong, J. Shang, X. Wu, B. Cao, N. Peimyoo, C. Qiu, L. Sun, and T. Yu, "Synthesis and optical properties of large-area single-crystalline 2D semiconductor WS_2 monolayer from chemical vapor deposition," *Advanced Optical Materials*, vol. 2, pp. 131–136, dec 2013.

[158] A. Rossi, D. Spirito, F. Bianco, S. Forti, F. Fabbri, H. Büch, A. Tredicucci, R. Krahne, and C. Coletti, "Patterned tungsten disulfide/graphene heterostructures for efficient multifunctional optoelectronic devices," *Nanoscale*, vol. 10, no. 9, pp. 4332–4338, 2018.

[159] K. V. Emtsev, A. Bostwick, K. Horn, J. Jobst, G. L. Kellogg, L. Ley, J. L. McChesney, T. Ohta, S. A. Reshanov, J. Röhrl, E. Rotenberg, A. K. Schmid, D. Waldmann, H. B. Weber, and T. Seyller, "Towards wafer-size graphene layers by atmospheric pressure graphitization of silicon carbide," *Nature Materials*, vol. 8, pp. 203–207, feb 2009.

[160] A. J. V. Bommel, J. E. Crombeen, and A. V. Tooren, "LEED and auger electron observations of the SiC(0001) surface," *Surface Science*, vol. 48, pp. 463–472, mar 1975.

[161] K. V. Emtsev, F. Speck, T. Seyller, L. Ley, and J. D. Riley, "Interaction, growth, and ordering of epitaxial graphene on SiC(0001) surfaces: A comparative photoelectron spectroscopy study," *Physical Review B*, vol. 77, apr 2008.

[162] C. Virojanadara, A. A. Zakharov, R. Yakimova, and L. I. Johansson, "Buffer layer free large area bi-layer graphene on SiC(0001)," *Surface Science*, vol. 604, pp. L4–L7, jan 2010.

[163] C. Riedl, C. Coletti, T. Iwasaki, A. A. Zakharov, and U. Starke, "Quasi-free-standing epitaxial graphene on SiC obtained by hydrogen intercalation," *Physical Review Letters*, vol. 103, dec 2009.

[164] S. Forti, A. Rossi, H. Büch, T. Cavallucci, F. Bisio, A. Sala, T. O. Menteş, A. Locatelli, M. Magnozzi, M. Canepa, K. Müller, S. Link, U. Starke, V. Tozzini, and C. Coletti, "Electronic properties of single-layer tungsten disulfide on epitaxial graphene on silicon carbide," *Nanoscale*, vol. 9, no. 42, pp. 16412–16419, 2017.

[165] F. Fabbri, F. Dinelli, S. Forti, L. Sementa, S. Pace, G. Piccinini, A. Fortunelli, C. Coletti, and P. Pingue, "Edge defects promoted oxidation of monolayer WS_2 synthesized on epitaxial graphene," *The Journal of Physical Chemistry C*, vol. 124, pp. 9035–9044, mar 2020.

[166] C. L. Frewin, C. Coletti, C. Riedl, U. Starke, and S. E. Saddow, "A comprehensive study of hydrogen etching on the major SiC polytypes and crystal orientations," *Materials Science Forum*, vol. 615-617, pp. 589–592, mar 2009.

[167] A. Berkdemir, H. R. Gutiérrez, A. R. Botello-Méndez, N. Perea-López, A. L. Elías, C.-I. Chia, B. Wang, V. H. Crespi, F. López-Urías, J.-C. Charlier, H. Terrones, and M. Terrones, "Identification of individual and few layers of WS_2 using Raman spectroscopy," *Scientific Reports*, vol. 3, apr 2013.

[168] V. Carozo, Y. Wang, K. Fujisawa, B. R. Carvalho, A. McCreary, S. Feng, Z. Lin, C. Zhou, N. Perea-López, A. L. Elías, B. Kabius, V. H. Crespi, and M. Terrones, "Optical identification of sulfur vacancies: Bound excitons at the edges of monolayer tungsten disulfide," *Science Advances*, vol. 3, p. e1602813, apr 2017.

[169] E. Malic and A. Knorr, *Graphene and carbon nanotubes: ultrafast optics and relaxation dynamics*. John Wiley & Sons, 2013.

[170] S. Brem, C. Linderälv, P. Erhart, and E. Malic, "Tunable phases of moiré excitons in van der Waals heterostructures," *Nano Letters*, vol. 20, pp. 8534–8540, sep 2020.

[171] S. Brem, K.-Q. Lin, R. Gillen, J. M. Bauer, J. Maultzsch, J. M. Lupton, and E. Malic, "Hybridized intervalley moiré excitons and flat bands in twisted WSe_2 bilayers," *Nanoscale*, vol. 12, no. 20, pp. 11088–11094, 2020.

[172] J. wei Wei, Z. wei Ma, H. Zeng, Z. yong Wang, Q. Wei, and P. Peng, "Electronic and optical properties of vacancy-doped WS_2 monolayers," *AIP Advances*, vol. 2, p. 042141, dec 2012.

[173] B. Schuler, D. Y. Qiu, S. Refaely-Abramson, C. Kastl, C. T. Chen, S. Barja, R. J. Koch, D. F. Ogletree, S. Aloni, A. M. Schwartzberg, J. B. Neaton, S. G. Louie, and A. Weber-Bargioni, "Large spin-orbit splitting of deep in-gap defect states of engineered sulfur vacancies in monolayer WS_2," *Physical Review Letters*, vol. 123, aug 2019.

[174] S. Ulstrup, A. G. Cabo, J. A. Miwa, J. M. Riley, S. S. Grønborg, J. C. Johannsen, C. Cacho, O. Alexander, R. T. Chapman, E. Springate, M. Bianchi, M. Dendzik, J. V. Lauritsen, P. D. C. King, and P. Hofmann, "Ultrafast band structure control of a two-dimensional heterostructure," *ACS nano*, vol. 10, no. 6, pp. 6315–6322, 2016.

[175] F. Liu, M. E. Ziffer, K. R. Hansen, J. Wang, and X. Zhu, "Direct determination of band-gap renormalization in the photoexcited monolayer MoS_2," *Physical review letters*, vol. 122, no. 24, p. 246803, 2019.

[176] K. Yao, A. Yan, S. Kahn, A. Suslu, Y. Liang, E. S. Barnard, S. Tongay, A. Zettl, N. Borys, and P. J. Schuck, "Optically discriminating carrier-induced quasiparticle band gap and exciton energy renormalization in monolayer MoS_2," *Physical Review Letters*, vol. 119, p. 087401, aug 2017.

[177] R. W. Boyd, *Nonlinear Optics*. Academic Press, 2008.

[178] R. Long and O. V. Prezhdo, "Quantum coherence facilitates efficient charge separation at a $MoS_2/MoSe_2$ van der Waals junction," *Nano letters*, vol. 16, no. 3, pp. 1996–2003, 2016.

[179] H. Wang, J. Bang, Y. Sun, L. Liang, D. West, V. Meunier, and S. Zhang, "The role of collective motion in the ultrafast charge transfer in van der Waals heterostructures," *Nature communications*, vol. 7, no. 1, pp. 1–9, 2016.

[180] Y. Wang, Z. Wang, W. Yao, G.-B. Liu, and H. Yu, "Interlayer coupling in commensurate and incommensurate bilayer structures of transition-metal dichalcogenides," *Physical Review B*, vol. 95, mar 2017.

[181] L. Li, R. Long, and O. V. Prezhdo, "Charge separation and recombination in two-dimensional MoS2/WS2: Time-domain ab initio modeling," *Chemistry of Materials*, vol. 29, pp. 2466–2473, nov 2016.

[182] X. Zhu, N. R. Monahan, Z. Gong, H. Zhu, K. W. Williams, and C. A. Nelson, "Charge transfer excitons at van der Waals interfaces," *Journal of the American Chemical Society*, vol. 137, pp. 8313–8320, jun 2015.

[183] E. Skoplaki and J. Palyvos, "On the temperature dependence of photovoltaic module electrical performance: A review of efficiency/power correlations," *Solar Energy*, vol. 83, pp. 614–624, may 2009.

[184] R. R. King, D. C. Law, K. M. Edmondson, C. M. Fetzer, G. S. Kinsey, H. Yoon, D. D. Krut, J. H. Ermer, R. A. Sherif, and N. H. Karam, "Advances in high-efficiency III-V multijunction solar cells," *Advances in OptoElectronics*, vol. 2007, pp. 1–8, 2007.

[185] A. Avsar, H. Ochoa, F. Guinea, B. Özyilmaz, B. van Wees, and I. Vera-Marun, "Colloquium: Spintronics in graphene and other two-dimensional materials," *Reviews of Modern Physics*, vol. 92, p. 021003, jun 2020.

[186] A. Raja, M. Selig, G. Berghäuser, J. Yu, H. M. Hill, A. F. Rigosi, L. E. Brus, A. Knorr, T. F. Heinz, E. Malic, and A. Chernikov, "Enhancement of exciton–phonon scattering from monolayer to bilayer WS_2," *Nano Letters*, vol. 18, pp. 6135–6143, aug 2018.

[187] Y. Li, X. Li, T. Yu, G. Yang, H. Chen, C. Zhang, Q. Feng, J. Ma, W. Liu, H. Xu, Y. Liu, and X. Liu, "Accurate identification of layer number for few-layer WS_2 and WSe_2 via spectroscopic study," *Nanotechnology*, vol. 29, p. 124001, feb 2018.

[188] E. A. A. Pogna, M. Marsili, D. D. Fazio, S. D. Conte, C. Manzoni, D. Sangalli, D. Yoon, A. Lombardo, A. C. Ferrari, A. Marini, G. Cerullo, and D. Prezzi, "Photo-induced bandgap renormalization governs the ultrafast response of single-layer MoS_2," *ACS Nano*, vol. 10, pp. 1182–1188, jan 2016.

[189] N. R. Wilson, P. V. Nguyen, K. Seyler, P. Rivera, A. J. Marsden, Z. P. Laker, G. C. Constantinescu, V. Kandyba, A. Barinov, N. D. Hine, X. Xu, and D. H. Cobden, "Determination of band offsets, hybridization, and exciton binding in 2d semiconductor heterostructures," *Science Advances*, vol. 3, p. e1601832, feb 2017.

[190] H. P. Maruska, W. C. Rhines, and D. A. Stevenson, "Preparation of Mg-doped GaN diodes exhibiting violet electroluminescence," *Materials Research Bulletin*, vol. 7, pp. 777–781, aug 1972.

[191] J. Y. Tsao, M. H. Crawford, M. E. Coltrin, A. J. Fischer, D. D. Koleske, G. S. Subramania, G. T. Wang, J. J. Wierer, and R. F. Karlicek, "Toward smart and ultra-efficient solid-state lighting," *Advanced Optical Materials*, vol. 2, pp. 809–836, jun 2014.

[192] J. Katoch, S. Ulstrup, R. J. Koch, S. Moser, K. M. McCreary, S. Singh, J. Xu, B. T. Jonker, R. K. Kawakami, A. Bostwick, E. Rotenberg, and C. Jozwiak, "Giant spin-splitting and gap renormalization driven by trions in single-layer WS_2/h-BN heterostructures," *Nature Physics*, vol. 14, no. 4, pp. 355–359, 2018.

[193] Y. Zhang, T.-R. Chang, B. Zhou, Y.-T. Cui, H. Yan, Z. Liu, F. Schmitt, J. Lee, R. Moore, Y. Chen, H. Lin, H.-T. Jeng, S.-K. Mo, Z. Hussain, A. Bansil, and Z.-X. Shen, "Direct observation of the transition from indirect to direct bandgap in atomically thin epitaxial $MoSe_2$," *Nature Nanotechnology*, vol. 9, pp. 111–115, dec 2013.

[194] L. Waldecker, A. Raja, M. Rösner, C. Steinke, A. Bostwick, R. J. Koch, C. Jozwiak, T. Taniguchi, K. Watanabe, E. Rotenberg, T. O. Wehling, and T. F. Heinz, "Rigid band

shifts in two-dimensional semiconductors through external dielectric screening," *Physical Review Letters*, vol. 123, p. 206403, nov 2019.

[195] D. Erben, A. Steinhoff, C. Gies, G. Schönhoff, T. O. Wehling, and F. Jahnke, "Excitation-induced transition to indirect band gaps in atomically thin transition-metal dichalcogenide semiconductors," *Physical Review B*, vol. 98, p. 035434, jul 2018.

[196] M. Rösner, E. Şaşıoğlu, C. Friedrich, S. Blügel, and T. O. Wehling, "Wannier function approach to realistic Coulomb interactions in layered materials and heterostructures," *Physical Review B*, vol. 92, p. 085102, aug 2015.

[197] M. Florian, M. Hartmann, A. Steinhoff, J. Klein, A. W. Holleitner, J. J. Finley, T. O. Wehling, M. Kaniber, and C. Gies, "The dielectric impact of layer distances on exciton and trion binding energies in van der Waals heterostructures," *Nano Letters*, vol. 18, pp. 2725–2732, mar 2018.

[198] S. ichiro Tanaka, "Utility and constraint on the use of pump-probe photoelectron spectroscopy for detecting time-resolved surface photovoltage," *Journal of Electron Spectroscopy and Related Phenomena*, vol. 185, pp. 152–158, aug 2012.

[199] S.-L. Yang, J. A. Sobota, P. S. Kirchmann, and Z.-X. Shen, "Electron propagation from a photo-excited surface: implications for time-resolved photoemission," *Applied Physics A*, vol. 116, pp. 85–90, nov 2013.

[200] I. Gierz, T. Suzuki, R. T. Weitz, D. S. Lee, B. Krauss, C. Riedl, U. Starke, H. Höchst, J. H. Smet, C. R. Ast, and K. Kern, "Electronic decoupling of an epitaxial graphene monolayer by gold intercalation," *Physical Review B*, vol. 81, p. 235408, jun 2010.

[201] J. C. Johannsen, S. Ulstrup, A. Crepaldi, F. Cilento, M. Zacchigna, J. A. Miwa, C. Cacho, R. T. Chapman, E. Springate, F. Fromm, C. Raidel, T. Seyller, P. D. C. King, F. Parmigiani, M. Grioni, and P. Hofmann, "Tunable carrier multiplication and cooling in graphene," *Nano Letters*, vol. 15, pp. 326–331, dec 2014.

[202] L. Liang, J. Zhang, B. G. Sumpter, Q.-H. Tan, P.-H. Tan, and V. Meunier, "Low-frequency shear and layer-breathing modes in Raman scattering of two-dimensional materials," *ACS nano*, vol. 11, no. 12, pp. 11777–11802, 2017.

[203] A. M. Weiner, G. P. Wiederrecht, K. A. Nelson, and D. E. Leaird, "Femtosecond multiple-pulse impulsive stimulated Raman scattering spectroscopy," *Journal of the Optical Society of America B*, vol. 8, p. 1264, jun 1991.

[204] Y.-X. Yan, E. B. Gamble Jr., and K. A. Nelson, "Impulsive stimulated scattering: General importance in femtosecond laser pulse interactions with matter, and spectroscopic applications," *The Journal of chemical physics*, vol. 83, no. 11, pp. 5391–5399, 1985.

[205] I. A. Walmsley, F. W. Wise, and C. L. Tang, "On the difference between quantum beats in impulsive stimulated Raman scattering and resonance Raman scattering," *Chemical Physics Letters*, vol. 154, pp. 315–320, jan 1989.

[206] H. Zhu, J. Wang, Z. Gong, Y. D. Kim, J. Hone, and X.-Y. Zhu, "Interfacial charge transfer circumventing momentum mismatch at two-dimensional van der Waals heterojunctions," *Nano Letters*, vol. 17, pp. 3591–3598, may 2017.

[207] Z. Ji, H. Hong, J. Zhang, Q. Zhang, W. Huang, T. Cao, R. Qiao, C. Liu, J. Liang, C. Jin, L. Jiao, K. Shi, S. Meng, and K. Liu, "Robust stacking-independent ultrafast charge transfer in MoS_2/WS_2 bilayers," *ACS Nano*, vol. 11, pp. 12020–12026, nov 2017.

[208] J. Choi, M. Florian, A. Steinhoff, D. Erben, K. Tran, D. S. Kim, L. Sun, J. Quan, R. Claassen, S. Majumder, J. A. Hollingsworth, T. Taniguchi, K. Watanabe, K. Ueno, A. Singh, G. Moody, F. Jahnke, and X. Li, "Twist angle-dependent interlayer exciton lifetimes in van der Waals heterostructures," *Physical Review Letters*, vol. 126, p. 047401, jan 2021.

[209] P.-C. Yeh, W. Jin, N. Zaki, J. Kunstmann, D. Chenet, G. Arefe, J. T. Sadowski, J. I. Dadap, P. Sutter, J. Hone, and R. M. Osgood, "Direct measurement of the tunable electronic structure of bilayer MoS_2 by interlayer twist," *Nano Letters*, vol. 16, pp. 953–959, jan 2016.

[210] D. A. Ruiz-Tijerina and V. I. Fal'ko, "Interlayer hybridization and moiré superlattice minibands for electrons and excitons in heterobilayers of transition-metal dichalcogenides," *Physical Review B*, vol. 99, p. 125424, mar 2019.

[211] E. M. Alexeev, D. A. Ruiz-Tijerina, M. Danovich, M. J. Hamer, D. J. Terry, P. K. Nayak, S. Ahn, S. Pak, J. Lee, J. I. Sohn, M. R. Molas, M. Koperski, K. Watanabe, T. Taniguchi, K. S. Novoselov, R. V. Gorbachev, H. S. Shin, V. I. Fal'ko, and A. I. Tartakovskii, "Resonantly hybridized excitons in moiré superlattices in van der Waals heterostructures," *Nature*, vol. 567, pp. 81–86, mar 2019.

[212] M. Puppin, Y. Deng, C. W. Nicholson, J. Feldl, N. B. M. Schröter, H. Vita, P. S. Kirchmann, C. Monney, L. Rettig, M. Wolf, and R. Ernstorfer, "Time- and angle-resolved photoemission spectroscopy of solids in the extreme ultraviolet at 500 kHz repetition rate," *Review of Scientific Instruments*, vol. 90, p. 023104, feb 2019.

[213] Y. Li, A. Chernikov, X. Zhang, A. Rigosi, H. M. Hill, A. M. van der Zande, D. A. Chenet, E.-M. Shih, J. Hone, and T. F. Heinz, "Measurement of the optical dielectric function of monolayer transition-metal dichalcogenides: MoS_2, $MoSe_2$, WS_2 and WSe_2," *Physical Review B*, vol. 90, p. 205422, nov 2014.

[214] S. Ulstrup, J. C. Johannsen, M. Grioni, and P. Hofmann, "Extracting the temperature of hot carriers in time- and angle-resolved photoemission," *Review of Scientific Instruments*, vol. 85, p. 013907, jan 2014.

[215] F. Andreatta, H. Rostami, A. G. Čabo, M. Bianchi, C. E. Sanders, D. Biswas, C. Cacho, A. J. H. Jones, R. T. Chapman, E. Springate, P. D. C. King, J. A. Miwa, A. Balatsky, S. Ulstrup, and P. Hofmann, "Transient hot electron dynamics in single-layer TaS2," *Physical Review B*, vol. 99, p. 165421, apr 2019.

[216] M. Selig, E. Malic, K. J. Ahn, N. Koch, and A. Knorr, "Theory of optically induced förster coupling in van der waals coupled heterostructures," *Physical Review B*, vol. 99, p. 035420, jan 2019.

[217] A. Kormányos, G. Burkard, M. Gmitra, J. Fabian, V. Zólyomi, N. D. Drummond, and V. Fal'ko, "k · p theory for two-dimensional transition metal dichalcogenide semiconductors," *2D Materials*, vol. 2, p. 022001, apr 2015.

[218] M. Kira and S. W. Koch, "Many-body correlations and excitonic effects in semiconductor spectroscopy," *Progress in Quantum Electronics*, vol. 30, no. 5, pp. 155–296, 2006.

Acknowledgements

First of all, I am very grateful to my advisor **Prof. Isabella Gierz-Pehla** for the opportunity to work at her group and her constant support and guidance especially for helping me finding the right words at every occasion.

I would like to thank **Prof. Ludwig Mathey** for co-supervison of my thesis and the interesting conversations we had.

I thank **Prof. Andrea Cavalleri** for the opportunity to be part of his department at the Max-Planck Institute for the Structure and Dynamics of Matter and for hosting me as a guest scientist in 2020-2021.

Thanks to the **many people at the Condensed Matter Department** who helped us out for countless times, supported with fruitful discussions and created a great work atmosphere. These are PD Dr. Guido Meier, Dr. Toru Matsuyama, Dr. Michael Fechner, Dr. Michal Först, Michael Volkmann, Boris Fiedler, Dr. Elena König, Dr. Michaela Petrich, Dr. Gregor Jotzu, Dr. Wanzheng Hu, Dr. Alice Cantaluppi, Dr. Michele Buzzi, Dr. Tobia Nova, Dr. Andrea Cartella, Dr. Eliza Casandruc, Hubertus Bromberger, Dr. Falk-Ulrich Stein, Dr. Srivats Rajasekaran, Dr. Matthias Budden, Dr. Thomas Gebert, Dr. Daniele Nicoletti, Dr. James McIver, Dr. Eryin Wang, Dr. Amit Ribak, Dr. Ankit Disa, Dr. Meredith Henstrigde, Dr. Alex von Hoegen, Dr. Ken Beyerlein, Benedikt Schulte, Gunda Kipp and many more.

Amongst them, my lab-mates **Dr. Sven Aeschlimann** and **Dr. Mariana Chávez-Cervantes** deserve special attention. You guys were a great team and I enjoyed working with you so much! Thank you for your support and friendship throughout the years.

Many thanks to the **Group of Prof. Camilla Coletti in Pisa**: Dr. Stiven Forti, Filippo Fabbri and Dr. Antonio Rossi for the high-quality WS_2/graphene samples and for their support at the Artemis beamtime 2018. At the **Artemis User Facility** I would like to thank Dr. Cephise

Cacho, Dr. Yu Zhang, Paulina Ewa Majchrzak, Dr. Richard Chapman and Dr. Emma Springate for the opportunity to conduct the beamtime in 2018 and the experimental help meanwhile.

I would like to thank the **Group of Prof. Ermin Malic** from Chalmers University of Technology, Raul Perea Causin and Dr. Samuel Brem, for the microscopic many-body calculations towards charge transfer rates. Further, I thank **Dr. Alexander Steinhoff** and **Dr. Tim Wehling** from Universität Bremen for the great collaboration and many interesting discussions. Thanks to **Dr. Simone Latini** and **Dr. Lede Xian** from the Theory department of the Max-Planck Institute for the Structure and Dynamics of Matter for the supercell calculations and **Dr. Sivan Refaely-Abramson** and **Dr. Daniel Hernangomez** from Weizmann Institute for many discussions.

I want to thank the **Ultrafast Electron Dynamics group** of Prof. Isabella Gierz-Pehla at Universität Regensburg, namely Magdalena Pfleger, Florian Pogrzeba, Michael Herb, Maria-Elisabeth Federl and Niklas Hofmann. I wish you all the best with the new laboratory.

Last but not least, I am thankful to **Kathrin** and **Chloé** for beeing my family, for beeing my anchor when storm rises at the sea and for taking me as I am.

Eidesstattliche Versicherung / Declaration on oath

Hiermit erkläre ich an Eides statt, dass ich die vorliegende Dissertationsschrift selbst verfasst und keine anderen als die angegebenen Quellen und Hilfsmittel benutzt habe.

Die eingereichte schriftliche Fassung entspricht der auf dem elektronischen Speichermedium.

Die Dissertation wurde in der vorgelegten oder einer ähnlichen Form nicht schon einmal in einem früheren Promotionsverfahren angenommen oder als ungenügend beurteilt.

Hamburg, den 01.07.2021

Razvan Krause